The Dissertation Committee for Yousef Ghomian Certifies that this is the approved version of the following dissertation:

Reservoir Simulation Studies for Coupled CO_2 Sequestration and Enhanced Oil Recovery

Committee:

Gary A. Pope, Co-Supervisor

Kamy Sepehrnoori, Co-Supervisor

Larry W. Lake

Steven L. Bryant

Gary Rochelle

Reservoir Simulation Studies for Coupled CO_2 Sequestration and Enhanced Oil Recovery

by

Yousef Ghomian, B.S., M.S.

Dissertation

Presented to the Faculty of the Graduate School of

The University of Texas at Austin

in Partial Fulfillment

of the Requirements

for the Degree of

Doctor of Philosophy

The University of Texas at Austin

May 2008

In The Name of God, The Most Gracious, The Most Merciful

Dedication To

my divine wife, Rezvan and my respected parents

without whose support and endurance

this achievement would not have been possible

and

to my lovely daughter, Aileen

whose addition to my family

made this experience even more pleasant

and

to all my great teachers

to whom I owe all of my knowledge

and

TO ALL THOSE WHO

COMMITTED TO REAL PEACE AND SERENITY IN THIS WORLD

Acknowledgements

I would like to express my special appreciation to my supervisors Dr. Gary A. Pope and Dr. Kamy Sepehrnoori for their constant encouragement, guidance, patience during my Ph.D. studies. I am very grateful for their contributions to my professional accomplishments. I would also like to appreciate all guidance and comments that I received from my supervising committee members, Dr. Larry Lake, Dr. Gary Rochelle, and Dr. Steven Bryant.

I greatly acknowledge financial support for my studies from Iranian Ministry of Research, Science and Technology and other funding for this study provided by the sponsors of the Geological CO_2 Storage Joint Industry Project at UT-Austin (BP, Chevron, CMG, ENI, ExxonMobil, Luminant and Shell) and also CMG, Ltd. for the use of their reservoir simulation software and special version of GEM-GHG (Green House Gas). Special gratitude goes to Jeff Simmons from Occidental Petroleum Corporation for useful technical discussions during this research.

It has been a great pleasure working with several colleagues. Special thanks to Ajitab Kumar and Robin Ozah for their generous helps at the beginning of my research. I also would like to thank technical discussions with my collogues at the Department of Petroleum and Geosystems Engineering, specially Dr. Maghsood Abbaszadeh, Glen Allen Anderson, Vishal Bang, Kiomars Eskandari, Gholamreza Garmeh, Davood Ghorbani, Abraham John, Yinghui Li, Baosheng Liang, Hourshad Mohammadi, Morteza Sayarpour, Rezvan Seied Azimi, Derek James Wood, Xingru Wu, Jiang Zhang, Elizabeth

Zuluaga. Special thanks to other graduate students in our Department, Renzo Angeles, Javad Behseresht, Nariman Fathi, Meghdad Roshanfekr, Frahad Tarahhom, Abdoljalil Varavei, and to other professors, departmental staff, Esther L. Barrientes, Joanna L. Castillo, Cheryl Kruzie, and other administrative personnel in the center for petroleum and geosystems engineering.

Finally, I would like to express my utmost gratitude to my wife Rezvan, my daughter Aileen, and all of my family members for their patience, persistent support, and love. I am indebted to their immense love and support.

Yousef Ghomian

March 2008

Reservoir Simulation Studies for Coupled CO_2 Sequestration and Enhanced Oil Recovery

Publication No._____

Yousef Ghomian, Ph.D.

The University of Texas at Austin, 2008

Co-Supervisors: Gary A Pope and Kamy Sepehrnoori

Abstract

Compositional reservoir simulation studies were performed to investigate the effect of uncertain reservoir parameters, flood design variables, and economic factors on coupled CO_2 sequestration and EOR projects. Typical sandstone and carbonate reservoir properties were used to build generic reservoir models.

A large number of simulations were needed to quantify the impact of all these factors and their corresponding uncertainties taking into account various combinations of the factors. The design of experiment method along with response surface methodology and Monte-Carlo simulations were utilized to maximize the information gained from each uncertainty analysis. The two objective functions were project profit in the form of $/bbl of oil produced and sequestered amount of CO_2 in the reservoir. The optimized values for all objective functions predicted by design of experiment and the response surface method were found to be close to the values obtained by the simulation study, but with only a small fraction of the computational time.

After the statistical analysis of the simulation results, the most to least influential factors for maximizing both profit and amount of stored CO_2 are the produced gas oil ratio constraint, production and injection well types, and well spacing. For WAG injection scenarios, the Dykstra-Parsons coefficient and combinations of WAG ratio and slug size are important parameters. Also for a CO_2 flood, no significant reduction of profit occurred when only the storage of CO_2 was maximized. In terms of the economic parameters, it was demonstrated that the oil price dominates the CO_2 EOR and storage. This study showed that sandstone reservoirs have higher probability of need for CO_2 incentives. In addition, higher CO_2 credit is needed for WAG injection scenarios than continuous CO_2 injection.

As the second part of this study, scaling groups for miscible CO_2 flooding in a three-dimensional oil reservoir were derived using inspectional analysis with special emphasis on the equations related to phase behavior. Some of these scaling groups were used to develop a new MMP correlation. This correlation was compared with published correlations using a wide range of reservoir fluids and found to give more accurate predictions of the MMP.

Table of Contents

List of Tables

List of Figures

Chapter 1: Introduction

In recent years green house gases such as carbon dioxide have increased in the atmosphere and caused some concerns about climate change (Herzog and et al. 2000). Geological sequestration is one way to reduce the CO_2 content in the atmosphere. This knowledge is based on capturing CO_2 from emission sources and injecting it into deep geological structures. There are several options for sequestrating CO_2 in geological sinks: Injecting CO_2 into deep saline aquifers, injecting CO_2 into mature oil and gas reservoirs for the purpose of both sequestration and production enhancement, injecting CO_2 into depleted oil and gas reservoirs, and finally injecting CO_2 into coal seams. Among these options, the estimated storage capacity for aquifers is 109 to 2727 Gt-C (1 Gt-C= 3.7 giga tons CO_2) and for oil and gas reservoirs is 300 Gt-C (Yamasaki, 2003).

Deep saline aquifers typically have no economic value, are separated from potable aquifers, which are much shallower, and are often located close to large CO_2 emission sources such as electric power plants. A large scale and practical CO_2 sequestration project in Sleipner has already been initiated and has shown the feasibility of performing these kind of projects. Mature oilfields also are one of the most favorable targets for the CO_2 sequestration. Injecting CO_2 into these reservoirs can increase the amount of oil produced, off setting some of the CO_2 storage expenses. Most of the CO_2 injection aspects into the reservoirs for the purpose of Enhanced Oil Recovery (EOR) and Enhanced Gas Recovery (EGR) have been known for decades (Wang, 1984, Khan, 1992, Lim, 1994, Guler, 2001). But there are some differences between injecting CO_2 for the purpose of pure EOR or EGR projects and the ones for both CO_2 sequestration and EOR or EGR projects. In EOR projects, the goal is to maximize profit by minimizing the total amount of CO_2 injected per each barrel of oil produced. The economics and incentives for combined EOR and sequestration are less clear at this time, but a first step in the

development process should be to do studies to investigate ways to both produce oil efficiently and maximize storage of the carbon dioxide.

1.1 RESEARCH OBJECTIVES AND TASKS

The goal of this research was to better understand the potential for both enhanced oil recovery and storage of CO_2 in mature oil reservoirs over a wide range of conditions. A compositional simulator was the main tool used to investigate this combined process, but scaling analysis and statistical analysis were also utilized as tools for this purpose. Vikas et al. (2002), Kumar et al. (2004) and Ozah et al. (2005) studied CO_2 storage in deep saline aquifers using a compositional reservoir simulator to determine the best storage strategy and most important parameters for aquifers. This research has mainly focused on coupled CO_2-EOR and sequestration processes.

The first task was to investigate different geological as well as engineering aspects of the reservoirs and also physical properties of CO_2 to find out key factors that help to reach the maximum oil recovery and maximum CO_2 sequestration. In addition, the effect of different oil compositions will determine the appropriate candidate reservoirs for the coupled sequestration and EOR.

The second task in this research was to study effective strategies to optimize the oil recovery and the amount of stored CO_2. These strategies include employing different injection and production schemes, applying various well control techniques, as well as different mobility control technologies such as WAG to delay early CO_2 breakthrough at production wells due to heterogeneity and its high mobility. The effect of the employing horizontal wells in improving sweep efficiency and incremental oil recovery of a CO_2 flood has been studied by Lim et al., 1994, Edwards et al., 2002 and Malik and Islam, 2000. It should be considered that due to the recent drilling technology improvements, drilling costs for horizontal wells is not much higher than vertical wells. Combination of

horizontal and vertical wells also might help to delay the CO_2 breakthrough and increases its storage.

The third task in this research was to derive dimensionless scaling groups for CO_2 flooding in a three-dimensional porous medium. Unlike previous studies for performing scaling group analysis, phase behavior equations were entered in the derivation process to achieve comprehensive scaling groups. Scaling groups corresponding scaling groups were then utilized to develop an all-inclusive Minimum Miscibility Pressure (MMP) correlation for CO_2 flooding.

The forth task in this research was to quantify the probability of need as well as amount of CO_2 incentives on coupled CO_2 sequestration and EOR projects. Unlike other similar studies, combination of different reservoir and economic parameters along with compositional simulations were employed to perform a systematic, efficient and accurate study

As it can be realized, vast amount of sensitivity analysis and reservoir simulation studies needed to be made to inspect the impact of different factors and their corresponding uncertainties affecting the whole process. Therefore, some statistical analysis by utilizing experimental design and response surface methodology were performed to reduce the number of simulations were needed to be run.

1.2 METHODOLOGY

Few studies have been reported on how to optimize coupled oil recovery and CO_2 storage. But, wide range of different reservoirs has been gone through the EOR- CO_2 flooding since late 70's and vast amount of information is available in this area. Therefore our first step in performing this research was to review the CO_2-EOR flooding literature to gain a better understanding of the different aspects of the CO_2 flooding

process and mark up issues that can be improved or modified to lead us toward both of our objectives.

As it can be realized, vast amount of sensitivity analysis and reservoir simulation studies were necessary to inspect the impact of different factors and their corresponding uncertainties affecting the whole process. Also having combination of aforementioned factors may give different results compared to the single variables sensitivity analysis. Therefore, performing large number of simulation runs was needed, to investigate the effect of different variables as well as combination of variables in the form of some scaling groups. Based on time and simulation expenses limitations, it was almost impossible to achieve a fully inclusive understanding of the process in a reasonable manner. For this reason performing some statistical analysis in order to reduce the number of simulations was inevitable. Design of experiment is one of the methods to maximize the information gained from each simulation and to investigate the significance of the different parameters. This method can be applied to develop response surfaces that identify the various factors that cause changes in the responses and also predicting these variations in a simple mathematical form.

Due to the importance of economics, the objective functions in our study were considered as profit (in the form of $/bbl of oil produced), sequestered amount of CO_2 (in the form of either gas saturation inside the reservoir), or $ value of each Mscf of stored CO_2. An effective approach was developed under uncertainty for a wide range of reservoir parameters, as well as the combination of parameters to obtain the optimum conditions for both of objective functions or each one of them individually. By applying these types of studies we were even able to define factors that affecting the storage and recovery outstandingly and then carry out optimization studies utilizing them.

1.3 REVIEW OF CHAPTERS

This dissertation is divided into nine chapters. Chapter 2 includes an extensive literature survey. Research papers are reviewed on CO_2 flooding projects and processes as well as on the limited studies on coupled CO_2 sequestration and EOR.

Chapter 3 presents the reservoir simulation studies that were performed to investigate compositional effects between aquifer fluid (brine) and injected supercritical CO_2 in the Frio brine formation as the first CO_2 sequestration pilot in the US.

In Chapter 4, the effect of hysteresis relative permeability on both CO_2 storage and oil recovery in the WAG injection process was studied. Also uncertainties in WAG ratio and slug size along with reservoir heterogeneity characteristics were studied to achieve optimum sequestration and recovery values.

Chapter 5 explains uncertainty analysis for flood design optimization. Different flood design parameters such as well spacing, different injection and production schemes, various well control techniques, and different mobility control methods including WAG were considered to optimize the flood design for coupled CO_2 sequestration and EOR processes.

Chapter 6 contains details for derivation of dimensionless scaling groups for CO_2 flooding process in three-dimensional porous media in a three-phase and three-pseudocomponent system.

Phase behavior-related scaling groups were utilized in Chapter 7 to develop a comprehensive MMP correlation between CO_2 and different reservoir oils

Chapter 8 discusses the exploratory economic analysis based upon systematic compositional simulations of CO_2 EOR that were performed to determine how much and what type of economic incentive might be needed for coupled CO_2 sequestration and EOR projects.

Chapter 9 summarizes the research and present conclusions of the research work and recommendation for future work.

Chapter 2: Literature Review

CO_2 sequestration studies started almost a decade ago (Bradshaw et al., 2004, Chadwick et al., 2004). Despite this fact, still vast areas of research have not been covered in detail in the area of coupled enhanced oil recovery and sequestration. This is also partly true about different aspects of aquifer storage.

The optimal operating conditions for higher oil recovery and for higher CO_2 storage will not in general be the same. Since the inception of CO_2 injection for enhanced oil recovery (EOR) in the 1970s, significant reservoir engineering effort has gone into reducing the volume of CO_2 required to recover a barrel of oil. The objective of combined EOR and CO_2 sequestration, however, is to increase the amount of CO_2 left behind when the reservoir is abandoned; thus, the engineering design objective is significantly different. Kovscek (2002) believes that there are three principal mechanisms by which CO_2 may be sequestered within an oil reservoir. The first is physical containment or so-called hydrodynamic trapping of CO_2 as a gas or supercritical fluid beneath a cap rock (Law and Bachu, 1996). Next, CO_2 can dissolve directly in the water and oil phases. This is sometimes called solubility trapping (Reichle et al., 1999). Lastly, CO_2 can react either directly or indirectly with reservoir minerals and organic matter and be converted into a solid phase (Bachu et al., 1994). This process may be rather slow. Kovscek did not mention capillary trapping as residual gas saturation, which has been shown by Kumar (2004) to be still another way to store CO_2 and is the one that has significant advantages over hydrodynamic trapping.

Candidate reservoirs for CO_2-EOR and sequestration have diverse geology and characteristics. For example, reservoirs near the U.S. Gulf coast overlie salt domes and tertiary oil exists in a series of steeply dipping sandstone layers in several different fault blocks located on the flanks of a salt dome (Nute, 1983). These reservoirs are highly

heterogeneous with very high permeability and porosities. In contrast, some of the reservoirs suitable for CO_2 flooding, e.g. Weyburn, are almost horizontal carbonate reservoirs with low permeability and a different type of heterogeneity (Elsayed et al. 1993). Also, some studies have been reported on CO_2 flooding and sequestration in fractured carbonate reservoirs (Schechter et al., 2001).

Some aspects of oil reservoirs that should be considered for combined EOR and CO2 sequestration include reservoir depth, oil density, storage capacity, water and oil volumes in place, and formation thickness. Usually CO_2 injection projects in oil reservoirs have focused on oil with densities between 29 and 48 °API (855 to 711 kg/m3) and reservoir depths from 760 to 3700 m (2500 to 12,000 ft) below ground surface (Taber et al., 1997). Formation type and thickness are not main factors that affect oil recovery, but formation thickness is a key factor in the process of storage. On the other hand, CO_2 density is also one of the main issues; It increases with depth (Hendrinks et al., 1993) but it has been shown that the density of pure CO_2 will be greatest at a given depth in a reservoir where the fluid pressure gradient is largest while the geothermal gradient is the least. Therefore, geothermal gradients reduce the CO_2 density significantly (Kovscek, 2002). The result is that in the absence of a geothermal gradient, CO_2 phase density exceeds water density at a depth of roughly 2750 m (≈ 9450 ft). Thus, the CO_2 would tend to migrate downward rather than upward for depths greater than 2750 m. With the inclusion of the geothermal gradient, CO_2 will not approach water density even at depth of 4000 m. This is a deterministic issue in the aquifer storage of CO_2.

Reservoir capacity is another criterion for the candidate reservoirs. For this, the specific capacity or the mass of CO_2 per volume of rock is a good measure to differentiate sequestration potential among reservoirs (Kovscek, 2002). Of course, over injecting of CO_2 into the reservoir based on reservoir capacity and rock and fluid compressibility, is detrimental to the reservoir integrity. A conservative idea is that reservoir pressure should not exceed greatly the initial reservoir pressure. Over

pressurization of fluids within the reservoir pore space can cause a breach of any type of barrier which will lead to the either natural hydraulic fracturing of seal or slip of sealing faults or both.

CO_2 injectivity issues for sequestration have been addressed in the context of aquifers (Law and Bachu, 1996; Gupta et al., 1999); they have stated that in the aquifer storage process, the high permeability pathways increase the injectivity and a high volume of CO_2 can be stored. But the heterogeneous, high permeability paths are a negative factor for CO_2 flooding process; because they result in lower sweep efficiency causing lower oil recovery and early breakthrough. In the reservoirs connected to an aquifer, the bottom water aquifer is either active or inactive. Injectivity is an important issue in the oil reservoirs with bottom water. Bachu (2000) believes that reservoirs with inactive bottom aquifers (so-called closed reservoirs) might be the most attractive targets for CO_2 injection because there is no need to displace water that invaded from an aquifer. Also, the initial oil saturation is likely larger compared to reservoirs with water influx, and thus the potential for incremental recovery is larger.

Malik and Islam (2000) have investigated different scenarios for the Weyburn field that could result in maximum oil recovery or maximum storage. Based on their results, injecting CO_2 into the producing formation will give higher storage and higher recovery, whereas in reservoirs with bottom water (presence of higher remaining oil saturation), injecting CO_2 into the bottom water will result in higher mobilized oil in the transition zone and therefore higher oil recovery (Perry, 1982). In addition, because of utilizing the aquifer volume and formation of dissolved CO_2 in water, the CO_2 storage will increase significantly. It should be mentioned that in some cases CO_2 flooding could be done after primary production (in place of secondary oil recovery) leading to a huge difference in terms of oil recovery and CO_2 sequestration.

From a pore scale perspective, when gas enters a pore containing a residual oil globule, capillary forces sometimes cause the oil to spread between the water coating the

pore wall and the gas bubble in the center of the pore. This condition allows the oil phase to become a continuous oil film (Malik and Islam, 2000). If gas is injected above the pressure that miscibility is achieved (the minimum miscibility pressure for multiple contact miscibility), then a higher fraction of residual oil can be displaced from the pores. Minimum miscibility pressure (MMP) is a direct function of oil and injected gas composition (Stalkup, 1983; Lake, 1989). Injected gas composition should be designed in a way that MMP can be achieved. Nute (1983) used methane as an additive to lighten the injected CO_2 in Bay St. Elaine field. He showed that addition of methane to CO_2 tends to increase the MMP. To prevent the loss of miscibility, he found out that the CO_2-methane mixture could be enriched with n-butane to reduce the minimum miscibility pressure to the original design conditions. Guler et al., (2001) also studied employing CO_2 and NGL mixtures as a method to enhance oil recovery. Zhang et al. (2004) have shown that MMP for their oil samples increased as the N2 or CH4 concentration increased in the CO_2 stream. Based on their study, CO_2 containing 37-mol % propane reduced the pure CO_2 MMP by 45%.

Since CO_2 sources are rarely pure and costs for separation of impurities from CO_2 is very expensive; existence of impurities in the injected stream and their role in the process of CO_2 flooding is very important and deserve a broad study. Malik and Islam (2000) has investigated the effect of nitrogen contamination in the gas stream in the Weyburn field. They believe that the presence of contaminants decreases the solubility and diffusivity of carbon dioxide into the oil, consequently leading to reduction in swelling of oil by carbon dioxide. The molecular diffusion of carbon dioxide into the oil is considered to be controlling mechanism in the carbon dioxide flood. An impure CO_2 gas stream affects the diffusion rate. The negative impact on production is due to the presence of the nitrogen content that tends to form a stagnant phase between the oil and carbon dioxide, through which carbon dioxide has to diffuse before contacting oil. The

presence of nitrogen also increases the viscosity of the carbon dioxide-oil mixture, resulting in an inefficient displacement from the pores.

Due to low viscosity, CO_2 has a high mobility, which is a major issue in the optimizing oil recovery and sequestration. High mobility causes lower reservoir sweep and early production of CO_2, which can lead to lower oil recovery and lower storage. Several different techniques such as WAG, SAG and foam have been used for controlling the CO_2 mobility for the purpose of enhanced oil recovery. Prieditis and Paulett (1992) studied the use of a surfactant-foam to reduce the CO_2 mobility for San Andres cores. They have shown that injecting a slug of surfactant solution prior to CO_2 injection or simultaneous injection is required to effectively generate foam in rock matrix. Wang, (1984) believes that CO_2 foam can be generated in a porous media but it is unable to be displaced. He also showed that CO_2-foam generated either externally or internally is susceptible to fast deterioration upon contact with crude oil and, therefore, the control of CO_2 mobility using a foaming agent could be effective only within a short distance form the injector. Rossen et al. (1999) showed that fractional-flow methods indicate that the effectiveness of foam processes that alternate injection of liquid and gas (SAG processes) depends on foam strength at extremely high foam quality, conditions difficult to control in the laboratory. Foams can improve oil recovery by reducing gas mobility and the effects of reservoir heterogeneity. Numerous studies report that foam flow in porous media comprises two regimes. In the “high-quality regime,” pressure gradient is nearly independent of gas superficial velocity. In the “low-quality regime,” pressure gradient is nearly independent of liquid superficial velocity. Previous published data from CO_2 foam studies lay either in the high- or low-quality regime, but no single study shows both regimes. Kim et al. (2004) delineated that the two foam-flow regimes is essential to modeling and predicting the behavior of CO_2 foam in petroleum applications.

Water alternating gas (WAG) is another technique to control high mobility of CO_2. Pariani (1992), and Hill and Tinney (1994), show the optimized WAG ratio as a

method to maximize the net present value for the purpose of oil recovery with CO_2 flooding. The economy and project goal will play a main role in the WAG ratio design in the process of both recovery and sequestration. Ghomian et al. (2008) studied optimized WAG flood design for coupled CO_2 sequestration and EOR in two- and three-dimensional heterogeneous reservoirs. They optimized project profit as $/bbl of oil and amount of stored CO_2 using response surface and experimental design methodology. The simultaneous flow of gas and water yields, generally, a net mobility that is less than that of the injection gas alone.

Flood pattern and design strategy should be implemented based on the economic and oil recovery point of view along with the sequestration objective. Different design and strategies should be employed for different reservoirs considering various objectives. For instance, as one of the initial steps, if the reservoir pressure is less than the MMP, main challenge would be to return the reservoir pressure back to its original one to provide the MMP (Kleinstelber, 1990).

Steeply dipping reservoirs are often suitable for downward CO_2 displacement to utilize gravity forces to stabilize the displacement and increase the sweep of the injected CO_2 (Kleinstelber, 1990; Perry, 1982; Nute, 1983). The critical superficial velocity to achieve a gravity stable displacement can be calculated from:

$$U_c = \frac{k\lambda_{r1}^{\circ}\Delta\rho g \sin\alpha}{M^{\circ} - 1} \tag{2.1}$$

where k is the permeability, λ_{r1}° is the end point mobility of displacing fluid, $\Delta\rho$ is the density difference between displacing fluid and displaced fluid, α is the reservoir dip angle, and M° is the end point mobility ratio.

As it can be seen form Equation 2.1, reservoirs with high permeability will have a higher critical rate and therefore may be candidates for gravity stable displacement,

whereas those of lower permeability will have a critical rate too low for economically flooding in a gravity stable mode. Effect of reservoir dip angle and injected gas mobility is also significant. In this type of displacement process because of late CO_2 breakthrough and highest sweep possible both of maximum storage and oil recovery can be achieved if the feasibility of project is validated.

For reservoirs with no dip or low dip, as the gravity to viscous force ratio decreases, the tendency of solvent to override decreases and vertical sweep efficiency improves. Therefore the vertical permeability is a key factor in determining vertical sweep efficiency and oil recovery in CO_2 floods (Elsayed et al. 1993). In addition to above mentioned issues on gravity stable displacement, by adjusting the CO_2 density, CO_2 slug can be spread between the less dense gas cap and the more dense oil column causing more contact between CO_2 and reservoir oil (Johnston, 1988).

There are some other strategies that can help to optimize recovery and storage. Employing horizontal or combination of horizontal and vertical wells depending on the project conditions can be one of these techniques (Lim et al. 1994). The application of CO_2 flooding using horizontal wells significantly shortens project life, thus substantially improving project economics. For very tight reservoirs where CO_2 and brine injectivities strongly affect project economics, the use of horizontal injectors may be a more attractive alternate than vertical wells. The use of horizontal injectors in conjunction with vertical producers in tertiary CO_2-WAG flood generally resulted in oil recovery that was as good or better than using both horizontal injector and producer and always higher than using all vertical wells (Lim et al. 1992). The injectivity of CO_2 and brine using horizontal wells, and hence the oil recovery at reasonable project life, is very sensitive to the permeability in the vicinity of the wells.

Malik and Islam (2000) believe that in the Weyburn field, horizontal injection wells have proved to be efficient for CO_2 flooding process to improve recovery while increasing the storage of CO_2. Besides employing horizontal wells, applying different

well control techniques including partial completion of both injection and production wells can improve the amount of injected and stored CO_2 as well as oil recovery (Jessen et al. 2005). Murray et al. (2001) have introduced an alternative method in the category of well control techniques, which they call Soak Alternating Gas, to optimize oil recovery and sequestered CO_2. This method is to periodically inject CO_2 and shut in the well for some time. Kovscek et al. (2004) have introduced an objective function combining dimensionless oil recovery and reservoir utilization as follows:

$$f = w_1 \frac{N_p^*}{OIP} + w_2 \frac{V_{CO2}^R}{V^R} \tag{2.2}$$

where w_1 ($0 \leq w_1 \leq 1$) and w_2 ($=1-w_1$) are weights and V_{CO2}^R is the volume of CO_2 stored in the reservoir and V^R is the volume of pore space of the reservoir. Also *OIP* is the volume of the oil in place at the start of CO_2 injection and N_p^* is the net production of oil. The design objective will be the maximizing this function with respect to the specified set of weights. If the main aim is to maximize oil recovery, w1 is taken as 1, whereas if the goal is to maximize CO_2 storage, w2 is taken as 1. The regulatory and tax structure for sequestration remains unclear and likely will vary from nation to nation. In practice, weights will be chosen based on the revenue produced by both oil recovery and CO_2 sequestered.

As examples of several case studies, Ghomian et al. (2008) have modeled the storage of CO2 in Frio brine pilot, as the first US pilot study. They compared the results from simulation model, with the actual field data and validated simulation model with a high accuracy. Scharf and Clemens (2006) have evaluated the potential for CO_2 storage in eleven largest oil and thirteen largest gas fields in Austria and have found huge potential for CO_2 storage in these fields. Bank et al. (2007) have performed reservoir simulation using detailed, representative data from major oilfields throughout the Appalachian basin and indicated that 1,230 million barrels may become technically

recoverable which provide huge potential for CO_2 storage in this basin. This of course depends on future oil prices and CO_2 costs. Ravagnani (2007) has presented a technical-economic methodology to evaluate the feasibility of the process in a hypothetical mature oilfield. It considers a cash-flow model besides a sensitivity analysis considering the main components such as revenues, investments, operating costs, taxes according the carbon credits to be earned due to the project. The methodology takes into account the quantification of emissions and energy used in the process, emphasizing the technology contribution to the environment. Ghomian et al. (2007) studied the probabilities of need for tax incentives and quantified CO2 credit which makes coupled CO2 sequestration and EOR projects feasible. This is important because the cost of CO2 capture and transportation dominates the economics of these type of projects.

Chapter 3: Reservoir Simulation of CO_2 Sequestration Pilot in Frio Brine Formation

3.1 INTRODUCTION

In recent years, the amount of greenhouse gas in the atmosphere has increased, causing concerns about climate change (Herzog et al.,2000). One approach to reducing the carbon content in the atmosphere is based on capturing CO_2 from large emission sources and injecting it into deep geological formations. There are several ways to do this: by injecting CO_2 into deep saline aquifers, by injecting CO_2 into mature oil and gas reservoirs for the purpose of enhanced oil and gas recovery (EOR or EGR), by injecting CO_2 into depleted oil and gas reservoirs, or by injecting CO_2 into coal seams. These are structures that have stored crude oil, natural gas, brine and other types of gases over millions of years. Also, many power plants and other large emission sources for CO_2 are located near geological formations that are amenable to CO_2 storage. Furthermore, in many cases, injection of CO_2 into a geological formation can enhance the recovery of hydrocarbons, providing value-added by-products that can offset the cost of CO_2 capture and sequestration.

One of the primary goals of research in the area of CO_2 sequestration is to understand the behavior of CO_2 when it is stored in geological formations. For example, studies are being performed to determine the extent to which the CO_2 moves within the geological formation, and what physical and chemical changes occur in the formation when CO_2 is injected. This information is key to ensuring that sequestration will not impair the geological integrity of an underground formation and that CO_2 storage is secure and environmentally acceptable.

In this research we have focused on CO_2 sequestration in deep saline aquifers. In this method the most important issues are to monitor and simulate the injection process,

to keep track of injected CO_2, and also to evaluate behavior of CO_2 plume when it reaches the region with high vertical permeability, even in the distant future (a geological time scale, e.g. more than 1000 years). There are also different mechanisms that can be employed to store CO_2 in an aquifer. Therefore, evaluating the CO_2 distribution in different phases and forms (in the form of residual gas, CO_2 as dissolved in aqueous phase, and CO_2 in the form of free gas) is crucial. Among these forms, CO_2 in the residual gas phase is very important, because this portion of injected CO_2 will remain immobile in the reservoir in a trapped form. Both trapped and dissolved forms of CO2 are most desirable forms of storing CO_2 for long period of time. However, CO_2 as a free mobile gas will be the least desirable form, because it can potentially leak from the reservoir and ultimately return to the atmosphere. It should be mentioned that CO_2 also can be stored and trapped as a mineral due to the geochemical reactions which occur when low pH brine reacts with minerals in the host rock formation, forming insoluble carbonate precipitates (Kumar et al., 2004). However, time scale for this process to occur in the aquifer is significantly long (tens of thousands years) (Kumar et al., 2004), and we decided not to include this aspect of storage in the current study which happened in a very short time period.

3.2 FRIO BRINE PILOT

Recently, attempts have been made to better understand and recognize the process of CO_2 sequestration (Bachu, 2000; Gunter et al., 1997; Law and Bachu, 1996). Before carrying out a large full-scale CO_2 injection for greenhouse gas emissions reduction, it is desirable that some pilot experiments be performed in order to gather valuable data (during monitoring) and to show and test that CO_2 injection in the aquifers can be performed without any concern. The Gulf Coast, in which both sinks and sources for CO_2 can be found, is one of the most desirable target areas in the United States. As

shown in Figure 3.1, there are a high number of CO_2 emission source points in nearby areas.

This pilot site was selected after a national evaluation of saline formations (Hovorka et al., 2000), which screened large areas with high storage capacity that underlie numerous point sources of anthropogenic CO_2. Among several candidates for the CO_2 sequestration pilot in the Gulf Coast, the Frio formation was chosen by the University Of Texas Bureau Of Economic Geology (BEG) as the first field experiment in the United States for CO_2 sequestration for several reasons. First, this formation is a brine-bearing sand in a well-known onshore oil field and 3D seismic data and well logs data were available for reservoir characterization. In addition, the existing infrastructure of the wells and roads could be reused for injection purposes. An existing production well was recompleted as an observation well and a new injection well was drilled and completed 30 meters (100 ft) down-dip (Hovorka et al., 2006).

The injection took place in brine-bearing sandstone, the Oligocene Frio Formation, at about 1,500 m (≈5000 ft) below the ground surface, on the southwestern flank of the South Liberty salt dome. Hydrocarbon production in this part of the field comes from sandstone of the Eocene-age Yegua/Cockfield and Cook Mountain Formations between 2,500 and 2,750 m (8,200 and 9,000 ft) below ground level. The interval between the production (Yegua/Cockfield) and injection (Frio) formations is a shale-dominated section that includes the Eocene Jackson and Oligocene Vicksburg formations. The Frio is overlain by the 75 m thick (250 ft) Oligocene Anahuac shale, which, in turn, is overlain by an approximately 1,300 m thick (~4,200 ft) interval of Miocene inter-bedded sandstone and shale (Knox et al., 2003).

Shale layers, varying between 3 to about 15 m (10-50 ft) in thickness, separate various layers of sandstones at the top of the Frio Formation. The sandstone intervals have been given some informal names (A, B, C). The shallowest layer is “A”, and the thicker layer, “C”, is the deepest one, and was also the injection target (Figure 3.2). The

Frio Formation dips toward the south with a variable dip angle between 5º-25º, decreasing with the distance from the salt dome. The salt flank has been affected by some faults, which were mapped from 3-D seismic data, originating from the dome (Figure 3.3). Large throw faults were assumed to be sealing because of shale gouge ratio assumptions (Hovorka et al., 2006). Several small throw faults were mapped from seismic discontinuities; the exact placements and hydrologic function of these features is unclear (Hovorka et al., 2006).

The main simulation studies for the pilot test (with some geological and modeling simplifications) were performed by Lawrence Berkeley National Lab (LBNL) using the TOUGH2 simulator (Doughty et al., 2005). In our study, an actual geo-cellular model specifically constructed for the Frio aquifer (obtained from BEG), as well as accurate PVT information to account for precise density calculations and CO_2 solubility in brine, were applied to build the simulation model for the aquifer. In addition, detailed modeling on relative permeability hysteresis, along with some measured capillary pressure data, were utilized to simulate the CO_2 injection pilot before the actual field test began. The pilot plan included injection of 3000 tons of CO_2 in the upper 6 m (20 ft) aquifer interval (the upper part of the "C" sand) over a period of 12 days, and monitoring it in a well 30 m (100 ft) apart from the injection well. It is important to note that 1600 tons actually were injected in the field because CO_2 breakthrough occurred earlier than anticipated, and also the data collection objectives were completed early. The objective of monitoring was to observe the behavior of injected supercritical gas in the subsurface, investigate the physics of the process, and obtain data for further validation of simulation results.

In order to gain experience in modeling and simulating of these type of field experiments, our study was carried out to duplicate the field experiment, using simulation and modeling techniques. Different scenarios besides of actual field test scenario were simulated to investigate the ability and accuracy of current simulation models to perform similar studies in the future.

3.3 RESERVOIR MODELING AND CHARACTERIZATION:

For aquifer properties, we used the geological model obtained from BEG. The data included corner-point gridblock coordinates. Based on existing well data and 3-D seismic information, porosity, and horizontal and vertical permeability values had been assigned for each gridblock. In addition, we used initial pressure, temperature, and salinity values, which were obtained from BEG. Table 3.1 shows the summary of the input data in more detail.

At the next stage, a new series of measured properties of the cores from the drilling of the new injection well was obtained (BEG digital communication). Since the measured values were core data acquired from the injection well, we did not have values for any grids other than the ones that included the injection well. Considering the grid sizes and also the 30m (100 ft) distance between the injection and monitoring wells, the best estimate for the properties of other gridblocks around the injection well was based on the values that were reasonably close to that of the injection well blocks. A deterministic interpolation technique (inverse of distance method) was applied to assign these values. Figure 3.4 shows the horizontal permeability distribution in the NE-SW cross sectional view around injection well. Because horizontal permeability and porosity had not been measured in the whole interval of the injection well, a correlation between permeability and porosity was established using available core data. Figure 3.5 shows a correlation graph between porosity and permeability. By applying the following power law equation (where permeability is in millidarcy and porosity is in fraction of pore volume), permeability and porosity values were correlated in other gridblocks around injection and monitoring wells.

$$k = 6 \times 10^{6} \times \phi^{7.5054} \tag{3.1}$$

Two new capillary pressure measurements on core samples with two different porosity and permeability values, obtained from the new injection well, were used as a

part of the input file. Furthermore, Holtz's (2002) correlations for maximum residual gas saturation and irreducible water saturation in terms of porosity and permeability (Equations 2 and 3) were used as the main parameter in developing relative permeability data.

$$S_{wirr} = 5.6709 \times \left(\frac{\log(k)}{\varphi} \right)^{-1.6349} \tag{3.2}$$

$$S_{gr}^{max} = 0.5473 - 0.9696\varphi \tag{3.3}$$

where φ is porosity, k is permeability, S_{gr}^{max} is maximum residual gas saturation, and S_{wirr} is irreducible water saturation which is same as residual water saturation (S_{wr}) in this study. Corey's model (Corey, 1954) was used to construct the relative permeability curves for a two-phase brine-gas system.

In the modeling of the relative permeability data, all gridblocks were divided into three rock type categories based on their porosity. Therefore, for each rock type a specific relative permeability, capillary pressure, and maximum residual gas saturation (for hysteresis calculations) were assigned. From a geological point of view, the first rock type was considered for shale layers, the second set corresponded to low-porosity sandstone blocks, and the third one was assumed for high-porosity blocks of the C sand. Figure 3.6 shows the drainage relative permeability graph along with the hysteresis curves for the imbibition process for rock type two, which is the representative of middle class rock type data among the three rock types. It should be noted that the same Corey's exponents were used for all three rock types; other parameters used in constructing different relative permeability data are shown in Table 3.2. In our study, hysteresis in the gas relative permeability curve was modeled using a modified Land's equation (Land, 1971). In this method, gas and water relative permeabilities during the drainage process are calculated using Corey-type relative permeability models. But during imbibition, gas

relative permeability is calculated by accounting for shifted gas saturation ($S_{g(shifted)}$) in the same drainage model, i.e.,

$$k_{rg(imb)} = K^{o}_{rg}\left(\frac{S_g(\text{shifted}) - S_{gr}}{1 - S_{wr} - S_{gr}}\right)^{e_{wg}} \tag{3.4}$$

where

$$S_g(\text{shifted}) = S_{gr} + \frac{(S_g - S_{grh})(S_{gh} - S_{gr})}{(S_{gh} - S_{grh})} \tag{3.5}$$

and S_{gh} (hysteresis gas saturation) is the value of S_g where the shift to imbibition occurs. By definition, the values of S_{gh} are the values of gas saturations corresponding to the highest capillary pressures at all times. Hysteresis residual gas saturation (S_{grh}) is the value of S_{gr} (residual gas saturation during drainage which is considered as zero in this study) corresponding to S_{gh} via the modified Land's equation given below:

$$\frac{1}{S^{max}_{gr} - S_{gr}} - \frac{1}{S^{max}_{g} - S_{gr}} = \frac{1}{S_{grh} - S_{gr}} - \frac{1}{S_{gh} - S_{gr}} \tag{3.6}$$

where S^{max}_{gr} is the user input value for the maximum residual gas saturation, and S^{max}_{g} is the maximum gas saturation and normally is equal to 1-S_{wr}. In this study, due to the water dry-out effect, especially around the injection well where the viscous forces are very high and the dry-out effect can be observed, it was considered equal to unity. Based on this observation, gas relative permeability values were also extrapolated below irreducible water saturations.

Using an equation of state compositional simulator, CMG's GEM (2004), several steps of the preliminary simulations were performed on the Frio aquifer for the purpose of data calibration. In the beginning, our goal was to calibrate the primary input data for further simulations. Like the CO_2, the brine was treated as an independent component (represented by H_2O in the model) in order to allow for mass transfer between these two components. It is important to realize that if water had been treated as an individual phase

and not a component, the thermo-physical interactions between CO_2 as a component and water as a phase would have been impossible.

The modified Peng-Robinson equation of state (PR78-EOS) was employed to fit the experimental data for CO_2 solubility and brine density (Pedersen et al., 1984; Scharlin, 1996; Garcia, 2001; Zaytsev and Aseyev, 1992). Carbon dioxide solubility, brine density, and brine viscosity are functions of salinity, temperature, and pressure. Also, the brine density and viscosity depend on the CO_2 concentration. Brine density as well as CO_2 solubility in brine were calibrated against a correlation established by Kumar et al. (Kumar, 2004). Solubility of CO_2 in the brine with 100,000 ppm salinity, at 57 ºC (134.5 ºF) and 15.17 MPa (2200 psi), (i.e. Frio aquifer conditions), is 1.158 mole percent (Scharlin, 1996). Figure 3.7 shows the brine density with and without CO_2 saturation at different salinities. Brine densities with and without CO_2 at T=57 ºC (134.5 ºF) and P=15.17 MPa (2200 psi), are 1025.9 kg/m^3 (64.05 lbm/ft3) and 1033.2 kg/m^3 (64.5 lbm/ft^3), respectively (Garcia, 2001). As it can be seen, there is a slight increase in brine density due to dissolution of supercritical CO_2. This difference is smaller for the brines with higher salinities. The binary interaction coefficient between CO_2 and H_2O was tuned to match the experimental data for CO_2 solubility. In addition, volume shift parameters of both components were tuned to match the experimental data for brine density. Also, by running several simulations, brine viscosity calibration against experimental data was performed. Based on experimental data (Zaytsev and Aseyev, 1992) for temperature, pressure, and salinity very similar to those in the Frio formation, the brine viscosity will be 0.593 mPa.s (cp). Using the Pederson et al. (Pedersen et al.,1984) correlation for different fluids' viscosity, we found Pedersen's coefficients, for which the brine viscosity in the simulation and experimental data (Scharlin, 2006) were matching. These coefficients were then used in the simulation input data.

3.4 RESERVOIR SIMULATIONS AND DISCUSSION:

The aquifer grid model that we obtained from BEG was very large (over 130,000 grid blocks) and contained a large area (slightly over 600 acres ≈ 2.7 km^2). Because the time and computational expenses required for simulation of such a large area were excessive, and also considering the relatively small amount of CO_2 to be injected in the field, it didn't seem reasonable or necessary to perform the simulations in such a large model. Therefore, the target area was reduced to a reasonable number of gridblocks while honoring the nature of the real field situation. In order to achieve this, the initial model was first established using the data for the entire field. Then, taking into consideration some geological features like faults and other geological compartments in the original model, it was possible to reduce the model to a smaller target area (Figure 3.3).

Some preliminary simulations were performed to check the CO_2 movement in the selected area. Even after a long injection period, the new established boundaries were far from the gas plume. Also, two sides of this area were surrounded by two major faults, which were assumed to be sealing (i.e., impervious) by considering them as null blocks; this helped us to assume there were no flow boundaries in the blocks adjacent to these faults. In order to maintain the hydrostatic initial conditions (i.e., 15.7 MPa) at the boundary of the simulated area to allow for fluid movements out of the model, 23 equally-spaced boundary wells were placed in the parts of the model boundary that were not confined by these sealing faults. In the vertical direction, 5 geological layers (the A, B, and C sands and the two intervening shale layers) were divided into 26 grid layers. The two shale layers were each represented by one numerical layer (Figure 3.2).

Since the distance between the injection and monitoring wells was so small and considering the amount of injected CO_2, we recognized the need for Local Grid Refinement (LGR) around the injection and monitoring wells to obtain more accurate results. Fortunately, this was possible using the CMG's LGR option. Before carrying out the main simulation cases, a grid refinement around the injection and monitoring wells

was performed to determine the optimum degree of refinement necessary to carry out an accurate and consistent simulation study. Local Grid Refinement is a useful way to increase the numerical accuracy of the simulations without refining the entire grid, which would take much more computer time. Several ways of using LGR were tested and are described below. In these simulations with LGR, the same petrophysical properties as those of the coarse (or parent) grid block are assigned to all the refined (or child) grid blocks.

The local grid refinement option in GEM is a very practical way to quickly assess the effect of grid block size, and should definitely be used in similar studies in order to accurately model CO_2 movements. Figure 3.8 shows the average gas saturation in the refined area at the end of the CO_2 injection period versus the reciprocal of the degree of refinement for different cases. This plot is basically representative of the grid-convergence behavior for the simulation results and its sensitivity to the number of gridblocks used in the simulation. As can be observed, the convergence of the simulation results is achieved by dividing each main block into nine refined grids in the X and Y directions. Therefore, the size of each gridblock was reduced from almost 27.5 m (90 ft) to 3 m (10 ft) in each direction. The same study was performed for the Z direction, and the gridblock size in this direction was also reduced from 1.52 m (5 ft) to 0.76 m (2.5 ft). It should be noted that this was the optimum degree of refinement in terms of the computation time and the temporary computational memory (RAM memory) needed to perform the simulations.

As mentioned before, the pilot plan included injection of 3000 tons of pure CO_2 (1600 tons were actually injected in the field) over 12 days (250 tons per day); therefore, all of our simulations were performed to simulate 12 days of injection and 10 years of monitoring. Since this simulation study was performed before the field test began in October 2004, and since the main goal was not a history matching of the field test but a prediction of the CO_2 behavior underground, 3000 tons of CO_2 were injected in the

simulation cases. Because the permeability in the upper part of the C sand where injection took place is higher than in the lower part, injection of the CO_2 was carried out in a 6 m (20 feet) interval at the top of the Frio C unit, right below the shale layer. This strategy was chosen in order to have a successful two-well test study (to increase the likelihood that breakthrough would occur with less than the 3000 tons of CO_2 permitted) by trying to minimize the vertical extent of the plume and by maximizing its lateral spread by injecting high in the C sand. According to the results from previous studies on aquifer storage of CO_2 by Kumar (2004) and Ozah et al. (2005), we also decided to simulate the CO_2 injection process at the bottom as well as the top of the formation and provide a sensitivity study for future field pilot tests. We observed that in the scenarios with injection at the top, CO_2 migration extends farther laterally than if injection is performed in the lower part of the aquifer. Figures 3.9 through 3.14 show the model predicted-gas saturation distribution around the injection and monitoring wells for both scenarios.

Figures 3.9 through 3.11 show the model results for the injection at the top scenario. During the injection period (first 12 days), CO_2 accumulates around the injection well and gradually starts to move laterally under the shale layer. Simulation results predicted that after 10 years, CO_2 will migrate more than 300 m (1000 feet). The reason for this elongated plume is that the CO_2 plume hits a permeability barrier (because of the updated high permeability region based on new core data and keeping lower permeability area in the rest of the original model). Cross-sectional views (NE-SW cross sections, passing through the monitoring well block) of CO_2 saturation also show that the plume movement will be up dip due to buoyancy. After the injection period ends, the counter-current down-dip flow of aquifer brine and up-dip flow of injected gas due to buoyancy, leads to a decrease in gas saturation around the injection well. Also, in the blocks around the injection well, a portion of the injected gas is being trapped as residual gas due to the relative-permeability hysteresis effect. Because of its value in the

sequestration process, confidence in ability to model the amount of CO_2 in the trapped form under various injection strategies is important. Figure 3.11 shows the predicted residual gas saturation distribution after 10 years in the aquifer. This amount increases rapidly after the CO_2 injection ends and the brine invasion begins.

In the case of injection at the bottom, as can be seen from Figures 3.12 through 3.14 at 12 days of simulation, the shape of the CO_2 plume around the injection well (Figure 3.12) is very similar to that for the top injection case (Figure 3.9). There are some differences in the evolution of the plume after 10 years, based on the simulated models. In the injection at the top case, CO_2 tends to migrate laterally by accumulating under the shale barrier, while in the injection at the bottom case; it spreads vertically due to buoyancy effects. In the cross sectional view, lateral migration of CO_2 is much wider if CO_2 is injected at the top rather than at the bottom of the aquifer. This difference would be more substantial if a large volume of CO_2 had been injected. Comparison of these two scenarios shows that the effect of the vertical counter-current flow in the injection at the top case is much smaller than the injection at the bottom scenario.

Table 3.3 shows the CPU time for different simulation cases, with and without local grid refinements. In general, simulations of cases with injection at the top took more CPU time than the cases with injection at the bottom. This is probably because of the need for more computations to account for the wider and bigger plume evolution and consequently more calculations because of capillary pressure and hysteresis effects. When LGR is implemented in the models, CPU time increases more than three times when injection occurs in the bottom case compared to an increase of less than two times in the top injection case. Therefore, it is seen that when LGR is added, the simulation time for both cases becomes almost the same. This change in the CPU time can be interpreted in terms of the equal number of refined grids in these two cases, which seems to be the most important parameter in controlling the simulation time. It is interesting to note that simulation run time was approximately increased by a factor of 2-3 when the

number of grid blocks was increased by a factor of 9 in X and Y directions and 2 in the Z direction, using local grid refinement. It can be seen that gas moves farther along some paths. Also, higher gas saturation values were seen for the grid blocks having higher permeability values. Since CO_2 will preferentially move along pathways of higher permeability, simulations with LGR reproduce better this flow effect. The question, then, is how small can we go using finite-difference simulators such as GEM and what happens when we go to very small grid block size? It should also be noted that in the larger field scale CO_2 sequestration projects that are under execution in the other parts of the world, such as Sleipner (Chadwick et al., 2004; Baklid et al., 1996), a longer injection time and a much longer modeling time period (usually on the order of a thousand years) is necessary to determine the fate of CO_2, requiring much higher computational expenses.

When CO_2 is injected into the aquifer, a part of it dissolves in the brine, a portion of it is trapped as a residual gas, and the rest will be in the form of free and mobile gas. The distribution of CO_2 in three different phases was calculated for both scenarios within the simulated time period (10 years). Figure 3.15 shows the results for both scenarios. In both cases, most of the CO_2 dissolves in the aqueous phase or gets trapped as residual gas soon after injection ends. For injection at the bottom, after three years there is no free gas in the reservoir. In contrast, in the case of injection at the top, after 10 years about 5 percent of injected CO_2 is in the form of free gas. After 10 years, only 5 percent of injected CO_2 is in the form of free gas. Due to buoyancy effects, when CO_2 is injected at the bottom of the aquifer it will move upward and will have more contact with the brine, resulting in more dissolved CO_2 in the aqueous phase. We have observed that the amount of trapped CO_2 in both cases is almost the same, but in the case of injection at the bottom, a higher amount of dissolved gas is present in the aquifer. This results in a reduction in the free gas portion; therefore, the case of injection at the top shows a larger amount of free gas.

3.5 SIMULATION RESULTS VALIDATION

This simulation study was carried out before the field injection began. One of the main goals of the field pilot study was to monitor CO_2 movement and its behavior underground. Breakthrough time of the injected CO_2 at the monitoring well is one of the vital quantified parameters to be measured in the field. Correct modeling of reservoir heterogeneities, such as flow channels, is crucial in quantifying the breakthrough in simulation models, especially considering the very short distance between the injection and monitoring wells. In our simulations, CO_2 breakthrough at the monitoring well occurred in the dissolved form in 2.7 days after injection began and CO_2 breakthrough in the gaseous phase occurred slightly after the breakthrough of CO_2 in dissolved form. Figure 3.16 shows the mass fraction rate of CO_2 in the aqueous and gas phases versus time at the observation well from the simulation results. Later, the field results showed the actual period of 2.1 days (51 hrs), which is in agreement with the simulation results. Figure 3.16 also shows the pH and the alkalinity of the samples taken at 1 to 2 hours frequency from the observation well (Freifeld et al., 2005). These properties can be interpreted as an indirect indication for CO_2 presence in the brine. This agreement between field and simulation results shows the effect of accurate and comprehensive tuning studies as well as the accuracy of the whole model. The important effect of local grid refinement in the short distance between the monitoring and injection wells should not be disregarded.

Monitoring CO_2 plume evolution after injection ended was another goal of this pilot study. Predicting the shape of the CO_2 plume in the subsurface and also quantifying the CO_2 saturation around the observation well was crucial in order to better understand the CO_2 movement and behavior around the wells. By comparing the field results and simulated values, the validity of the geological model as well as the entire simulation process can be verified. Predicted gas saturation profiles at the monitoring well after 66 and 142 days were in relatively good agreement with the saturation values calculated

from the RST (Reservoir Saturation Tool) logs (Sakurai et al., 2005) taken from the observation well at the same times. Figure 3.17 shows the comparison of the modeled gas saturation profile and the values calculated from RST logs. There are some differences in the observed and simulated values in the lower part of the formation. This may be partly because of errors in the interpretation and conversion of log data in calculating CO_2 saturation. In addition, as was mentioned, all of the simulation studies were performed before the field test began. Three thousand tons of CO_2 were injected in the simulation cases compared to 1600 tons of CO_2 injected in the field. This may be another reason for the presence of more CO_2 mass in the simulation results than in the actual field test results.

Since this dissertation was prepared for publication after all field data have been gathered, we decided to modify the simulation model and inject 1600 tons of CO_2 (same as what was injected in the field). Since the rate of injection in the first few days of the pilot test in the simulation model was independent of the total CO_2 volume injected (it was same as in the field test), breakthrough time did not change in the case that 1600 tons of CO_2 was injected compared to the original 3000 tons of injection case. Saturation profiles at the monitoring well, inferred from RST logs, were compared to the gas saturation profile from the simulation results of 1600 tons of CO2 injection. Figure 3.18 shows the results of this comparison. It is clear that much better agreement was achieved between field data and simulation results, but there are still some discrepancies. As it was mentioned previously, an update in porosity and permeability values was only performed in the blocks around injection and monitoring wells and for other blocks relatively far from these wells, original porosity and permeability data were kept. Therefore, it is possible that porosity values in blocks far from wells were underestimated and consequently CO_2 was not able to move and reside more and faster when it hit these blocks. One consequence of this can be more accumulation of CO_2 (therefore higher saturation values) around monitoring well after 66 and 142 days in the simulation model.

In addition, possible errors in log data interpretation should always be taken into consideration.

3.6 SUMMARY AND CONCLUSIONS:

The main objective of this simulation research study was to build a predictive and accurate simulation model to study the injection of CO_2 in the Frio aquifer pilot and also to check the validity of developed simulation models for similar future CO_2 sequestration studies. The reservoir simulation model for the Frio sequestration pilot was developed carefully and different injection scenarios were simulated using GEM; CMG's compositional simulator.

Accurate and careful calibration of input data such as CO_2 solubility, CO_2-saturated brine density, and viscosity were performed. Three different rock types were modeled, with their corresponding relative permeability and capillary pressure data, along with hysteresis relative permeability, which is a very important factor to account for the effect of trapped gas on the CO_2 movement. Local grid refinement, with very small gridblock sizes in X, Y, and Z directions, was carried out around the injection and observation wells in order to predict CO_2 movement accurately. This was crucial to our simulation model because of the relatively small amount of injected CO_2 and the short distance between injection and observation wells.

Two different injection scenarios, injection at the top and at the bottom of C sand, were simulated. It was very inexpensive to provide comparable insight for future field tests by simulating different injection scenarios, utilizing a validated simulation model. The simulation outcomes for the injection at the top scenario were verified against some of the results of the field data that were gathered by the research groups performing the field injection. Simulations of the Frio CO_2 pilot were performed primarily to predict the CO_2 breakthrough time and CO_2 plume movement and behavior underground.

The CO_2 breakthrough time in the form of free gas and CO_2 dissolved in the brine at the observation well were very close to each other and were predicted as 2.7 days in the simulation results, compared to 2.1 days (51 hours) observed in the pilot test. Also, the predicted gas saturation profiles after 66 and 142 days at the monitoring well were in good agreement with the results inferred from the RST logs taken in the field.

For all simulation cases, CO_2 distribution in three different phases (CO_2 in the aqueous phase, in the trapped form and in free gas form) was calculated. Based on the results, CO_2 in the trapped form has the highest value in comparison to the two other phases in both simulation scenarios. This is an important conclusion obtained from our simulation. This form of injected CO_2 will remain unaltered over a long period of time, so the main objective of CO_2 sequestration will be achieved. CO_2 in free and mobile form has the potential for escape from the reservoir, but only 2 to 5 percent of CO_2 will be in free and mobile gas form and even this small amount is far from reaching the top during the simulation period.

Table 3.1: Summary of input data for simulations.

Length, m	1072
Width, m	700
Dip, degree	5-35
Thickness, m	30.5-61
Number of blocks	43×28×26
Depth at top of formation at injection well,m	1540
Vertical to horizontal Perm. Ratio	0.1
Average horizontal permeability, m^2	3.74×10^{-5}
Average vertical permeability, m^2	3.74×10^{-6}
Average porosity, frac	0.214
Initial pressure, MPa	15.14
Maximum injection pressure, MPa	24.82
Temperature, °C	57
Salinity, ppm	100000

Component	**CO_2**	**Brine**
Critical P., MPa	7.38	22.09
Critical T., ºC	31.05	374.2
Critical vol., m^3/mol	9.4×10^{-5}	5.6×10^{-5}
Molecular weight	44.01	18.02
Accentric factor	0.224	0.344
Parachor	78	52
Volume shift parameters	0.0247	0.234
Binary interaction coefficient	-0.06027385	

Table 3.2: Summary of parameters for three rock types.

	Rock type 1	Rock Type 2	Rock Type 3
Average permeability, md	5×10^{-7}	1×10^{-5}	1.5×10^{-4}
Average Porosity, frac.	0.145	0.22	0.33
Residual water saturation (Swr), frac.	0.43	0.15	0.135
Maximum residual gas saturation (Sgrmax), frac.	0.4	0.33	0.22
Residual gas saturation (Sgr), frac.	0	0	0

Table 3.3: CPU time required for simulations with and without local grid refinement.

CPU time (second)	With LGR	Without LGR
Injection at the bottom	1230.1	410.9
Injection at the top	1249.5	811.3

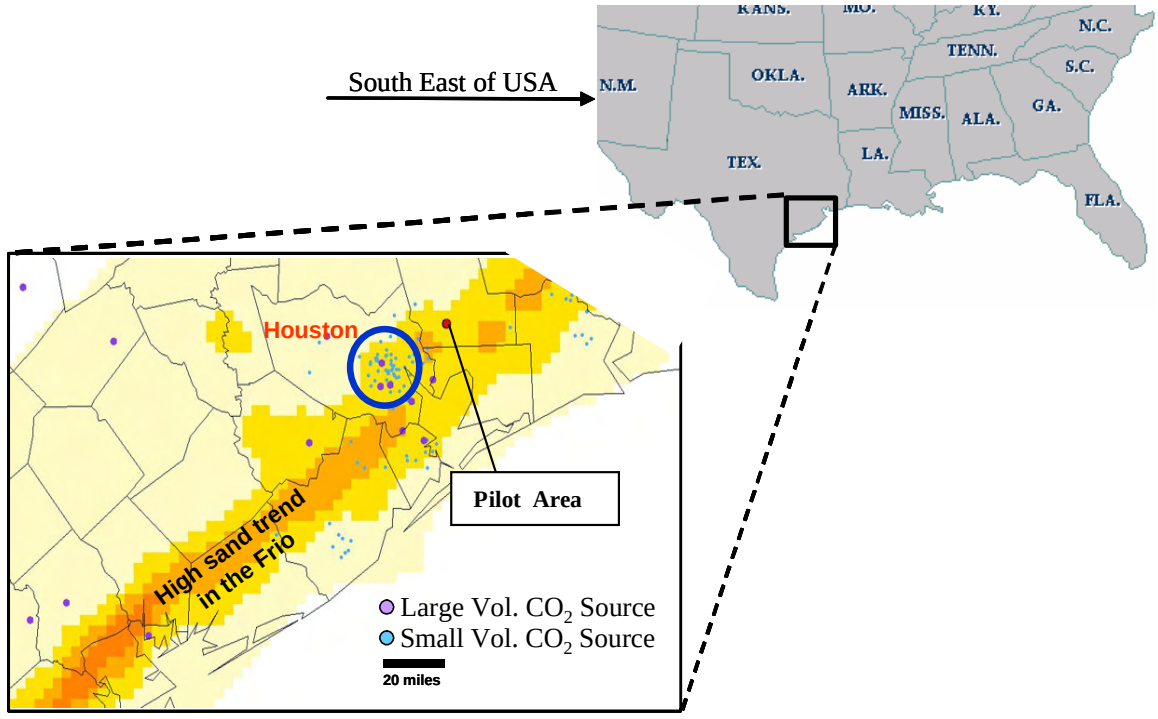

Figure 3.1- Geographic location of Frio pilot area (Knox, et al. 2002)

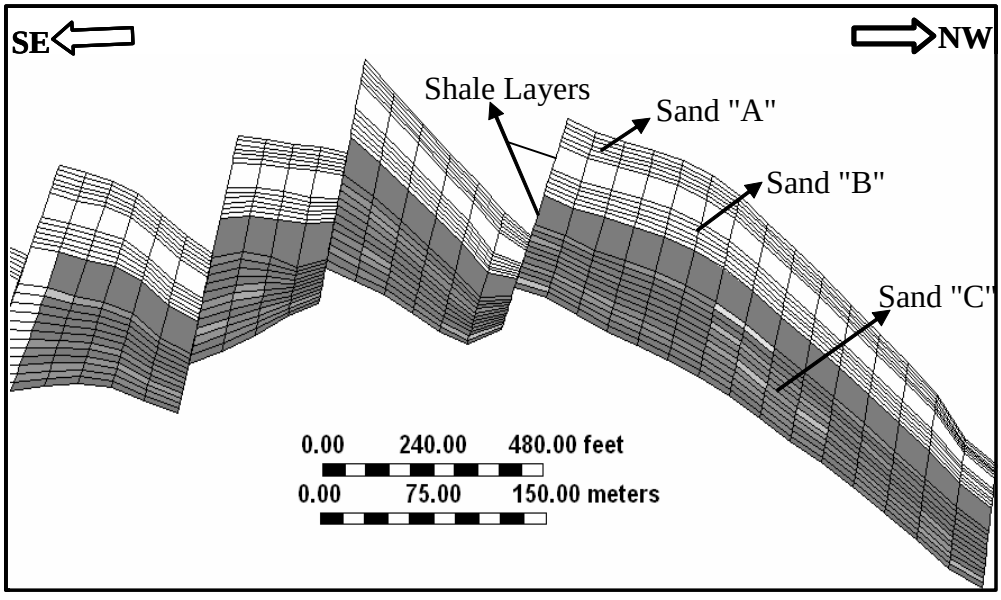

Figure 3.2-A, B, and C sand and inter-bedded shale layers in the Frio Formation (vertical to horizontal aspect ratio of 2)

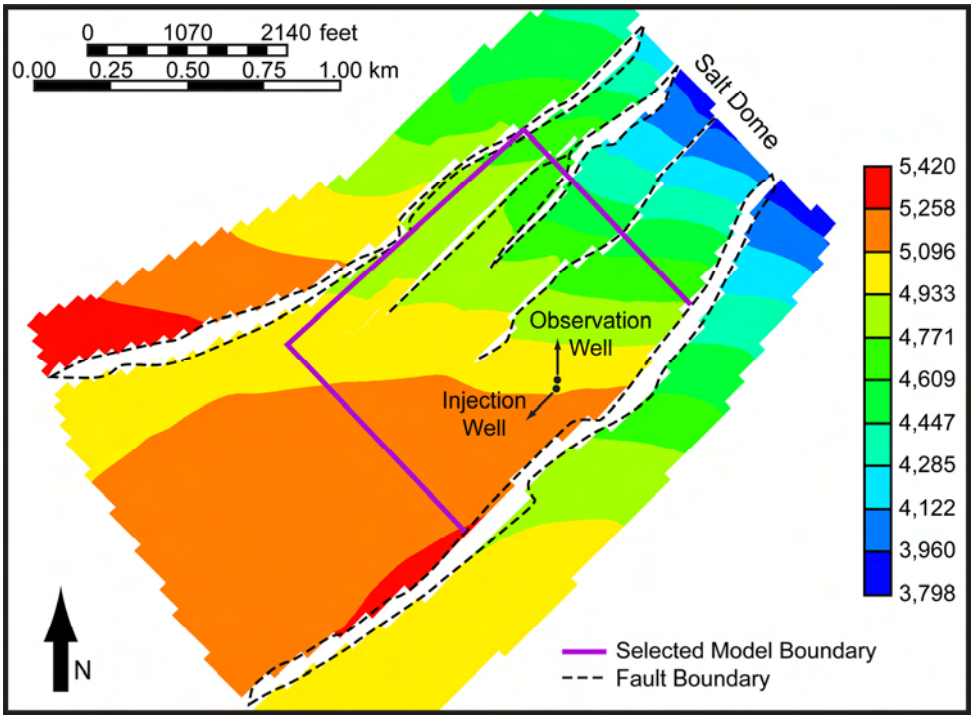

Figure 3.3- Contour map of formation depth from the initial geological model and its structural features, along with targeted simulation area

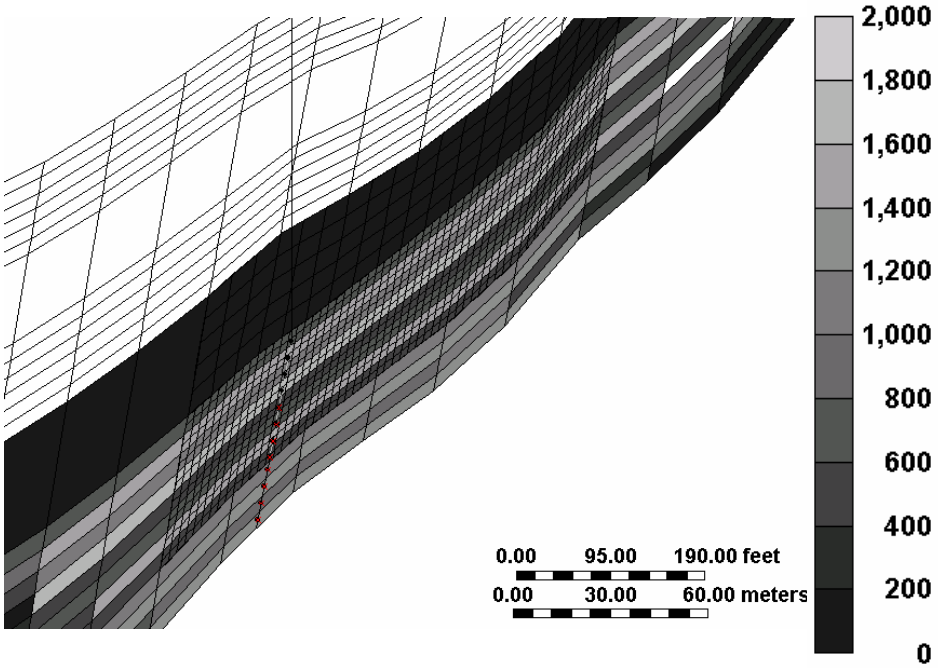

Figure 3.4- NE-SW cross sectional view of permeability distribution around injection well

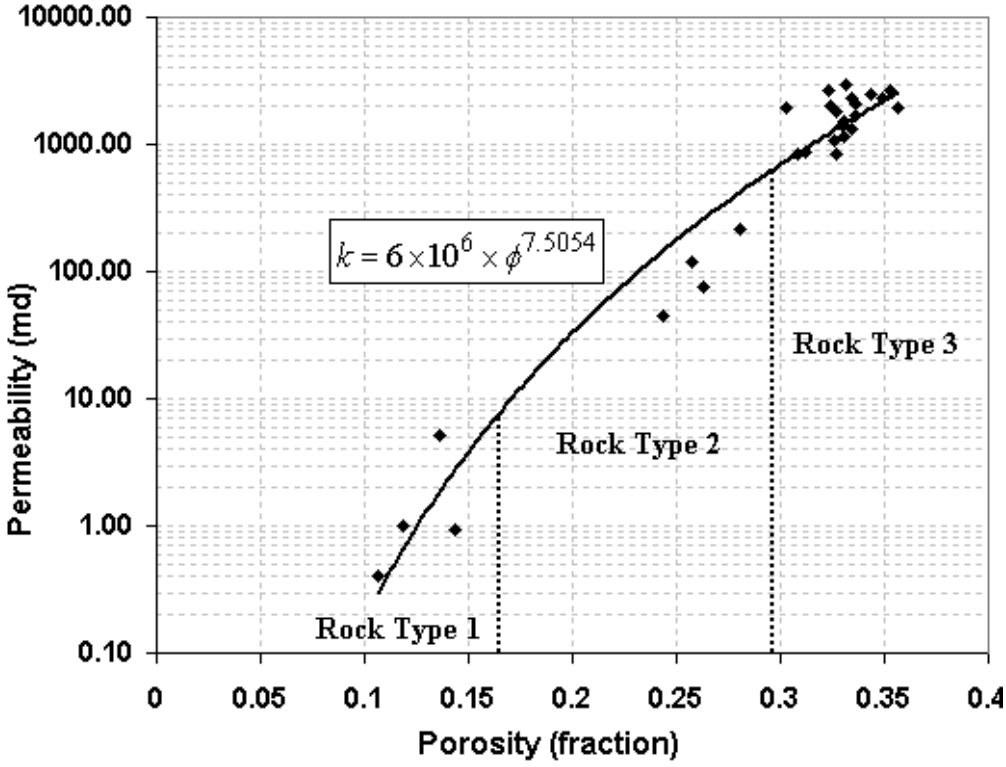

Figure 3.5- Correlation between permeability and porosity data from the new injection well

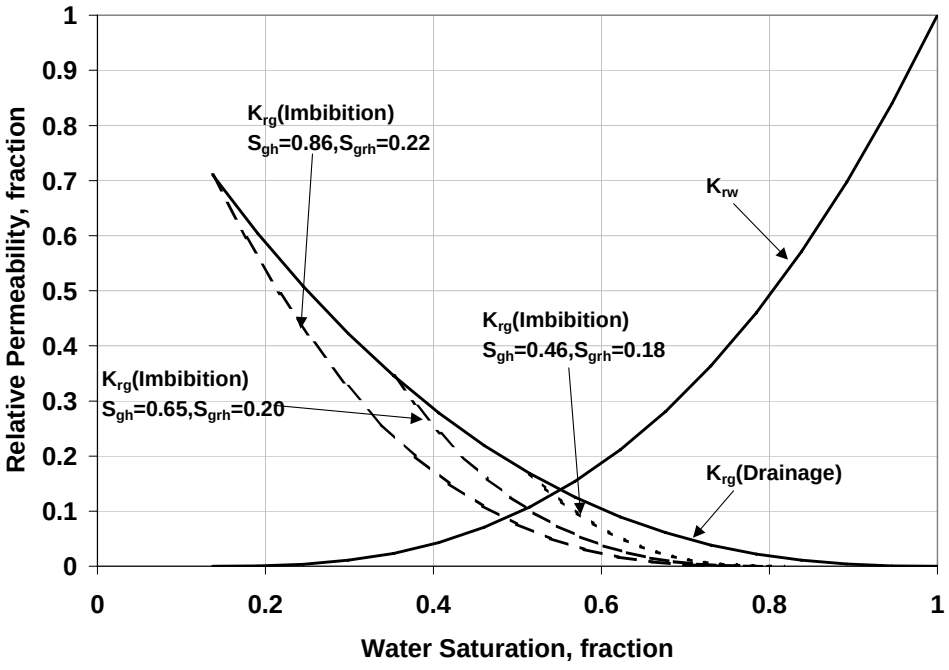

Figure 3.6- Gas-brine relative permeability data for low porosity sandstone blocks (rock type 2) with gas phase hysteresis parameters

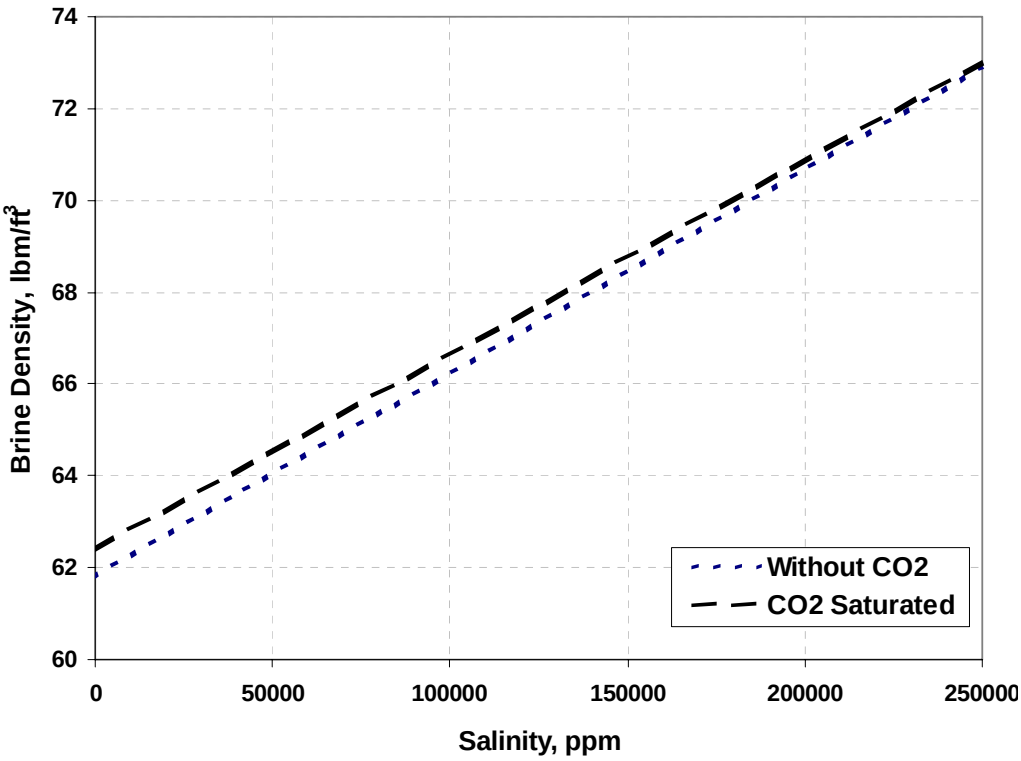

Figure 3.7- Brine density with and without CO_2 saturated at T= 57 ºC (134.5 ºF) and P=15.17 MPa (2200 psi)

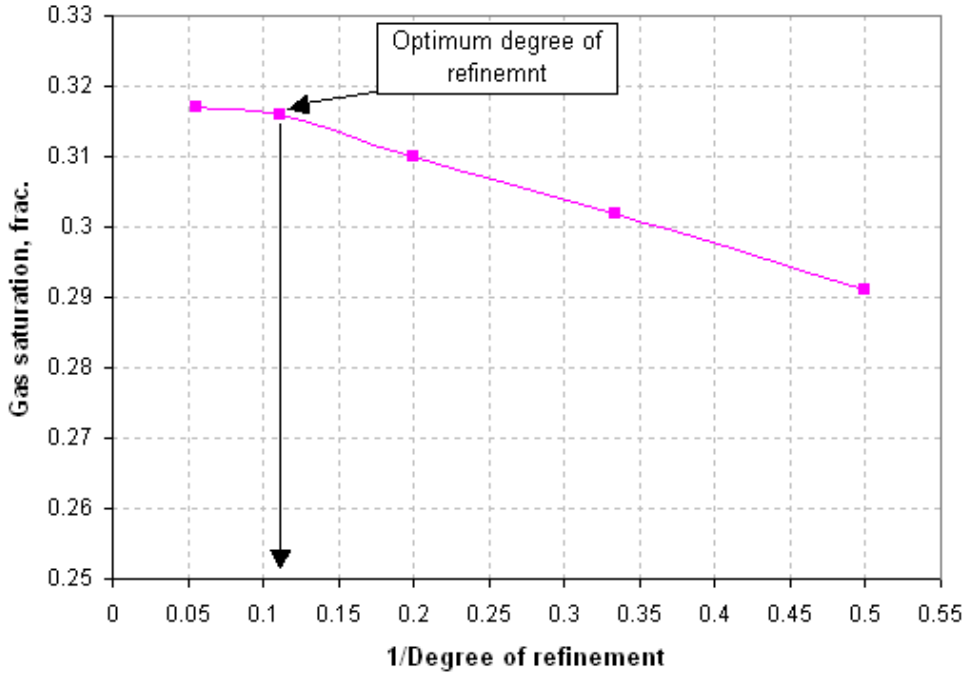

Figure 3.8- Convergence behavior for the simulation cases based on the degree of refinement

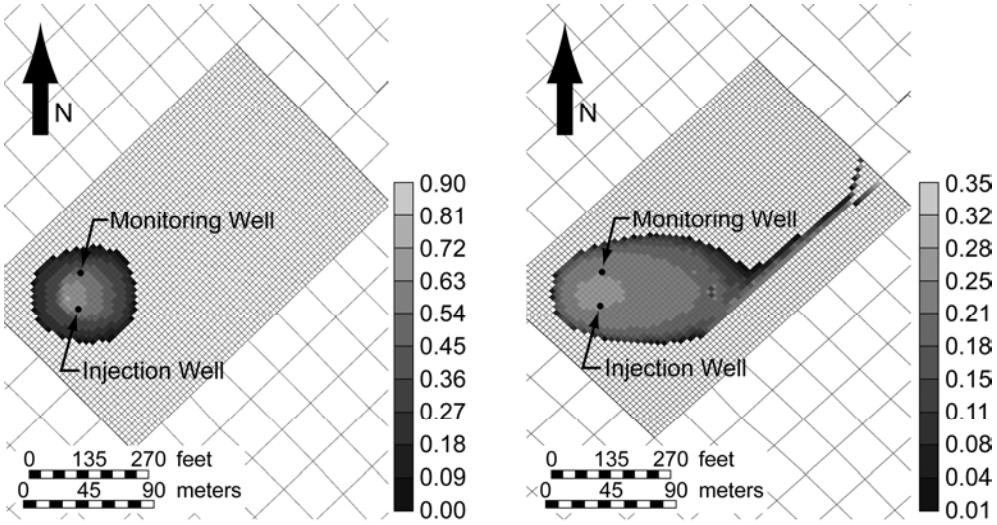

Figure 3.9- Simulation result of areal view for CO_2 plume in the case of injection at top case, 12 days (left) and 10 years after injection starts (right)

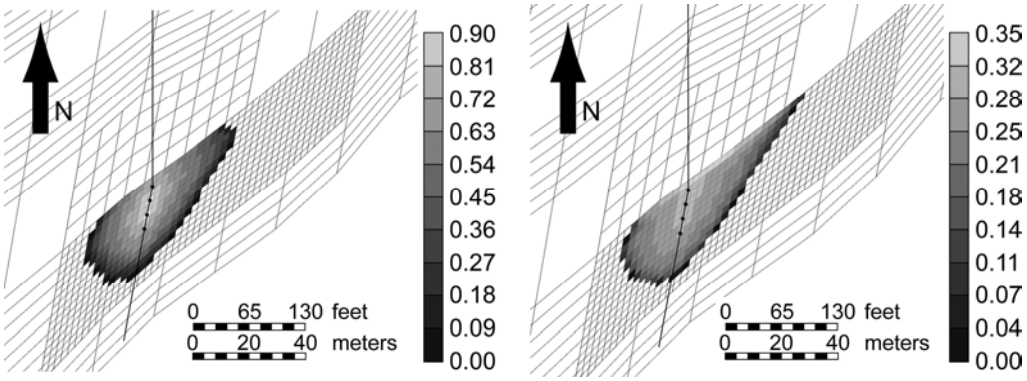

Figure 3.10- NE-SW cross sectional view of CO_2 plume in the case of injection at top, 12 days (left) and 10 years after injection begins (right)

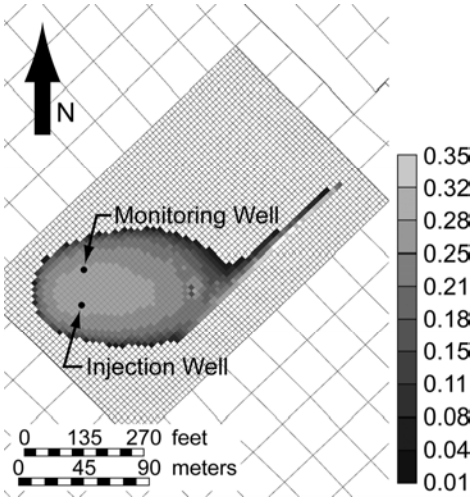

Figure 3.11- Areal view of residual gas saturation in the case of injection at top, 10 years after injection begins

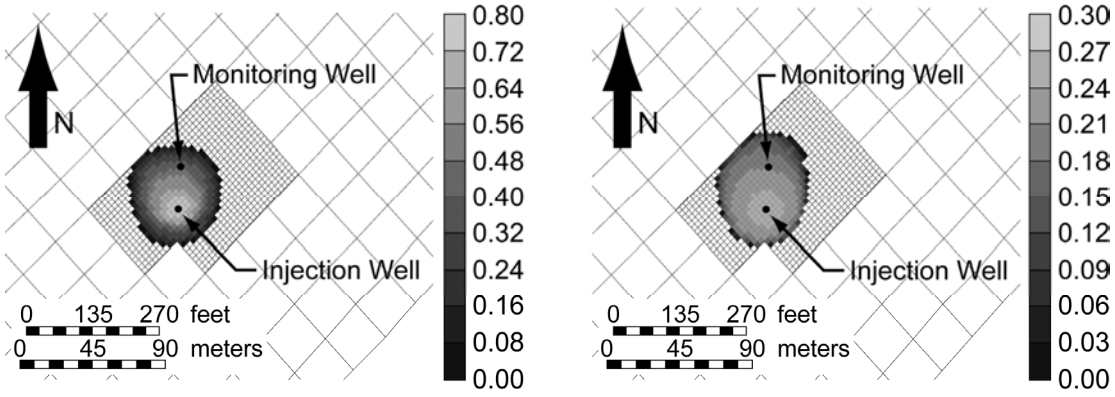

Figure 3.12- Areal view of CO_2 plume in the case of injection at bottom, 12 days (left) and 10 years after injection begins (right)

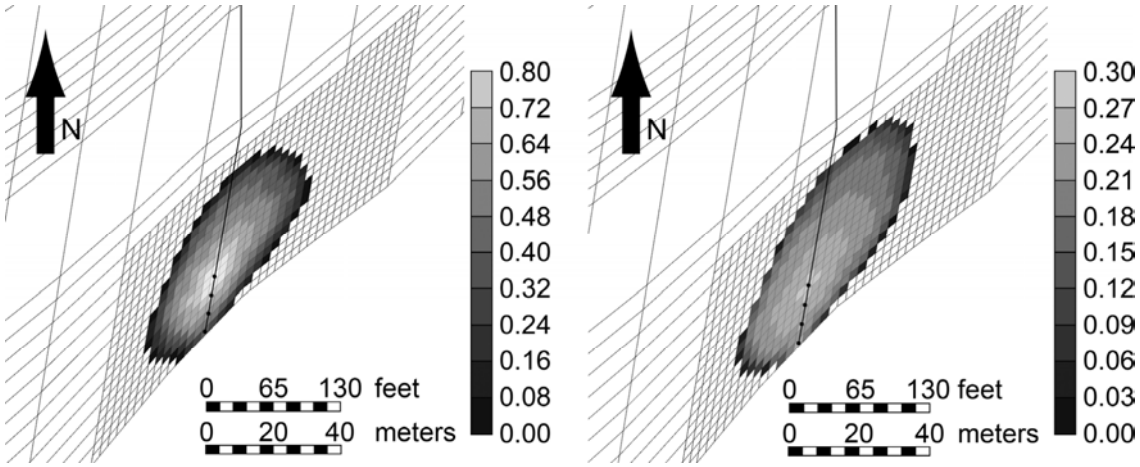

Figure 3.13- NE-SW cross sectional view of CO_2 plume in the case of injection at bottom, 12 days (left) and 10 years after injection begins (right)

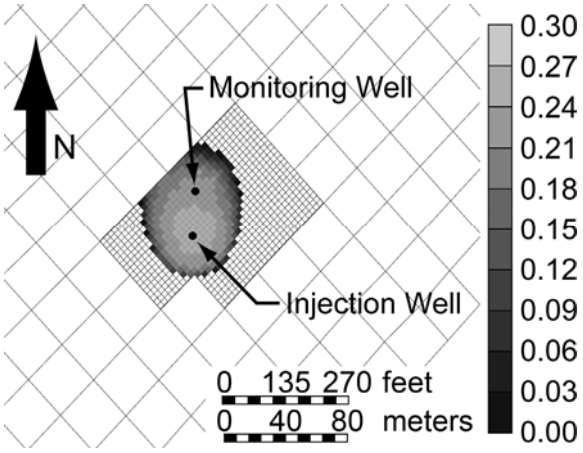

Figure 3.14- Areal view of residual gas saturation in the case of injection at bottom, 10 years after injection begins

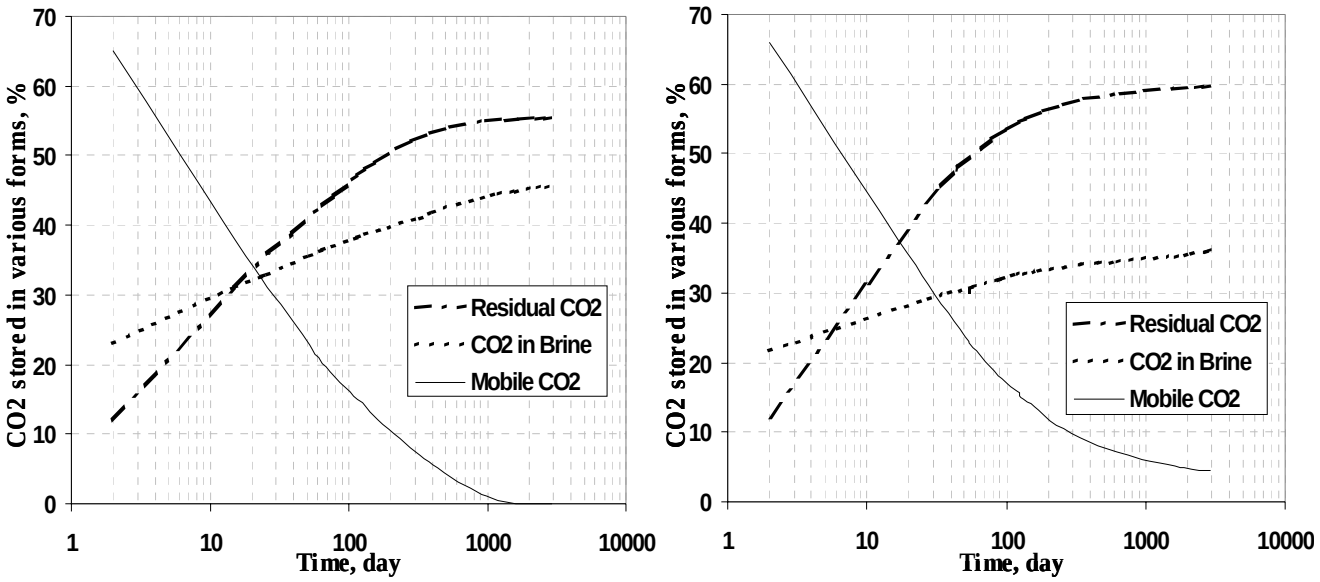

Figure 3.15- CO_2 distribution in three different phases in the injection at bottom (left) and at the top (right) cases

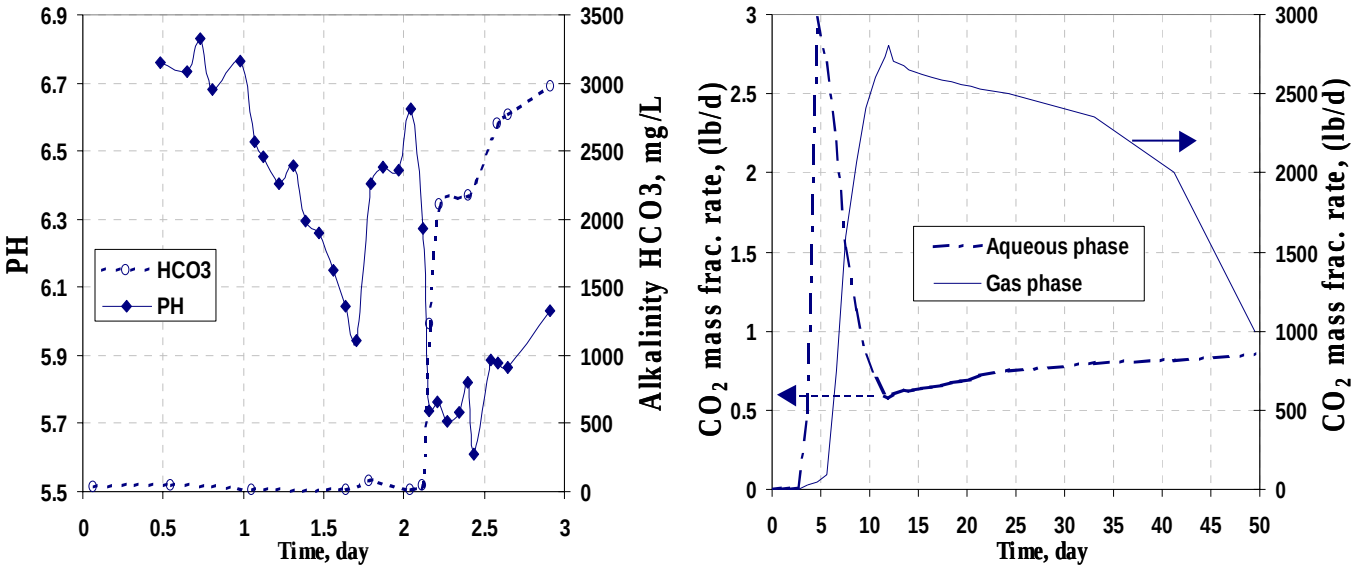

Figure 3.16- Alkalinity and pH of water samples collected with U-tube from field data (Freifeld et al., 2005) (left) and simulation results for the breakthrough of CO_2 in the gas phase and dissolved in the aqueous phase at the observation well (right)

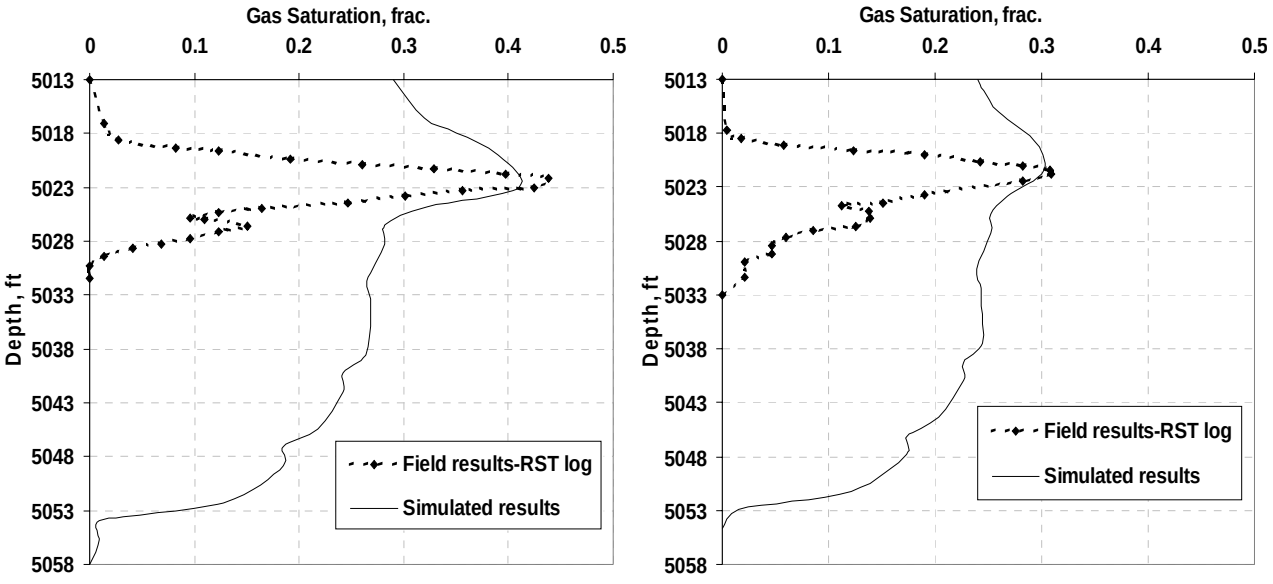

Figure 3.17- Comparison of CO_2 saturation profile between values calculated from RST logs (Freifeld et al., 2005) and simulation results (injection of 3000 tons of CO_2) after 66 days (left) and 142 days (right) at the observation well

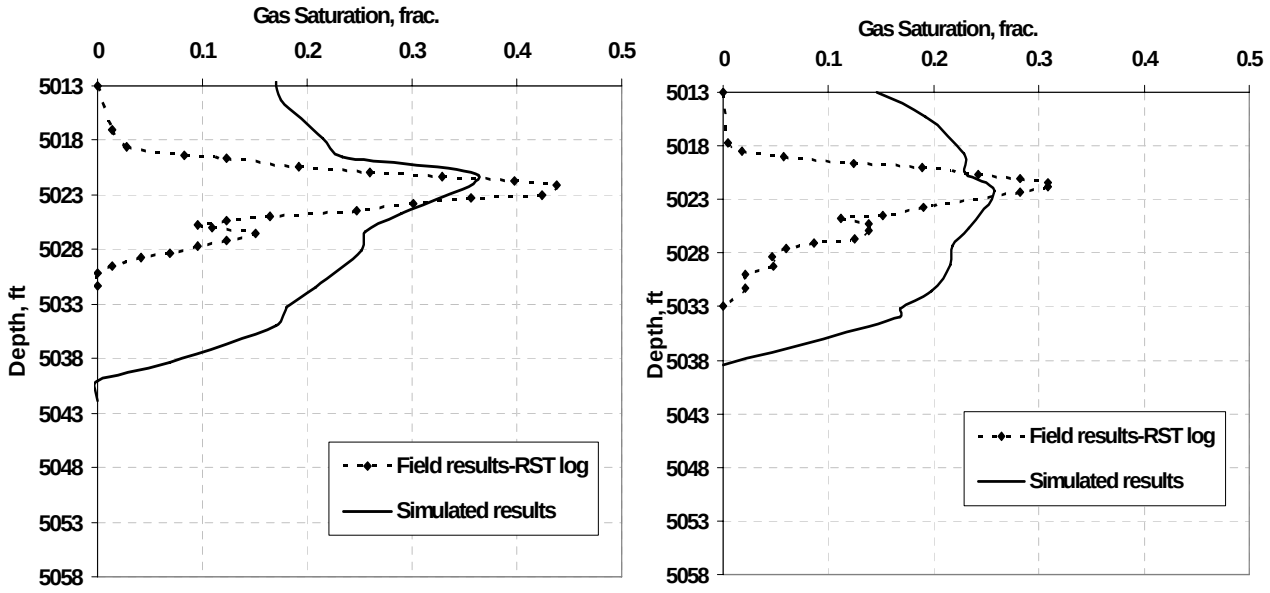

Figure 3.18- Comparison of CO_2 saturation profile between values calculated from RST logs (Freifeld et al., 2005) and simulation results (injection of 1600 tons of CO_2) after 66 days (left) and 142 days (right) at the observation well

Chapter 4: Hysteresis and Field-scale Optimization of WAG Injection for Coupled f-EOR and Sequestration

4.1 INTRODUCTION

The effect of relative permeability hysteresis in modeling storage of CO_2 in saline aquifers has been studied in recent years (Kumar et al., 2004; Ozah et al., 2005; Spiteri et al., 2005). The maximum number of phases considered in these type of studies are two (gas and aqueous phases). In coupled CO_2 sequestration and Enhanced Oil Recovery (EOR) processes, the degree of complexity for the case studies is higher due to the nature of multiphase flow in the reservoir. Usually three or more phases (Guler et al. 2001) are present, depending on temperature and pressure in the reservoir during CO_2 injection. Also, in order to account for the phase behavior effect of phenomena that occur when CO_2 is injected into the reservoir, full compositional simulations should be performed. Moreover, when the fluid saturations experience cyclic changes, relative permeabilities and capillary pressure data show hysteresis behavior. Hysteresis is defined as path irreversibility of relative permeability and capillary pressure curves during drainage and imbibition periods. The imbibition oil and gas relative permeability curves are generally lower than the drainage curve at the same saturation. But the imbibition water relative permeability curve is slightly greater than the drainage curve. This phenomenon is more evident in respect to the gas phase than in other phases.

In the coupled CO_2-EOR and sequestration studies, one of the key issues is the effect and importance of the trapping and hysteresis model on the amount of stored CO_2 in the reservoir. If gas remains in the reservoir in the form of trapped gas, the risk of gas migration and its escape from the reservoir will be minimized. Some studies have been performed to investigate the effect of hysteresis residual gas saturation on the amount of stored CO_2 in the saline aquifers using compositional (Kumar et al., 2004; Ozah et al., 2005) and black oil simulators (Spiteri et al., 2005). It should be noted that the degree of

complexity of fluid flow in porous media in the studies which are involved in the coupled CO_2-EOR and sequestration is much higher than in the aquifer storage cases; therefore careful selection of relative permeability models and their associated parameters have an important role in the final results.

One of the main issues in the EOR and sequestration studies, which can jeopardize the storage side, is early CO_2 break through due to its high mobility and reservoir heterogeneity. Effective strategies should be investigated to optimize oil recovery and the amount of stored CO_2. These strategies can include employing different injection and production schemes, and applying various well control techniques, as well as different mobility control technologies (WAG, SAG, foam, etc.) to delay early CO_2 breakthrough at production wells. Water Alternating Gas (WAG) is a common technique that has been used for a long time to control high mobility of CO_2. The simultaneous flow of gas and water generally yields a net mobility that is less than that of the injection gas alone. This can cause some improvement in sweep efficiency during gas injection. When complete miscibility is developed by injecting the CO_2, gas starts displacing trapped oil, while the injection of water slug increases the volumetric sweep efficiency; therefore the residual oil saturation will be low after the miscible front has passed. It should be mentioned that WAG ratio and slug size of the injected gas are two important factors in any WAG process in order to achieve the highest possible oil recovery. On the other hand, injecting water into the reservoir decreases the total volume of CO_2 that could be injected as continuous slug. Therefore, the optimum amount of water should be injected into the reservoir to satisfy the other goal of this study which is CO_2 storage. Investigations should be made to co-optimize both recovery and storage by employing the best scenario for WAG process specifications such as WAG ratio and CO_2 half cycle size.

Oil recovery and CO_2 storage predictions in these types of investigations are being made by performing reservoir simulation studies. Relative permeability function

and PVT data for the models used in the simulators are two key factors that greatly affect the simulation results. Careful consideration should be given in order to select the appropriate relative permeability model and generate accurate PVT data. More importantly, due to the importance of mass transfer and miscibility in these types of processes, compositional simulation should be employed to provide better estimates of the combined fluid flow and compositional effects on oil recovery and the amount of stored CO_2. As mentioned before, because of the cyclic behavior of saturations, accurate hysteresis relative permeability and capillary pressure models should be selected to reduce the degree of uncertainty in the predictions. Compositional simulation of WAG injection for EOR purposes, with and without hysteresis-included, has been proven to predict different results in 2-D and 3-D cases (Christensen et al. 2000). In addition, they have shown that simulations of this process can have considerable compositional effects; therefore, applying compositional simulation will give more accurate results than using black oil simulations.

4.2 Hysteresis and Relative Permeability Models

A short description of the relative permeability as well as hysteresis models which were used in this study is given in this section. We used experimental data and correlation models presented by Jerauld (1996). These relative permeability data belong to Prudhoe Bay, a mixed wet sandstone (Jerauld and Rathmell, 1997) reservoir, which has gone through a series of successful secondary and tertiary recoveries such as WAG injection. These data include vast amount of descent two-, and three-phase relative permeabilities along with hysteresis in gas, oil and water phases. The correlation that has been presented in his paper is also particularly useful in situations where both compositional effects and gas or oil relative permeability hysteresis are important.

Since we do not want to use only one value for maximum residual gas saturation for all of the permeability and porosity values in the gridblocks, three different rock types were defined to obtain more accurate results. Maximum residual gas saturation is used to calculate residual gas saturation in the reservoir. Residual gas saturation is the most important parameter in evaluating the storage performance of the flood. The effect of trapped gas on oil recovery should also be investigated. Residual gas saturation, as well as some of the relative permeability parameters are correlated with different rock types. The correlations of Holltz (2002), were used to construct a relationship between petropysical data and generated stochastic reservoir fields. These correlations were initially developed using sandstone data and are applicable to CO_2 sequestration studies.

$$k = 7E7 \times \phi^{9.61} \tag{4.1}$$

$$S_{wirr} = 5.6709 \times \left(\frac{\log(k)}{\phi} \right)^{-1.6349} \tag{4.2}$$

$$S_{gr}^{max} = 0.5473 - 0.9696\phi \tag{4.3}$$

where ϕ is the porosity, k is the permeability, S_{gr}^{max} is the maximum residual gas saturation, and S_{wirr} is the irreducible water saturation. Figure 4.1 shows the relation between maximum residual gas saturation and porosity using experimental data from different rock types as well as Holtz's equation for sandstones.

4.2.1 Two-Phase Water Relative Permeability

The water relative permeability in the two-phase oil and water system was modeled using Jerauld's (1996) correlation. This model matches experimental data for Purdhoe Bay mixed-wet sandstone. It denotes that to fit the imbibition water relative permeability a more S-shaped, rather than a simple Corey relative permeability model, is required. i.e.,

$$k_{rwo} = \frac{(1+C_{wo5})\left(\frac{S_w - S_{wro}}{1-S_{wro}}\right)^{C_{wo4}}}{1+C_{wo5}\left(\frac{S_w - S_{wro}}{1-S_{wro}}\right)^{C_{wo4}}} \tag{4.4}$$

where C_{wo5} and C_{wo4} are empirically derived constants. To calculate the residual water saturation in the above equation we used the Holtz correlation.

4.2.2 Two-Phase Gas relative Permeability

For this set of data we also adopted the two-phase relative permeability data proposed by Jerauld and Rathmell (1997). Gas relative permeability data are well represented by the equation below:

$$k_{rg} = \frac{(1+C_{g2})\left(\frac{S_g - S_{gr}}{1-S_{gr}}\right)^{C_{g1}}}{1+C_{g2}\left(\frac{S_g - S_{gr}}{1-S_{gr}}\right)^{C_{g1}(1+1/C_{g2})}} \tag{4.5}$$

where C_{g1} and C_{g2} are empirically derived constants. Residual gas saturation was taken as zero for all three rock types. It can be shown that at low gas saturations, the numerator of this equation dominates and approaches the conventional Corey (1954) equation. At higher gas saturations, the second term of the denominator becomes dominant and causes a continuously decreasing slope of the K_{rg} curve.

4.2.3 Two-Phase Oil relative Permeability

The oil relative permeabilities with respect to water and gas fit well with the Corey model given below:

$$k_{row} = k^{o}_{row}\left(\frac{S_o - S_{orw}}{1 - S_{wr} - S_{orw}}\right)^{e_{ow}} \tag{4.6}$$

$$k_{rog} = k^{o}_{rog}\left(\frac{1 - S_g - S_{Lrg}}{1 - S_{Lrg} - S_{gr}}\right)^{e_{og}} \tag{4.7}$$

4.2.4 Two-Phase Capillary Pressure

Two-phase capillary pressure for any rock type is modeled using the Leverett J-function:

$$Pc = \sigma\sqrt{\frac{\phi}{k}}\,j \tag{4.8}$$

where ϕ is the porosity, k is the permeability, σ is interfacial tension between water-oil and that of gas-liquid at reservoir temperature and pressure, and j is the dimensionless Leverett j-function:

$$j = S_1^{-n} + j_e - 1 \tag{4.9}$$

where S_1 is the wetting phase saturation as fraction, j_e is the entry value of j-function (here equal to 0.4), and "n" is the pore size distribution index; large "n" means well sorted and small values mean poorly sorted rock. Data for interfacial tension were obtained from Yang et al. (2005).

4.2.5 Hysteresis and Gas Trapping Model

In the reservoir simulation studies, hysteresis effects should be considered whenever there is a change in the injected fluid or the displacement mechanism is switched from drainage to imbibition, and vice versa. Figure 4.2 shows these cyclic changes between imbibition and drainage gas relative permeability curves. The WAG process is an example of this phenomenon. Therefore, it is critical to include a valid

hysteresis model in order to obtain accurate results in the WAG simulations. In the simulations in which hysteresis is not modeled and accounted for, only drainage gas relative permeability data are being used during the drainage and imbibition processes. This can cause the effect of trapped gas in the oil recovery to remain unaccounted for. Moreover, residual gas saturation predictions, which are the most important factors in the CO_2 sequestration studies, can only be performed by employing the hysteresis model in the simulation.

Trapped gas saturation influences water injectivity and is the primary determinant of the amount of miscible injected fluid retained in the reservoir, and therefore unavailable for oil displacement. In most studies (Jerauld and Rathmell, 1997; Christensen et al., 2000; Kumar et al., 2004) it has been shown that the trapped gas data are poorly fit by the Land (1971) equation but are reasonably well approximated by a modified form of the Land equation. Following, is a short description of this model.

Based on Land's equation, gas saturation is divided into two parts, residual (or trapped) gas saturation and free gas saturation. His original empirical equation correlates the maximum residual gas saturation to the initial gas saturation (the point where drainage is shifted to imbibition). The equations below show this concept:

$$S_g = S_{gf} + S_{gr} \tag{4.10}$$

$$\frac{1}{S_{gr}} - \frac{1}{S_{gi}} = C \tag{4.11}$$

where S_{gi} is the initial gas saturation, S_{gf}, the mobile gas saturation, C is the Land's constant, S_{gr}, the residual gas saturation, and S_g is the gas saturation.

In our study, hysteresis in gas relative permeability curves was modeled using a modified Land's equation. In this method, gas relative permeability during the drainage process is calculated using user-defined relative permeability models. During imbibition, gas relative permeability is calculated using shifted gas saturation, i.e.,

$$k_{rg} = \frac{(1+C_{g2})\left(\frac{S_g(\text{shifted}) - S_{gr}}{1 - S_{gr}}\right)^{Cg1}}{1 + C_{g2}\left(\frac{S_g(\text{shifted}) - S_{gr}}{1 - S_{gr}}\right)^{C_{g1}(1+1/C_{g2})}} \tag{4.12}$$

where

$$S_g(\text{shifted}) = S_{gr} + \frac{(S_g - S_{grh})(S_{gh} - S_{gr})}{(S_{gh} - S_{grh})} \tag{4.13}$$

and S_{gh} (hysteresis gas saturation) is the value of S_g where the shift to imbibition occurs. By definition, the values of S_{gh} are the values of gas saturations corresponding to the highest capillary pressures at all times. Hysteresis residual gas saturation (S_{grh}) is also the values of S_{gr} corresponding to S_{gh} via modified Land's equation given below:

$$\frac{1}{S_{gr}^{max} - S_{gr}} - \frac{1}{S_g^{max} - S_{gr}} = \frac{1}{S_{grh} - S_{gr}} - \frac{1}{S_{gh} - S_{gr}} \tag{4.14}$$

where S_{gr}^{max} is the user input value for the maximum residual gas saturation, and S_g^{max} is maximum gas saturation which was considered equal to 1 in our study. After performing a set of 1-D homogeneous simulations, performance and accuracy of the hysteresis modeling in the simulator were checked. Figure 4.3 shows the relation between gas saturation and residual gas saturation using modified Land's equation. It is also observed that our simulated values as well as experimental data from Jerauld and Rathmell (1997) follow this relation.

4.2.6 Three-Phase Relative Permeability

Since gas phase is the most non-wetting phase in a three phase oil, water and gas system therefore, gas phase relative permeability is only function of gas saturation. The water phase is also non-wetting phase with respect to oil and wetting-phase with respect to the gas phase. In fact this is the reason that shows slight hysteresis, but in our modeling

we assumed that hysteresis effect to be negligible. Furthermore, we assumed that the three-phase water relative permeability is only a function of water saturation, and is a weak function of the saturations of other present phases. Relative permeability of the oil phase, which is the intermediate wetting phase, is more influenced by interaction with other phases. There are different correlations to predict three-phase oil relative permeabilities, and extensive studies have been performed comparison these models (Baker, 1988; Jerauld, 1996; Spiteri and Juanes, 2004). In this study, we selected the saturation weighted interpolation method proposed by Baker (1988), since it has shown better correlation with experimental data so far (Delshad and Pope, 1989). Therefore, three-phase oil relative permeability data are constructed based on saturation-weighted interpolation between water-oil and gas-oil data as given by Equation 4.15:

$$k_{ro} = \frac{(S_w - S_{wc})k_{row} + (S_g - S_{gr})k_{rog}}{(S_w - S_{wc}) + (S_g - S_{gr})} \tag{4.15}$$

Table 4.1 shows all of the parameters used to generate the two-phase relative permeability and capillary pressure data for the three rock types used in the simulation models.

4.3 NUMERICAL SIMULATION STUDIES

In this section, we present the results for compositional simulation studies that were performed in two-dimensional and three-dimensional heterogeneous generic reservoirs. The effect of important factors in the WAG processes, on the oil recovery and the amount of stored CO_2 was investigated to determine the optimum situation for a WAG process to achieve highest possible recovery and amount of CO_2 trapped in the reservoir. Since WAG injection processes are strictly dependent on reservoir heterogeneity, the effect of reservoir heterogeneity parameters such as Dykstra Parsons coefficient and the correlation lengths in all three spatial directions were studied to

achieve comprehensive results for coupled CO_2 sequestration and WAG processes under these uncertain variables.

4.3.1 Two-Dimensional Simulation Model

4.3.1.1 Model Description

A cross sectional stochastic 2-D X-Z dipping model was built in the Cartesian coordinate. The reservoir lithology was considered as sandstone, therefore all reservoir properties were selected based on this important assumption. The reservoir grid was initially set to 40×1×20. Table 4.2 shows the summary data for this reservoir. Figure 4.4 shows the reservoir stochastic permeability field. The average horizontal permeability is 110 md and the average porosity is 0.22 fraction of reservoir bulk volume. Rock-fluid interaction parameters were also calculated using the previously explained method and compared to data from Jerauld (1996). GEM, CMG's (2006) advanced general equation-of-state compositional simulator was used to perform the simulations.

Accurate characterization of a crude oil and then tuning of the EOS model, used in a compositional EOS simulator, are important first steps in simulating WAG and CO_2 flooding processes. Khan (1992) studied several light crude oils for this purpose and reported a systematic approach for selecting pseudo components and their properties that showed very good agreement with experimental data for conditions when both two- and three-phase flow are formed between the CO_2 and crude oil. In addition, 1-D slim tube simulations were performed to check the accuracy of the model and determine the minimum miscibility pressure (MMP) between injected CO_2 and reservoir fluid. Figure 4.5 shows the comparison of simulated results and experimental data. As part of this preliminary study, the minimum miscibility pressure of reservoir oil with CO_2 was calculated using Calsep's PVTSim (2004) using the modified Peng-Robinson EOS option and the same components and parameters used by Khan. The computed MMP was 1224

psia, which is in good agreement with experimental data. Table 4.3 shows the PVT parameters used in our study.

4.3.1.2 Simulation Results and Discussion

Before carrying out the main simulation cases, grid refinement was performed to determine the optimum number of gridblocks to carry out an accurate and consistent study. Also, to obtain the most resemblance to real world cases, water was injected up-dip into the reservoir to establish the initial condition for the WAG process. Using the CMG's RESTART option, all of the WAG injection simulations were then carried out by restarting the previous simulation. For all refinement study simulations, a WAG ratio of 0.6 and a CO_2 half-cycle of 3% HCPV were applied. In addition, an initial CO_2 slug size was selected as 15% HCPV. Figure 4.6 shows the convergence graph for all of the refined cases. The water flood cases converged by using 100 blocks in the X direction and 40 blocks in the Z direction. The WAG process, with hysteresis-included, converged by taking 60 gridblocks in the Z direction and 125 gridblocks in the X direction. Considering the computational expenses and time, a 100×1×40 grid was chosen as the optimum case for all 2-D simulations.

For the cases with a higher degree of refinement, it was necessary to apply a higher-order approximation scheme to reduce the numerical dispersion of the simulations. In addition, since very small grid sizes were used, the physical dispersion effect also was taken into account. By inputting the physical dispersion along with hysteresis model in the relative permeability data in the compositional simulation run, and due to the effect of the mathematical nature of physical dispersion (creating a second-order derivative in the governing partial differential equation), severe numerical instabilities such as pressure overshooting and convergence problems were observed. To solve this problem, a fully implicit formulation along with two-point up-stream weighting

method under the control of a Total Variation Limiting (TVD) flux limiter was employed. The TVD limiter eliminates over- and under-shoots in the calculations. The limiter also allows the higher-order flux calculation to predominate in regions away from the edges of saturation fronts and fluid banks, and reverts the calculations to a more stable upstream scheme near these frontal regions where compositional variable and saturations were changing rapidly.

After selecting the optimum number of gridblocks to continue the study, water was injected into the reservoir. In the water flooding stage, 48 percent of original oil in place (OOIP) was produced before the water cut reached 95 percent in the production well. Average remaining oil saturation after water flooding was 39 percent. Water breakthrough happened after almost 4.1 years and after about 12.6 years the water cut in the producing well reached 95 percent.

The hysteresis effect is vital in obtaining accurate results for WAG process simulations. From the sequestration point of view, including the hysteresis in the simulation processes provides an accurate prediction for amount of trapped gas. Residual gas is the immobile form of the gas and will reside in the reservoir for a long period of time. This is basically the ultimate goal for storing CO_2 underground. By including hysteresis in the simulation model it will be possible to calculate portions of the gas in both residual and free forms. It should be noted that the residual gas saturation for each gridblock will be different depending on the rock type for that gridblock. By employing a special version of GEM provided to The University of Texas at Austin by CMG, Ltd., we were able to calculate corresponding S_{gh} (hysteresis gas saturation, which is the maximum gas saturation in each gridblock at any time the during entire simulation period), as well as S_{grh} (residual gas saturation corresponding to its S_{gh} value in each gridblock). Figure 4.7-a shows the hysteresis gas saturation (S_{gh}), Figure 4.7-b shows the residual hysteresis gas saturation (S_{grh}), and Figure 4.7-c shows the gas saturation (S_g) distribution at the end of WAG injection. Residual hysteresis gas saturation data in Figure 4.7-b shows the

actual trapped portion of the gas during simulation. The difference between gas saturation data, shown in Figure 4.7-c and residual hysteresis gas saturation values will show the portion of CO_2 in free form or mixed with the hydrocarbon phase. It can be observed that due to the effect of higher heterogeneity, some parts of the reservoir have not been swept by gas, resulting in a very high remaining oil saturation and low gas saturation areas.

From production perspective, hysteresis is responsible for trapping CO_2 in the reservoir as residual gas, causing a higher efficiency of the flood. Figure 4.8 shows the comparison of oil recovery factor for different simulation cases, with and without hysteresis and at different WAG ratios, but all at the same CO_2 slug sizes. Injection of water after each gas cycle causes gas to be trapped in the reservoir due to hysteresis, reducing gas mobility. Consequently, this can make barriers to the water phase resulting in lower water cut as well as lower gas-oil ratio. In addition, gas trapping can help achieving better sweep, which results in higher recovery compared to the simulations without the hysteresis model. It is also seen from Figure 4.8 that due to the reduction in the oil relative permeability, because of the existence of trapped gas, oil mobility reduces, which causes better sweep but over a longer period of time.

The effect of hysteresis is more obvious from the CO_2 storage perspective. Figure 4.9 shows the comparison of average gas saturation in the reservoir sector for cases with and without hysteresis, applied in the model. By applying hysteresis, the predictions for CO_2 saturation are 60 percent higher than in the cases without hysteresis at the end of the simulation. But, from a recovery viewpoint, there seems to be little difference between these two cases. Oil recovery is almost 3 percent higher in the cases that hysteresis was applied in the simulation. It should be noted that depending on the hysteresis parameters used, oil recovery predictions, and more importantly CO_2 saturation in the reservoir, can change.

4.3.2 Field-scale Simulations

Based on our initial observations from the 2-D WAG injection simulation results, quantifying the effect of WAG parameters (e.g. WAG ratio and CO_2 slug size), hysteresis, and reservoir heterogeneity characteristics (e.g. Dykstra-Parsons coefficient, dimensionless correlation length in X, Y, and Z direction) in the WAG injection processes was crucial for coupled EOR and sequestration studies. Field-scale compositional simulations of WAG injection were performed to investigate these effects in a more detailed manner. In order to carry out a comprehensive study of the mentioned parameters, an experimental design method was applied.

Design of experiment (DOE) is a tool to perform a comprehensive sensitivity study on the factors or parameters with some range of uncertainties in order to understand their individual or combined effects on pre-defined process(es), called Response variable(s). Responses are representatives of the objectives of the process as the output, and the settings for the parameters and decision variables as the input. Experimental design is based on the application of different sampling methods (e.g. Latin hyperbolic method) to identify a subset of experiments from a larger set, according to the number of factors that need to be analyzed. By applying this method, attempt is made to maximize information obtained from this subset of experiments in order to achieve a comprehensive level of information on the whole set of necessary experiments. Results from these limited experiments are statistically evaluated to define the significance of the different factors on the main process(es). An experimental design study is used to generate Response Surfaces (RS) that are able to predict the effect of variations of factors in a simple mathematical form. There are different techniques, such as two-level factorial design, three-level factorial design, D-optimal, and etc., to perform a successful experimental design study (Montgomery, 2001).

The two-level factorial design method was used to carry out the sensitivity analysis. It should be noted that the main goal of this study was to determine the optimum

values or scenarios of the mentioned parameters, to achieve both maximum possible oil recovery and the stored amount of CO_2. It was also desired to investigate the interaction between hysteresis modeling and importance of bigger scale phenomena such as areal sweep and reservoir heterogeneity. Table 4.4 shows the design parameters and their corresponding range of variation for this study. Defined range of the variables was taken from Jarrel et al. (2002) and Christensen et al. (2001).

4.3.2.1 Reservoir Model

A 3-D corner point reservoir grid was constructed for our simulation case studies and then stochastic permeability and porosity values were assigned for the gridblocks. The reservoir lithology was considered as sandstone; therefore, all reservoir properties were based on this important assumption. The average horizontal permeability is 113 md and the average porosity is 0.23 fraction of reservoir bulk volume for all of the stochastic fields. Figure 4.10 shows two cases of the reservoir stochastic permeability fields. The same hysteresis parameters were used as in the 2-D simulation cases. Reservoir geometry comprised two anticline domes adjacent to each other with a 200 ft thickness at the depth of 6100 ft. The reservoir grid was set to 28×40×15 gridblocks. Table 4.5 shows the summary data for the reservoir properties. For rock-fluid and PVT data, we used the same relative permeability and hysteresis models as in the 2-D simulation models. The same PVT data that were used in the 2-D cross sectional simulations was applied here as well. Reservoir fluid was considered in a vertical equilibrium condition with water-oil contact of 6400 ft. The bottom aquifer was not considered an active supporting energy source for the reservoir. Table 4.5 shows the average oil and water saturation in the reservoir. Since all of the reservoir blocks were classified into three different rock types, maximum residual gas saturation values were calculated for each rock type according to the previously stated correlations (Holtz, 2002).

Similar to the 2-D simulations, and to obtain the most resemblance to the real world cases, all of the WAG injection simulations restarted at the end of the waterflood. Water was injected nearly up dip using 6 vertical wells and oil was produced by 13 vertical wells in the oil zone. Figure 4.11 shows the 3-D view of the remaining oil saturation at the end of the water flood in one of the simulation cases. By the end of the primary and water flooding stages, an average of 42 percent of original oil in place (OOIP) was produced in different simulation cases (considering 98 percent water cut as the production limit for each well). The average remaining oil saturation after water flooding was 31 percent. The duration of water flooding was almost 5.3 years. After water flooding, WAG injection simulations were performed. In this stage, water and CO_2 were injected alternately with three injection wells, and oil was produced using 15 production wells. The injection rate was controlled by a maximum Bottom Hole Pressure (BHP) constraint set to 3300 psi (fracture pressure at the depth of 6000 ft). The production wells operated under a minimum bottom hole pressure constraint of 1400 psi. The injected volumes of the fluids at the reservoir condition were controlled for each cycle to honor the WAG ratio and CO_2 slug sizes. Therefore, injection fluids were automatically being switched during the period of simulation time. By applying extensive well completion scenarios, it was tried to control the amount of water and CO_2 production. For instance, when the water cut reached 98% or gas-oil ratio reached 20000 scf/STB, most offending layers were plugged and checked periodically to see whether previously violated monitored constraints had ceased being violated. If so, the layer was reopened automatically. As another well control operation for WAG injection simulations, the total minimum production of the field was limited to 10 STB/day.

4.3.2.2 Simulation Results and Discussion

Considering the results from 2-D simulations of the WAG flooding process, it can be inferred that more simulations needed to be performed to examine the effect of other factors, such as reservoir heterogeneity as well as a combination of different parameters on the considered objective functions in field-scale cases. Ranking the effect of considered parameters on oil recovery and the amount of stored CO_2 can also be made possible by applying statistical analysis on the simulation results. This can be a powerful tool in screening the candidate reservoirs and the flood design parameters for any WAG process.

In this study, the oil recovery factor and the amount of stored CO_2 (CO_2 saturation) were initially chosen as our objective functions, and the main goal was to determine the optimal combination of design variables under the range of variation for each one. Two-level factorial design method was utilized to plan the number of simulation runs and status/value of each uncertain parameter in any simulation case. If classical sensitivity analysis was supposed to be applied, 64 simulation cases were necessary to be performed in order to obtain the final results; but according to the number of factors and selected experimental design method, 16 different compositional simulation cases were selected out of those 64 (2^6) simulation runs. Therefore, the amount of computational time and engineering expenses was reduced by 75 % . Table 4.6 shows the selected simulation runs and status/value of different parameters in each case. Based on this plan, 16 input data series were set up and CO_2-WAG simulations were carried out for all of them. Table 4.7 shows the results for all of the objective functions obtained from performing those simulation runs.

It is clear from Table 4.7 that because of constraint in the GOR and water-cut (WC) of the production wells, the duration of the simulation runs (to reach GOR/WCUT of production wells to 20000 SCF/STB) was different for each case. Therefore, it was necessary to enter the factor of time as another criterion to account for its effect in the

previously considered objective functions. The best way to apply this was to consider Net Present Value (NPV) for each simulation as the third objective function. Table 4.7 shows the results for oil recovery, CO_2 saturation, and NPV as final objective functions in different simulation cases. In order to perform the NPV calculations, the economical parameters shown in Table 4.8 were assumed. It can be observed from Table 4.7 that the incremental oil recovery varies from 14.7% to 25.9% for various simulation cases. CO_2 saturation varies between 0.04 and 0.26 and the NPV of the simulations is changing from 20.6 to 41.8 $MM.

Figure12 shows the simulation results for oil recovery factor for several sensitivity cases listed in Table 4.6. Run numbers 1 and 15 have hysteresis included in the models compared to the two other runs in which hysteresis was not applied. It is seen that in the cases with hysteresis oil recovery seems slightly higher but over a longer period of simulation time. This is due to the effect of trapped gas blocking the oil flow. Figure 4.12 also shows that simulation runs 1 and 16 have overall lower recoveries compared to the two other runs. This is mostly due to the effect of higher heterogeneity (more specifically, higher Dykstra-Parson's coefficient) in the runs 1 and 16. Despite the fact that these two runs have lower WAG ratios and slug sizes, and intuitively they should have higher oil recoveries, however, due to the effect of higher heterogeneity they have lower oil recoveries compared to the two other runs. This clearly shows that reservoir heterogeneity has higher impact on oil recovery than WAG ratio and slug size.

Figure 4.13 shows the average gas saturation distribution over time in the reservoir for aforementioned sensitivity runs. Bigger oscillations in the gas saturation in runs 1 and 15, compared to two other scenarios, indicate higher slug sizes and WAG ratios. Comparing runs 1 and 16, where both runs have the same WAG ratio and slug sizes, shows that due the effect of hysteresis which has been accounted for in run 1, higher gas saturation is achieved in the reservoir. Due to the same reason, run 15 has higher gas saturation than run 11.

Figure 4.14 shows the results of statistical analysis on the simulation results. It shows the effect of all six factors on both estimated oil recovery and CO_2 storage objective functions using two-level factorial design method. The effect on the X axis represents the change in the average response when a factor varies from its low to high value within the range of uncertainty. The effect is negative (blue colors) when the increase in the factor from the low side to the high side decreases the response value, and the effect is positive when the increase in the factor from the low side to the high side increases the response value. High influential factors (first-order effects) on the recovery and storage objective functions are shown in Figure 4.14. Based on the parameters and the reservoir conditions studied, the order from most to least influential factors on the recovery objective are Dykstra-Parsons coefficient, combination of WAG ratio and slug size, and slug size by itself. Whereas, for the storage objective by far the most influential factor is WAG ratio, then a combination of WAG ratio and hysteresis, and then hysteresis by itself. It should be noted that some of these parameters have negative and positive effects on the responses. For instance, it is evident from the statistical analysis that when WAG ratio increases, it can greatly decrease the storage response. Also, if hysteresis models were not applied in the model, the storage objective function is reduced significantly. After defining sensitive parameters and ranking them based on their importance on each objective function, the response surfaces are generated. Figure 4.15 demonstrates the response surfaces for CO_2 saturation and Figure 4.16 shows the responses for recovery objective function. These response surfaces are presented at different WAG ratio and slug sizes but other uncertain parameters corresponding to these response surfaces are shown in the figure. According to Figure 4.15, storage response shows relatively linear trend; it decreases with the increase in the WAG ratio and does not change significantly with variation in slug size. In addition, it is shown that if hysteresis was applied in the simulation model, storage responses have qualitatively similar trend (function) with respect to the other parameters, but is quantitatively lower

than the cases in which hysteresis was not applied. According to Figure 4.16, the oil recovery response surfaces are demonstrating fairly non-linear trend. As with the storage responses, it is shown that applying hysteresis in the model generally causes an increase in oil recovery. It also shows that at relatively low WAG ratios, smaller slug sizes are needed in order to achieve higher recoveries and vice versa.

Mathematical forms of generated response surfaces were utilized to perform optimization on oil recovery and the amount of stored CO_2 as well as Net Present Value (NPV) for the WAG process. Therefore, optimization processes were performed to define conditions for any of six uncertain factors by which the highest possible recovery, storage, and net present value is achieved. An equally-weighted combination of recovery and storage objective functions was also considered as another optimization scenario. It should be noted that the dollar value of each cubic feet of stored CO_2 and the dollar value of each standard barrel of oil produced as two dimensionless-type parameters were both considered as representative for net present value of each simulation case. They were calculated by dividing NPV of each simulation case by the total amount of stored CO_2 and also the total amount of oil produced. Table 4.9 shows the results of four different optimization scenarios that were defined in this study. In addition, status/values for each uncertain parameter in order to achieve optimum value for defined objective functions were suggested by the method of response surfaces for each scenario. These results are shown in Table 4.9 as well.

Another advantage of applying experimental design and the method of response surfaces to perform the optimization process is that the optimized values for all scenarios can be predicted with a specified margin of error. In this study, these predicted values for each scenario are shown in Tale 9. Predicted response values for each optimization scenario were very close to the values that were acquired by performing their corresponding simulation runs. It is also evident that the effect of hysteresis modeling is vital in obtaining accurate results for recovery predictions and particularly for the amount

of stored CO_2. Table 4.9 shows that hysteresis has a very large impact on the behavior of CO_2 in terms of both oil recovery and storage in heterogeneous oil reservoirs. In addition, it can be seen that the CO_2 storage is greater for oil reservoirs with low heterogeneity and at lower WAG ratio and CO_2 slug sizes. Profit gained from a CO_2-EOR project is expected to be greater for oil reservoirs with low heterogeneity and at high WAG ratio and large CO_2 slug sizes.

4.4 SUMMARY AND CONCLUSIONS

Two-dimensional and field-scale compositional reservoir simulation study was performed to investigate the effect of hysteresis on the amount of stored CO_2 and oil recovery in a coupled EOR and sequestration study. Results of this study show the effect of hysteresis gas saturation on CO_2 storage as well as on the oil recovery. Hysteresis gas saturation and residual hysteresis gas saturation are two of the main factors in performing a CO_2 sequestration study, especially when cyclic saturation behavior (similar to that in the WAG injection) is being modeled. These two parameters can be modeled when hysteresis is taken into account. Hysteresis is responsible for trapping the CO_2 in the reservoir as residual gas, causing higher efficiency of the flood. It should be mentioned that due to the reduction in the oil relative permeability because of the existence of trapped gas, oil mobility is reduced. This causes better sweep but takes a longer period of time. In addition, by applying hysteresis, the predictions for CO_2 saturation are higher than in the cases without hysteresis at the end of the simulation. From the recovery viewpoint, there seem to be few differences between these two cases. In this study, experimental relative permeability data (Jerauld, 1996) along with a modified Land's model (to account for hysteresis) was applied in all of the simulation cases.

The impact of hysteresis on the simulation results of a vertical cross sectional model was investigated. Grid refinement was performed to study the convergence

behavior of the model. Due to the application of very small grid sizes, the physical dispersion effect also was taken into account. Because of the complicated nature of the problem (compositional simulation with hysteresis and physical dispersion included in the model), some numerical oscillations occurred during the simulations even while using a higher-order approximation scheme with TVD limiter.

Field-scale 3-D compositional simulations of WAG injection were performed to quantify the effect of WAG parameters (e.g. WAG ratio and CO_2 slug size), hysteresis, and reservoir heterogeneity (such as Dykstra-Parsons coefficient and dimensionless correlation length in three dimensions) in the WAG injection processes by applying a two-level factorial experimental design method. After the statistical analysis of the simulation results, the effect of all six uncertain parameters on oil recovery and CO_2 storage as well as project economics was determined. Based on the parameters and the reservoir conditions studied, the most to least influential factors for recovery objective are Dykstra-Parsons coefficient, combination of WAG ratio and slug size, and slug size by itself. However, for storage objective, by far the most influential factor is WAG ratio, followed by combination of WAG ratio and hysteresis, and lastly hysteresis by itself.

The optimization process was carried out to define conditions for all six parameters by which the highest possible recovery and storage can be achieved. All of the optimized values for all objective functions predicted by design of experiment and response surface method are close to the values obtained by an exhaustive simulation study, but using fraction of computational time for the exhaustive simulations. It was also shown that hysteresis has a very large impact on the behavior of CO_2 in terms of both oil recovery and storage in heterogeneous oil reservoirs. In addition, it has been shown that CO_2 storage is greater for oil reservoirs with low heterogeneity and at lower WAG ratio and CO_2 slug sizes. Profit gained from a CO_2-EOR project is expected to be greater for oil reservoirs with low heterogeneity and at high WAG ratio and Large CO_2 slug sizes. This study demonstrates that compositional reservoir simulation in conjunction with

experimental design and the method of response surfaces can be used efficiently in optimization studies in coupled CO_2 sequestration and enhanced oil recoveries.

Table 4.1: Parameters used in constructing the rock-fluid data for 3 different rock types

	Rock Type 1	**Rock type 2**	**Rock Type 3**
Average porosity, frac.	0.16	0.25	0.34
Average permeability, md	1.82	114	2420
Maximum trapped gas saturation, frac.	0.45	0.3	0.2
End point water relative permeability, $k°_{rw}$	0.4	0.5	0.65
End point oil relative permeability, $k°_{ro}$	0.45	0.8	0.95
Irreducible water saturation, S_{wirr}	0.45	0.2	0.15
Residual oil saturation, S_{or}	0.35	0.3	0.25
Residual gas saturation, S_{gr}	0	0	0
Water phase exponent, C_{wo4}	2.5	2.5	2.5
Water phase exponent, C_{wo5}	2	1	1
Gas phase exponent, C_{g1}	2.7	3.2	3.2
Gas phase exponent, C_{g2}	5	6.5	6.5
Water-oil interfacial tension, σ (dyne/cm)	25	25	25
Gas-oil interfacial tension, σ (dyne/cm)	18	18	18
Entry value of J-function-Gas phase, J_e	0.2	0.2	0.2
Entry value of J-function-Water phase, J_e	0.4	0.4	0.4
pore size distribution index, n	1	1	1

Table 4.2: Summary of input data for 2-D cross sectional reservoir cases

	40×1×20
Length, ft	2000
Dip, Degree	10
Thickness, ft	200
Number of Blocks	40×1×20
Gridblock Size, ft	50×1×10
Number of Gridblocks	800
Vertical to horizontal Perm. Ratio	0.1
Average horizontal permeability, md	110
Average vertical permeability, md	11
Average porosity	0.224
Initial Pressure, psia	2200
Initial Oil Saturation, frac.	0.75
Initial Water Saturation, frac.	0.25
Residual Oil Saturation	0.3-0.35
Residual Water Saturation	0.15-0.2
End Point Mobility Ratio	12-18
Temperature, °F	110
Reservoir Aspect Ratio (R_L)	3.16
Dykstra-Parsons coefficient	0.8
Correlation Length in x and y direction (λ_x,λ_y), ft	500
Correlation Length in z direction (λ_z), ft	40
Pore Volume, M. RB	780
OOIP, M STB	520
HCPV, M RB	582

Table 4.3: Equation-of-state parameters for different components used in the simulation study

Component / **Property**	**CO_2**	**C1**	**C2-C3**	**C4-C6**	**C7-C16**	**C17-C29**	**C30+**
Mole fraction, frac.	0.0192	0.0693	0.1742	0.1944	0.3138	0.1549	0.0742
Critical P, atm	72.799	45.400	44.932	33.238	20.676	15.675	15.636
Critical T, deg K	303.89	166.67	338.34	466.12	611.116	777.784	972.23
Acentric Factor	0.225	0.008	0.126	0.244	0.639	1.000	1.281
Mw, gm/gmol	44.010	16.043	36.013	70.520	147.182	301.476	562.81
Volume Shift	0.140	-0.154	-0.009	-0.041	0.064	0.179	0.301
Parachor	49.000	71.000	135.00	231.62	439.147	788.222	1112.5
Omega A	0.4572	0.3496	0.4572	0.4572	0.45724	0.45724	0.4572
Omega B	0.0778	0.0680	0.0778	0.0778	0.07780	0.07780	0.0778

Table 4.4: Experimental design parameters for WAG injection

Factors	Type	Low	High
A: WAG Ratio	Numeric	0.25	3
B: Slug Size, %HCPV	Numeric	0.5	8
C: Dykstra-Parsons coefficient	Numeric	0.6	0.9
D: Hysteresis	Categoric	D1 (Applied)	D2 (Not applied)
E: Dimensionless Correlation Length in X, Y Direction, $\lambda_{Dx,y}$	Numeric	0.2	2
F: Dimensionless Correlation Length in Z Direction, λ_{Dz}	Numeric	0.3	0.4

Table 4.5: Summary input data for 3-D reservoir case

Length, ft	3500
Width, ft	2500
Thickness, ft	150
Number of Blocks	28×40×15
Gridblock Size, ft	90×90×10
Number of Gridblocks	16800
Vertical to horizontal Perm. Ratio	0.1
Average horizontal permeability, md	113
Average vertical permeability, md	11
Average porosity	0.22
Reference Initial Pressure, psia	3000
Reference Depth, ft	6140
Initial Average Oil Saturation, frac.	0.64
Initial Average Water Saturation, frac.	0.36
Temperature, °F	110
Dykstra-Parsons coefficient	0.6 , 0.9
Dimensionless Correlation Length in x, y directions (λ_x, λ_y), ft	0.2-2.0
Dimensionless Correlation Length in z direction (λ_z), ft	0.3-0.4
Pore Volume, MM. RB	52.11
OOIP, MM STB	17.2
HCPV, MM RB	19.30

Table 4.6: Combination of parameters for each simulation run

Run #	Factor 1 A: WAG Ratio (0.25-3.0)	Factor 2 B: Slug Size (0.5-8.0)	Factor 3 C: Vdp (0.6-0.9)	Factor 4 D: Hysteresis (D1-D2)	Factor 5 D: $\lambda_{Dx,y}$ (0.2-2.0)	Factor 6 D: λ_{Dz} (0.3-0.4)
1	0.25	0.5	0.9	D1	2.0	0.4
2	0.25	8.0	0.6	D2	2.0	0.3
3	0.25	0.5	0.6	D1	0.2	0.3
4	0.25	8.0	0.9	D2	0.2	0.4
5	3.0	8.0	0.9	D1	2.0	0.3
6	0.25	8.0	0.9	D1	0.2	0.3
7	3.0	8.0	0.9	D2	2.0	0.4
8	3.0	0.5	0.6	D1	2.0	0.3
9	3.0	0.5	0.9	D2	0.2	0.3
10	0.25	0.5	0.6	D2	0.2	0.4
11	3.0	8.0	0.6	D2	0.2	0.3
12	3.0	0.5	0.9	D1	0.2	0.4
13	0.25	8.0	0.6	D1	2.0	0.4
14	3.0	0.5	0.6	D2	2.0	0.4
15	3.0	8.0	0.6	D1	0.2	0.4
16	0.25	0.5	0.9	D2	2.0	0.3

Table 4.7: Results for objective functions of simulation cases

Run #	Duration Of WAG Flood, yrs	Response 1: **Oil Recovery,** %OOIP	Response 2: **CO_2 Saturation,** frac.	Response 3: **NPV,** $mm
1	15	23.3	0.26	29.3
2	4.8	16.9	0.16	25.8
3	4.6	20.5	0.21	31.6
4	8.8	21.3	0.18	25.3
5	41	22.7	0.12	30.2
6	35	25.9	0.25	31.5
7	44	21.3	0.08	31.9
8	21	14.7	0.07	22.1
9	52	19.6	0.07	20.6
10	2.1	19.8	0.21	31.7
11	18	20.3	0.06	40.6
12	54	20.0	0.09	21.6
13	4.7	15.9	0.16	25.1
14	18	14.9	0.04	22.4
15	21	19.4	0.10	41.8
16	38	25.8	0.26	34.6

Table 4.8: Important economical parameters for NPV calculations

Oil Price	$45 /bo
Oil Price Increase	10 %
Royalty	12.5 %
CO_2 Price	$0.85 /mcf
Operational Cost Inflation	1.5 %
Recycle Cost	$0.35 /mcf
Lift Cost	$0.2 /bbl
Discount Rate	12 %
Fed. Tax Rate	32 %
EOR Tax Credit	20 %

Table 4.9: Suggested simulation runs and predicted response values for each optimization scenario

Objectives →		**Maximizing Oil Recovery**	**Maximizing CO_2 Storage**	**Maximizing Profit**	**Equal weight for oil recovery and CO_2 storage**
Factor 1 **A: WAG Ratio**		0.26	0.29	3	0.25
Factor 2 **B: % Slug Size**		0.63	1.51	8	0.57
Factor 3 **C: V_{dp}**		0.9	0.8	0.6	0.9
Factor 4 **D: Hysteresis**		D2 (Not Applied)	D1(Applied)	D1(Applied)	D1(Applied)
Factor 5 **E: $\lambda_{Dx,y}$**		0.3	1.33	0.3	0.45
Factor 6 **F: λ_{Dz}**		0.2	0.23	0.4	0.2
Oil Recovery, % OOIP		25.9	24.3	18.6	25.2
CO_2 Saturation, frac. P.V.		25.5	28.0	6.2	26.6
$ Value	**$/MCF** CO_2 Stored	1.1	1.4	0.42	0.95
	$/STB Prod.	6.9	6.2	8.7	6.7

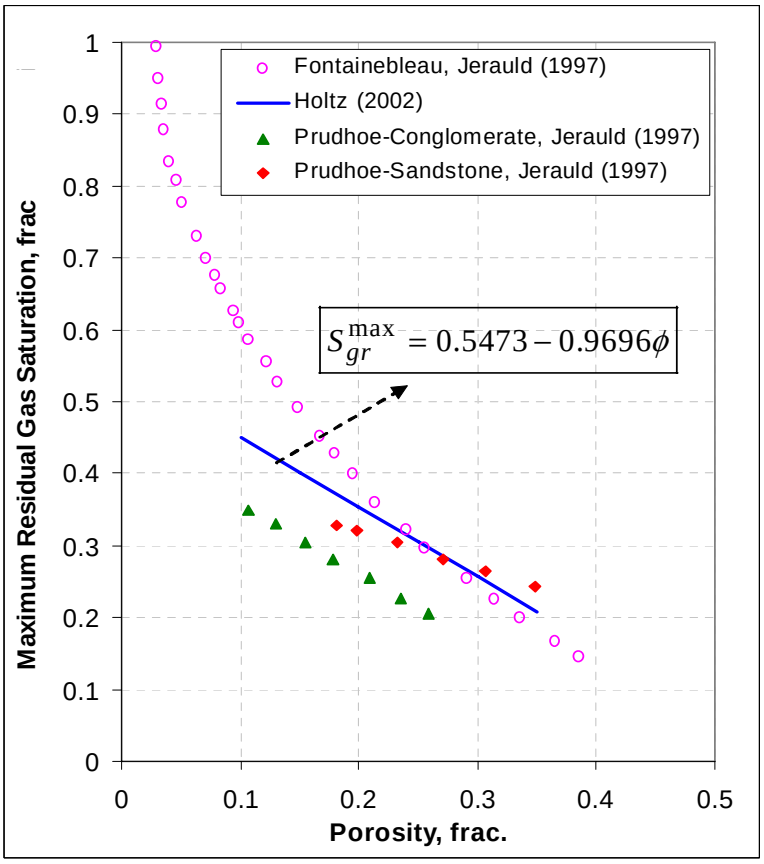

Figure 4.1- Correlation between porosity and maximum residual gas saturation

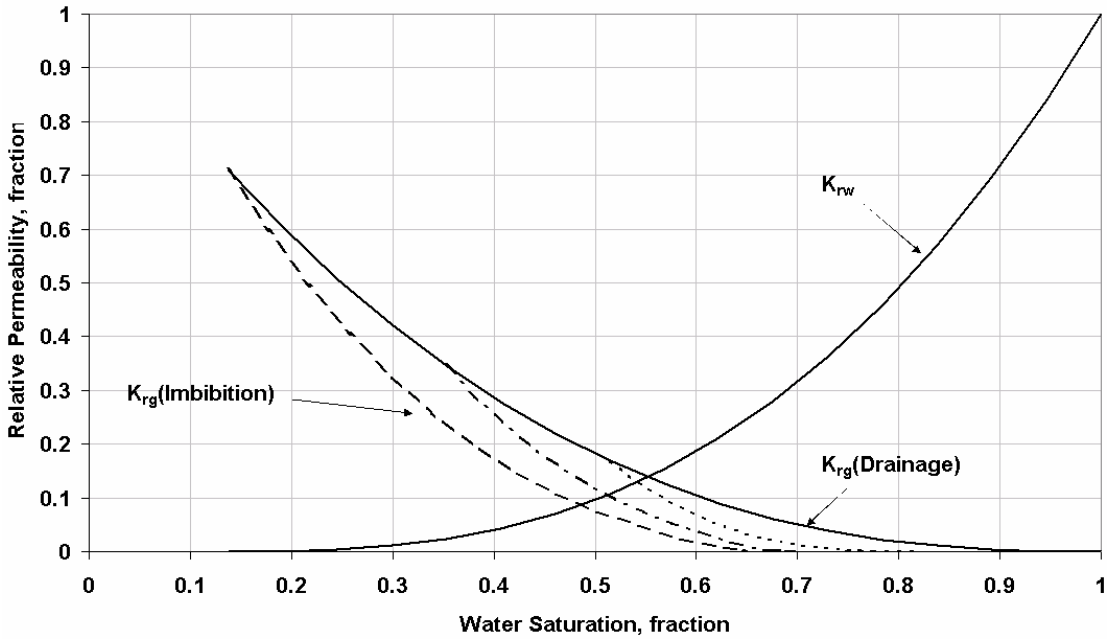

Figure 4.2- Cyclic behavior of the gas relative permeability with hysteresis-included in the model during a WAG process.

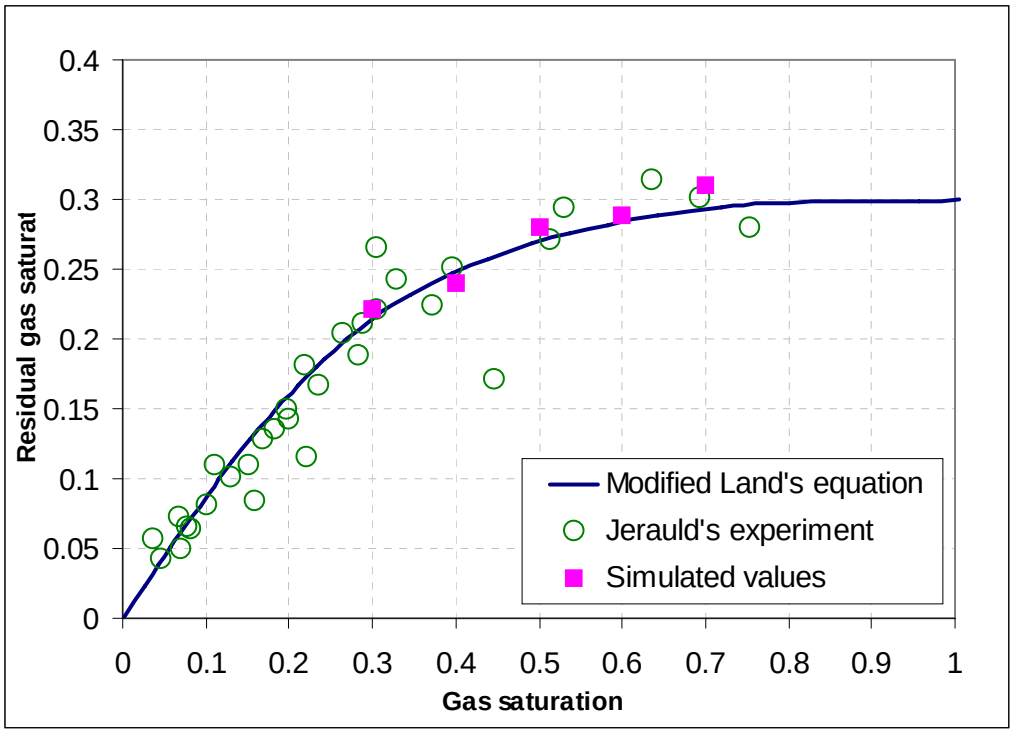

Figure 4.3- Relation between gas saturation and residual gas saturation presented by Modified Land's equation along with some experimental and simulated values

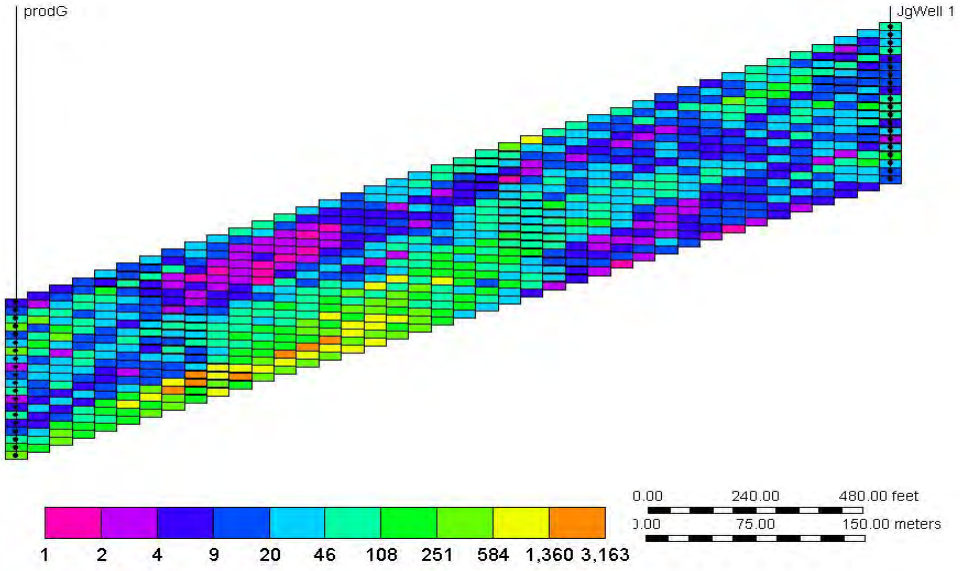

Figure 4.4- Two-dimensional cross sectional view of stochastic permeability field; scale in the Z direction has been magnified by the factor of 2

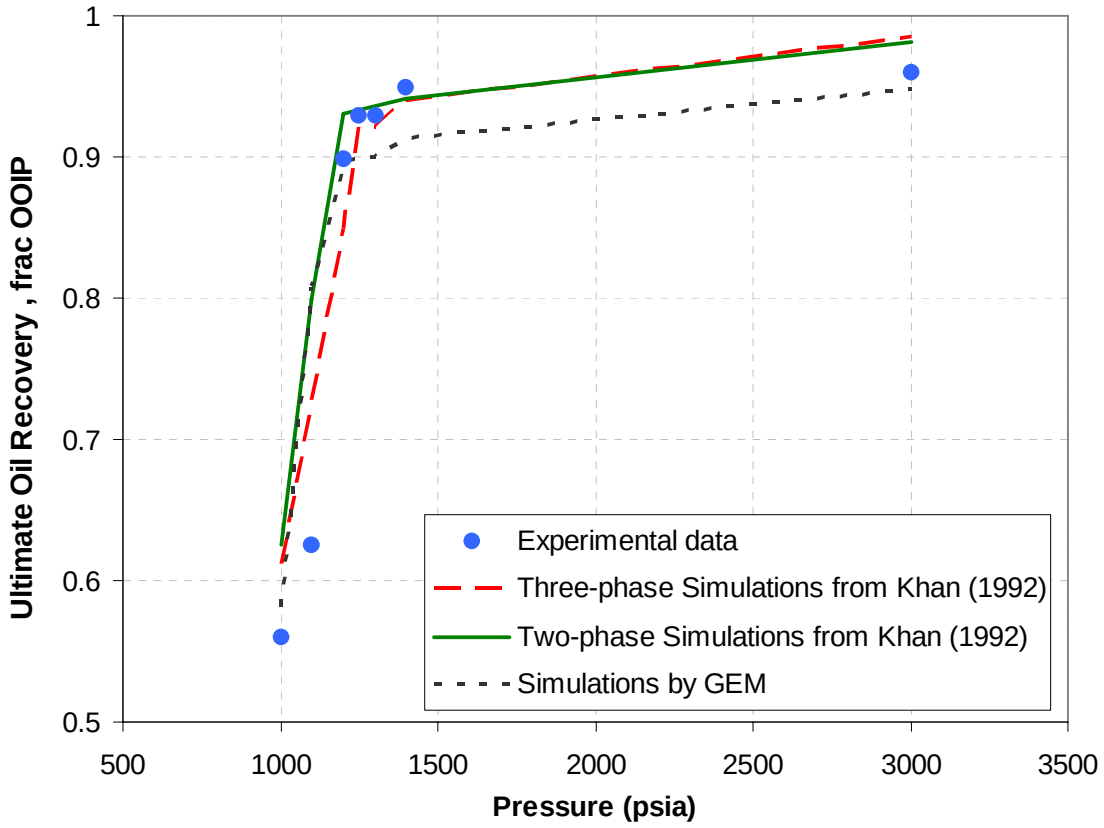

Figure 4.5- One-dimensional slim tube experimental and simulation data to determine the MMP between injected CO_2 and reservoir fluid.

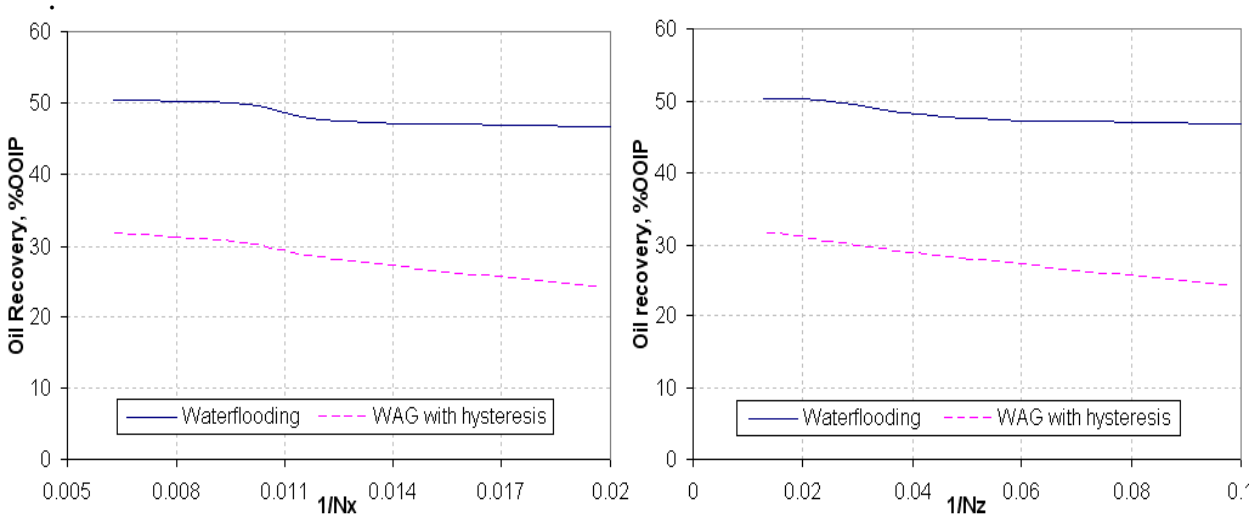

Figure 4.6- Grid convergence behavior in X and Y direction for 2-D cross sectional reservoir.

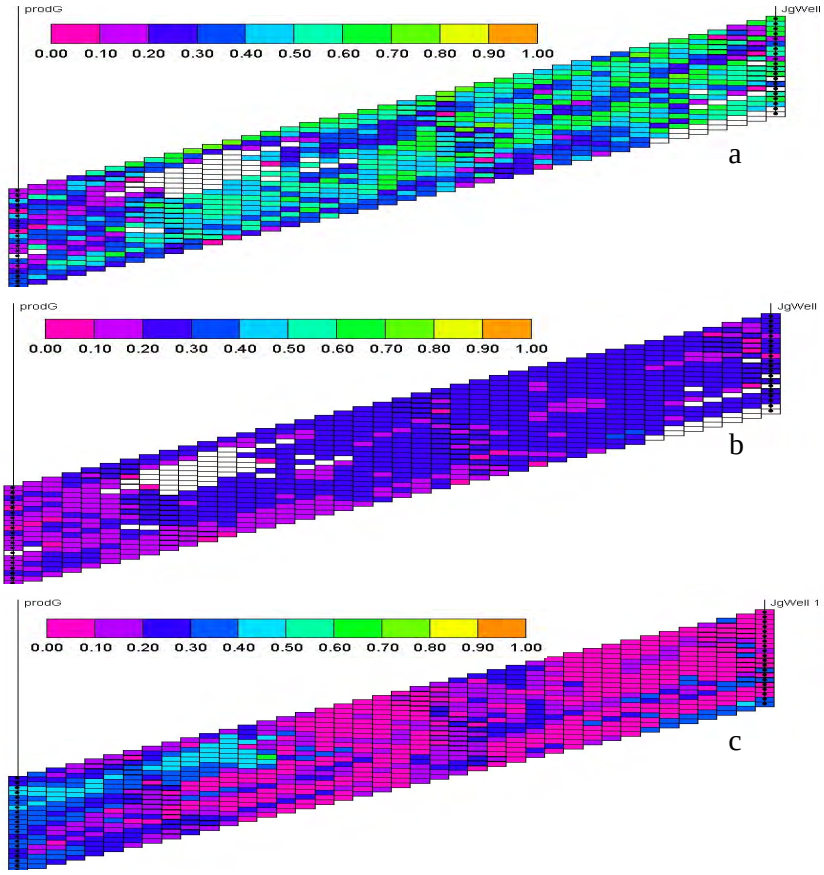

Figure 4.7- Maximum gas saturation (S_{gh}) in each gridblock at any time during simulation, (a), residual gas saturation (Sgrh) in each gridblock at the end of the simulation taking into account hysteresis (b), and gas saturation (Sg) at the end of WAG injection (c)

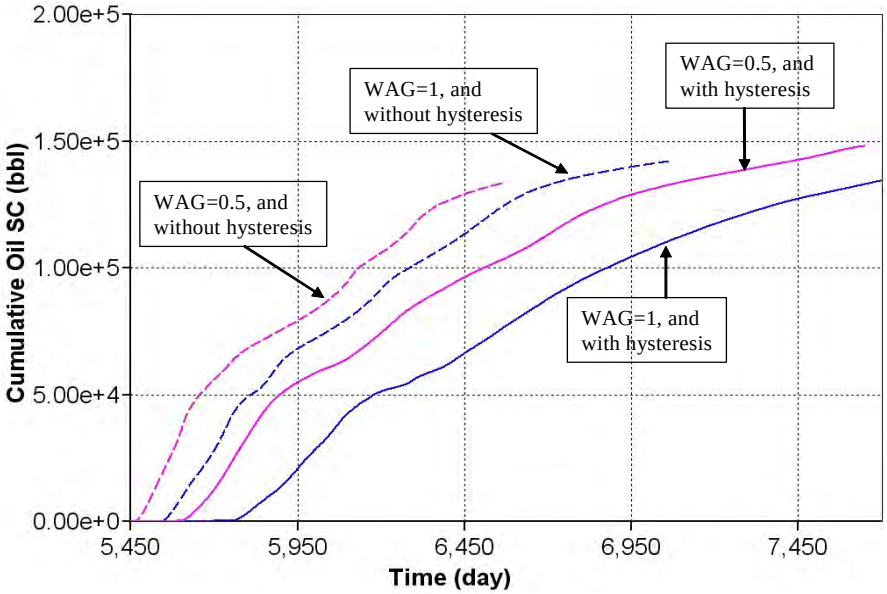

Figure 4.8- Comparison of cumulative oil recovery in simulation cases with and without hysteresis and at different WAG ratios (same slug size).

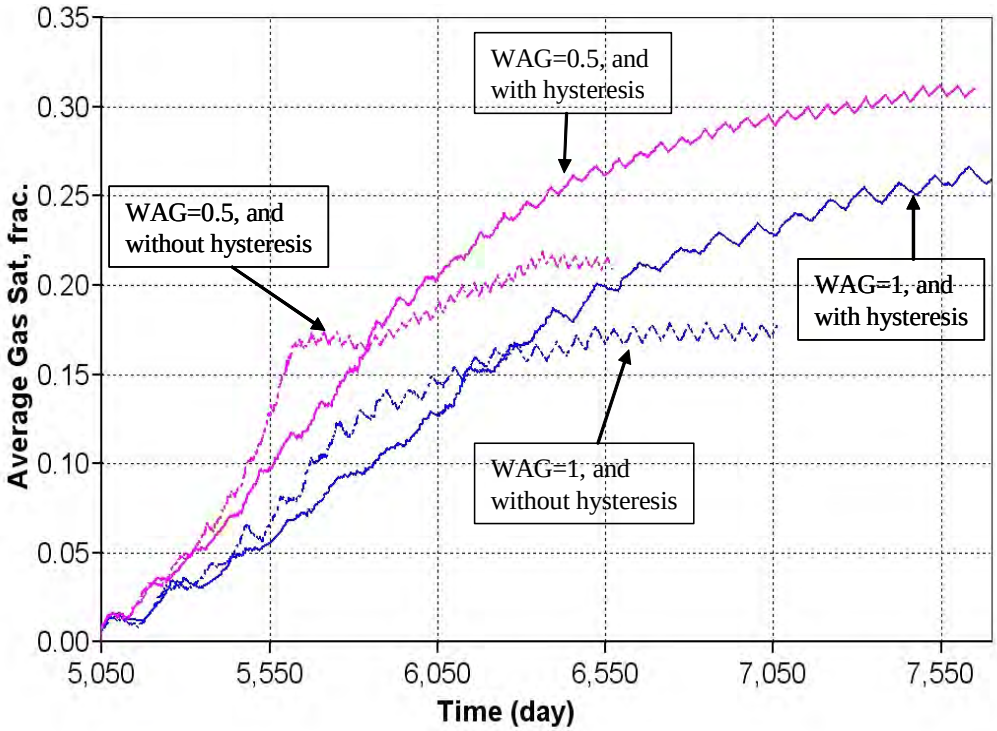

Figure 4.9- Effect of hysteresis and WAG ratio on the gas saturation in 2-D vertical cross sectional reservoir

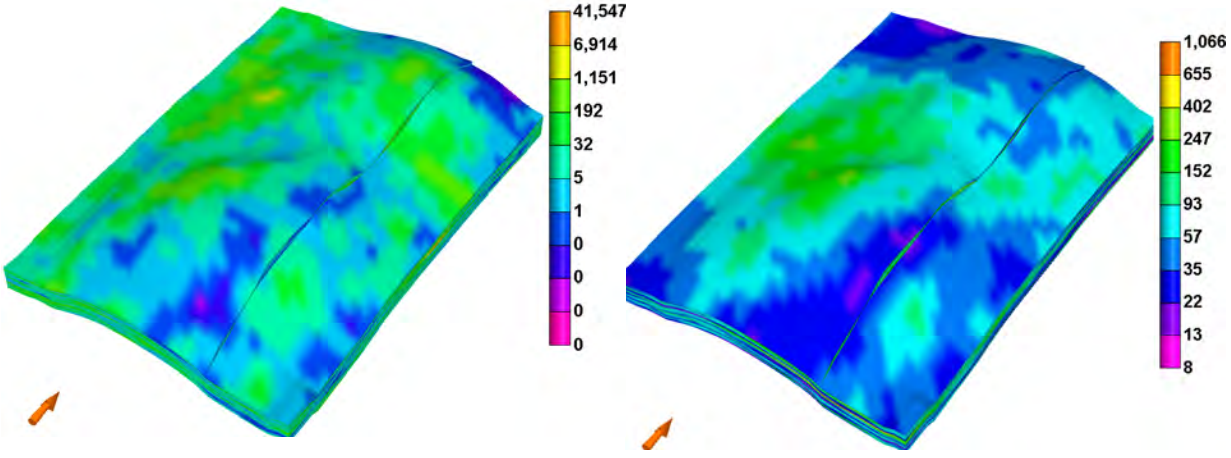

Figure 4.10- 3-D view of a realization of the stochastic permeability field for run numbers 2 and 6 listed in Table 6

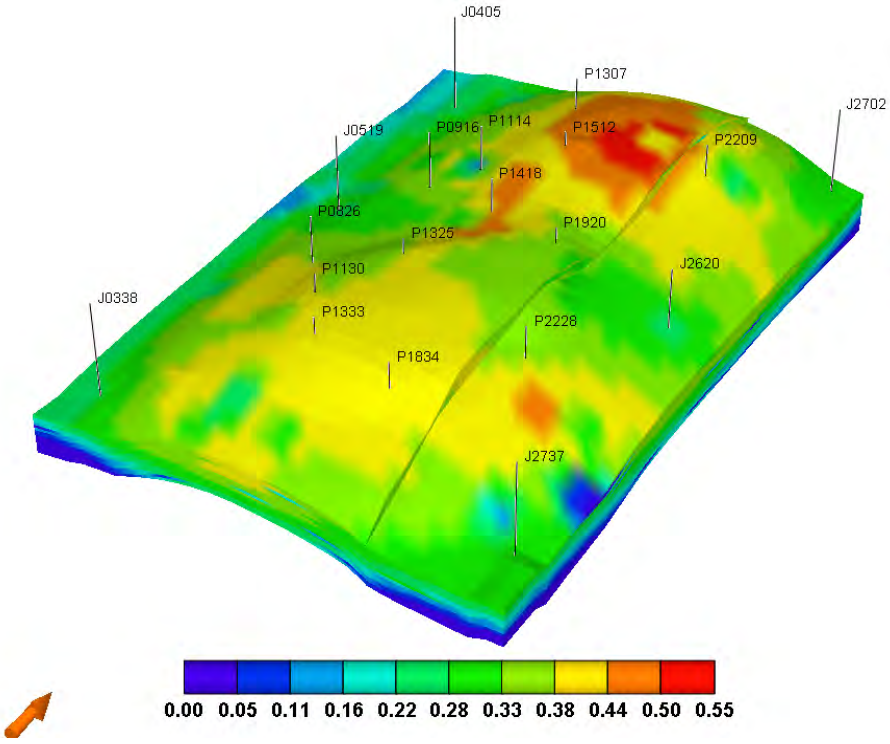

Figure 4.11- 3-D view of remaining oil saturation at the end of waterflood (Run number 11 listed in Table 3)

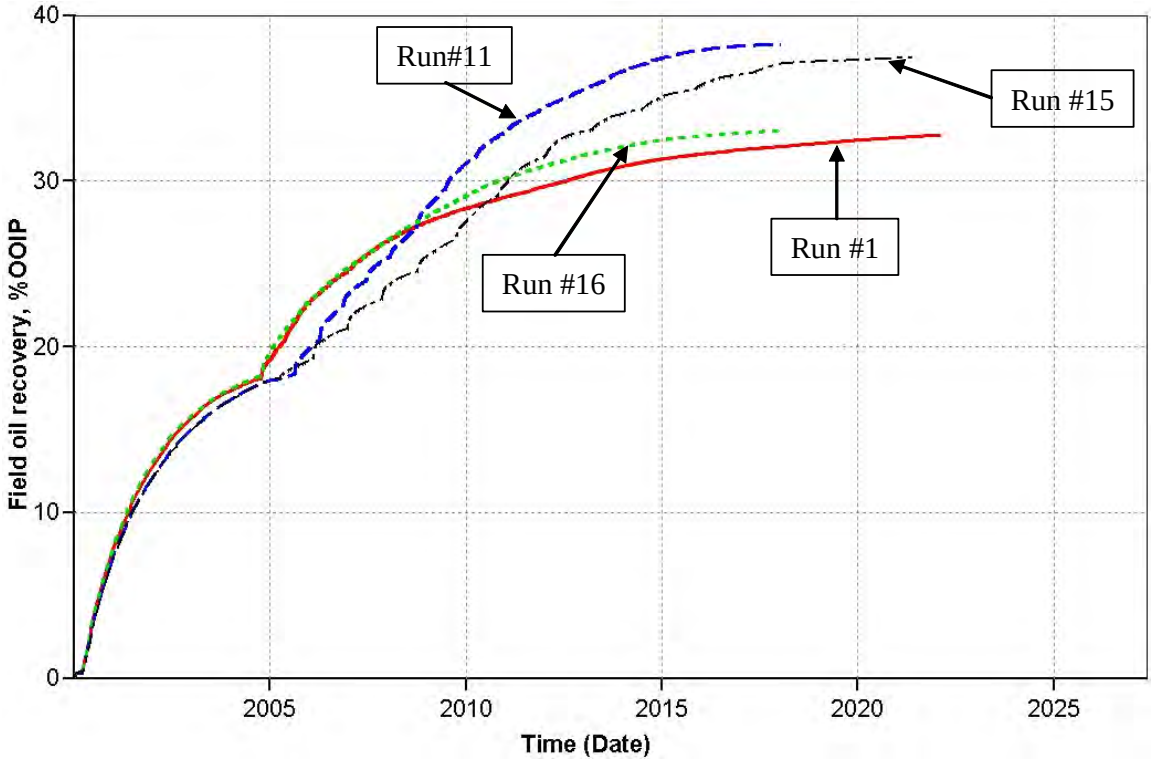

Figure 4.12- Oil recovery factor for several sensitivity cases, listed in Table6

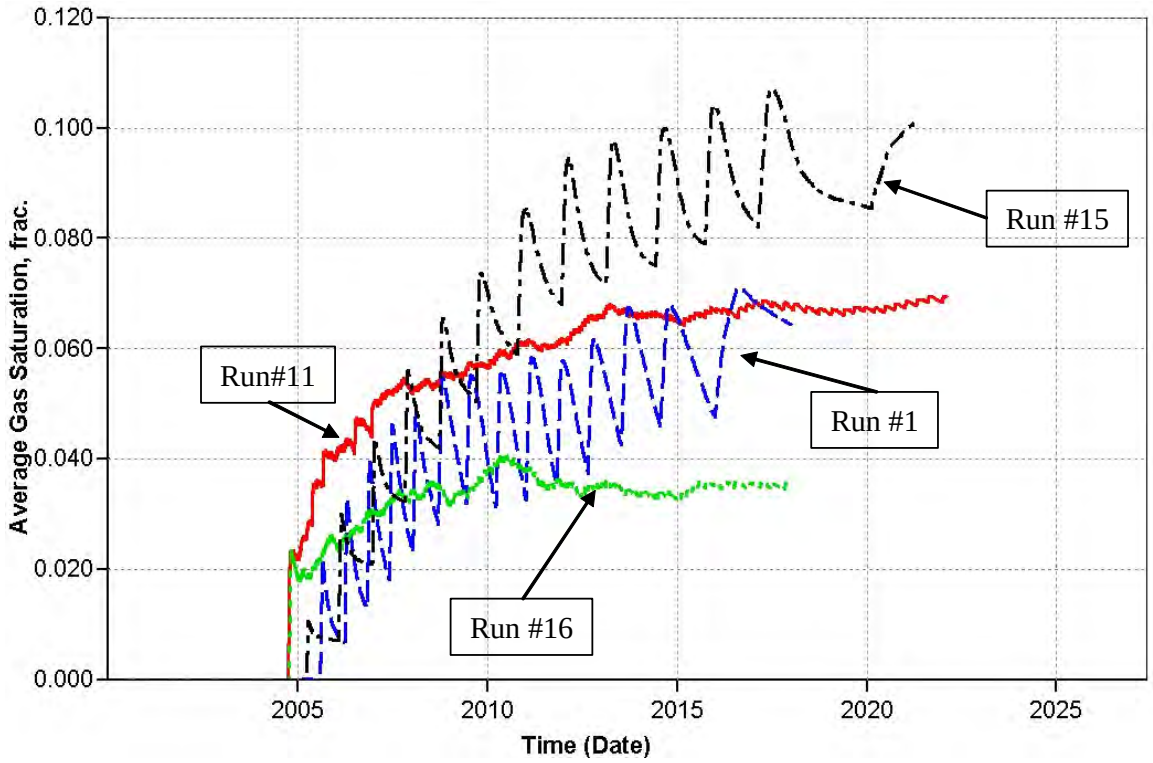

Figure 4.13- Average gas saturations variation at several sensitivity cases, listed in Table6

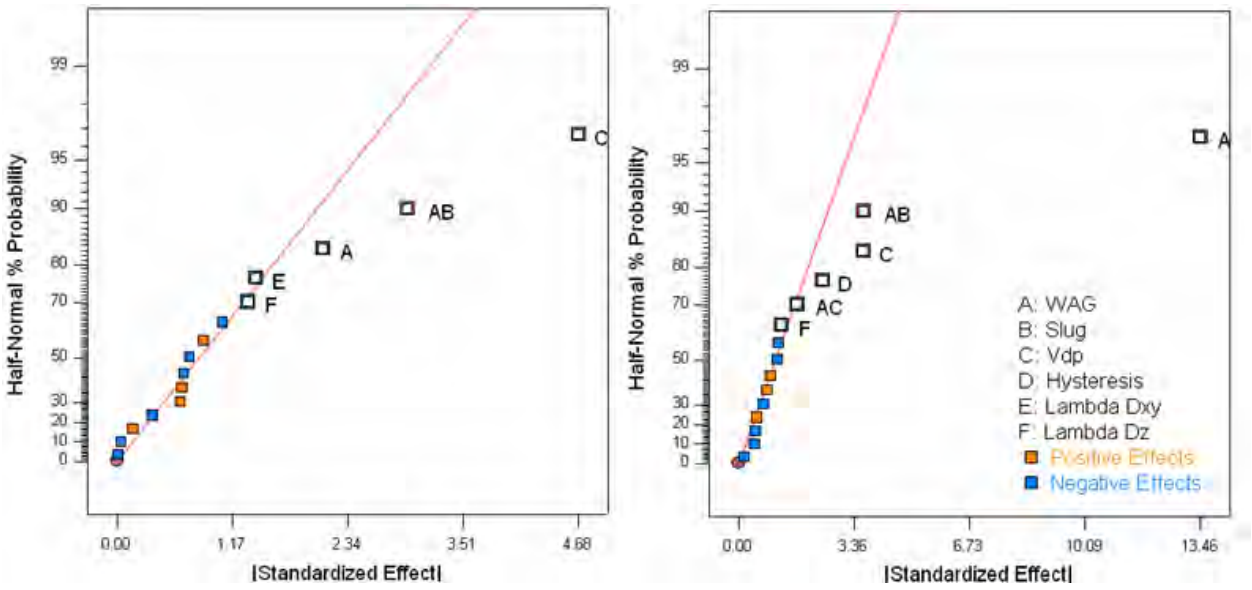

Figure 4.14- Evaluating effect of all four factors on recovery factor (left) and storage (right) with two-level factorial design

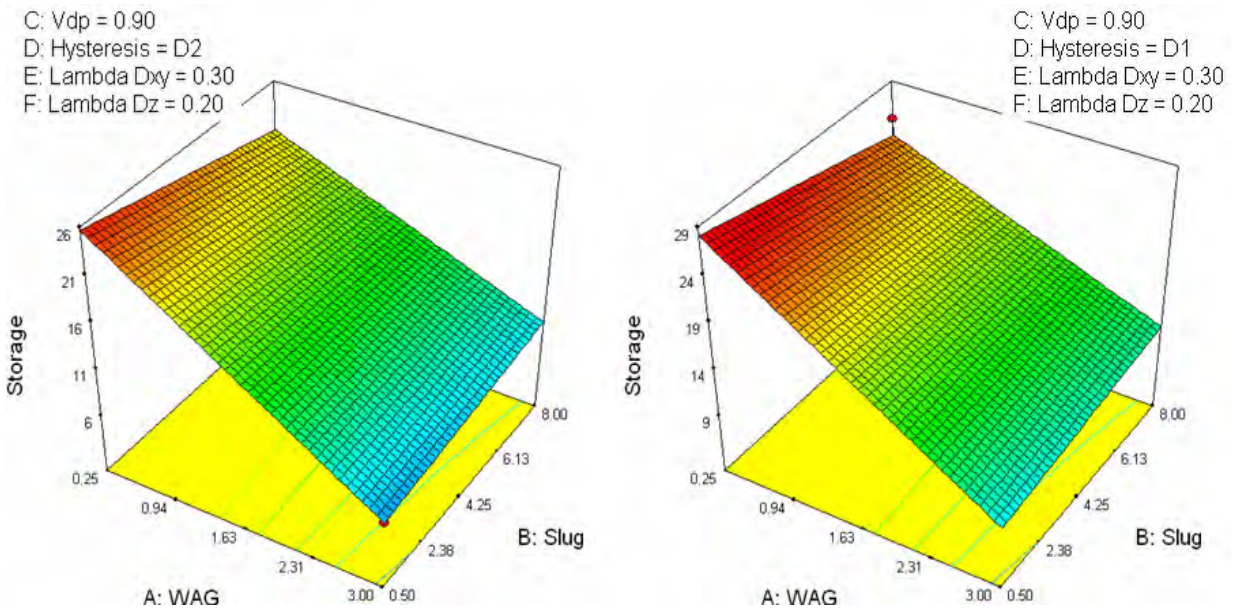

Figure 4.15- Response surfaces generated for CO_2 storage objective function at different WAG ratio and slug sizes and other specified parameters (Note: D1 in hysteresis parameter denotes that hysteresis has been applied in the simulation model and D2 means it has not been applied in the model)

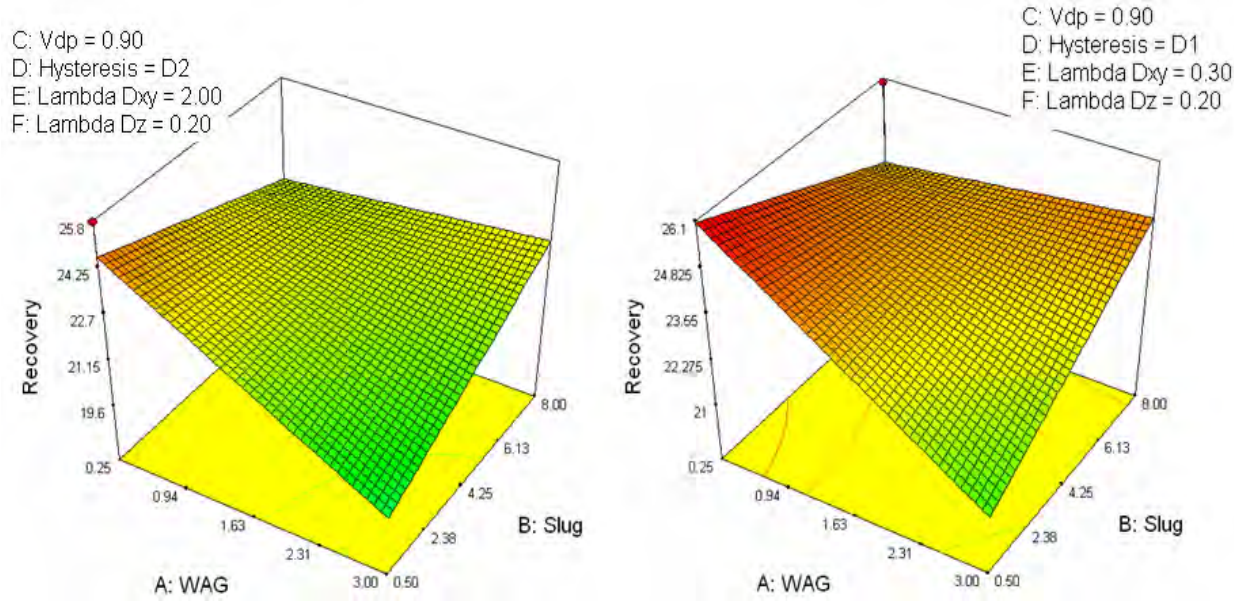

Figure 4.16- Response surfaces generated for oil recovery objective function at different WAG ratio and slug sizes and other specified parameters (Note: D1 in hysteresis parameter denotes that hysteresis has been applied in the simulation model and D2 means it has not been applied in the model)

Chapter 5: Flood Design Optimization for Coupled CO_2 Sequestration and Enhanced Oil Recovery

5.1 INTRODUCTION

Sequestration of carbon dioxide in geological formations is the most direct carbon management strategy for long term reduction of anthropogenic CO_2 from the atmosphere. There are several options for storing CO_2 underground. Injecting CO_2 into deep saline aquifers probably is one of the main CO_2 options for future large scale projects. This method of carbon mitigation has shown to be costly and sometimes accompany risks associated with leakage. Injecting CO_2 into the mature oil and gas fields is another option for storing CO_2. Most of the aspects of CO_2 injection into the reservoirs for the purpose of Enhanced Oil Recovery (EOR) have been known for decades (Wang et al., 1984; Khan et al., 1992; Lim et al., 1992; Guler et al., 2001). But there are some differences between injecting CO_2 for the purpose of pure EOR and the one for both CO_2 sequestration and EOR projects. Carbon dioxide injection for the purpose of Enhanced Oil Recovery (EOR) has been proven to be one of the most effective methods in tertiary hydrocarbon recovery.

In particular, miscible displacement of crude oil by CO_2 is caused through extraction of hydrocarbons from oil into the CO_2 and by dissolution of CO_2 into the oil. When injection of CO_2 is coupled with storing it in the oil reservoirs, that might prove to be environmentally safe as well. This is mostly due to the extensive available information about target reservoir properties and other subsurface mechanisms. Also oil and gas reservoirs have been known to be effective in preventing the upward migration of fluids over geological time periods which is vital for long term fate of CO_2 storage. These type of coupled EOR and sequestration projects are cost effective as well. Due to the fact that, surface and subsurface infrastructure already exists in oil and gas fields that can be

utilized during sequestration phases. However, storing CO_2 in the oil reservoirs is a complex issue spanning a wide range of scientific, technological, economic, safety, and regulatory issues.

Due to the current relatively high oil prices, special attention has been made toward coupled CO_2-EOR and sequestration projects in different parts of the world. This will serve industry in both reducing anthropogenic CO_2 level as well as increasing oil production. Currently, total oil production from CO_2-EOR projects are slightly over 205000 bbl/d (Moritis, 2004) , and if we assume that in average 10 bbl of oil are produced for every ton of CO_2 injected (Jessen et al., 2005), it can be concluded that roughly 20500 tons of CO_2 are injected per day into the oil reservoirs. The main issue is currently shortage of available CO_2 sources for injection into the reservoirs (Moritis, 2007). If regulations are set for CO_2 sequestration, it is obvious that vast amount of CO_2 sources can be made available to the EOR projects and this could increase storage capacity of the projects. In EOR projects the goal is to make a profit by minimizing the use of CO_2 and reusing the gas once it has been produced for the reservoir undergoing the CO_2 flood. Whereas, with coupled EOR and sequestration, the goal is to maximize the storage of the CO_2. To a large extent, these appear to be competing goals. Especially engineering and operational design parameters are substantially different.

The purpose of this research is to better quantify the potential for two main objectives: enhanced oil recovery and storage of CO_2 in mature oil reservoirs, over a wide range of uncertainty in the design variables. Sensitivity analysis is preformed to investigate the effect of uncertainties in the design and reservoir parameters. Statistical analysis such as Design of Experiment (DOE) and Response Surfaces Methodology (RSM) were applied to achieve efficient and comprehensive results.

5.2 PRELIMINARY STUDIES FOR FLOOD DESIGN OPTIMIZATION

A three-dimensional model was established as a base model for the preliminary CO_2 flood simulation studies. Table 5.1 shows the summary of input data for the generic reservoir model. It should be mentioned that stochastic permeability as well as porosity field were created with given characteristics in Table 5.1. We assume the reservoir is limited by four sealing faults in its boundaries. The average horizontal permeability is 100 md and average porosity is 0.22. Figure 5.1 shows the cross sectional and areal view of the permeability field. Holtz's (2002) correlation was used to create the reservoir porosity field. A corner point grid was used to model the geology. Using the two-phase relative permeability data, a linear iso-perm function built-in GEM, was applied in order to obtain three-phase relative permeability data.

Before CO_2 flooding, water injection was simulated to establish an initial condition for CO_2 flooding and then different schemes of CO_2 flooding were performed to investigate the best plan for maximizing oil production and CO_2 sequestration. Water was injected using one horizontal well (numerical layer 17) and oil was replaced in the up dip direction and produced by another horizontal well at one of the top layers (third numerical layer). In this process, 38.2 percent of original oil in place (OOIP) was produced before the water cut reaches 95 percent in the production well. Average remaining oil saturation after water flooding was 0.41 (in contrast with 0.65, initial oil saturation). Water breakthrough occurred after almost 22 years and after about 68 years water cut in the producing well was reached to 95 percent. To obtain consistency with real world cases and obtain more reasonable results, the CO_2 injection simulation started form the time that water injection simulation had been terminated.

Fourteen different scenarios were simulated based on two main schemes: producing the whole reservoir at one stage, or sweeping reservoir in three stages. In most of these cases employing different well control techniques including various injection and production pressures, shut it and open strategies, and combination of horizontal and

vertical wells were investigated toward maximizing oil recovery and CO_2 storage. Table 5.2 shows the list of the different runs with their corresponding flood design settings. In the one-stage operations, CO_2 was injected down dip all the way through whole length of the reservoir. Gravity stable displacement was simulated in one stage scheme but due to the low average reservoir permeability and very low CO_2 front velocity; it did not seem to be proper scenario for the designed reservoir. Non-gravity stable displacements in one stage scheme were more effective in achieving the both objectives. Table 5.3 shows the results for the one-stage simulations including gravity stable displacement scenario. Figure 5.2 compares the differences in the CO_2 front shape and position in gravity stable displacement versus that of non-gravity stable mode at two outstandingly different time scales.

In three stages operations, CO_2 was injected down dip and oil was produced in a well at distance equal to one-third of the reservoir length. When the Gas Oil Ratio (GOR) at the production well reached 30,000 Scf/STB, the simulation was stopped and current production well was switched to injection well for the second step and a new production well was placed in the next one-third portion of the reservoir, down dip. This was continued until the whole reservoir was swept. Figure 5.3 shows the schematic view of the three-stage flood design in the reservoir. Figure 5.4 compares differences in the results between one-stage and three-stage operations. In the one-stage design, by end of the CO_2 flood, 17.6 % OOIP was recovered, 72.9 % of injected CO_2 was stored, 10.4 MScf of CO_2 was injected per each barrel of produced oil, and 7.6 MScf of CO_2 was stored per any barrel of oil which was produced. In the three-stage design, by end of the CO_2 flood, 20.7 % OOIP was recovered, 57.4 % of injected CO_2 was stored, 14.1 MScf of CO_2 was injected per each barrel of produced oil, and 8.1 MScf of CO_2 was stored per any barrel of oil which was produced. It is seen that applying a three-stage strategy helped to sweep the reservoir effectively (higher oil recovery) and to increase the amount of stored CO_2 (higher storage performance).

A total of nine different scenarios were simulated based using three-stage design. Applying various well specifications in both producers and injectors was the main difference among these scenarios. Figure 5.5 shows remaining oil saturation and sweep efficiency differences at the end of CO_2 flood between cases where vertical and horizontal producers have been applied. In the case that both production and injection wells were horizontal, by end of the CO_2 flood, 19.8 % OOIP was recovered, 44.3 % of injected CO_2 was stored, 13.7 MScf of CO_2 was injected per each barrel of produced oil, and 6.1 MScf of CO_2 was stored per any barrel of oil which was produced. In the case of employing horizontal injection and vertical production wells, by end of the CO_2 flood, 13.9 % OOIP was recovered, 50.5 % of injected CO_2 was stored, 15.6 MScf of CO_2 was injected per each barrel of produced oil, and 7.9 MScf of CO_2 was stored per barrel of oil which was produced. Table 5.4 presents a summary of the results for all of the three-stage simulations.

We also investigated the open and shut-in strategy for the injection well (3 months injection and one month shut-in) to stabilize the CO_2 front and try to increase sweep efficiency along with the amount of storage. By applying this design, the oil recovery increased significantly but storage did not change much. In this scenario, by the end of CO_2 flood, 26.8 % OOIP was recovered, 42.1 % of injected CO_2 was stored, 13.4 MScf of CO_2 was injected per each barrel of produced oil, and 7 MScf of CO_2 was stored per barrel of oil which was produced. Figure 5.6 shows both areal and cross sectional views of the remaining oil saturation at the end of the CO_2 flood.

According to our preliminary study on co-optimizing flood design for coupled CO_2 sequestration and EOR, it is seen that there are different uncertain parameters which affect the final flood results significantly and they have to be studied systematically to achieve comprehensive results.

5.3 UNCERTAINTIES IN FLOOD DESIGN PARAMETERS

Both of the objectives for coupled EOR and sequestration projects (maximum recovery and maximum storage), depend on the large number of parameters and on the strategy used to flood the oil reservoir. Different mobility control techniques such as WAG injection can enhance and help in increasing sweep efficiency and consequently higher oil recovery but may jeopardize the storage objective. In addition, parameters such as type of injection and production wells and their operating constraint can affect the results significantly. For instance, gravity stable displacement of CO_2 (which can be achieved by relatively small injection and production rates) can greatly enhance the oil recovery and amount of stored CO_2. But, in most of the cases, only reservoirs with very high permeability are proper candidates for these type of displacements. Well spacing is another parameter that affects objectives in a CO_2 flooding project. Optimum well spacing is required to meet both goals of the projects. Higher well spacing may delay the CO_2 breakthrough time in the production wells, therefore, increasing storage objective but can cause huge delay in the oil production peak as well. On the other hand, by choosing smaller well spacing, CO_2 is produced early in the time of project but sweep efficiency is much higher compared to the large well spacing scenarios. Besides to all of these operational and design factors, reservoir properties also can affect the design variables as well as project objectives. For instance, vertical to horizontal permeability ratio can have big influence on cross flow mechanisms in the vertical directions causing gravity override issues in the CO_2 flooding projects.

Any particular oil reservoir also, can be an attractive sequestration target considering all of its reservoir engineering and characteristics aspects. All of these aspects should be examined rationally in order to identify specific qualities of a reservoir in order to be appropriate candidate for CO_2 enhanced oil recovery. In addition, these characteristics along with all design variables should be determined for different reservoirs to be promising sequestration prospect. In this respect, a conceptual model can

be established for reservoirs which are proper CO_2 sequestration and enhanced oil recovery candidates.

One of the most important reservoir characteristics is reservoir heterogeneity. In the field scale injection of carbon dioxide, presence of high permeability paths can confine the ultimate amount of stored CO_2. These paths provide least resistance to the injected gas resulting in early breakthrough. Gas breakthrough in the producers will lead to early recycling and lower sweep efficiency. It is evident that produced CO_2 can be re-injected into reservoir but at the very high cost of recycling plant in the injection site. According to these, reservoir heterogeneity need to be considered closely in the design of any coupled CO_2-EOR and sequestration project.

All major reservoirs in the world fall into two main categories: Carbonate and Sandstone reservoirs. Both type of reservoirs can be attractive targets for both sequestration and EOR targets if they contain proper reservoir engineering and characteristic aspects. There are underlying major differences between these two type of reservoirs in terms of the nature of their reservoir heterogeneity. This is mainly due to the different depositional and digenetic processes that carbonate and sandstone reservoirs have gone through. This can easily cause differences in the types of spatial distribution of their petropysical properties. Carbonate reservoirs are usually characterized by their layered nature with medium to low matrix permeability values while sandstone reservoirs are represented by stochastic-type permeability distributions with relatively higher permeability values.

In the process of investigating appropriate flood design and reservoir parameters for coupled CO_2-EOR and sequestration projects, final decisions must be made on both financial and technical issues. The principle financial factor in this study is considered as discounted cash flow of any project. Measure of profitability of any project is the only deterministic function in evaluating its successfulness. In coupled CO_2 sequestration and EOR projects, value and amount of stored CO_2 is also considered as the second objective

in deciding on the performance of the project. Therefore, these two objectives needed to be optimized at the same time to decide on the project successfulness.

It is widely known that any of the existing mathematical models for CO_2 flooding in three-dimensional heterogeneous fields can determine optimal decisions for coupled EOR and sequestration projects. Even if a perfect model exists, the profitability and performance of the project would be difficult to be established because of all economic variables which impact the project. Considering all these, clearly a method is required that can help us make optimal decisions in spite of all uncertainties. Exploratory systematic compositional simulations of CO_2 injection in heterogeneous three-dimensional reservoirs should be performed to establish effective flood design strategies for coupled CO_2 Enhanced Oil Recovery (EOR) and sequestration to maximize project profitability and amount of stored CO_2. Besides of this, detailed economic investigation such as discounted cash flow analysis should be implemented properly to be able to handle overall performance of coupled CO_2 sequestration and EOR projects. Lastly, an algorithm is needed that can identify the optimal design and reservoir parameters while accounting for uncertainty in the models and their input data.

Combination of experimental design and method of response surfaces has been proven to be extremely useful for the reduction and characterization of parametric uncertainty in computationally demanding studies. Applying experimental design minimizes the number of simulations required to be performed. It also helps in defining most effective variables and their combinational effects on the decision variables. This is crucial because of the compositional nature of simulation cases for coupled EOR and sequestrations. These information can be used for screening purposes in order to identify effect of each variable on the final objectives. Regression models are fit based on the information obtained from previous step relating responses to the influent variables. Utilizing response surface methodology will also help to predict objective function values for any possible scenario of uncertain variables.

5.4 FLOOD DESIGN PARAMETERS FOR CARBONATE RESERVOIRS

Considerable amount of world's hydrocarbon reservoirs are in carbonate reservoirs. Carbon dioxide injection is one of the most important EOR recovery processes in the U.S. carbonate reservoirs since the early 1980's (Leonard, 1984; Moritis, 2004). Based on the information from the current CO_2 flooding projects in U.S., 67% of them are in the carbonate reservoirs especially in west Texas (Moritis, 2004). CO_2 flooding projects are also expected to expand more considering the efforts on CO_2 sequestration projects expansion. Power plant generated CO_2 can provide vast additional resources to the current natural CO_2 supplies. Considering all of these, it is seen that carbonate reservoirs are going to play important role on the coupled CO_2-EOR and sequestration projects. Carbonate reservoirs generally show low porosity and permeability distributions and usually are represented by layered reservoir heterogeneity. There have been extensive studies on CO_2 injection into the carbonate reservoirs since 1990 for the purpose of enhanced oil recovery (Paul et al., 1984; Lim et al., 1992; Roper et al., 1992; Dria et al., 1993; Khan et al., 1994; Lim et al., 1994; Guler et al., 2001;). Each one of these studies has investigated different aspect of CO_2-EOR recovery such as phase behavior, relative permeability, engineering design, reservoir characterization, etc. If sequestration to be considered as another goal of CO_2 injection into the mature oil reservoirs, some revisions are needed to be performed on previous CO_2-EOR studies. In this study we have focused on flood design parameters for coupled EOR and sequestration processes. Sensitivity analysis should be performed on the defined parameters in order to identify their individual and combinational effects on both of EOR and sequestration objectives.

Effect of important flood design factors in the CO_2 injection processes, such as oil recovery and the amount of stored CO_2 is investigated to determine the optimum conditions for flood design parameters to achieve the highest possible recovery and amount of CO_2 stored in the reservoir. Following are some of the major uncertain design

factors for coupled CO_2-EOR and sequestration projects which were considered in this study for the carbonate reservoirs.

Produced Gas-Oil Ratio: Gas Oil Ratio (GOR) in the production well is one of the most important engineering design parameters for any CO_2 flood project. It is obvious that due to the higher mobility of the CO_2 than an oil reservoir fluid, it will rapidly move toward production wells and then will start to be produced and recycled from the production wells. When this happens, incremental sweep efficiency will start to decrease and more and more gas will be produced which in turn will cause higher costs due to the facility limit and/or expansion for compression. On the hand, projects benefits from incremental sweep and therefore higher recovery. Carbon dioxide retention may also increase due to the higher injected amount of CO_2. In the coupled sequestration and EOR projects, optimum GOR ratio should be defined where optimum amount of oil is produced and optimum CO_2 retention amount is achieved as well.

Production and Injection Well Type: Production and injection well types are also critical factors that affect reservoir sweep as well as the amount of stored CO_2 in the reservoir. Lim et al. (1992) has studied using horizontal wells in CO_2 flooding. They have shown that application of horizontal wells significantly shorten project life and consequently improve project economics. In some occasions, using combination of horizontal and vertical wells as producers or injectors also will results in better injection and production performance. Reservoir heterogeneity plays an important role in deciding well type configuration for the CO_2 flooding projects. For instance, in layered-type reservoirs due to the existence of higher permeability zones, vertical wells may result in better performance; but, when using horizontal wells, the wrong choice of layers for injection and production might results in decrease in sweep and storage.

Operational Constraint for Injection and Production Wells: Reservoirs with high permeability might be better candidates for scenarios with higher injection and production rates compared to the low permeability ones. Production and injection wells

can be assigned maximum possible rate by operating them under bottom hole pressure (BHP) constraint. In addition, assigning constant bottom hole pressure will assist in monitoring the reservoir pressure to stay above MMP during flood. In these type of reservoirs, lower injection and production rates sometimes result in gravity stable type of displacement (Nute, 1983) that go along with very high sweep efficiency and higher CO_2 retention in the field. Projects with low injection and production rates are hardly economic and very long flood duration time is the main problem in this regard. Gravity stable displacements have been proven inefficient because of the mentioned problem. In the coupled EOR and sequestration projects, one of the main issues is to study the effect of different well operation constraints to achieve higher recovery and retained CO_2 in a reasonable project life.

WAG or Continuous CO_2 Injection: High CO_2 mobility is a major issue in causing faster CO_2 breakthrough. Higher mobility causes lower reservoir sweep and early production of CO_2, which can lead to a lower oil recovery and lower storage. WAG injection of CO_2 has been proven to increase sweep efficiency but it jeopardizes the total injected amount of CO_2 causing lower stored CO_2. On the other hand, injecting pure CO_2 as continuous stream, results in higher CO_2 mass injected into the reservoir, therefore increasing amount of retained CO_2. This optimization problem is also one of the major issues in the coupled EOR and sequestration to determine efficient injection scheme.

Well Spacing: Well performance is a key factor in determining the economic viability of candidate reservoirs for CO_2 flooding projects. Optimized well spacing should be defined for coupled EOR and sequestration projects. Smaller well spacing would accelerate the recovery process and will perform in the favor of overall Net Present Value (NPV) of the project; but, due to close distance between wells, CO_2 breakthrough will happen fast and the total amount of stored CO_2 will be small. On the other hand, it is important to realize that the minimum number of wells (large well spacing) to establish complete drainage of the reservoir is usually not optimum spacing,

because of the very long time required to sweep the pattern. It should be noted that reservoir characteristics such as heterogeneity will be a deterministic factor in this regard.

Since CO_2 injection process is also dependent on the reservoir heterogeneity therefore, the effect of reservoir heterogeneity along with vertical to horizontal permeability ratio is studied to establish comprehensive and optimized design variables for coupled CO_2 sequestration and EOR processes under these uncertain variables.

Due to the large number of engineering design parameters, limited number of variables but the most important design factors were chosen. Table 5.5 shows all of the 9 uncertain design parameters and their corresponding range of variation for this study. It is seen that there are both categorical and numeric type of variables and also some of them have two levels and others have three levels of uncertainty. The most suitable experimental design method for these type of mixed variables and ranges is D-optimal design. Since it was also expected well spacing and produced Gas Oil Ratio (GOR) factors might have quadratic response surfaces, three level of changes were selected for them and two level of changes for the rest of the variables. According to the selected experimental design method and the number of factors, 61 simulation cases were defined to be performed. Table 5.6 shows all of the 61 simulation cases as well as settings for uncertain factors in each one of 61 simulation runs. They have been selected out of more than $3^2*2^7=1152$ cases that had to be performed if conventional sensitivity analysis were supposed to be applied.

5.4.1 Reservoir Simulation Models

After defining the sensitivity runs, based on the selected experimental design method, simulation models have to be built for each simulation scenario. For all of the simulation cases, a three-dimensional Cartesian coordinate grid was selected and then layered permeability and porosity fields were created for this corner point grid. The

reservoir lithology was considered as carbonate; therefore, all reservoir properties were based on this important assumption. Reservoir geometry was considered similar to the West Texas reservoirs with 150 ft thickness at the depth of 5000 ft. All of the simulation cases were based on quarter of five-spot pattern. Reservoir gridblock size was set to 22, 22, and 7.5 ft in the X, Y and Z directions, respectively. Table 5.7 shows the summary data for the carbonate reservoir models. Figure 5.7 shows layered permeability distribution for one of the simulation cases. The average horizontal permeability in this figure is 5 md and average porosity is 19.5 percent of reservoir bulk volume. Following power law equation (Lucia and Fogg, 1990) was applied to correlate permeability and porosity values in the model; where permeability is in millidarcy and porosity is in fraction of pore volume.

$$k = 7.38 \times 10^{6} \times \phi^{6.72} \qquad (1)$$

Reservoir fluid was considered in a vertically equilibrium condition with water-oil contact of 5200 ft. Compositional PVT data were same as the ones used in Chapter 4. The initial reservoir temperature is 110 °F. There is no free gas initially in the reservoir.. Table 5. 7 shows the average oil and water saturation in the reservoir.

A short description of the reservoir petrophysical data as well as relative permeability model which were used in this study is provided here. We used experimental data and correlation models presented by Prieditis and Paulett (1992), Schneider (1976), and Potter (1987). These relative permeability data, mostly belong to San Andres formation of West Texas, a mixed wet carbonate reservoir, and has gone through a series of successful secondary and tertiary recoveries such as CO_2 injection. These data include vast amount of descent two- and three-phase relative permeability measurements.

To obtain more accurate results, three different rock types were defined based on porosity values in the grid blocks, and consequently three sets of relative permeability data were considered in all of the simulation models. For the simulation cases that water alternative gas scheme was supposed to be injected instead of continuous CO_2, hysteresis was applied in the relative permeability models.

In order to obtain the most resemblance to the real world cases, all of the CO_2 injection simulations started at the end of the waterflooding. By the end of primary and water flooding stages, 35-40 percent of originally oil in place (OOIP) was produced in different simulation scenarios, considering 98 percent water cut as production limit for each well. Remaining oil saturation after water flooding was varying from 38 to 42 percent. After water flooding, all 61 CO_2 injection scenarios, shown in Table 5.6, were simulated. The minimum flowing bottom hole pressure at production wells was set to 1300 psi and maximum injection pressure was set to assumed fracture pressure of 3300 psi at depth of 5100 ft. For the simulation cases that injection or production constraint was based on constant rate, two-third of the average rate when wells were operating under BHP constraint was considered as the target rate. Both horizontal and vertical wells were completed in the whole interval. By applying extensive well completion scenarios, it was tried to control the amount of water and CO_2 production. For instance, when the water cut reached 98% or gas-oil ratio reached maximum allowable value in each case, the layers with water/gas productions higher than allowable values were plugged and checked periodically to see whether previously violated monitored constraint has ceased to be violated. Then they were being re-opened automatically. Furthermore, as another strategy to maximize CO_2 storage, when total field oil production was below 10 STB/day, production well was being closed for the rest of the simulation and CO_2 was being injected until average reservoir pressure reaches to right below fracture pressure (3300 psi). This allows for maximum possible amount of CO_2 to be stored in the reservoir. It is

important to note that well operation constrains were defined in a way that reservoir pressure in all of the simulation cases were above minimum miscibility pressure.

5.4.2 Simulation Results and Discussion

Three-dimensional compositional simulations were performed according to all of the aforementioned assumptions and scenarios. Table 5.8 shows the results for all of the simulation runs. Incremental recovery factor for CO_2 flooding is widely changing from nearly 1 percent to 42 percent in the simulated cases. Also, the minimum CO_2 saturation among all of the cases is 0.1 and its maximum is more than 0.43 fraction of pore volume. Some of the floods did really well in terms of the amount of CO_2 retained in the reservoir resulting in more than 40 Mscf of CO_2 stored in the reservoir per each standard barrel of oil, but in contrast there was a case for which only 2 Mscf/STB was stored in the reservoir. Figure 5.8 shows recovery factor plots for combined waterflooding and CO_2 flooding periods in some of simulation cases. It is seen that starting point for CO_2 flooding is changing in different scenarios due to the difference in well spacing, and other reservoir characteristics. Also duration of CO_2 flooding is different in all of the cases which is mainly due to the well monitoring constraints in the production wells. Figure 5.9 shows average gas saturation for same simulation runs. It is seen that CO_2 saturation is zero before CO_2 flooding starts. The cases that gas saturation shows some oscillations are WAG injection scenarios and more smooth curves indicate continuous CO_2 injection runs. It should be noted that not necessarily the case with higher amount of retained CO_2 resulted in higher recovery and vise versa. But, there should be an optimum value for both recovery and amount of stored CO_2 considering all of the uncertainties.

It is also clear from Table 5.8 that duration of simulation runs are different for each case because of the constraint in the GOR and water-cut (WCUT) of the production wells. Therefore, it was necessary to enter the time factor as another criterion to account

for its effect in the simulation results. The best way to apply this was to perform discounted cash flow (DCF) analysis and calculate dollar value of produced oil and stored CO_2 to make the final conclusion of the best strategies to optimize flood design. Table 5.8 shows these calculated values as well as all other simulation results.

In order to perform the DCF calculations, economical parameters shown in Table 5.9 were assumed. Based on all of these variables, NPV for each project was calculated and in order to get better sense of DCF calculations, NPV was divided by total oil production to calculate present value for each barrel of produced as $/bbl of oil in any scenario. Since this value is somewhat dimensionless, it is easier and more manageable than actual NPV to work with. Therefore, it was chosen as our objective functions (column 7 in Table 5. 8) instead of oil recovery factor. We call this objective function as "Profit" for each scenario. Besides, CO_2 saturation in the reservoir (as direct measure of retained CO_2) which is in dimensionless form as well, was selected as second objective function (column 4 in Table 5. 8). This objective function is called "Storage".

5.4.3 Flood Design Optimization

Multivariate statistical analysis was performed on the design factors to determine their individual effect on each one of objective functions. Table 5.10 shows the results of statistical analysis on the simulation results. It shows the effect of most important design factors on profit as well as CO_2 storage objective functions. Effect can be defined as change in the average response when a factor varies from its low to the high value within the range of uncertainty. According to this, experimental design identifies the high influential factors (ranked in the order from highest to lowest effects) on the profit and storage functions as shown in Table 5.10. Based on the parameters and the reservoir conditions studied, the order from most to least influential factors for profit objective are well spacing, combination of operation constraints for injection and production wells,

combination of average reservoir permeability and Kv/Kh, and produced GOR constraint. For storage objective, by far the most influential factors are produced GOR constraint then injection scheme (continuous CO_2 or WAG), respectively. Next set of important factors are combination of average reservoir permeability and Kv/Kh, and combination of operation constraints for injection and production wells. Other important variables are shown in Table 5.10 in the order from highest to lowest importance.

After defining sensitive parameters and ranking them based on their importance on each objective function, response surfaces are generated. Figure 5.10 demonstrates one of the response surfaces for profit objective at different GOR constraint and average reservoir permeability and constant values for other factors. It simply shows that there is an optimum value for GOR in which profit is the maximum. In this given response surface, GOR of ~30000 Mscf/Stb will maximize the profit. Also it is observed from this figure that generally, as average reservoir permeability increases, profit is increasing as well.

Figure 5.11 shows one of the response surfaces for storage objective at different GOR constraint and average reservoir permeability and constant values for other factors. It shows that there is an optimum value for well spacing (~50 acres) for which CO_2 storage objective is maximum. It also demonstrates that as Kv/Kh ratio increases in the reservoir, storage objective increases as well. The figure also shows that in this specific response surface, production and injection wells are both vertical and completed in the whole interval. Injection scheme is WAG and it somewhat controls the CO_2 mobility. Since the reservoir structure is layered with relatively high permeability contrast, and considering all other mentioned factors, it can be concluded that higher the Kv/Kh allows for better vertical communication among different layers causing better sweep in all of the layers and consequently more CO_2 can be injected and stored in the reservoir.

Mathematical forms of the generated response surfaces were utilized to perform optimization on profit and storage objective functions. Optimizations were performed to

define conditions for any of the nine uncertain factors by which the highest possible CO_2 storage is achieved. Equally weighted combination of profit and storage objective functions was also considered as another optimization scenario. Table 5.11 shows these two different optimization scenarios. In addition, status/values for each uncertain parameter were suggested by method of response surfaces for each scenario to achieve optimum value for the defined objective functions and are shown in Table 5.11.

One of other advantages of applying experimental design and method of response surfaces to perform optimization process is that the optimized values for each objective function in all optimization scenarios can be predicted with a specified margin of error. These predicted values for each scenario are shown in Table 5.11. Predicted response values for each optimization scenario were very close to the values, were acquired by performing their corresponding simulation runs. It is observed in the table that maximum of 44 percent CO_2 saturation can be achieved in these type of the layered carbonate reservoirs. Continuous CO_2 is suggested to be injected in order to reach maximum storage while WAG injection is suggested to obtain optimized profit and CO_2 storage. In addition, high permeable carbonate reservoirs with low Kv/Kh ratio show both higher profit and storage while low permeable carbonate reservoirs with high Kv/Kh ratio lead to higher storage only. Furthermore, well spacing should be smaller when optimizing both profit and storage compared to the scenario that CO_2 storage is maximized.

5.5 Flood Design Parameters for Sandstone Reservoirs

Sandstone reservoirs in general have high permeability. They have completely different reservoir characteristics compared to the carbonate reservoirs. In addition, there are large number of sandstone reservoirs in U.S., primarily Gulf Coast as well as mid-continent and Rocky Mountains. The vast majority of CO_2 flood projects are currently being conducted in carbonate reservoirs in the Permian Basin. Industry efforts in the Gulf

Coast have been limited in scope and usually are on a smaller scale. Gulf Coast sandstone reservoirs differ from those in the Permian Basin in terms of their matrix, reservoir architecture, oil composition, drive mechanism and recovery rates. Their suitability to CO_2 flooding also varies. Usually these reservoirs have very low residual oil saturation in the swept area, which has often led to poor performance under CO_2 flooding. Most of these projects proved to be technical successes but not economical ones.

Considering the concept of coupled EOR and sequestration, one big advantage of Gulf Coast mature sandstone reservoirs is availability of vast amount of anthropogenic CO_2 sources in the area. This can make them attractive and better candidates economically, for the coupled CO_2-EOR and sequestration projects. Transportation costs will be extremely low for these reservoirs and it can add huge economic advantage to perform CO_2 flooding and sequestration in sandstone reservoirs in Gulf Coast. Because of the major differences in carbonate and sandstone reservoirs, flood design and strategies would be different in each type of these reservoirs. Deposition settings for sandstone reservoirs commonly are shallow marine environments. Therefore, there is a great degree of lateral variation within the reservoir. Heterogeneities within the reservoir are attributed to lateral and vertical facies variations.

It is realized that sandstone reservoirs have potential for future coupled EOR and sequestration especially in Gulf Coast as well as some other parts of the world. Sandstone reservoirs generally show high porosity and permeability distributions and usually are represented by stochastic reservoir heterogeneity. Appropriate flood design should be applied for these reservoirs to achieve optimum recovery and sequestration. In our study, we have focused on the flood design parameters for coupled EOR and sequestration processes. Sensitivity analysis has been performed on the defined parameters in order to identify their individual and combinational effects on both EOR and sequestration objectives.

Effect of important flood design factors in the CO_2 injection processes, on the oil recovery and the amount of stored CO_2 is investigated to determine the optimum situation for flood design parameters. All of the design parameters that were considered in the carbonate reservoir sensitivity analysis were utilized here except average reservoir permeability and Kv/Kh ratio. These two factors do not vary drastically in the sandstone reservoirs and therefore we decided to introduce two additional variables instead of them for sandstone flood design sensitivity study to keep the same number of 9 uncertain factors.

Shut-In/Open Strategy: Since sandstone reservoirs have high permeability, and therefore high viscosity forces are present while flooding in these reservoirs, CO_2 moves faster through high permeable zones and causes rapid breakthrough. Of course, there are some mobility control techniques such as WAG, SAG etc which are known for long time and they have been used in the field scale applications. Another strategy that we thought might help smoothing out fast moving CO_2 front was to inject CO_2 for a period of time and then shut the injection well for next period and repeat this cycle over and over. This might increase sweep as well as stored CO_2 in the flooded reservoir. This strategy was considered as one of the design factors specifically in sandstone reservoirs.

Recycling Options: At some point during flood, CO_2 will start to be produced and unfortunately, most of the produced gas will be the injected CO_2. It is necessary to gather and compress CO_2 in a pre-designed plant and reuse it in different ways. This produced gas can either be re-injected into the reservoir, re-injected into the aquifer close to the reservoir (for the purpose of storage), or the compressed gas can be re-sold. These scenarios either will add new expenses to the project or add some value to it. When economic analysis is carried out to measure flood performances, these options should be accounted properly. For sensitivity analysis, we have considered two of three above recycling options: either CO_2 is re-injected into the reservoir or it just simply is sold to the assumed third party. It is evident that comparing both alternatives of re-selling

produced CO_2 and/or re-compressing and injecting it, some of the economic options such as new CO_2 purchase requirement or cost and size of compression and re-injection plant are different in the project. We have tried to consider this factor as one of our sensitivity parameters to achieve optimum flood design parameters for coupled EOR and sequestration projects.

Due to the large number of engineering design parameters, only the most important design variables were chosen. Table 5.12 shows the design parameters and their corresponding range of variation. It is seen that there are only categorical type of variables and all of them have two levels of variations. Therefore, quadratic 2-level fractional factorial design approach was utilized. According to the selected experimental design method and number of factors, 32 simulation cases were defined to be performed. Table 5.13 shows all of the 32 simulation cases as well as settings of uncertain factors in each one of them. They have been selected out of more than 2^9=512 cases that had to be performed if conventional sensitivity analysis were supposed to be applied.

5.5.1 Reservoir Simulation Models

In order to carry out all 32 simulation runs, simulation models have to be created for each simulation scenario. For all of the simulation cases, A 3-D corner point reservoir grid was selected and then stochastic permeability and porosity field were created for this corner point grid. All properties were based on typical sandstone reservoirs. Reservoir geometry comprised of two anticline domes adjacent to each other with 200 ft thickness at depth of 6100 ft. The reservoir was set to 28×40×15 gridblocks. Table 5.14 shows the summary data for the reservoir properties. Figure 5.12 shows 3-D view of reservoir geometry and its stochastic permeability field. The average horizontal permeability is 100 md and average porosity is 0.22 fraction of reservoir bulk volume.

For rock-fluid and PVT data, we used the same relative permeability and hysteresis in relative permeability model as in Chapter 4. Reservoir fluid was considered in a vertically equilibrium condition with water-oil contact of 6400 ft with no water influx and therefore no energy support from aquifer. Table 5.14 shows the average oil and water saturations in the reservoir. To obtain more accurate results, three different rock types (according to the previously stated correlations in Chapter 4) were defined based on the porosity values in the grid blocks, and consequently three sets of relative permeability data were considered in all of the simulation models. For the simulation cases that water alternated with gas was employed as injection scheme instead of continuous CO_2, hysteresis was applied in the relative permeability models.

Similar to the carbonate reservoirs, and to obtain the most resemblance to the real world cases, all of the simulations started at the end of the waterflood. Water was injected nearly up dip using 6 vertical wells and oil was produced in the oil zone. Figure 5.13 shows the 3-D view of the remaining oil saturation at the end of the water flooding in one of the simulation cases. By the end of primary and water flooding stages, close to 42 percent of originally oil in place (OOIP) was produced in different simulation cases (considering 98 percent water cut as production limit for each well). Average remaining oil saturation after water flooding was 39 percent. Duration of water flooding was almost 10 years. After water flooding, all 32 CO_2 injection scenarios, shown in Table 5.15, were simulated. Similar to the carbonate cases, the minimum flowing bottom hole pressure at production wells was set to 1300 psi and maximum injection pressure was set to assumed reservoir fracture pressure of 3300 psi. For the simulation cases that injection or production constraint were based on constant rate, two-third of the average rate when wells were operating under BHP constraint, was considered as maximum target rate. Both horizontal and vertical wells were completed in the whole interval. By applying extensive well completion scenarios, it was tried to control the amount of water and CO_2 production. For instance, when the water cut reached 98% or gas-oil ratio reached

maximum allowable value in each case, most offending layers were plugged and checked periodically to verify whether previously violated monitored constraint has ceased to be violated, then layer was re-opened automatically. Ultimately, when the total field oil production was below 10 STB/day, production well was being closed for the rest of the simulation and CO_2 was being injected until average reservoir pressure reaches fracture pressure of 3300 psi. This provides an effective strategy to maximize CO_2 storage. This allows for maximum possible amount of CO_2 to be produced in the reservoir. It is important to note that well operation constrains were defined in a way that reservoir pressure in all of the simulation cases were above minimum miscibility pressure.

5.5.2 Simulation Results and Discussion

Three-dimensional compositional simulations were performed according to all of the aforementioned assumptions and scenarios. Table 5.15 shows the results for all of the simulation runs. Recovery factor for CO_2 flooding is widely changing from nearly 3 percent to 28 percent in the simulated cases. Also, the minimum CO_2 saturation among all of the cases is 0.12 and its maximum is more than 0.36 fraction of pore volume. Some of the floods did really well in terms of the amount of retained CO_2 in the reservoir resulting in more than 17 Mscf of CO_2 stored in the reservoir per each standard barrel of oil produced but, in contrast there was a case for which only 3.9 Mscf/Stbo was stored in the reservoir. Figure 5.14 shows 3-D view of remaining oil saturation as well as CO_2 saturation distributions in one of the simulation cases at the end of the flooding process. It is seen that most of oil zone has been swept by CO_2 and average gas saturation is in the order of 0.4 fraction of pore volume.

Similar to the carbonate sensitivity analysis, Table 5.15 indicates that duration of simulation runs are different for sandstone sensitivity cases because of the constraint in the GOR and water-cut (WC) of the production wells. Discounted cas flow analysis was

performed for all of the simulation scenarios and dollar value of produced oil and stored CO_2 were calculated to obtain final conclusion on the best strategies to optimize flood design. Table 5.15 also shows these calculated values as well as all other simulation results.

Economic parameters for DCF calculations were same as the ones in the Table 5.9. This facilitates making final comparison of the results for flood design sensitivity study between carbonate and sandstone reservoirs as well as making final conclusion within each reservoir category. Based on all these economic variables, net present value for each project was calculated and in order to get better sense of DCF calculations and also flood performance, NPV was divided by total produced oil to calculate present value for any produced oil in each scenario. Since this value is more understandable than actual NPV to work with, it was chosen as our one of objective functions (column 7 in Table 5.15). Same as carbonate reservoirs study, this objective function is called as "Profit" for each scenario. Besides of this, CO_2 saturation in the reservoir (as direct measure of retained CO_2) which is in dimensionless form as well, was selected as second objective function (column 4 in Table 5.15). This objective function is also called "Storage".

5.5.3 Flood Design Optimization

After building geological models, all of simulation runs were performed and then multivariate statistical analysis was performed on the simulation results to determine individual effect of each factor on both of objective functions. Figure 5.15 shows the results of statistical analysis on the simulation results in the sandstone reservoirs. Using these type of plots help to identify and rank the effect of each factor on pre-defined objective functions. Effect can be defined as change in the average response when a factor varies from its low to high value within the range of uncertainty. This figure simply shows that whenever standardized effect of a specific factor is higher and also

probability of occurring this effect is higher too; thus, that specific factor will achieve higher coefficient in the mathematical form of the response surface equation compared to other variables. Therefore, we can rank all of the variables and their combinational effects on the response surfaces, in terms of magnitude of their effect on the objective function. Figure 5.15 shows the effect of all nine factors on both profit and CO_2 storage objective functions. As it is observed, the effect is negative (blue colors) when the increase in the factor from its low to its high value causes decrease in the response, and the effect is positive when the increase in the factor from low to its high value increases the response value. According to this, experimental design identifies the high influential factors (first order effects) on the profit and storage functions.

Based on the parameters and the reservoir conditions studied, the order from most to least influential factors for recovery objective are by far produced GOR, and then well spacing, production well type, and combination of them. For storage objective, by far the most influential factor is produced GOR, type of production well, type of injection strategy (WAG or continuous CO_2), and then combination of these variables. Table 5.16 summarizes the order of important factors on both objective functions for sandstone reservoirs.

After defining sensitive parameters and ranking them based on their importance on each objective function, response surfaces are generated. Figure 5.16 demonstrates one of the response surfaces for storage objective at different injection and production well types and constant parameters for other design factors. It is important to realize that since all of the design factors were considered as categorical factors, generated response surfaces are not in the form of continuous functions and they are rather discrete function of design factors. Figure 5.16 shows that combination of vertical production wells (A2) and horizontal injection wells (B1) will result in the highest CO_2 saturation. In this specific response surface, combination of horizontal injection and production wells will result in the lowest sequestration value. Figure 5.17 shows the generated response surface

for the profit objective function at different produced GOR, injection scheme (WAG or continuous CO_2) and constant parameters for other design factors. According to this figure, profit increases when injection scheme changes from continuous CO_2 to WAG injection. Also it decreases when produced GOR changes from 50000 MScf/bbl to 10000 Mscf/bbl. The highest value in the represented profit response is achieved when allowable produced GOR is high and CO_2 is injected in the form of WAG into the reservoir.

Mathematical forms of the generated response surfaces were utilized to perform optimization on profit and storage objective functions. The optimization process was performed to define conditions for all of nine uncertain factors by which the highest possible CO_2 storage is achieved. In addition, equally weighted combination of profit and storage objective functions was considered as another optimization scenario. Table 5.17 shows these two different optimization scenarios. In addition, status/values for each uncertain parameter were suggested by method of response surfaces for each scenario to achieve optimum values for defined objective functions and they are presented in Table 5.17 as well.

One of other advantages of applying experimental design and method of response surfaces to perform optimization study is that the optimized values for each objective function in all of the optimization scenarios can be predicted with an specified margin of error. In this study, these predicted values for each scenario are shown in Table 5.17 as well. Predicted response values for each optimization scenario were very close to the values that were acquired by performing their corresponding simulation runs. It is observed in the table that maximum of 34 percent CO_2 saturation can be achieved in the similar sandstone reservoirs while only 3.8 $/bbl of oil is gained. When both objectives are maximized at the same time, storage objective is jeopardized for the benefit of increasing project profit. Similar to the carbonate reservoirs optimization study, continuous CO_2 is suggested to be injected in order to reach maximum storage while

WAG injection is suggested to obtain optimized profit and CO_2 storage. Combination of horizontal injection wells with vertical production wells will result in both higher project profit as well as CO_2 saturation at the end of the flood. In addition, re-injecting produced CO_2 in both optimization scenarios will be better design option compared to re-selling produced CO_2. This is possibly because of huge reduction in project expenses for CO_2 purchase; since produced gas will contain some impurities re-sell value (added to the project profit) of the produced gas will be much less than value to purchase fresh pure CO_2. Furthermore, shut-in/open strategy seems to help increase CO_2 storage and project profit and it should be considered as one of the important design variables for coupled EOR and sequestration projects. Smaller well spacing is needed to achieve maximum profit and storage values compared to the scenario in which storage is maximized only.

5.6 SUMMARY AND CONCLUSIONS

Exploratory systematic compositional simulations of CO_2 injection in heterogeneous three-dimensional reservoirs were performed to establish effective flood design strategies for coupled CO_2-EOR and sequestration to maximize both flood performance and amount of stored CO_2. Experimental design and method of response surfaces were utilized to achieve efficient and comprehensive results. Detailed economic analysis was performed on reservoir simulation results to establish solid basis for the conclusions of this study. In addition, due to the variation in the petrophysical properties in different reservoirs especially major differences between carbonate and sandstone reservoir characteristics, they were studied separately.

Our approach is based on the construction of quadratic response models of reservoir simulation outputs by applying 2-leve fractional factorial design for sandstone reservoirs and D-optimal design for carbonate reservoirs. It should be noted that all of the optimized values for all objective functions predicted by design of experiment and

response surface method are close to the values obtained by an exhaustive simulation study but with a very efficient computational time. Results from this study clearly showed that in general, carbonate reservoirs are better candidates for coupled CO_2-EOR and sequestration projects compared to sandstone reservoirs. Also it was concluded that individual and combinational effect of design parameters such as produced gas oil ratio constraint, well spacing, production and injection well types, and injection scheme (WAG or continuous CO_2 injection) along with some important reservoir characteristics such as Kv/Kh are the most sensitive parameters in almost all of the optimization cases for maximizing both profit (economic performance of the flood) and amount of stored CO_2. All of the optimized values obtained from applying response surface methodology were for both of the objective functions were in close agreement with the values from their corresponding simulation results as if exhaustive simulation study had been performed.

Impact of production and injection well types on the sweep efficiency and consequently amount of stored CO_2 is significant. Based on this study, optimal well types to achieve highest possible profit and storage are defined. In sandstone reservoirs using combination of vertical producers and horizontal injectors will provide best results for both of objective functions. While, in carbonate reservoirs applying both vertical production and injection wells results in optimum storage as well as project performance. This difference in the well type of carbonate and sandstone reservoirs can be interpretated according to the difference in their reservoir structure. In the carbonate reservoirs, which were introduced as layered-type reservoirs, due to the existence of high permeability layers, vertical wells may result in better performance. Because, wrong choice of layers for injection and production wells, might result in decrease in sweep and storage. But, in sandstone reservoirs due to the stochastic-type distribution of reservoir properties, horizontal injectors help in increasing sweep efficiency and there is no need to be concerned about vertical variation of high permeable zones.

Well spacing is a key factor determining the economic viability of candidate reservoirs for CO_2 flooding projects. It is also concluded that smaller well spacing would accelerate the recovery process and will perform in the favor of overall net present value of the project; but, due to close distance between wells, CO_2 breakthrough will occur faster and total amount of stored CO_2 will be small. Based on the results from our study, well spacing is more important when optimizing both profit and storage objectives compared to the scenario in which only storage is maximized. It was also shown that optimum well spacing are smaller for carbonate reservoirs than that of sandstone reservoirs. In addition, when optimizing both of the objective functions is the main goal, smaller well spacing should be considered compared to the cases that only maximizing storage is the final objective.

Table 5.1: Summary of input data for the EOR simulations

Grid	50×50×20
Vertical to horizontal Perm. Ratio	0.1
Average horizontal permeability, md	100
Average porosity	0.22
Initial Oil Saturation	0.65
Residual Oil Saturation	0 .35
Temperature, °F	110
Effective Aspect Ratio (R_L)	4.74
Critical Rate, ft/D	0.02
End Point Mobility Ratio	16.9
Gravity Number at 20 MMSCF/D	0.22
Pore Volume (MMRB)	70
OOIP, MM STB	40.8

Table 5.2: Injection and production well design for first stage of CO_2 flooding

GEOR-	Injection				Production		
	Vertical layer No.	Rate**	BHP, psi	Completion length*	Vertical layer No.	BHP, psi	Completion length*
8R2	14	20	-	2400	5	1500	2400
9R2	14	25	-	2400	5	1500	2400
10R2	5	20	-	2400	5	1500	2400
14R2	5	-	3300	2400	5	1500	2400
15R2	5	-	3300	2400	5	1200	2400
16R2	5	-	3300	2760	5	1500	2760
12R2* **	5	20	-	60	4:10	1500-1500-1500	2400
13R2* **	5	25	-	60	4:10	1400-1300-1400	2400
3AA	3	0.25	-	2400	5	2000	2400
4	3	-	3300	2400	3	1000	2400
7A	14	20	-	2400	4	1500	2400

* Unit: ft ** MM Scf/D *** Vertical production well

Table 5.2 (continued): Injection and production well design for second stage

GEOR-	Injection				Production		
	Vertical layer No.	Rate**	BHP, psi	Completion length*	Vertical layer No.	BHP, psi	Completion length*
8R2	5	20	-	2400	5	1500	2400
9R2	5	25	-	2400	5	1500	2400
10R2	5	20	-	2400	5	1500	2400
14R2	5	-	3300	2400	5	1500	2400
15R2	5	-	3300	2400	5	1200	2400
16R2	5	-	3300	2760	5	1500	2760
12R2* **	5	20	-	60	4:10	1500-1500-1500	2400
13R2* **	5	25	-	60	4:10	1400-1300-1400	2400

* Unit: ft ** MM Scf/D *** Vertical production well

Table 5.2 (continued): Injection and production well design for third stage

GEOR-	Injection				Production		
	Vertical layer No.	Rate**	BHP, psi	Completion length*	Vertical layer No.	BHP, psi	Completion length*
8R2	5	20	-	2400	8	1500	2400
9R2	5	25	-	2400	8	1500	2400
10R2	5	20	-	2400	5	1500	2400
14R2	5	-	3300	2400	5	1500	2400
15R2	5	-	3300	2400	5	1200	2400
16R2	5	-	3300	2760	5	1500	2760
12R2* **	5	20	-	60	4:10	1500-1500-1500	2400
13R2* **	5	25	-	60	4:10	1400-1300-1400	2400

* Unit: ft ** MM Scf/D *** Vertical production well

Table 5.3: Simulation results injection and production at only one-stage cases.

Run number-GEOR series	3AA	7A	4	Open & Shut-In
Cumulative gas injected, MM SCF	9125	0.75E5	2.21E5	146900
Cumulative Oil Recovery, MM. STB	0.45	7.2	14.2	10.9
Oil Recovery as % of OOIP	1.15	17.57	28.29	26.8
Average remaining oil saturation (fract.)	0.4	0.27	0.21	0.22
Length of CO_2 flood, D	36500	6480	6500	9253
Total CO_2 Sequestered, MM SCF	8289	54739	64899	61800
Sequestered portion of injected CO_2, %	90.8	72.9	29.3	42.1
CO_2 Injected per Barrel of Oil Produced	20.28	10.42	15.56	13.48
CO_2 Stored per Barrel of Oil Produced	18.42	7.60	4.57	5.67

Table 5.4: Simulation results for injection and production in three-stage cases.

Run number-GEOR series	8R2	9R2	10R2	14R2	15R2	16R2	12R2	13R2
Cumulative gas injected, MM SCF	1.11E5	1.19E5	1.08E5	1.49E5	1.55E5	1.49E5	89.2	93.3
Cumulative Oil Recovery, MM. STB	8.06	8.41	7.3	9.11	9.34	9.45	5.7	6.5
Oil Recovery as % of OOIP	19.8	20.7	17.8	22.3	22.9	23.2	13.9	14.8
Average remaining oil saturation (fract.)	0.29	0.27	0.29	0.24	0.24	0.236	0.291	0.287
Length of CO_2 flood, D	5736	5232	5571	5277	4816	4740	4816	4816
Total CO_2 Sequestered, MM SCF	49164	68260	57960	58681	58731	59231	45080	45400
Sequestered portion of injected CO_2, %	44.3	57.4	53.7	39.3	37.9	39.9	50.5	48.7
CO_2 Injected per Barrel of Oil Produced, Mscf/STBO	13.77	14.15	14.79	16.36	16.60	15.77	15.65	14.35
CO_2 Stored per Barrel of Oil Produced, Mscf/STBO	6.10	8.12	7.94	6.44	6.29	6.27	7.91	6.98

Table 5.5: Flood design parameters for carbonate reservoirs

Factors	Type	Low	Medium	High
A: Produced GOR, SCF/STB	Numeric	10000	30000	50000
B: Production well type	Categoric	Horizontal	-	Vertical
C: Injection well type	Categoric	Horizontal	-	Vertical
D: Production well constraint	Categoric	Rate	-	BHP
E: Injection well constraint	Categoric	Rate	-	BHP
F: Injection scheme	Categoric	Continuous CO_2	-	WAG
G: Average field permeability	Numeric	5	-	50
H: Kv/Kh	Numeric	0.01	-	1
J: Well spacing	Numeric	10	40	90

Table 5.6: Setting of uncertain factors for all of 61 simulation runs

Run #	A	B	C	D	E	F	G	H	J
1	23300	Vertical	Horizontal	BHP	BHP	WAG	5	0.01	40
2	10000	Vertical	Vertical	BHP	BHP	Cont. CO_2	50	1	90
3	50000	Vertical	Horizontal	BHP	BHP	Cont. CO_2	5	0.01	90
4	50000	Vertical	Vertical	Rate	BHP	Cont. CO_2	5	1	90
5	50000	Horizontal	Horizontal	BHP	BHP	Cont. CO_2	50	1	90
6	10000	Vertical	Vertical	Rate	BHP	WAG	50	1	10
7	20000	Vertical	Vertical	BHP	BHP	Cont. CO_2	5	0.01	10
8	50000	Horizontal	Vertical	BHP	BHP	Cont. CO_2	50	0.01	10
9	20000	Vertical	Vertical	Rate	Rate	Cont. CO_2	50	0.01	40
10	36600	Horizontal	Horizontal	BHP	Rate	WAG	5	0.01	90
11	30000	Horizontal	Horizontal	Rate	Rate	WAG	50	0.01	40
12	10000	Vertical	Horizontal	BHP	Rate	Cont. CO_2	50	1	10
13	20000	Vertical	Vertical	Rate	Rate	WAG	50	0.01	90
14	20000	Horizontal	Vertical	Rate	BHP	WAG	5	1	40
15	10000	Vertical	Horizontal	Rate	Rate	WAG	50	0.01	10
16	23300	Horizontal	Horizontal	Rate	BHP	Cont. CO_2	5	0.01	40
17	10000	Horizontal	Vertical	BHP	Rate	Cont. CO_2	50	1	40
18	50000	Vertical	Horizontal	Rate	Rate	Cont. CO_2	50	1	90
19	10000	Vertical	Vertical	BHP	Rate	Cont. CO_2	5	1	40
20	50000	Horizontal	Horizontal	Rate	Rate	Cont. CO_2	50	0.01	90
21	50000	Vertical	Horizontal	Rate	Rate	WAG	5	0.01	40
22	50000	Vertical	Vertical	BHP	BHP	WAG	5	0.01	90
23	50000	Horizontal	Vertical	Rate	Rate	Cont. CO_2	5	0.01	40
24	10000	Horizontal	Vertical	BHP	Rate	WAG	5	1	90
25	50000	Vertical	Horizontal	BHP	Rate	WAG	5	0.01	10

Table 5.6: Continued

26	36600	Horizontal	Vertical	BHP	BHP	WAG	50	1	40
27	23300	Vertical	Horizontal	Rate	BHP	Cont. CO_2	50	0.01	90
28	40000	Horizontal	Horizontal	Rate	BHP	WAG	50	1	10
29	10000	Horizontal	Horizontal	Rate	Rate	Cont. CO_2	50	0.01	90
30	20000	Horizontal	Vertical	BHP	Rate	WAG	5	0.01	40
31	20000	Horizontal	Vertical	Rate	Rate	WAG	5	0.01	10
32	50000	Vertical	Vertical	Rate	Rate	WAG	50	1	40
33	36600	Horizontal	Vertical	BHP	Rate	Cont. CO_2	5	1	90
34	10000	Horizontal	Horizontal	Rate	BHP	WAG	50	1	90
35	10000	Horizontal	Vertical	Rate	BHP	Cont. CO_2	50	0.01	10
36	10000	Vertical	Horizontal	BHP	BHP	WAG	50	0.01	40
37	50000	Horizontal	Vertical	Rate	BHP	Cont. CO_2	5	1	10
38	50000	Vertical	Horizontal	BHP	Rate	Cont. CO_2	50	0.01	40
39	50000	Horizontal	Vertical	BHP	Rate	WAG	50	1	10
40	23300	Horizontal	Horizontal	Rate	Rate	Cont. CO_2	5	1	90
41	30000	Vertical	Vertical	BHP	Rate	WAG	5	1	10
42	10000	Horizontal	Horizontal	BHP	Rate	Cont. CO_2	5	0.01	10
43	20000	Vertical	Horizontal	Rate	Rate	WAG	5	1	90
44	40000	Vertical	Horizontal	BHP	BHP	WAG	50	1	90
45	50000	Vertical	Horizontal	Rate	BHP	WAG	5	1	40
46	50000	Vertical	Horizontal	BHP	BHP	Cont. CO_2	50	1	10
47	20000	Horizontal	Vertical	BHP	BHP	WAG	50	0.01	90
48	10000	Vertical	Horizontal	BHP	Rate	Cont. CO_2	5	0.01	90
49	10000	Horizontal	Horizontal	BHP	BHP	WAG	5	1	10
50	10000	Vertical	Horizontal	Rate	BHP	Cont. CO_2	5	0.01	10
51	50000	Horizontal	Horizontal	BHP	BHP	WAG	5	0.01	10
52	10000	Horizontal	Vertical	Rate	BHP	Cont. CO_2	5	0.01	90
53	30000	Horizontal	Vertical	Rate	Rate	Cont. CO_2	50	1	10
54	50000	Vertical	Vertical	BHP	BHP	Cont. CO_2	5	0.01	40
55	10000	Vertical	Horizontal	Rate	Rate	WAG	5	1	40
56	50000	Horizontal	Vertical	Rate	Rate	WAG	5	1	90
57	50000	Vertical	Vertical	Rate	Rate	Cont. CO_2	50	0.01	10
58	10000	Vertical	Vertical	Rate	Rate	Cont. CO_2	5	1	10
59	50000	Horizontal	Horizontal	BHP	Rate	Cont. CO_2	5	1	40
60	10000	Vertical	Horizontal	BHP	BHP	Cont. CO_2	5	1	40
61	50000	Horizontal	Vertical	Rate	BHP	WAG	50	0.01	40

Table 5.7: Summary input data for 3-D carbonate reservoir case

Gridblock Size, ft	22×22×7.5
Reference Initial Pressure, psia	2500
Reference Depth, ft	5200
Reservoir Depth at the Top, ft	5000
Initial Average Oil Saturation, frac.	0.65
Initial Average Water Saturation, frac.	0.35
Temperature, °F	110

Table 5.8: Simulation results for carbonate reservoirs flood design uncertainty analysis

Run#	Percentage recovery (Gas Flooding)	Duration of gas flooding, Year	Ave. CO_2 Saturation, frac.	CO_2 Injected per Barrel of Oil Produced, Mscf/STBO	CO_2 Stored per Barrel of Oil Produced, Mscf/STBO	Value of produced oil, $/bbl
R01	28.14	23.82	0.27	5.7	4.79	19.08
R02	7.83	1.11	0.19	6.65	12.12	20.36
R03	19.89	16.79	0.31	17.1	7.65	20.7
R04	34.87	22.82	0.42	14.97	6.17	18.98
R05	27.88	3.31	0.39	15.87	6.86	19.78
R06	18.96	0.82	0.18	2.97	4.44	4.81
R07	15.35	0.87	0.27	6.39	8.39	2.66
R08	20.65	2.19	0.29	18.91	6.31	11.11
R09	14.48	5.06	0.27	8.34	8.8	19.04
R10	28.8	92.81	0.24	2.91	3.91	11.27
R11	33.91	17.27	0.31	5.24	4.88	20.64
R12	2.54	0.09	0.15	7.29	17.41	-35.1
R13	19.32	23.33	0.24	4.9	5.64	21.6
R14	32.07	24.93	0.28	4.92	4.14	18.67
R15	5.15	0.68	0.14	4.68	7	-22.02
R16	28.2	33.33	0.37	11.26	6.37	16.16
R17	4.79	0.67	0.16	6.41	14.23	0.59
R18	17	6.58	0.32	14.07	8.68	19.91
R19	16.53	3.92	0.27	4.04	8.24	17.03
R20	30.84	23.92	0.44	17.47	7.18	19.81
R21	33.96	44.5	0.32	9.71	5.12	17.83
R22	35.35	72.81	0.31	5.96	4.4	16.03
R23	17.29	21.1	0.25	16.99	6.89	16.61
R24	23.01	21.88	0.24	2.37	4.86	19.53

Table 5.8: Continued

R25	28.06	10.39	0.29	9.85	5.37	8.23
R26	27.38	5.74	0.25	7.11	4.22	19.45
R27	14.68	11.53	0.25	11.78	8.71	20.86
R28	35.87	2.9	0.27	6.2	3.5	16.88
R29	11.38	10.46	0.23	5.98	11.08	20.51
R30	25.26	85.52	0.21	6.72	3.61	12.89
R31	20.67	31.93	0.17	4.75	3.6	5.09
R32	24.06	9.95	0.25	6.6	5.27	19.14
R33	27.77	11.89	0.4	1.18	17.75	20.33
R34	13.9	5.89	0.15	3.55	5.1	20.2
R35	6.98	0.96	0.16	4.89	9.99	-12.83
R36	19.9	2.61	0.22	4.46	5.05	22.33
R37	31.71	2.11	0.42	13.25	6.37	9.3
R38	18.45	4.1	0.41	20.99	8.89	20.42
R39	33.51	4.5	0.33	9.59	5.12	11.26
R40	22.85	13.89	0.3	10.47	6.94	19.26
R41	30.08	4.05	0.28	6.55	4.83	7.8
R42	12.95	8.21	0.24	4.26	8.69	-4.69
R43	27.93	42	0.23	5.75	3.77	17.34
R44	21.44	5.87	0.18	9.4	3.72	22.19
R45	33.76	27.32	0.26	10.23	3.69	18.49
R46	20.99	0.22	0.35	16.6	7.85	2.93
R47	27.6	23.72	0.25	7.71	4.34	20.91
R48	1	5.64	0.1	16.19	40.66	5.51
R49	30.38	4.87	0.23	2.71	3.46	11.16
R50	1.71	0.45	0.1	11.11	14.85	-40.1
R51	42.52	85.28	0.31	9.11	3.6	9
R52	4.71	15.99	0.13	6.95	13.54	17.09
R53	11.34	0.57	0.22	11.31	8.97	2.91
R54	23.81	7.04	0.36	17.8	7.27	18.24
R55	22.35	11.15	0.21	3.59	4.15	18.05
R56	39.71	79	0.32	8.89	4.04	16.31
R57	20.87	1.69	0.34	12.25	7.63	10.38
R58	14.8	1.11	0.24	4.69	8.1	-6.88
R59	31.46	8.4	0.4	17.75	6.55	18.46
R60	41.01	19.57	0.3	9.84	2.88	13.34
R61	0.91	11.16	0.13	2.82	7.66	1.88

Table 5.9: Important economical parameters for flood design DCF calculations

Oil Price	$45 / bbl
Oil Price Increase	10 %
Royalty	12.5 %
CO_2 Price	$0.85 / mcf
Op. Cost Inflation	1.5 %
Recycle Cost	$0.35 / mcf
Lift Cost	$0.2 / bbl
Discount Rate	12 %
Fed. Tax Rate	32 %
EOR Tax Credit	20 %

Table 5.10: Ranked effect of flood design factors for carbonate reservoirs

Rank	Storage objective	Profit objective
1	A	J
2	A^2	DE
3	F	GH
4	GH	AJ
5	BC	AC
6	AE	A^2
7	J^2	D
8	D	EJ
9	G	BJ
10	CF	CG

Table 5.11: Optimization scenarios for flood design variables in carbonate reservoirs

Objectives	**<u>Optimizing</u> Profit ($/bbl) & CO_2 Storage**	**Maximizing only CO_2 Storage**
A: Produced GOR, SCF/STB	31000	40000
B: Production well type	Vertical	Vertical
C: Injection well type	Vertical	Vertical
D: Production well constraint	BHP	BHP
E: Injection well constraint	BHP	BHP
F: Injection scheme	WAG	Cont. CO_2
G: Average field permeability	50	5
H: Kv/Kh	0.1	1.0
J: Well spacing	45	65
CO_2 Saturation, frac.	**0.29**	**0.44**
Profit, $/bbl	**23**	**21**

Table 5.12: Uncertain parameters in flood design parameters for sandstone reservoirs

Factors	Type	Low	High
A: Production well type	Categoric	Horizontal	Vertical
B: Injection well type	Categoric	Horizontal	Vertical
C: Production well constraint	Categoric	Rate	BHP
D: Injection well constraint	Categoric	Rate	BHP
E: Recycling	Categoric	Yes (re-inject)	No (re-sell)
F: Produced GOR, SCF/STB	Categoric	10000	50000
G: Shut-In/Open strategy	Categoric	Yes	No
H: Injection scheme	Categoric	WAG	Continuous CO_2
J: Well spacing, acre	Categoric	50	90

Table 5.13: Setting of uncertain factors in all of 32 simulation runs for sandstone reservoirs sensitivity study

Run #	A	B	C	D	E	F	G	H	J
1	Vertical	Horizontal	Rate	BHP	Yes	50000	Yes	Cont. CO_2	90
2	Vertical	Horizontal	Rate	BHP	NO	50000	NO	WAG	50
3	Horizontal	Horizontal	BHP	BHP	Yes	50000	Yes	WAG	90
4	Horizontal	Vertical	BHP	BHP	Yes	10000	NO	Cont. CO_2	90
5	Horizontal	Horizontal	Rate	Rate	NO	50000	Yes	WAG	50
6	Vertical	Horizontal	Rate	Rate	NO	10000	NO	Cont. CO_2	90
7	Horizontal	Vertical	Rate	BHP	Yes	50000	Yes	Cont. CO_2	50
8	Horizontal	Vertical	BHP	BHP	NO	10000	Yes	WAG	50
9	Vertical	Vertical	BHP	Rate	Yes	10000	Yes	Cont. CO_2	90
10	Vertical	Horizontal	BHP	Rate	Yes	50000	NO	WAG	90
11	Vertical	Horizontal	BHP	BHP	NO	10000	Yes	WAG	90
12	Horizontal	Vertical	BHP	Rate	NO	50000	Yes	Cont. CO_2	90
13	Vertical	Vertical	Rate	BHP	Yes	10000	NO	WAG	90
14	Vertical	Vertical	Rate	Rate	NO	50000	Yes	WAG	90
15	Vertical	Vertical	Rate	Rate	Yes	50000	NO	Cont. CO_2	50
16	Horizontal	Horizontal	BHP	Rate	NO	10000	NO	WAG	90
17	Horizontal	Vertical	Rate	Rate	NO	10000	NO	Cont. CO_2	50
18	Vertical	Horizontal	Rate	Rate	Yes	10000	Yes	WAG	50
19	Vertical	Vertical	BHP	BHP	Yes	50000	Yes	WAG	50
20	Vertical	Vertical	BHP	Rate	NO	10000	NO	WAG	50
21	Vertical	Vertical	Rate	BHP	NO	10000	Yes	Cont. CO_2	50
22	Horizontal	Horizontal	Rate	BHP	Yes	10000	NO	WAG	50
23	Horizontal	Vertical	Rate	Rate	Yes	10000	Yes	WAG	90
24	Horizontal	Vertical	BHP	Rate	Yes	50000	NO	WAG	50
25	Horizontal	Horizontal	Rate	BHP	NO	10000	Yes	Cont. CO_2	90

Table 5.13: Continued

26	Horizontal	Horizontal	BHP	Rate	Yes	10000	Yes	Cont. CO_2	50
27	Horizontal	Vertical	Rate	BHP	NO	50000	NO	WAG	90
28	Horizontal	Horizontal	Rate	Rate	Yes	50000	NO	Cont. CO_2	90
29	Horizontal	Horizontal	BHP	BHP	NO	50000	NO	Cont. CO_2	50
30	Vertical	Horizontal	BHP	Rate	NO	50000	Yes	Cont. CO_2	50
31	Vertical	Vertical	BHP	BHP	NO	50000	NO	Cont. CO_2	90
32	Vertical	Horizontal	BHP	BHP	Yes	10000	NO	Cont. CO_2	50

Table 5.14: Summary of 3-D sandstone reservoir input data for flood design sensitivity

Length, ft	3500
Width, ft	2500
Thickness, ft	150
Number of Blocks	28×40×15
Gridblock Size, ft	90×90×10
Number of Gridblocks	16800
Vertical to horizontal Perm. Ratio	0.1
Average horizontal permeability, md	100
Average vertical permeability, md	10
Average porosity	0.22
Reference Initial Pressure, psia	3000
Reference Depth, ft	6140
Initial Average Oil Saturation, frac.	0.65
Initial Average Water Saturation, frac.	0.35
Temperature, °F	150
Dykstra-Parsons coefficient	0.8
Dimensionless Correlation Length in x, y directions (λ_x,λ_y), ft	0.5
Dimensionless Correlation Length in z direction (λ_z), ft	0.3
Pore Volume, MM. RB	53.25
OOIP, MM STB	30.74
HCPV, MM RB	34.62

Table 5.15: Simulation results for sandstone reservoirs flood design uncertainty analysis

Run#	Percentage recovery (Gas Flooding)	Duration of gas flooding, Year	Ave. CO_2 Saturation, frac.	CO_2 Injected per Barrel of Oil Produced, Mscf/STBO	CO_2 Stored per Barrel of Oil Produced, Mscf/STBO	Value of produced oil, $/bbl
R01	13.64	16.11	0.30	15.93	9.64	14.38
R02	27.67	66.33	0.24	11.24	3.97	11.70
R03	9.71	7.56	0.24	12.10	8.68	10.85
R04	13.28	2.14	0.23	15.27	8.48	11.88
R05	13.31	11.87	0.19	13.60	5.60	8.67
R06	3.66	0.90	0.13	7.57	16.14	2.58
R07	13.33	2.30	0.26	14.64	8.08	5.57
R08	5.40	1.13	0.16	6.79	13.53	-3.07
R09	7.86	7.56	0.18	6.20	11.21	10.22
R10	5.51	3.04	0.18	7.23	12.43	7.45
R11	8.02	7.00	0.21	6.88	12.02	10.43
R12	16.16	8.00	0.29	15.38	8.36	12.75
R13	14.18	13.18	0.19	15.08	5.24	12.83
R14	7.44	2.05	0.17	5.67	10.48	9.82
R15	20.21	38.08	0.35	17.37	7.88	5.57
R16	10.38	10.11	0.17	5.97	8.27	12.29
R17	3.52	3.00	0.14	7.78	17.38	-12.58
R18	13.74	78.76	0.20	4.65	6.48	8.86
R19	24.28	37.13	0.22	13.18	4.13	10.66
R20	14.11	86.05	0.19	4.89	6.00	8.06
R21	11.99	19.32	0.22	6.25	9.36	7.10
R22	5.79	1.28	0.15	6.96	12.64	-3.58
R23	13.54	4.74	0.23	14.51	7.10	11.51
R24	13.87	12.02	0.19	13.67	5.36	7.85
R25	5.44	3.97	0.12	6.78	9.29	7.89
R26	2.77	2.63	0.13	8.10	17.25	-21.48
R27	23.90	14.17	0.22	13.31	4.26	4.16
R28	18.64	19.69	0.25	15.06	5.98	17.72
R29	12.02	2.00	0.23	15.37	8.98	5.84
R30	18.60	38.05	0.36	17.13	8.51	8.88
R31	8.93	9.34	0.17	5.65	8.60	11.38
R32	12.20	15.92	0.23	6.14	9.15	7.87

Table 5.16: Ranked effect of flood design factors for sandstone reservoirs

Rank	Storage objective	Profit objective
1	F	F
2	J	A
3	A	H
4	DH	FH
5	DJ	AH
6	EJ	J
7	H	AJ

Table 5.17: Optimization scenarios for flood design variables in sandstone reservoirs

Objectives	**Optimizing Profit ($/bbl) & CO_2 Storage**	**Maximizing only CO_2 Storage**
A: Production well type	Vertical	Vertical
B: Injection well type	Horizontal	Horizontal
C: Production well constraint	Rate	Rate
D: Injection well constraint	BHP	BHP
E: Recycling	Yes (re-inject)	Yes (re-inject)
F: Produced GOR, SCF/STB	50000	50000
G: Shut-In/Open strategy	Yes	Yes
H: Injection scheme	WAG	Continuous CO_2
J: Well spacing, acre	50	90
CO_2 Saturation, frac.	**0.22**	**0.34**
Profit, $/bbl	**17.7**	**3.8**

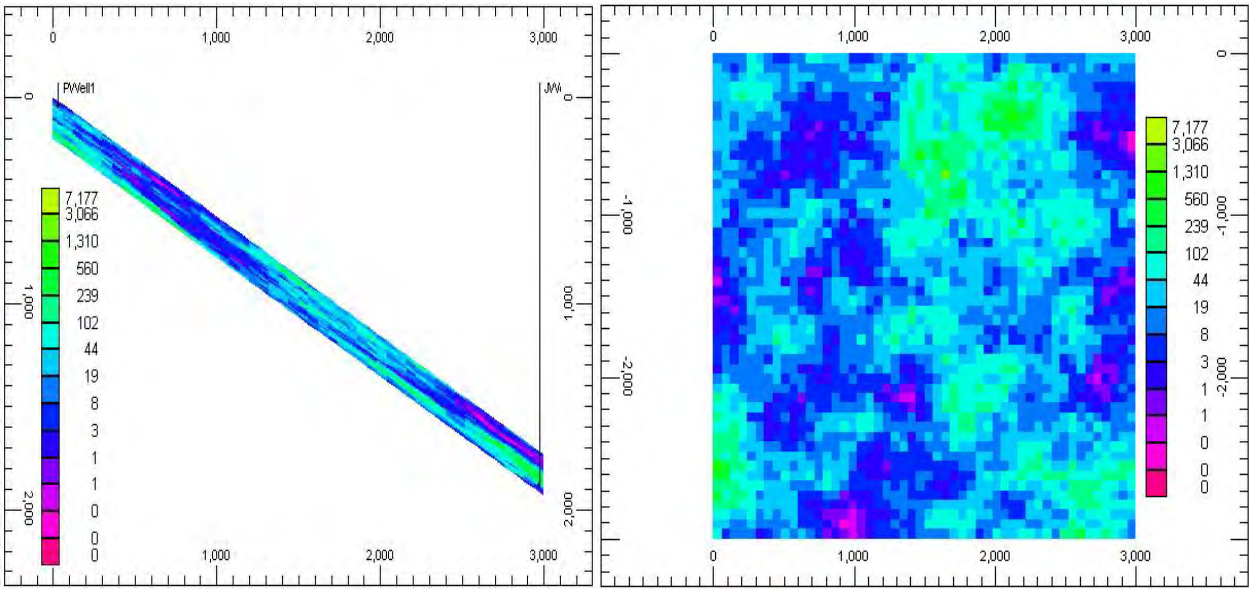

Figure 5.1- Cross section and areal view of the permeability field

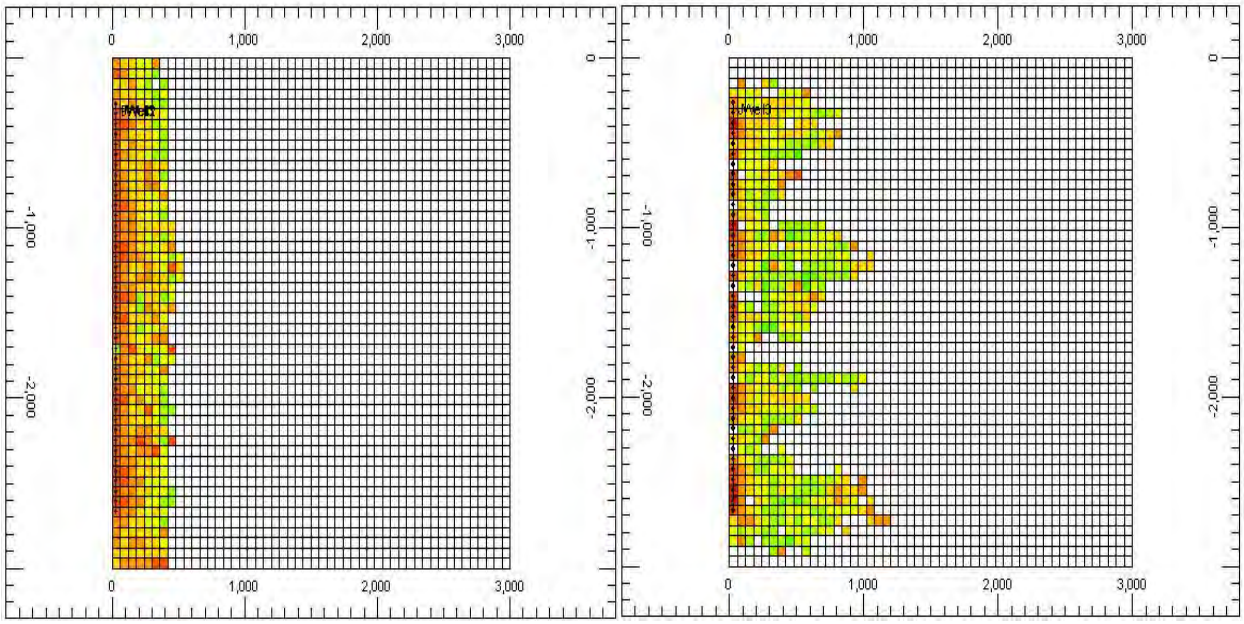

Figure 5.2- Gas saturation and CO_2 front comparison in gravity stable (after 85 years of injection) and non gravity stable displacement modes (after 2 years of injection)

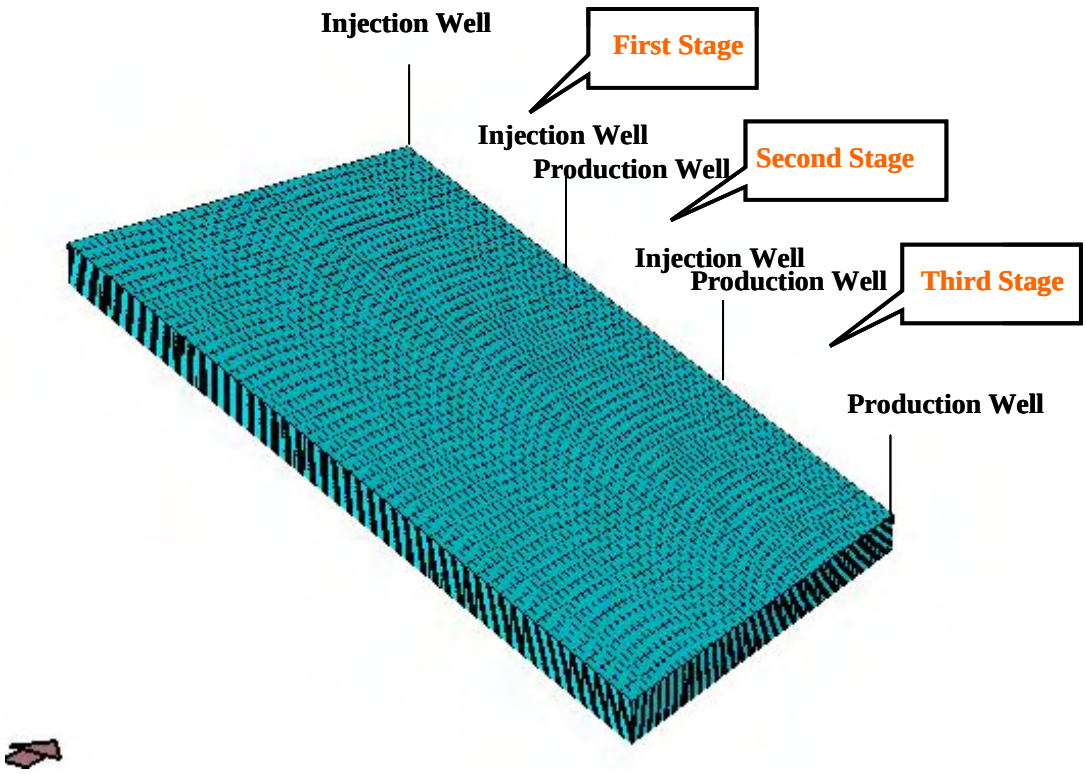

Figure 5.3- Schematic view of the three-stage flood design to sweep the reservoir

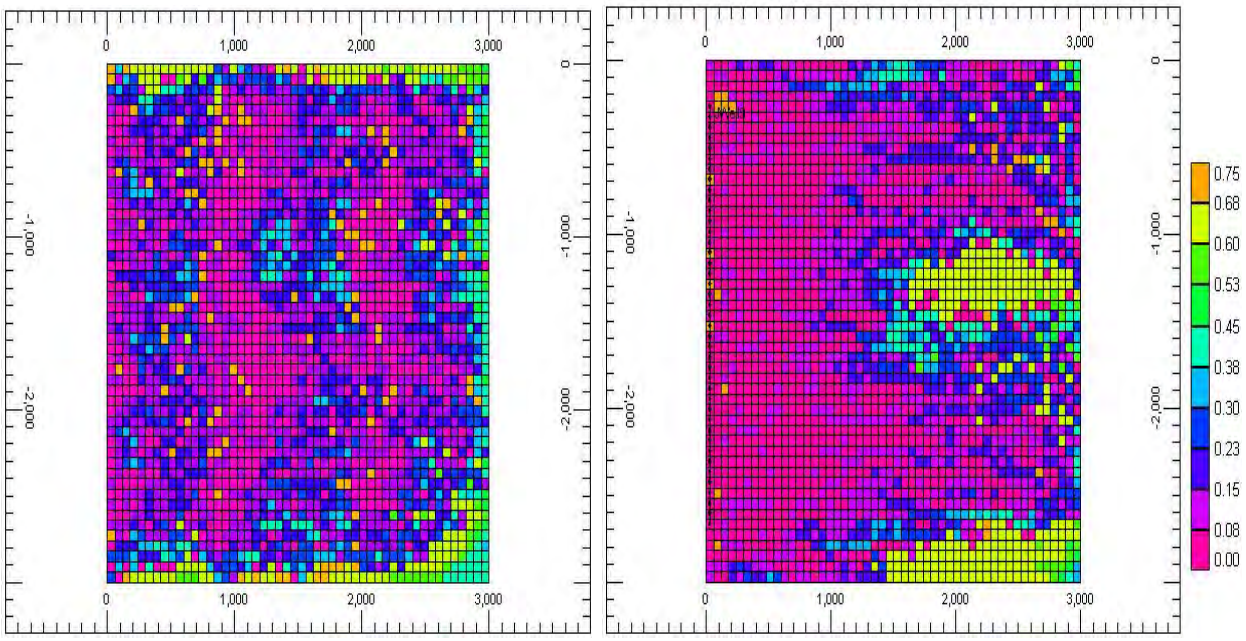

Figure 5.4- Comparison between on-stage (right) and three-stage (left) operations. Oil saturation in areal view at the end of CO_2 flooding

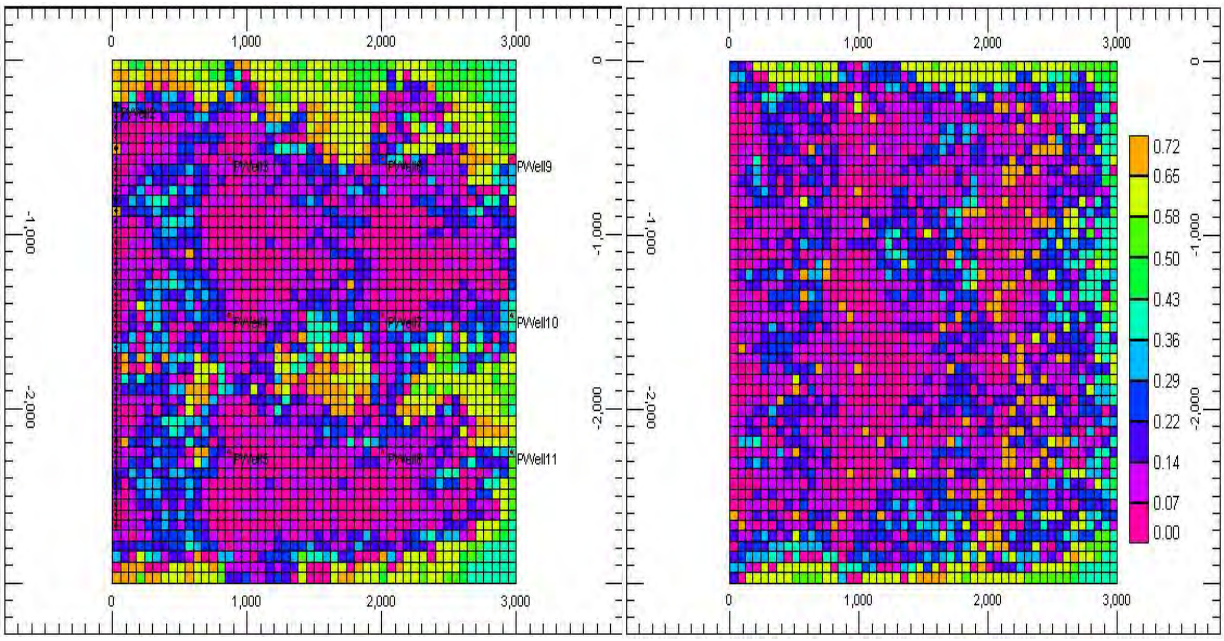

Figure 5.5- Comparison between employing vertical producer wells (right) and horizontal producers (left). Oil saturation in areal view at the end of CO_2 flooding

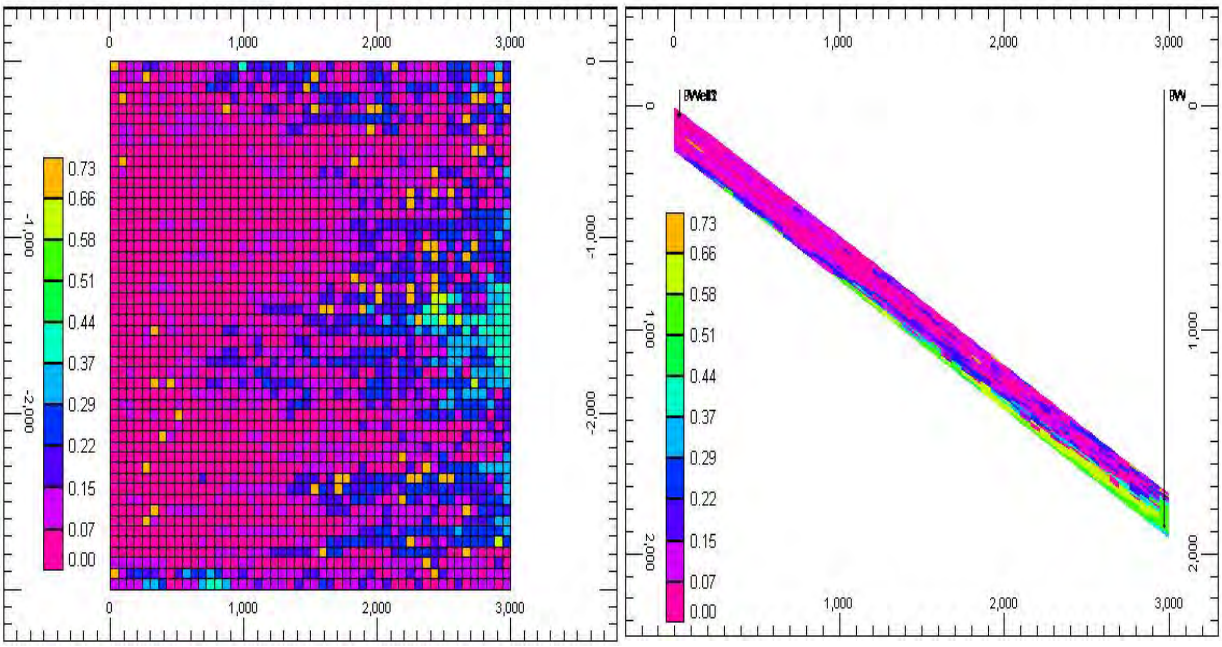

Figure 5.6- Areal and cross sectional view of oil saturation in at the end of CO_2 flooding in open and shut-in strategy operation

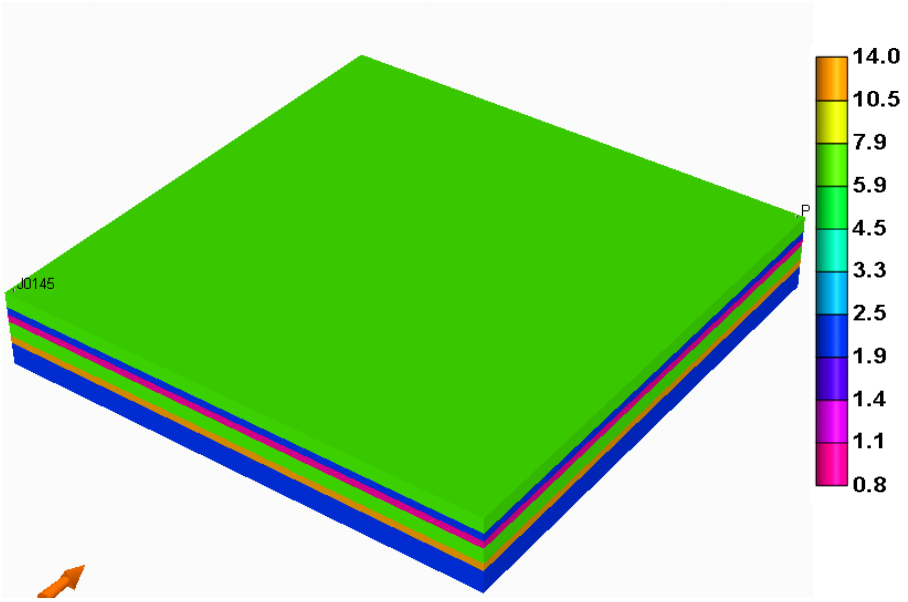

Figure 5.7- Three-dimensional view of carbonate reservoir geometry and its layered permeability distribution, for flood design sensitivity study

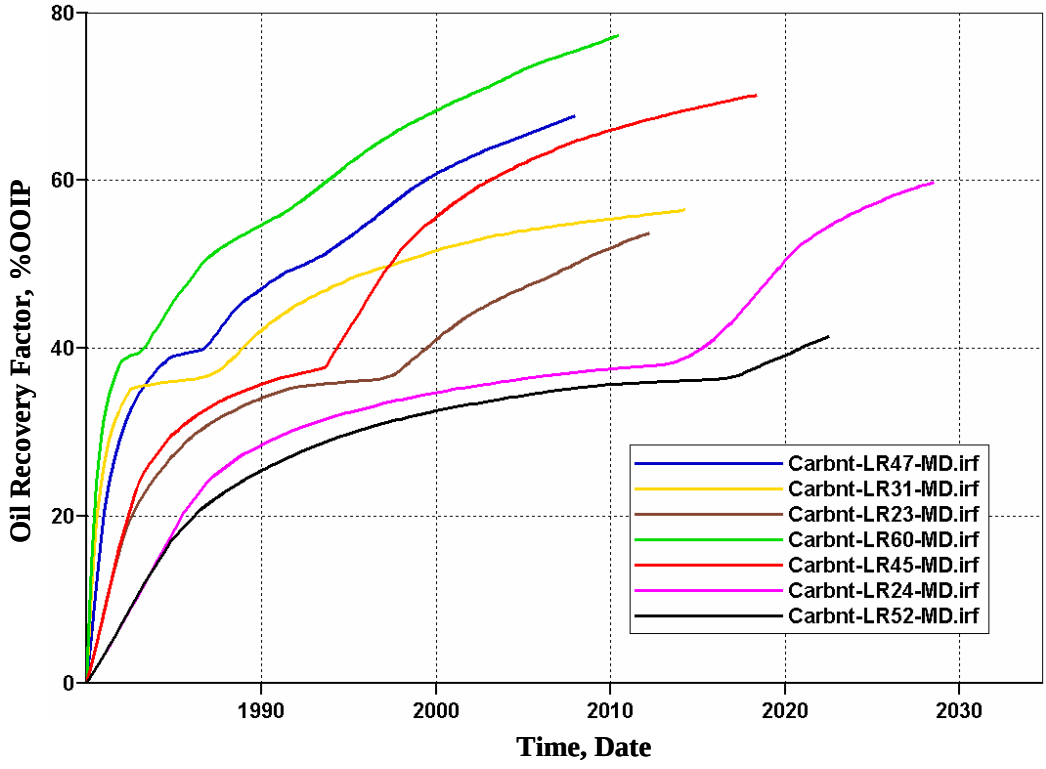

Figure 5.8- Oil recovery factor for some of the simulation cases

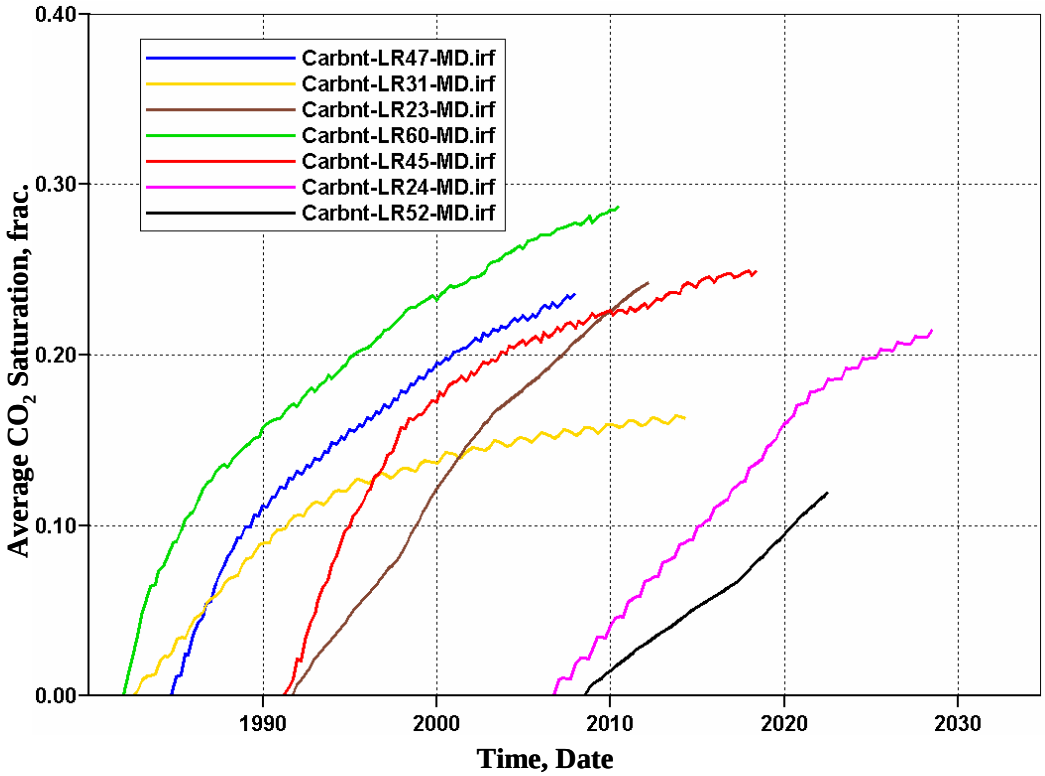

Figure 5.9- Average CO_2 saturation for some of the simulation cases

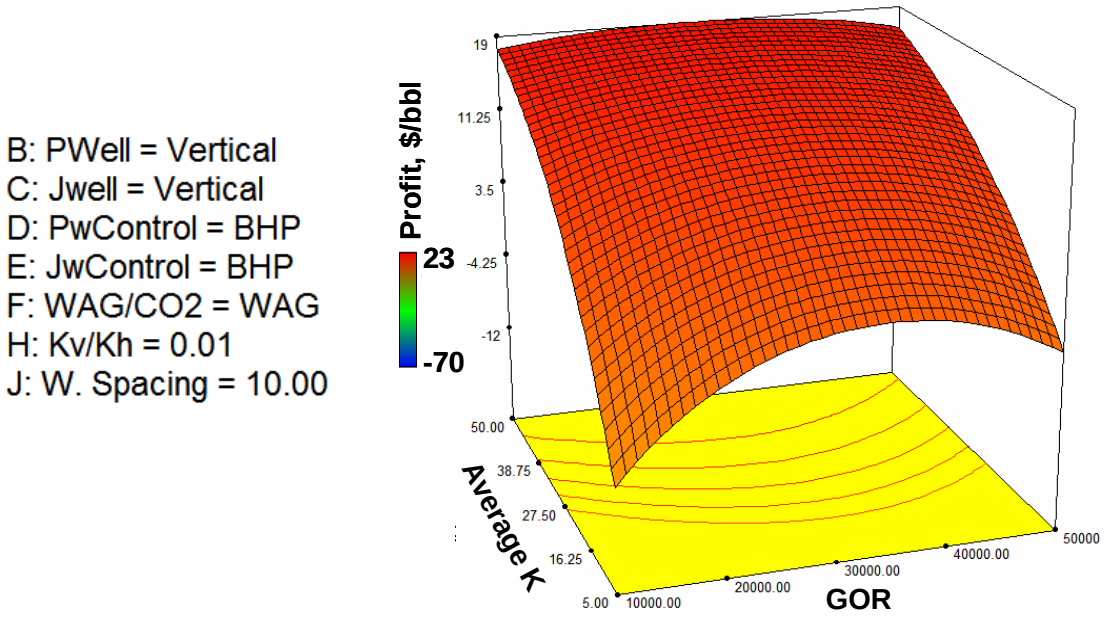

Figure 5.10- Response surface for profit objective at different GOR constraint and average reservoir permeability and constant values for other factors (shown in the left) in carbonate reservoirs

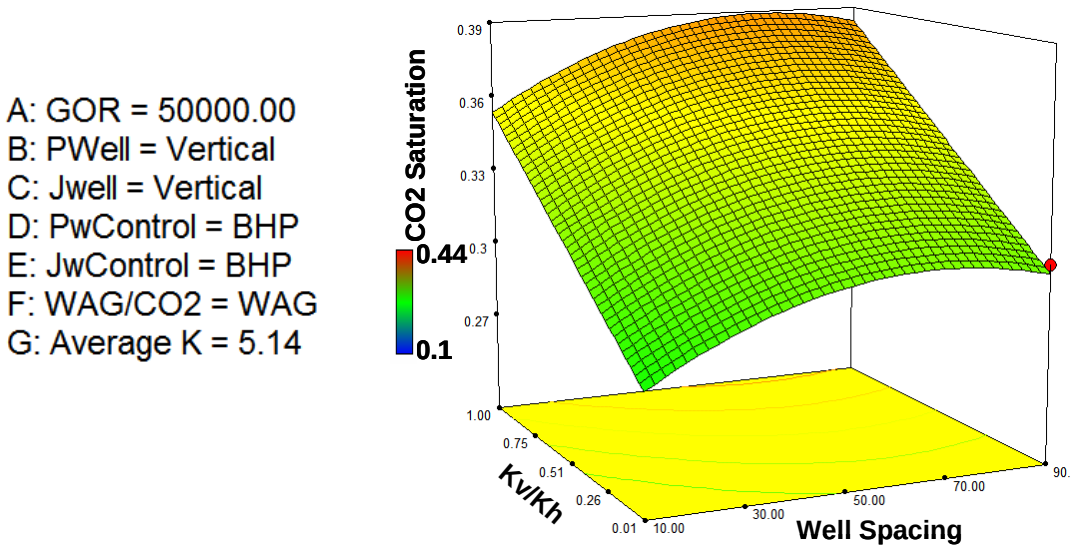

Figure 5.11- Response surface for storage objective at different well spacing and Kv/Kh ratio and constant values for other factors (shown in the left) in carbonate reservoirs

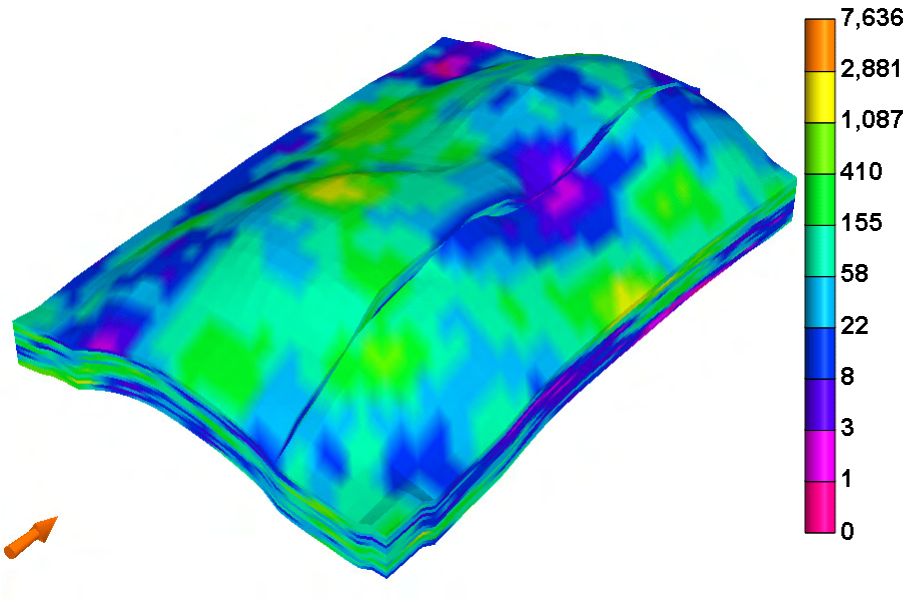

Figure 5.12- Three-dimensional view of sandstone reservoir geometry and its stochastic permeability distribution, for flood design sensitivity study

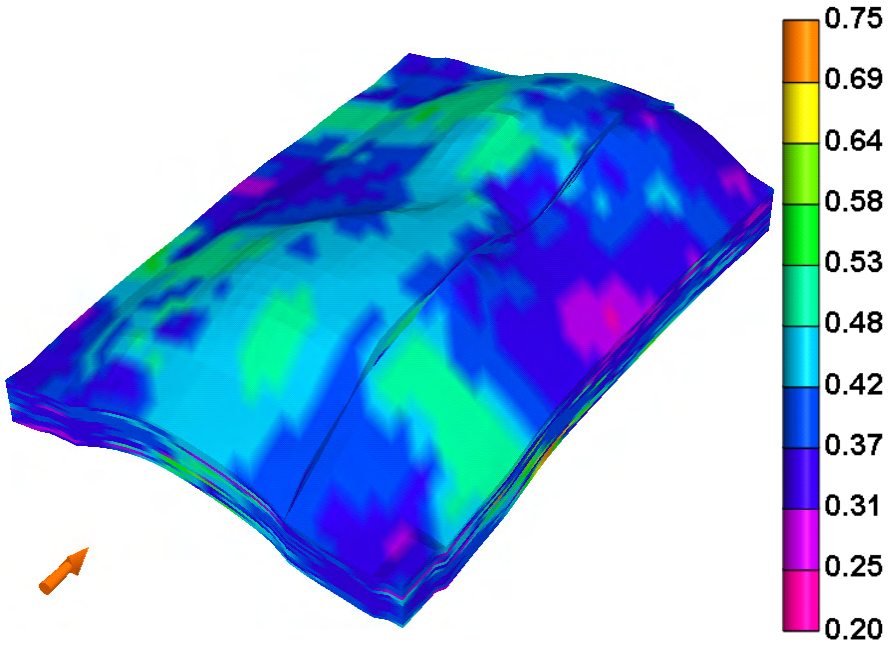

Figure 5.13- Three-dimensional view of remaining oil saturation at the end of water flooding for one of the sensitivity cases

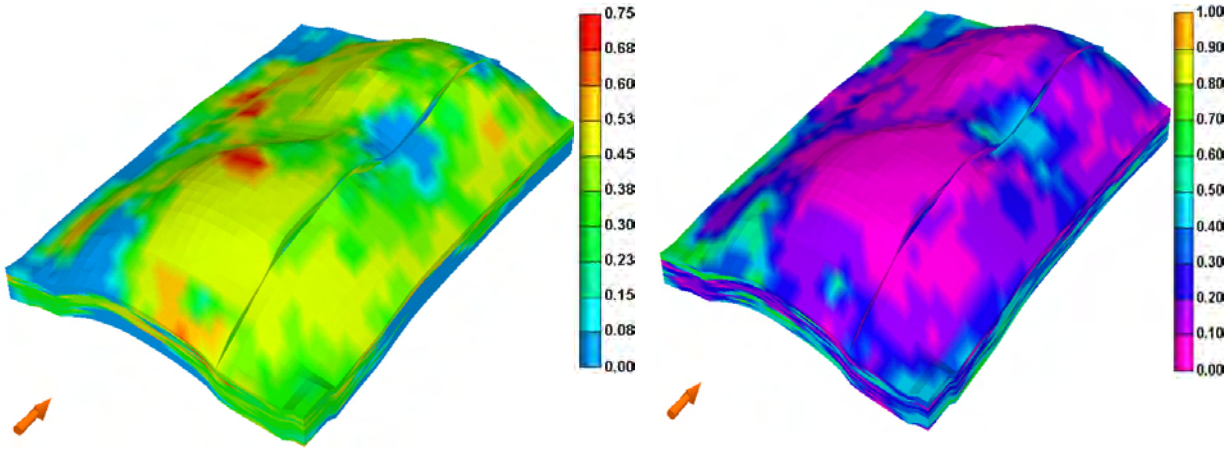

Figure 5.14- Remaining oil saturation (right) and CO_2 saturation (left) distributions at the end of one of CO_2 flooding simulation cases

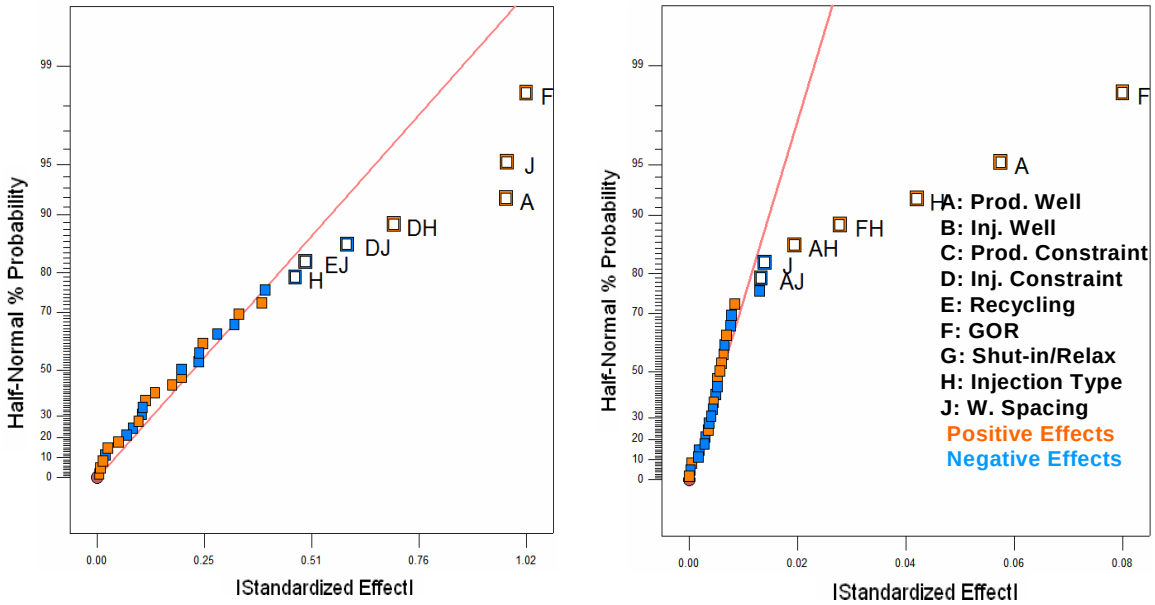

Figure 5.15- Statistically analyzed effect of all flood design factors on profit (left) and storage objective functions (right) with two-level factorial design

C: Rate Constraint
D: BHP Constraint
E: Re-sell CO2
F: High GOR Constr.
G: Yes (Shut-In/Open)
H: WAG Injection
J: Small well sapcing

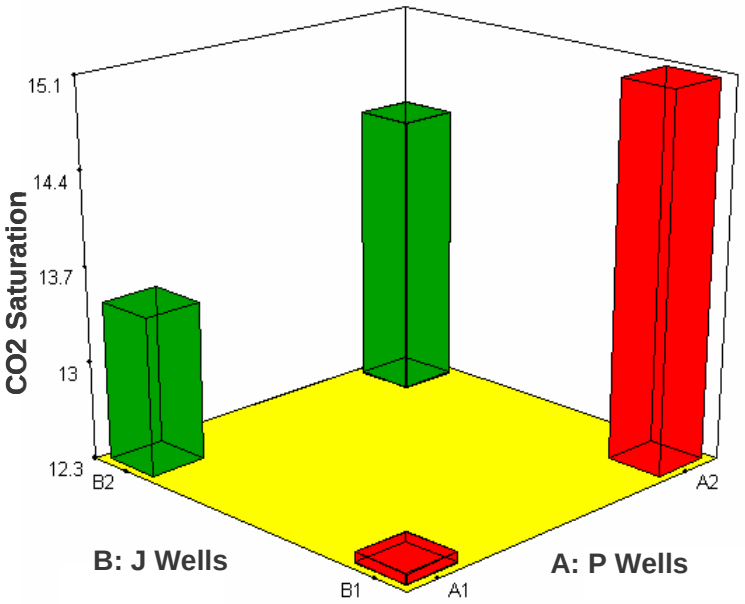

Figure 5.16- Response surface for storage objective at different injection and production well types and constant parameters for other design factors (shown in the left) in sandstone reservoirs

A: Horizontal well
B: Horizontal well
C: Rate Constraint
D: Rate Constraint
E: Re-Injection CO2
G: No (Shut-In/Open)
J: Large well spacing

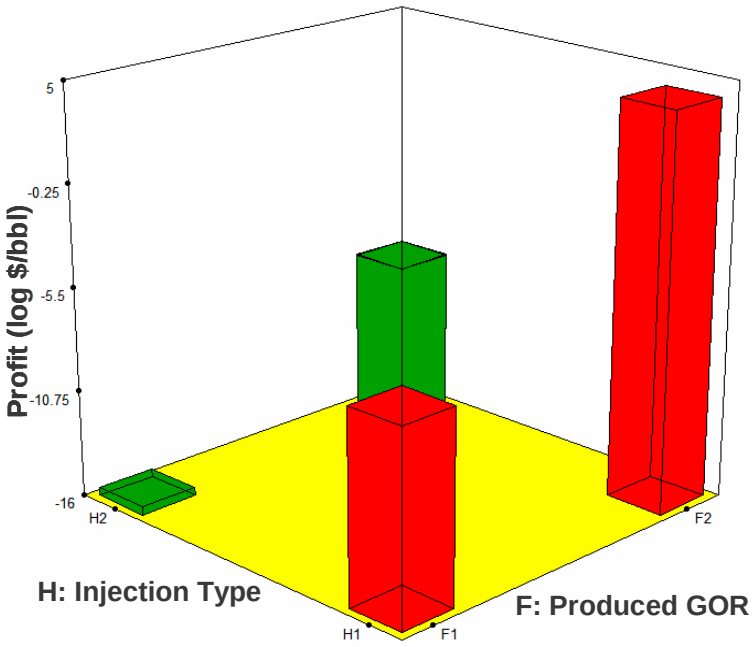

Figure 5.17- Response surface for profit objective at different produced GOR and injection scheme (WAG or continuous CO_2) and constant parameters for other design factors (shown in the left) in sandstone reservoirs

Chapter 6: Derivation of Dimensionless Scaling Groups for Miscible CO_2 Flooding

6.1 INTRODUCTION

In order to assess the capability and performance of a CO_2 flooding project (for enhanced oil recovery, sequestration, or both), dimensionless scaling groups can be utilized as an efficient tool to quickly monitor reservoirs with different sizes and different operating conditions. Then, the best possible scenarios can be employed to maximize any objective function. Dimensionless scaling groups are derived by applying different methods on the governing equations or variables for any processes. Inspectional analysis, which is one of these methods, involves non-dimensionalizing the equations that describe the physical process. Shook et al. (1992) used inspectional analysis to derive the dimensionless scaling groups for immiscible flow (water flooding) through permeable media. In this approach, the equations that describe the process (including the boundary conditions), are gathered and arbitrary scale factors are introduced and replace actual variables in the equations. The scale factors are then amassed into dimensionless groups in a way that the number of the final scaling groups is minimized. Defining arbitrary values for scale factors is somewhat subjective; they have to be assigned in a way that final dimensionless form of the equations would not be different than that of initial governing equations.

6.2 PROBLEM STATEMENT AND ASSUMPTIONS

This section describes methodology in deriving dimensionless scaling groups for CO_2 flooding displacement process in a three-dimensional porous media. Phase behavior relations have been entered in the derivations to achieve comprehensive scaling groups. Peng Robinson Equation of State (PR-EOS) and its auxiliary equations are considered as

governing formulation for the phase behavior section of derivations. Despite the large number of variables and parameters involve in this type of full field-scale processes, dimensional analysis reduces them substantially. Main assumptions for derivations are three-dimensional field scale geometry, three-pseudo components, as solvent (subscript 3), light-oil component (subscript 2), and heavy-oil component (subscript 4), three-phases, as water (subscript 1) oil (subscript 2) and gas (subscript 3), no chemical reactions, no adsorption, and no diffusion. Figure 6.1 shows schematic of reservoir geometry in this study. It is a dipping reservoir with dip angle of α. Sides as well as top and bottom of the reservoir are impermeable boundaries. Pure CO_2 is injected down-dip into the reservoir.

6.3 INSPECTIONAL ANALYSIS FOR MISCIBLE CO_2 FLOODING PROCESS

Miscible displacement of residual oil phase (subscript 2) by gas phase (subscript 3) which is considered as pure CO_2, following by water flooding is non-dimensionalized. Governing equations for these type of processes are conservation equations, Darcy's equations, capillary pressure equations, phase equilibrium equations and two auxiliary equations given below.

$$\frac{\partial}{\partial t}\phi\sum_{j=1}^{n_p} x_{ij}\rho_j S_j + \nabla\bullet\sum_{j=1}^{n_p} x_{ij}\rho_j \vec{u}_j - \nabla\bullet\phi\sum_{j=1}^{n_p}\overline{\overline{K}}_{ij}\cdot\nabla\rho_j x_{ij} = 0 \qquad i=1,...,n_c \qquad j=1,...,n_p \tag{6.1}$$

$$\vec{u}_j = -\frac{kk_{rj}}{\mu_j}(\nabla P_j + \rho_j \overrightarrow{g}) \qquad j=1,...,n_p \tag{6.2}$$

$$P_j - P_k = P_{ckj} = j(S)\sigma_{kj}\sqrt{\frac{\phi}{k}} \qquad j=1,...,n_p, \qquad k=1,...,n_p, \qquad k\neq j \tag{6.3}$$

$$K_i^{j,k} = \frac{C_{ij}}{C_{ik}} \qquad i=1,...,n_c, \qquad j=1,...,n_p, \qquad k=1,n_p, \qquad k\neq j \tag{6.4}$$

$$\sum_{i=1}^{n_c} x_{ij} = 1 \qquad i=1,...,n_c \qquad j=1,...,n_p \tag{6.5}$$

$$\sum_{j=1}^{n_p} S_j = 1 \qquad j = 1, ..., n_p \tag{6.6}$$

It should be noted that conservation equations are slightly modified in order to reduce the number of variables that have to be dealt with. In order to do this, $\rho_j x_{ij}$ (product of phase density and component mole fraction) was assumed to be C_{ij} which is the concentration of component i in phase j. Table 6.1 shows the equations and unknowns and their corresponding numbers entered in these equations. Figure 6.1 also shows the schematic describing the flooding process.

All flow equations constitute 29 parameters $(\rho_1, \rho_2, \rho_3, \mu_1, \mu_2, \mu_3, k_x, k_y, k_z, k_{r1}, k_{r2}, k_{r3}, \sigma_{21}, \sigma_{23}, S_{2r}, \alpha, g, \phi, j, p_{wf}, L, H, W, p_{inj}, u_{inj}, C_2^I, C_3^I, C_4^I, C_3^J)$ and 24 dependent variables $(C_{21}, C_{22}, C_{23}, C_{31}, C_{32}, C_{33}, C_{41}, C_{42}, C_{43}, S_1, S_2, S_3, P_1, P_2, P_3, u_{x1}, u_{x2}, u_{x3}, u_{z1}, u_{z2}, u_{z3}, u_{y1}, u_{y2}, u_{y3})$ which are affecting the CO_2 flooding process.

6.4 INTRODUCING ARBITRARY SCALING FACTORS

Two arbitrary scaling factors are introduced for each variable in the equations. In total, 56 scaling factors are introduced (corresponding to 28 original variables) in which 28 of them are additive and the rest are multiplicative scaling factors. Relationship between scale factors and original variables is considered as linear function. The original variables in the equations are then replaced with these scaling factors. Following linear transformations convert all of the original variables into dimensionless format. In all of these equations scaling parameters with "*" sign as superscript are considered as arbitrary scaling factors. In addition, variables with subscript "D" are final dimensionless variables that are going to replace dimensional variables.

$$C_{21} \equiv C^*_{212} C_{21D} + C^*_{211} \qquad S_1 \equiv S^*_{12} S_{1D} + S^*_{11} \qquad P_1 \equiv P^*_{12} P_{1D} + P^*_{11} \qquad u_{x1} \equiv u^*_{x12} u_{x1D} + u^*_{x11}$$

$$C_{22} \equiv C^*_{222} C_{22D} + C^*_{221} \qquad S_2 \equiv S^*_{22} S_{2D} + S^*_{21} \qquad P_2 \equiv P^*_{22} P_{2D} + P^*_{21} \qquad u_{x2} \equiv u^*_{x22} u_{x2D} + u^*_{x21}$$

$$C_{23} \equiv C^*_{232} C_{23D} + C^*_{231} \qquad S_3 \equiv S^*_{32} S_{3D} + S^*_{31} \qquad P_3 \equiv P^*_{32} P_{3D} + P^*_{31} \qquad u_{x3} \equiv u^*_{x32} u_{x3D} + u^*_{x31}$$

$$C_{31} \equiv C^*_{312} C_{31D} + C^*_{311} \qquad u_{z1} \equiv u^*_{z12} u_{z1D} + u^*_{z11}$$

$$C_{32} \equiv C^*_{322} C_{32D} + C^*_{321} \qquad u_{z2} \equiv u^*_{z22} u_{z2D} + u^*_{z21}$$

$$C_{33} \equiv C^*_{332} C_{33D} + C^*_{331} \qquad x \equiv x^*_2 x_D + x^*_1 \qquad u_{z3} \equiv u^*_{z32} u_{z3D} + u^*_{z31}$$

$$C_{41} \equiv C^*_{412} C_{41D} + C^*_{411} \qquad y \equiv y^*_2 y_D + y^*_1 \qquad u_{y1} \equiv u^*_{z12} u_{z1D} + u^*_{z11}$$

$$C_{42} \equiv C^*_{422} C_{42D} + C^*_{421} \qquad z \equiv z^*_2 z_D + z^*_1 \qquad u_{y1} \equiv u^*_{z12} u_{z1D} + u^*_{z11}$$

$$C_{43} \equiv C^*_{432} C_{43D} + C^*_{431} \qquad t \equiv t^*_2 t_D + t^*_1 \qquad u_{y1} \equiv u^*_{z12} u_{z1D} + u^*_{z11}$$

6.5 REPLACING DIMENSIONAL VARIABLES WITH SCALING FACTORS IN CONSERVATION EQUATIONS

By expanding the derivatives in each conservation equation, and then by entering scaling factors, their number will grow rapidly and it will be hard to handle all of the terms at the same time. Hence, it was decided to split the conservation equations into different terms and continue with each term separately and then lump the final results back into the original equation. Following is the general form for conservation equation considering all of the assumptions that were made at the beginning of our derivation.

$$\frac{\partial}{\partial t}\phi \sum_{j=1}^{n_p} C_{ij} S_j + \nabla \bullet \sum_{j=1}^{n_p} C_{ij} \vec{u}_j = 0 \qquad i = 1,...,n_c \qquad j = 1,...,n \tag{6.7}$$

Following are expanded version for Equation 6.7 for each component. For light oil component (subscript 2):

$$\begin{aligned} &\frac{\partial}{\partial t}(\phi C_{21} S_1 + \phi C_{22} S_2 + \phi C_{23} S_3) + \frac{\partial}{\partial x}(u_{1x} C_{21} + u_{2x} C_{22} + u_{3x} C_{23}) + \\ &\quad + \frac{\partial}{\partial y}(u_{1y} C_{21} + u_{2y} C_{22} + u_{3y} C_{23}) + \frac{\partial}{\partial z}(u_{1z} C_{21} + u_{2z} C_{22} + u_{3z} C_{23}) = 0 \end{aligned} \tag{6.8}$$

for gas, (CO_2), component (subscript 3):

$$\frac{\partial}{\partial t}(\phi C_{31}S_1 + \phi C_{32}S_2 + \phi C_{33}S_3) + \frac{\partial}{\partial x}(u_{1x}C_{31} + u_{2x}C_{32} + u_{3x}C_{33}) + \\ + \frac{\partial}{\partial y}(u_{1y}C_{31} + u_{2y}C_{32} + u_{3y}C_{33}) + \frac{\partial}{\partial z}(u_{1z}C_{31} + u_{2z}C_{32} + u_{3z}C_{33}) = 0 \tag{6.9}$$

and for heavy oil components (subscript 4):

$$\frac{\partial}{\partial t}(\phi C_{41}S_1 + \phi C_{42}S_2 + \phi C_{43}S_3) + \frac{\partial}{\partial x}(u_{1x}C_{41} + u_{2x}C_{42} + u_{3x}C_{43}) + \\ + \frac{\partial}{\partial y}(u_{1y}C_{41} + u_{2y}C_{42} + u_{3y}C_{43}) + \frac{\partial}{\partial z}(u_{1z}C_{41} + u_{2z}C_{42} + u_{3z}C_{43}) = 0 \tag{6.10}$$

According to the detailed derivations presented in Appendix A, the conservation equation for component 2 is converted into the following dimensionless form:

$$\frac{\partial}{\partial t_D}\left(C_{21D}S_{1D} + C_{22D}S_{2D} + C_{23D}S_{3D}\right) + \\ + \left[\frac{u_{x2}^* t_2^*}{\phi S_2^* x_2^*}\right]\frac{\partial}{\partial x_D}\left(u_{1xD}C_{21D} + u_{2xD}C_{22D} + u_{3xD}C_{23D}\right) + \\ + \left[\frac{u_{y2}^* t_2^*}{\phi S_2^* y_2^*}\right]\frac{\partial}{\partial y_D}\left(u_{1yD}C_{21D} + u_{2yD}C_{22D} + u_{3yD}C_{23D}\right) + \\ + \left[\frac{u_{z2}^* t_2^*}{\phi S_2^* z_2^*}\right]\frac{\partial}{\partial z_D}\left(u_{1zD}C_{21D} + u_{2zD}C_{22D} + u_{3zD}C_{23D}\right) = 0 \tag{6.11}$$

In a similar way, conservation equations for other two components, CO_2 (subscript 3) and heavy oil component (subscript 4), can be written as following:

$$\frac{\partial}{\partial t_D}\left(C_{31D}S_{1D}+C_{32D}S_{2D}+C_{33D}S_{3D}\right)+$$
$$+\left[\frac{u_{x2}^{*}t_2^{*}}{\phi S_2^{*}x_2^{*}}\right]\frac{\partial}{\partial x_D}\left(u_{1xD}C_{31D}+u_{2xD}C_{32D}+u_{3xD}C_{33D}\right)+$$
$$+\left[\frac{u_{y2}^{*}t_2^{*}}{\phi S_2^{*}y_2^{*}}\right]\frac{\partial}{\partial y_D}\left(u_{1yD}C_{31D}+u_{2yD}C_{32D}+u_{3yD}C_{33D}\right)+ \tag{6.12}$$
$$+\left[\frac{u_{z2}^{*}t_2^{*}}{\phi S_2^{*}z_2^{*}}\right]\frac{\partial}{\partial z_D}\left(u_{1zD}C_{31D}+u_{2zD}C_{32D}+u_{3zD}C_{33D}\right)=0$$

and for heavy oil component:

$$\frac{\partial}{\partial t_D}\left(C_{41D}S_{1D}+C_{42D}S_{2D}+C_{43D}S_{3D}\right)+$$
$$+\left[\frac{u_{x2}^{*}t_2^{*}}{\phi S_2^{*}x_2^{*}}\right]\frac{\partial}{\partial x_D}\left(u_{1xD}C_{41D}+u_{2xD}C_{42D}+u_{3xD}C_{43D}\right)+$$
$$+\left[\frac{u_{y2}^{*}t_2^{*}}{\phi S_2^{*}y_2^{*}}\right]\frac{\partial}{\partial y_D}\left(u_{1yD}C_{41D}+u_{2yD}C_{42D}+u_{3yD}C_{43D}\right)+ \tag{6.13}$$
$$+\left[\frac{u_{z2}^{*}t_2^{*}}{\phi S_2^{*}z_2^{*}}\right]\frac{\partial}{\partial z_D}\left(u_{1zD}C_{41D}+u_{2zD}C_{42D}+u_{3zD}C_{43D}\right)=0$$

6.6 REPLACING DIMENSIONAL VARIABLES WITH SCALING FACTORS IN DARCY'S EQUATIONS

For three-dimensional displacement of CO_2 injection with three phases present in the process, there are 9 Darcy's law equations.

$$u_{1x}=-\frac{k_x k_{r1}}{\mu_1}\left(\frac{\partial P_1}{\partial x}+\rho_1 g\sin\alpha\right) \tag{6.14}$$

$$u_{1y}=-\frac{k_y k_{r1}}{\mu_1}\left(\frac{\partial P_1}{\partial y}+\rho_1 g\cos\alpha\right) \tag{6.15}$$

$$u_{1z}=-\frac{k_z k_{r1}}{\mu_1}\left(\frac{\partial P_1}{\partial z}+\rho_1 g\cos\alpha\right) \tag{6.16}$$

$$u_{2x}=-\frac{k_x k_{r2}}{\mu_2}\left(\frac{\partial P_2}{\partial x}+\rho_2 g\sin\alpha\right) \tag{6.17}$$

$$u_{2y} = -\frac{k_y k_{r2}}{\mu_2}\left(\frac{\partial P_2}{\partial y} + \rho_2 g\right) \tag{6.18}$$

$$u_{2z} = -\frac{k_z k_{r2}}{\mu_2}\left(\frac{\partial P_2}{\partial z} + \rho_2 g\cos\alpha\right) \tag{6.19}$$

$$u_{3x} = -\frac{k_x k_{r3}}{\mu_3}\left(\frac{\partial P_3}{\partial x} + \rho_3 g\sin\alpha\right) \tag{6.20}$$

$$u_{3y} = -\frac{k_y k_{r3}}{\mu_3}\left(\frac{\partial P_3}{\partial y} + \rho_3 g\right) \tag{6.21}$$

$$u_{3z} = -\frac{k_z k_{r3}}{\mu_3}\left(\frac{\partial P_3}{\partial z} + \rho_3 g\cos\alpha\right) \tag{6.22}$$

According to the detailed derivations shown in Appendix A, Darcy equations are converted into the following dimensionless forms.

$$u_{1xD} = -\left[\frac{k_x k_{r1} P_{12}^*}{u_{1x2}^* \mu_1 x_2^*}\right]\left(\frac{\partial P_{1D}}{\partial x_D} + \left[\frac{x_2^* \rho_1 g\sin\alpha}{P_{12}^*}\right]\right) - \left[\frac{u_{1x1}^*}{u_{1x2}^*}\right] \tag{6.23}$$

$$u_{1yD} = -\left[\frac{k_y k_{r1} P_{12}^*}{u_{1y2}^* \mu_1 y_2^*}\right]\left(\frac{\partial P_{1D}}{\partial y_D} + \left[\frac{y_2^* \rho_1 g}{P_{12}^*}\right]\right) - \left[\frac{u_{1y1}^*}{u_{1y2}^*}\right] \tag{6.24}$$

$$u_{1zD} = -\left[\frac{k_z k_{r1} P_{12}^*}{u_{1z2}^* \mu_1 z_2^*}\right]\left(\frac{\partial P_{1D}}{\partial z_D} + \left[\frac{z_2^* \rho_1 g\cos\alpha}{P_{12}^*}\right]\right) - \left[\frac{u_{1z1}^*}{u_{1z2}^*}\right] \tag{6.25}$$

$$u_{2xD} = -\left[\frac{k_x k_{r2} P_{22}^*}{u_{2x2}^* \mu_2 x_2^*}\right]\left(\frac{\partial P_{2D}}{\partial x_D} + \left[\frac{x_2^* \rho_2 g\sin\alpha}{P_{22}^*}\right]\right) - \left[\frac{u_{2x1}^*}{u_{2x2}^*}\right] \tag{6.26}$$

$$u_{2yD} = -\left[\frac{k_y k_{r2} P_{22}^*}{u_{2y2}^* \mu_2 y_2^*}\right]\left(\frac{\partial P_{2D}}{\partial y_D} + \left[\frac{y_2^* \rho_2 g}{P_{22}^*}\right]\right) - \left[\frac{u_{2y1}^*}{u_{2y2}^*}\right] \tag{6.27}$$

$$u_{2zD} = -\left[\frac{k_z k_{r2} P_{22}^*}{u_{2z2}^* \mu_2 z_2^*}\right]\left(\frac{\partial P_{2D}}{\partial z_D} + \left[\frac{z_2^* \rho_2 g\cos\alpha}{P_{22}^*}\right]\right) - \left[\frac{u_{2z1}^*}{u_{2z2}^*}\right] \tag{6.28}$$

$$u_{3xD} = -\left[\frac{k_x k_{r3} P_{32}^*}{u_{3x2}^* \mu_3 x_2^*}\right]\left(\frac{\partial P_{3D}}{\partial x_D} + \left[\frac{x_2^* \rho_3 g\sin\alpha}{P_{32}^*}\right]\right) - \left[\frac{u_{3x1}^*}{u_{3x2}^*}\right] \tag{6.29}$$

$$u_{3yD} = -\left[\frac{k_y k_{r3} P_{32}^*}{u_{3y2}^* \mu_3 y_2^*}\right]\left(\frac{\partial P_{3D}}{\partial y_D} + \left[\frac{y_2^* \rho_3 g}{P_{32}^*}\right]\right) - \left[\frac{u_{3y1}^*}{u_{3y2}^*}\right] \tag{6.30}$$

$$u_{3xD} = -\left[\frac{k_z k_{r3} P_{32}^*}{u_{3z2}^* \mu_3 z_2^*}\right]\left(\frac{\partial P_{3D}}{\partial z_D} + \left[\frac{z_2^* \rho_3 g\cos\alpha}{P_{32}^*}\right]\right) - \left[\frac{u_{3z1}^*}{u_{3z2}^*}\right] \tag{6.31}$$

6.7 REPLACING DIMENSIONAL VARIABLES WITH SCALING FACTORS IN CAPILLARY PRESSURE EQUATIONS

For three-phase displacement of CO_2 injection, there are 2 capillary pressure equations as following:

$$P_2 - P_1 = P_{c21} = j(S)\sigma_{21}\sqrt{\frac{\phi}{k}} \tag{6.32}$$

$$P_3 - P_2 = P_{c32} = j(S)\sigma_{32}\sqrt{\frac{\phi}{k}} \tag{6.33}$$

After introducing the arbitrary scaling parameters in the equations 6.32 and 6.33 and then simplifying them, following dimensionless equations are resulted.

$$P_{2D} - \left[\frac{P_{12}^*}{P_{22}^*}\right]P_{1D} + \left[\frac{P_{21}^* - P_{11}^*}{P_{22}^*}\right] = j(S)\left[\frac{\sigma_{21}\sqrt{\frac{\phi}{k}}}{P_{22}^*}\right] \tag{6.34}$$

$$P_{3D} - \left[\frac{P_{22}^*}{P_{32}^*}\right]P_{2D} + \left[\frac{P_{31}^* - P_{21}^*}{P_{32}^*}\right] = j(S)\left[\frac{\sigma_{32}\sqrt{\frac{\phi}{k}}}{P_{32}^*}\right] \tag{6.35}$$

6.8 INITIAL AND BOUNDARY CONDITIONS

In order to solve all necessary equations for a CO_2 flooding displacement process, appropriate initial and boundary conditions are needed to achieve logical and comprehensive solutions. For three-dimensional, three-pseudo components, and three-phases displacement process of CO_2 injection, following are all of the initial and boundary conditions.

$$S_2 = S_{2r} \qquad at \qquad t = 0, \quad \forall \quad x, y, z \tag{6.36}$$

$$S_3 = 0 \qquad at \qquad t = 0, \quad \forall \quad x, y, z \tag{6.37}$$

Equations 6.36 and 6.37 denote the initial saturations for oil, which is assumed at residual after waterflooding, and gas saturation, which is assumed to be zero since reservoir is initially under-saturated.

$$C_{23} = C_{21} = 0 \qquad at \qquad t = 0, \quad \forall \quad x, y, z \tag{6.38}$$

$$C_{22} = C_2^I \qquad at \qquad t = 0, \quad \forall \quad x, y, z \tag{6.39}$$

$$C_{33} = C_{31} = 0 \qquad at \qquad t = 0, \quad \forall \quad x, y, z \tag{6.40}$$

$$C_{32} = C_3^I \qquad at \qquad t = 0, \quad \forall \quad x, y, z \tag{6.41}$$

$$C_{43} = C_{41} = 0 \qquad at \qquad t = 0, \quad \forall \quad x, y, z \tag{6.42}$$

$$C_{42} = C_4^I \qquad at \qquad t = 0, \quad \forall \quad x, y, z \tag{6.43}$$

Equations 6.38 through 6.43 show the initial conditions for all three components.

$$C_{33} = C_3^J \qquad at \qquad x = 0, \quad \forall \quad t, y, z \tag{6.44}$$

Equation 6.44 represents boundary conditions for CO_2 injection well, which is assumed as pure CO_2, in the gas form.

$$P_3 = P_2 = P_1 = P_{wf} + (\rho_j g \cos\alpha)(H - z) \qquad at \qquad x = L, \quad \forall \quad t, y, z \tag{6.45}$$

Equation 6.45 explains boundary settings for production well which is assumed under constant bottom hole pressure condition for all of the phases that are being produced.

$$u_{1z} = u_{2z} = u_{3z} = 0 \qquad at \qquad z = 0, \quad \forall \quad x, y, t \tag{6.46}$$

$$u_{1z} = u_{2z} = u_{3z} = 0 \qquad at \qquad z = H, \quad \forall \quad x, y, t \tag{6.47}$$

$$u_{1y} = u_{2y} = u_{3y} = 0 \qquad at \qquad y = 0, \quad \forall \quad x, z, t \tag{6.48}$$

$$u_{1y} = u_{2y} = u_{3y} = 0 \qquad at \qquad y = W, \quad \forall \quad x, z, t \tag{6.49}$$

$$u_{1x} = u_{2x} = u_{3x} = 0 \qquad at \qquad x = 0, \quad \forall \quad y, z, t \tag{6.50}$$

$$u_{1x} = u_{2x} = u_{3x} = 0 \qquad at \qquad x = L, \quad \forall \quad y, z, t \tag{6.51}$$

Equations 6.46 through 6.51 correspond to no flow boundary conditions in all for sides of the reservoir.

$$\frac{1}{W}\int_0^W \left(\frac{1}{H}\int_0^H u_{3x} dz \right) dy = u_{inj} \qquad at \qquad x = 0, \quad \forall \quad y, z, t \tag{6.52}$$

Equations 6.52 show the boundary settings for the injection well, which is assumed under constant injection rate.

Arbitrary scaling factors are entered into equations 6.36 through 6.53 and resulted equations are simplified and rearranged. Details of derivations are shown in Appendix A.

6.9 SATURATION AND CONCENTRATIONS CONSTRAINTS

It is one of the main and imperative principles in any flow and phase behavior calculations that saturations and concentrations should sum to one in the whole system. These two principles are usually coupled and lumped in the major calculations (when actually solving them), and they get embedded in those calculations. Since these equations are not actually solved in the process of deriving dimensionless scaling groups, these two basic principles should be presented separately. These equations are shown in Appendix A. Arbitrary scaling factors are introduced in these equations as well. Details of derivations for this section are shown in Appendix A.

6.10 PHASE EQUILIBRIUM EQUATIONS

An extensive amount of calculations in the compositional simulations of gas flooding-type of displacements are carried out to solve auxiliary phase behavior equations. Among all simulators, two type of approaches are considered; Equation of State (EOS) computations or partitioning coefficient calculations. In non-dimensionalizing phase behavior part of the equations, partitioning coefficient approach

did not provide any additional scaling groups. One reason for this would be dimensionless nature of partitioning coefficients. It should be noted that these coefficients provide approximate solutions for phase behavior model but more rigorous method would be utilizing EOS approach. Therefore, it was decided to use Peng-Robinson EOS in our derivations.

Equation (6.54) shows the original form of Peng-Robinson EOS. Phase behavior equations constitute of 12 parameters $(R, a, b, c, c', c'', \alpha, \omega, T_c, P_c, V_c, Z_c)$ and 3 independent variables (T, P, V) and are being utilized to supplement flow equations in order to model the CO_2 flooding process.

$$P = \frac{RT}{V-b} - \frac{a(T)}{(V+c)(V+2c+b)+(b+c)(V-b)} \tag{6.54}$$

where

$$a(T) = 0.45724\frac{R^2T_c^2}{P_c}\alpha(T) \qquad and \qquad b = 0.07780\frac{RT_c}{P_c}$$
$$\sqrt{\alpha} = 1+k\left(1-\sqrt{\frac{T}{T_c}}\right) \qquad and \qquad k = 0.37464+1.54226\omega-0.26992\omega^2 \tag{6.55}$$

$$c = c' + c''\left(T - 288.15\right)$$

where

(6.59)

$$c' = 0.40768\frac{RT_c}{P_c}\left(0.29441 - Z_{RA}\right)$$
$$Z_{RA} = 0.29056 - 0.08775\omega$$

Also c which is volume shift translation is defined in the Equation 6.59. It is the temperature dependent volume correction parameter and is found as the difference

between the molar volume at 80 °C given by the ASTM 1250-80 density correlation, and the Peneloux molar volume for the same temperature for any component.

It is observed that Equation 6.54 is in dimensional form. In order to convert this auxiliary equation, for CO2 flooding displacement process, into the dimensionless form similar approach to the inspectional analysis is taken. Reduced form of Peng-Robinson Equation of State (PR-EOS) would be ideal scaled equation for this purpose. In order to do this, equations 6.55 and 6.56 are substituted into the equation 6.54. Details are given in Appendix A. Comparing reduced forms of temperature, pressure, and molar volume, shown in Equation 6.57, with arbitrary scaling parameters for the same variables, shown in equation 6.58, denotes that reduced form of these variables are in fact modified form of arbitrary scaling factors and our approach, to derive the dimensionless EOS, is indeed modified version of the inspectional analysis approach; it just should be noted that since T_1^*, P_1^*, and V_1^* are arbitrary scaling factors, they can be set to zero; and in addition we can set $T_2^* = T_c$, $P_2^* = P_c$, and $V_2^* = V_c$; hence:

$$T_r = \frac{T}{T_c} \qquad P_r = \frac{P}{P_c} \qquad V_r = \frac{V}{V_c} \tag{6.57}$$

$$T = T_2^* T_D + T_1^* \qquad P = P_2^* P_D + P_1^* \qquad V = V_2^* V_D + V_1^* \tag{6.58}$$

After detailed derivations, presented in Appendix A, Equation 6.59 is the final form of dimensionless EOS. It can be used along with other dimensionless equations to scale the CO2 flooding displacement process. Three scaling groups, reduced temperature (T_r), reduced pressure (P_r), along with acentric factor, which is embedded in the definition of "*k*" in Equation 6.55, are three main scaling parameters which were derived from EOS as an auxiliary equations for CO_2 flooding displacement process. Since there are 3 components present in our assumed system, and three scaling groups are introduced

from phase behavior calculations therefore, 9 scaling groups should be considered for phase behavior segment of the equations.

$$\left[P_r + \frac{\Omega_a \sqrt{1+k\left(1-\sqrt{T_r}\right)}}{\left(Z\frac{T_r}{P_r}\right)^2\left(1+\frac{\Omega_b}{Z}\frac{P_r}{T_r}\right)+\Omega_b\frac{ZT_r}{P_r}\left(1-\frac{\Omega_b}{Z}\frac{P_r}{T_r}\right)}\right](Z\frac{T_r}{P_r}-\Omega_b)=T_r \qquad (6.59)$$

6.11 DIMENSIONLESS EQUATIONS

Based on this major principle that non-dimensionalizing must not change the form of the equations (Shook et al., 1992) and according to the assumptions that are made on arbitrary scaling factors, aforementioned dimensional equations are simplified to obtain following final dimensionless equations. Simplification approach is presented in Appendix A with more detail.

Conservation Equations:

$$\begin{aligned}&\frac{\partial}{\partial t_D}\left(C_{21D}S_{1D}+C_{22D}S_{2D}+C_{23D}S_{3D}\right)\\&\quad+\frac{\partial}{\partial x_D}\left(u_{1xD}C_{21D}+u_{2xD}C_{22D}+u_{3xD}C_{23D}\right)\\&\quad\quad+\frac{\partial}{\partial y_D}\left(u_{1yD}C_{21D}+u_{2yD}C_{22D}+u_{3yD}C_{23D}\right)\\&\quad\quad\quad+\frac{\partial}{\partial z_D}\left(u_{1zD}C_{21D}+u_{2zD}C_{22D}+u_{3zD}C_{23D}\right)=0\end{aligned} \qquad (6.60)$$

$$\begin{aligned}&\frac{\partial}{\partial t_D}\left(C_{31D}S_{1D}+C_{32D}S_{2D}+C_{33D}S_{3D}\right)+\\&\quad+\frac{\partial}{\partial x_D}\left(u_{1xD}C_{31D}+u_{2xD}C_{32D}+u_{3xD}C_{33D}\right)\\&\quad\quad+\frac{\partial}{\partial y_D}\left(u_{1yD}C_{31D}+u_{2yD}C_{32D}+u_{3yD}C_{33D}\right)\\&\quad\quad\quad+\frac{\partial}{\partial z_D}\left(u_{1zD}C_{31D}+u_{2zD}C_{32D}+u_{3zD}C_{33D}\right)=0\end{aligned} \qquad (6.61)$$

$$\frac{\partial}{\partial t_D}\left(C_{41D}S_{1D}+C_{42D}S_{2D}+C_{43D}S_{3D}\right)+$$
$$+\frac{\partial}{\partial x_D}\left(u_{1xD}C_{41D}+u_{2xD}C_{42D}+u_{3xD}C_{43D}\right)$$
$$+\frac{\partial}{\partial y_D}\left(u_{1yD}C_{41D}+u_{2yD}C_{42D}+u_{3yD}C_{43D}\right) \tag{6.62}$$
$$+\frac{\partial}{\partial z_D}\left(u_{1zD}C_{41D}+u_{2zD}C_{42D}+u_{3zD}C_{43D}\right)=0$$

Darcy's Equations:

$$u_{1xD}=-\left(\frac{\partial P_{1D}}{\partial x_D}+\frac{k_x\lambda^{\circ}_{r1}\rho_1 g\sin\alpha}{u_{inj}}\right) \tag{6.63}$$

$$u_{1yD}=-\left(\frac{k_y}{k_x}\frac{L^2}{W^2}\right)\left(\frac{\partial P_{1D}}{\partial y_D}+\left[\frac{k_x\lambda^{\circ}_{r1}\rho_1 g}{u_{inj}}\frac{W}{L}\right]\right) \tag{6.64}$$

$$u_{1zD}=-\left(\frac{k_z}{k_x}\frac{L^2}{H^2}\right)\left(\frac{\partial P_{1D}}{\partial z_D}+\left[\frac{k_x\lambda^{\circ}_{r1}\rho_1 g\cos\alpha}{u_{inj}}\frac{H}{L}\right]\right) \tag{6.65}$$

$$u_{2xD}=-\left(\frac{\partial P_{2D}}{\partial x_D}+\left[\frac{k_x\lambda^{\circ}_{r2}\rho_2 g\sin\alpha}{u_{inj}}\right]\right) \tag{6.66}$$

$$u_{2yD}=-\left(\frac{k_y}{k_x}\frac{L^2}{W^2}\right)\left(\frac{\partial P_{2D}}{\partial y_D}+\left[\frac{k_x\lambda^{\circ}_{r2}\rho_2 g}{u_{inj}}\frac{W}{L}\right]\right) \tag{6.67}$$

$$u_{2zD}=-\left(\frac{k_z}{k_x}\frac{L^2}{H^2}\right)\left(\frac{\partial P_{2D}}{\partial z_D}+\left[\frac{k_x\lambda^{\circ}_{r2}\rho_2 g\cos\alpha}{u_{inj}}\frac{H}{L}\right]\right) \tag{6.68}$$

$$u_{3xD}=-\left(\frac{\partial P_{3D}}{\partial x_D}+\left[\frac{k_x\lambda^{\circ}_{r3}\rho_3 g\sin\alpha}{u_{inj}}\right]\right) \tag{6.69}$$

$$u_{3yD}=-\left(\frac{k_y}{k_x}\frac{L^2}{W^2}\right)\left(\frac{\partial P_{3D}}{\partial y_D}+\left[\frac{k_x\lambda^{\circ}_{r3}\rho_3 g}{u_{inj}}\frac{W}{L}\right]\right) \tag{6.70}$$

$$u_{3zD}=-\left(\frac{k_z}{k_x}\frac{L^2}{H^2}\right)\left(\frac{\partial P_{3D}}{\partial z_D}+\left[\frac{k_x\lambda^{\circ}_{r3}\rho_3 g\cos\alpha}{u_{inj}}\frac{H}{L}\right]\right) \tag{6.71}$$

Capillary Pressure Equations:

$$P_{2D} - \left(\frac{\lambda^{\circ}_{r3}}{\lambda^{\circ}_{r1}}\right) P_{1D} = j(S)\left(\frac{\sigma_{21} k_x \lambda^{\circ}_{r2} \sqrt{\frac{\phi}{k_x}}}{u_{inj}.L}\right) \tag{6.72}$$

$$P_{3D} - \left(\frac{\lambda^{\circ}_{r3}}{\lambda^{\circ}_{r2}}\right) P_{2D} = j(S)\left(\frac{\sigma_{32} k_x \lambda^{\circ}_{r3} \sqrt{\frac{\phi}{k_x}}}{u_{inj}.L}\right) \tag{6.73}$$

Initial and Boundary Conditions:

$$S_{2D} = 1 \qquad at \qquad t_D = 0 \ \ \forall \ \ x_D, y_D, z_D \tag{6.74}$$

$$C_{21D} = C_{23D} = 0 \qquad at \qquad t_D = 0 \ \ \forall \ \ x_D, y_D, z_D \tag{6.75}$$

$$C_{22D} = \left[\frac{C_2^I}{C_3^J}\right] \qquad at \qquad t_D = 0 \ \ \forall \ \ x_D, y_D, z_D \tag{6.76}$$

$$C_{31D} = C_{33D} = 0 \qquad at \qquad t_D = 0 \ \ \forall \ \ x_D, y_D, z_D \tag{6.77}$$

$$C_{32D} = \left[\frac{C_3^I}{C_3^J}\right] \qquad at \qquad t_D = 0 \ \ \forall \ \ x_D, y_D, z_D \tag{6.78}$$

$$C_{41D} = C_{43D} = 0 \qquad at \qquad t_D = 0 \ \ \forall \ \ x_D, y_D, z_D \tag{6.79}$$

$$C_{42D} = \left[\frac{C_4^I}{C_3^J}\right] \qquad at \qquad t_D = 0 \ \ \forall \ \ x_D, y_D, z_D \tag{6.80}$$

$$C_{33D} = 1 \qquad at \qquad x_D = 0 \ \ \forall \ \ y_D, z_D, t_D \tag{6.81}$$

$$P_{1D} = \left[\frac{k_x \lambda^{\circ}_{r1} \rho_1 g \cos\alpha}{u_{inj}} \frac{H}{L}\right](1 - z_D) \qquad at \qquad x_D = 1, \ \ \forall \ \ z_D, t_D \tag{6.82}$$

$$P_{2D} = \left[\frac{k_x \lambda^{\circ}_{r2} \rho_2 g \cos\alpha}{u_{inj}} \frac{H}{L}\right](1 - z_D) \qquad at \qquad x_D = 1, \ \ \forall \ \ z_D, t_D \tag{6.83}$$

$$P_{3D} = \left[\frac{k_x \lambda^{\circ}_{r3} \rho_3 g \cos\alpha}{u_{inj}} \frac{H}{L}\right](1 - z_D) \qquad at \qquad x_D = 1, \ \ \forall \ \ z_D, t_D \tag{6.84}$$

$$u_{1zD} = u_{2zD} = u_{3zD} = 0 \qquad at \qquad z_D = 0 \ \ \forall \ \ x_D, y_D, t_D \tag{6.85}$$

$$u_{1zD} = u_{2zD} = u_{3zD} = 0 \qquad at \qquad z_D = 1 \;\; \forall \;\; x_D, y_D, t_D \tag{6.86}$$

$$u_{1yD} = u_{2yD} = u_{3yD} = 0 \qquad at \qquad y_D = 0 \;\; \forall \;\; x_D, z_D, t_D \tag{6.87}$$

$$u_{1yD} = u_{2yD} = u_{3yD} = 0 \qquad at \qquad y_D = 1 \;\; \forall \;\; x_D, z_D, t_D \tag{6.88}$$

$$u_{1xD} = u_{2xD} = u_{3xD} = 0 \qquad at \qquad x_D = 0 \;\; \forall \;\; y_D, z_D, t_D \tag{6.89}$$

$$u_{1xD} = u_{2xD} = u_{3xD} = 0 \qquad at \qquad x_D = 1 \;\; \forall \;\; y_D, z_D, t_D \tag{6.90}$$

$$\int_0^1 \left(\int_0^1 u_{3xD} dz_D \right) dy_D = 1 \qquad at \qquad x_D = 0 \;\; \forall \;\; y_D, z_D, t_D \tag{6.91}$$

Saturation and Concentrations Constraints:

$$S_{1D} + S_{2D} + S_{3D} = 1 \tag{6.92}$$

$$C_{21D} + C_{31D} + C_{41D} = 1 \tag{6.93}$$

$$C_{22D} + C_{32D} + C_{42D} = 1 \tag{6.94}$$

$$C_{23D} + C_{33D} + C_{43D} = 1 \tag{6.95}$$

Phase Behavior Equation:

$$\left[P_r + \frac{\Omega_a \sqrt{1 + k\left(1 - \sqrt{T_r}\right)}}{\left(Z \frac{T_r}{P_r} \right)^2 \left(1 + \frac{\Omega_b}{Z} \frac{P_r}{T_r} \right) + \Omega_b \frac{Z T_r}{P_r} \left(1 - \frac{\Omega_b}{Z} \frac{P_r}{T_r} \right)} \right] \left(Z \frac{T_r}{P_r} - \Omega_b \right) = T_r \tag{6.96}$$

Terms presented inside the brackets in Equations 6.63 through 6.96 are initial scaling groups. These twenty eight scaling groups completely satisfy the scaling requirements for three-dimensional, three-phase, and three-component problem. But yet,

they are not independent of each other and additional steps should be taken to make them independent.

6.12 FINAL DIMENSIONLESS SCALING GROUPS

In addition to the scaling groups that have been developed for CO_2 flooding process, if injection and production wells were set to constant bottom hole pressure constraint, following two new boundary conditions should be introduced to the system of equations that were being dealt with:

$$P_3 = P_{T_j} = P_{inj} \qquad at \qquad x = 0 \quad \forall \quad y, z, t \tag{6.97}$$

$$P_{T_p} = P_p \qquad at \qquad x = L \quad \forall \quad y, z, t \tag{6.98}$$

In which P_{T_j} and P_{Tp} are injection and production pressures, respectively. After introducing arbitrary scaling factors in Equations 6.97 and 6.98 and rearranging them, we have:

$$P_{T_j D} = \left[\frac{P_{inj} - P^*_{T_j 1}}{P^*_{T_j 2}} \right] \qquad at \qquad x_D = -\left[\frac{x^*_1}{x^*_2} \right] \quad \forall \quad y_D, z_D, t_D \tag{6.99}$$

$$P_{T_p D} = \left[\frac{P_P - P^*_{T_p 1}}{P^*_{T_p 2}} \right] \qquad at \qquad x_D = \left[\frac{L - x^*_1}{x^*_2} \right] \quad \forall \quad y_D, z_D, t_D \tag{6.100}$$

Since scaling factors are arbitrary, we can set $P^*_{T_p 1}$ and $P^*_{T_j 1}$ equal to zero and put $P^*_{T_p 2} = P^*_{T_j 2}$ and assume minimum miscibility pressure as reference for non-dimensionalizing of these scaling factors; therefore $P^*_{T_p 2} = P^*_{T_j 2} = P_{MMP}$; hence:

$$G_{22} = \frac{P_{inj}}{P_{MMP}}$$

and (6.101)

$$G_{23} = \frac{P_P}{P_{MMP}}$$

Finally, according to the detailed derivations which are presented in Appendix A, the number of final scaling groups was minimized to 13. These groups correspond to flow equations. Three dimensionless groups also were derived from equation of state. Followings are total 16 scaling groups derived from all of the governing equations for CO_2 flooding displacement. Superscript "f" stands for final scaling groups.

$$G_1^f = \frac{k_z}{k_x}\frac{L^2}{H^2}$$

$$G_2^f = \frac{k_y}{k_x}\frac{L^2}{W^2}$$

$$G_3^f = \frac{1}{G_3} = \frac{\lambda_{r1}^{\circ}}{\lambda_{r2}^{\circ}}$$

$$G_4^f = \frac{1}{G_4} = \frac{\lambda_{r2}^{\circ}}{\lambda_{r3}^{\circ}}$$

$$G_5^f = \frac{\sigma_{21} k_x \lambda_{r2}^{\circ} \sqrt{\frac{\phi}{k_x}}}{u_{inj}.L}$$

$$G_6^f = \frac{\sigma_{32} k_x \lambda_{r3}^{\circ} \sqrt{\frac{\phi}{k_x}}}{u_{inj}.L}$$

$$G_7^f = \frac{H}{L}\tan\alpha$$

$$G_8^f = \frac{\Delta\rho_{32}}{\Delta\rho_{13}}$$

$$G_9^f = \frac{k_x \lambda_{r2}^{\circ} \Delta\rho_{32} g \cos\alpha}{u_{inj}}\frac{H}{L}$$

$$G_{10}^f = \frac{k_x \lambda_{r2}^{\circ} \Delta\rho g \cos\alpha}{u_{inj}}\frac{H}{L}$$

$$G_{11}^{f} = \frac{C_2^I}{C_3^J}$$

$$G_{12}^{f} = \frac{C_3^I}{C_3^J}$$

$$G_{13}^{f} = \frac{C_4^I}{C_3^J}$$

and EOS-related scaling groups are:

$$G_{14}^{f} = \frac{P}{P_{ci}}$$

$$G_{15}^{f} = \frac{T}{T_{ci}}$$

$$G_{16}^{f} = \omega_i$$

Alternate scaling groups when CO_2 flooding is performed under bottom hole pressure constraint:

$$\overline{G_{17}^{f}} = \frac{P_{inj}}{P_{MMP}}$$

$$\overline{G_{18}^{f}} = \frac{P_P}{P_{MMP}}$$

6.13 SUMMARY AND CONCLUSIONS

Inspectional analysis approach was applied to derive the dimensionless scaling groups for CO2 flooding process in a three-dimensional, three-phase, and three-pseudo component system. The governing flow equations constitute of 29 parameters and 24 dependent variables. Phase behavior relations have also been entered in the derivations to achieve comprehensive scaling groups. Peng Robinson Equation of State (PR-EOS) and its auxiliary equations are considered as governing formulation for the phase behavior section of derivation. After deriving dimensionless groups, algebraic operations were utilized on the final coefficient matrix to minimize the number of final scaling groups.

Results show that, 17 dimensionless groups is needed to scale a CO2 flooding process in any porous media. Fourteen scaling groups are related to flow equation and the other three groups are the ones that derived from phase behavior equations. It should also be noted that if injection process is carried out under bottom hole pressure constraint, rather than under rate control, $\overline{G_{17}^{f}}$ and $\overline{G_{18}^{f}}$ also should be considered to scale the process.

Table 6.1: Equations and unknowns governing CO_2 flooding process

Equation	Number of Equations	Unknowns	Number of Unknowns
Conservation	$(N_c)=3$	$(C_{21}, C_{22}, C_{23}, C_{31}, C_{32}, C_{33}, C_{41}, C_{42}, C_{43})$	$(N_p \times N_c)=9$
Phase Equilibrium	$N_c \times (N_p-1)=6$	(S_1, S_2, S_3)	$(N_p)=3$
Capillary Pressure	$(N_p-1)=2$	(P_1, P_2, P_3)	$(N_p)=3$
Darcy's law	$(N_p \times N_D)=9$	$(u_{x1}, u_{x2}, u_{x3}, u_{z1}, u_{z2}, u_{z3}, u_{y1}, u_{y2}, u_{y3})$	$(N_p \times N_D)=9$
Saturations Sum to 1	1		
Compositions Sum to 1	$(N_p)=3$		

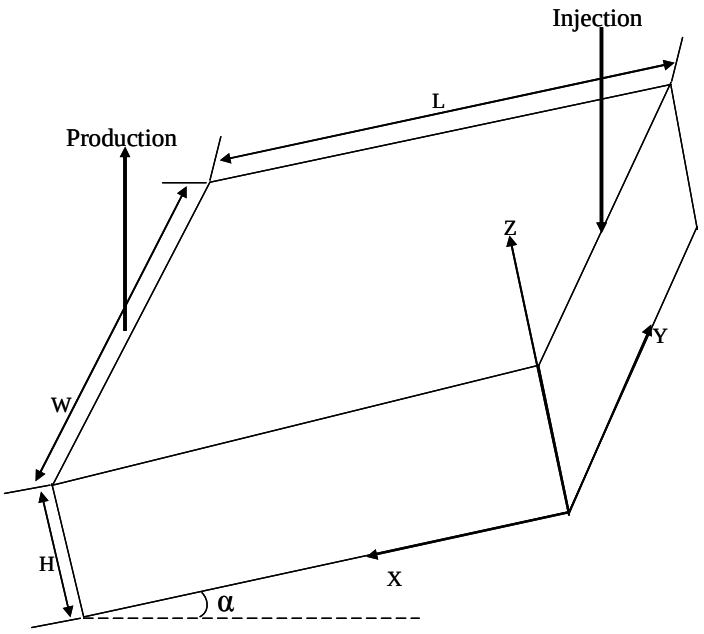

Figure 6.1- Schematic view of the displacement process and media geometry

Chapter 7: Development of a Response Surfaces-Based MMP Correlation

7.1 INTRODUCTION

Miscible CO_2 flooding is one of the most efficient displacement processes among the tertiary oil recovery methods. Based on a study by Stosur et al. (1990), on future potential of Enhanced Oil Recovery (EOR) methods in the US, miscible CO_2 gas injection is gaining more popularity and eventually will be more attractive than any other EOR techniques. This can be related to higher oil prices as well as availability of more CO_2 sources considering the global regulations and restrictions on CO_2 emissions. In a CO_2 displacement project, when full miscibility between injected CO_2 and reservoir fluid is reached, capillary forces are eliminated from displacement process which ideally results in no oil trapping and consequently higher recovery values. Difference between reservoir pressure (or displacement pressure) and Minimum Miscibility Pressure (MMP) is the most important factor to determine whether miscibility has bee achieved in the reservoir. Displacement pressure should be completely higher than MMP in order to achieve miscibility in the reservoir.

Miscibility in reservoir conditions is generally achieved by two different mechanisms. When the injected fluid and reservoir crude become fully miscible or in other word, First Contact Miscible (FCM) conditions are achieved, a single phase fluid is created and therefore, injected fluid completely displaces the reservoir fluid. One of the most obvious cases for this type of miscibility conditions is FCM of Butane with some crude oils at reservoir conditions. Other type of miscibility mechanism is called multiple contact miscible displacement. Carbon dioxide generally makes multiple contact miscibility with crude oils at some reservoir conditions. This means that many contacts are necessary (in the form of mass transfer) for crude oil components and CO_2 to be

mixed with each other. In these contacts, CO_2 starts first to be condensed into the reservoir oil and then light oil components are vaporized into the CO_2-rich phases. This continues until there is no interfacial tension between these two new phases and a single hydrocarbon phase is being produced. This process mainly depends on reservoir pressure since reservoir temperature is considered constant in the CO_2 flooding processes. As reservoir pressure increases, more CO_2 is dissolved in the oil and more oil components are vaporized by oil. It is known that the extraction of hydrocarbons depends greatly on the density of CO_2 (Lake, 1989). As CO_2 density increases, more hydrocarbon components are vaporized from crude. In general higher reservoir pressure results in higher CO_2 density. The pressure at which reservoir oil and CO_2 are in extremely close contact is called MMP.

Variety of different approaches have been suggested to measure and/or calculate the MMP. Analytical methods are simplistic methods which are based on phase equilibrium calculations. Johns and Orr (1996) and Wang and Orr (1998) have introduced phase equilibrium-based semi-analytical approaches to predict MMP values which showed some promises in the development of analytical theory of gas injection. This idea later was extended and improved by Jessen et al. (2001) to generate approximate solutions to the 1-D displacement of multi-component gas injection processes. The prediction of miscibility conditions from ternary diagrams is based on experimentally determined gas and liquid compositions in different mixtures. They finally concluded that in specific cases for which injected fluid is pure CO_2, slim tube experiments are better approaches to be considered. Besides of this, sufficient phase equilibrium data between injected gas and crude oil are needed, particularly near critical points. Without these type of accurate and adequate data, sometimes mathematical methods fail to predict MMP values. Experimental gas and liquid equilibrium data are not easy to acquire and are expensive and hard to obtain. Jaubert et al. (2002) used a characterization procedure based on Peng-Robinson Equation of State (EOS) and strived to address this question that

"would experimental MMP slim tube tests are necessary?" since less expensive phase equilibrium procedures are available.

Another approach to predict thermo-dynamic MMP is using one-dimensional slim tube simulations or experiments. Experimental slim tube data are gathered using long slim tubes packed with special type of sands which is saturated with reservoir oil at reservoir temperature. About 1.2 pore volume of injected gas is gradually entered into the reservoir in a wide range of pressure values. Recovery factor sharply increases at the lower pressure values but gradually starts to flatten and then no additional recoveries are gained by increasing displacement pressures. Figure 7.1 shows an example of slim tube plot. It is shown that ultimate recovery values for each displacement pressure are plotted and pressure at which, curve is bent is considered as MMP value. Slim tube tests are valuable methods of determining MMP but they can be really expensive.

One-dimensional flow simulations of slim tube experiments utilizing well-characterized EOS fluid models are decent substitutes for expensive slim tube experiments. This numerical approach is based on compositional simulation of solvent injection into a 1-D high permeability porous media with straight-line relative permeability data (which are representative of complete miscible displacement processes). Since small size gridblocks are needed due to the small nature of problem, effect of numerical and physical diffusion which has been mentioned previously by Stalkup (1990) should be carefully considered. In order to accurately perform these type of simulations, swelling test experiments have to be completed on the reservoir fluid. These experimental data are needed to tune the EOS model of properly characterized fluid. Besides of this, simulation of 1-D slim tube is also computationally expensive since different simulation cases (at various pressure conditions) have to carried out. The use of correlations to predict MMP is another method which has been widely used in the oil industry.

7.2 MINIMUM MISCIBILITY PRESSURE CORRELATIONS

The main factors affecting minimum miscibility pressure are the reservoir fluid composition, injection gas which is considered as CO_2 in our study, and reservoir temperature. MMP between CO_2 and any reservoir oil increases when a higher fraction of volatile components such as C_1 exist in the reservoir. In addition, higher fraction of intermediate components such as CO_2, C_2-C_4 in the reservoir fluid decreases the MMP value (Alston et al., 1985, and Sebastian, et al., 1984). Moreover, higher molecular weight of C_{7+} or C_{5+} fraction in the oil reservoir fluid results in higher MMP. In general higher reservoir temperature also causes increase in the MMP.

In order to quantify the effect of all variables on MMP, numerous amount of MMP correlations have been developed to quickly assess the MMP values. These correlations are generally inexpensive, fast and easy to use. But, developing a comprehensive MMP correlation has still remained a big challenge for researches since long time ago. Proposed correlations have their own limitations and mainly account for parameters such as reservoir temperature, oil composition, and molecular weight of different hydrocarbon components in the fluid, CO_2 density, and impurities in the injected fluid.

Holm and Josendal (1974) proposed first MMP correlation. They correlated MMP value based on reservoir temperature and molecular weight of C_{5+} components in the reservoir oil. Effect of temperature on CO_2 density was the main factor in their correlation. They presented another correlation in (1982), in which CO_2 density is empirically correlated to the extractable portion of the crude (which is mole fraction of C_5 through C_{30} hydrocarbons divided by mole fraction of C_{5+}). The MMP is then calculated by finding the pressure required to obtain that CO_2 density at reservoir temperature. Orr and Taber (1983) used this correlation and extend it to account for impurities in CO_2 stream.

National Petroleum Council (NPC) (1976) has another MMP correlation that predicts MMP according to reservoir temperature and reservoir oil °API gravity. Dunyushkin and Namiot (1978) also suggested similar correlation to that of Holm and Josendal (1974). Yellig and Metcalfe proposed (1980) simpler correlation and MMP was correlated by reservoir temperature for oils with bubble point pressures lower than MMP values. They used limited number of West Texas light oils. Their correlation did not consider the composition of oil as important factor on predicted MMP. Yuan et al. (2004) developed new MMP correlation for both pure and impure CO_2 injection scenarios using analytical theory for MMP calculation from equation of state. Their correlation is based on the reservoir temperature, molecular weight of C_{7+} and percentage of intermediate hydrocarbon components (C_2-C_6) in the reservoir fluid. Alston et al. (1985) also suggested a MMP correlation with temperature, oil composition, and a weight-averaged critical temperature for the impure CO_2. Orr and Jensen (1984) a MMP correlation with extrapolated vapor pressure of CO_2.

Johnson and Pollin (1981) empirically correlated MMP with the critical temperature, critical pressure, composition, and molecular weight of the injection gas, reservoir temperature, oil API gravity, density, and average molecular weight of oil. This correlation was limited to the cases that injected gas is binary mixture of CO_2 and N_2 or CO_2 and CH_4. Cronquist (1977, 1978) proposed correlations of MMP with reservoir temperature and several EOS parameters such as temperature, Methane mole percent in oil, and molecular weight of Pentane-plus fraction. Most of these previous correlations have been presented in the Appendix B.

7.3 DEVELOPMENT OF A NEW MMP CORRELATION

Almost all of the aforementioned correlations are mainly based on experiments, statistics, oil composition which directly represented by EOS parameters, and more

specifically reservoir temperature. It is inevitable to admit that MMP is directly or indirectly linked with all of these factors. But on the other hand, developing a correlation that could gather all of these variables and link them individually to the MMP, is almost impossible. Previously developed dimensionless scaling groups (Chapter 6 of this dissertation) helped us to lump all of these parameters together in order to provide accurate and complete MMP correlation model.

The goal of this study is to use four of the phase behavior related dimensionless scaling groups, which were developed in the chapter 6 of this dissertation, and then utilize multivariate regression analysis based on response surface methodology (RSM) and propose an all-inclusive MMP correlation for broad range of reservoir fluids. These dimensionless groups are in the form of pseudo properties of heavy and light hydrocarbon components. Since temperature has been proven to be one of the main factors in determination of MMP values, the reduced form of temperature is used in this study. Following are four dimensionless parameters:

$$A = T_{r2} = \frac{T}{T_{c2}} \tag{7.1}$$

$$B = T_{r4} = \frac{T}{T_{c4}} \tag{7.2}$$

$$C = W_2 \tag{7.3}$$

$$D = W_4 \tag{7.4}$$

In the above groups, T_{r2} is the reduced temperature for light pseudocomponent (C_1-C_6) of the oil, T_{r4} is the reduced temperature for heavy pseudocomponent (C_{7+}) , T_{c2} is critical temperature for light pseudocomponent of the oil, T_{c4} is critical temperature for heavy pseudocomponent, T is the reservoir temperature, W_2 is Acentric factor for light pseudocomponent of the oil, and W_4 is acentric factor for heavy pseudocomponent of the

oil. In order to calculate these pseudo properties, Pedersen and Christensen (2007) recommend a weight-based grouping, thus:

$$T_{c2} = \frac{\sum_{i=1}^{6} z_i M_{wi} T_{ci}}{\sum_{i=1}^{6} z_i M_{wi}} \tag{7.5}$$

$$T_{c4} = \frac{\sum_{i=7}^{\infty} z_i M_{wi} T_{ci}}{\sum_{i=7} z_i M_{wi}} \tag{7.6}$$

$$W_2 = \frac{\sum_{i=1}^{6} z_i M_{wi} \omega_{ci}}{\sum_{i=1}^{6} z_i M_{wi}} \tag{7.7}$$

$$W_4 = \frac{\sum_{i=7}^{\infty} z_i M_{wi} \omega_{ci}}{\sum_{i=7} z_i M_{wi}} \tag{7.8}$$

where z_i is the mole fraction, M_{wi} is the molecular weight, T_{ci} is the critical temperature, and ω_{ci} is the acentric factor of carbon number fraction i. It is seen that all of the important variables affecting MMP value such as reservoir temperature, molecular weight, mole fraction of different components (representing effect of oil composition), and some other important EOS parameters such as critical temperature and Acentric factor for wide range of components are lumped in these dimensionless groups. In addition, these dimensionless groups have been categorized in two distinct sets for light and heavy hydrocarbon components. These aforementioned variables are almost all of the factors affecting MMP value between CO_2 and injected fluid indirectly. It is realized that the number of variables are so ample to deal with and also manage them to see their individual affects and then, consequently define their combined effects on the MMP

value. In solving these type of problems, any multivariate statistical analysis can be utilized to define the effect of all these parameters on the final MMP value.

Response surface methodology is a powerful data-modeling tool which is capable of capturing and representing complex input/output relationships. Applying response surface method and multivariate regression analysis makes it possible to quantify and rank the effect of each one of these dimensionless groups on the predicted MMP values as final objective function for scaling groups.

Followings are step-by-step procedure which was followed in order to achieve comprehensive MMP correlation.

7.3.1 Fluid Database

First step in developing the MMP correlation, was constructing a reservoir fluid database which contains wide range of reservoir fluids. An extensive literature study was performed to gather reservoir fluid data from published sources besides of some other available fluids from internal sources in our Department. Table 7.1 shows all of fluid references and their molecular weight. It was decided to keep some of these fluids for validating the final developed MMP correlation; therefore, they obviously were not utilized in the process of developing MMP correlation. They are specified in Table 7.1 with * sign.

7.3.2 Fluid Characterization

Since full laboratory report was not available from mentioned references and we were not able to find large number of data sets in the literature therefore, it was decided to characterize all fluids in a way that 7 components were defined in the equation of state model for each fluid. For some of these fluid samples experimental bubble point pressure and some other available experimental data were matched by tuning the EOS parameters.

In addition, for EOS parameters of some of the fluids which didn't have enough experimental data, correlations from Pedersen et al. (1988) were employed. Table 7.2 and Table 7.3 show the final EOS parameters as examples for two fluid samples in the database. Additional tables for the rest of EOS parameters for other fluids can be found in Appendix B.

7.3.2 Slim Tube Simulations

Based on available EOS parameters for different fluids, critical temperature, acentric factor, and molecular weight can be calculated for light (C_1- C_6) and heavy (C_{7+}) pseudo-components for all of the fluid samples. Utilizing the final fluid database, slim tube simulation input files were set up for each one of the fluids. Since reservoir temperature is one of the main parameters therefore, slim tube simulations were performed at 4 different reservoir temperatures (90, 150, 180, and 220 °F) on all of the fluid models. According to this, for each fluid model, 4 MMP values were acquired and consequently corresponding reduced temperature and pseudo-acentric factors for the light and heavy hydrocarbon components were recorded for each MMP value. In total, close to 700 slim tube simulations were performed and 68 MMP values were determined for all fluid samples. Figures 7.2 and 7.3 show the ultimate recovery plots at different temperatures for two slim tube simulation cases as examples for two fluid samples. Additional tables for the rest of recovery plots for other fluids can be found in Appendix B. In order to be consistent in determining MMP value for each slim tube displacement simulation, pressure at which ultimate recovery curve is bent, considered as MMP value. Table 7.4 shows the final MMP values for all of the fluid samples at different temperatures.

7.4 CONSTRUCTING RESPONSE SURFACES

It should be noted that, corresponding to each MMP value presented in Table 7. 2, there are unique reduced temperature and acentric factor values for heavy and light pseudo-components of oil. By performing multi-variate regression analysis, MMP values can be correlated by the four EOS-related independent variables which were mentioned before. In fact, response surface is a fitted equation between simulated MMP values and scaling groups. In the response equation, MMP was defined as objective function which basically is a dependent variable and also four aforementioned dimensionless groups were also independent variables. Responses were considered as linear, quadratic, and third order equations. Following is the simplified version of the equation if we assume only three independent variables as Xi and i=1,2,3 along with one dependent variable as Y. Excluding the error term, below equation includes 14 terms but, if the number of independent variables increases to 4 (which is the case in this study), response equation will include 35 terms in a similar way.

$$\begin{aligned} Y = {} & \beta_0 + \beta_1 A + \beta_2 B + \beta_3 C \\ & + \beta_{12} AB + \beta_{13} AC + \beta_{23} BC + \beta_{11} A^2 + \beta_{22} B^2 + \beta_{33} C^2 \\ & + \beta_{123} ABC + \beta_{111} A^3 + \beta_{222} B^3 + \beta_{333} C^3 + error \end{aligned} \tag{7.9}$$

In the Equation 7.9, β_i s are coefficients, and A, B and C stand for our dimensionless groups such as T_{r2}, T_{r4}, W_2, W_4 shown in Equations 7.1 through 7.4, respectively. Therefore, the resulting coefficients for our study will be 34 plus one value for intercept which makes total number of coefficients 35.

MMP value is known as response and also all of dependent variables are known as quantities. Multivariate regression analysis was performed using Premium Solver© option within Microsoft Excel© to find coefficients which result in least error between calculated (using slim tube simulations) and estimated (from response surface equation)

MMP values. In order to do so, sum of the squares of differences of corresponding values in two arrays as well as relative error percentages between them were minimized. Utilizing Premium Solver option helped us to achieve global minimum for the correlation. Therefore, all coefficients were determined when this global minimum was reached. Based on the determined coefficients best correlation between estimated and determined MMP values was established. Figure 7.4 shows the relation between estimated and calculated MMP values. It represents a good agreement between determined MMP values through slim tube simulation and MMP values calculated from response surface equation.

Table 7.5 lists the coefficients and correlation coefficients for each term in the equation 7.9. The A, B, C, and D and their combinational parameters represent the values for reduced temperature, and acentric factors for pseudo-oil components shown in equations 7.1 through 7.4. The final Response Surface (RS)-based correlation has correlation coefficient of 99.2 %, its average relative error is 4.1 % and its standard deviation is 3.8%. These statistics regarding developed MMP correlation shows a near-perfect correlation.

One of the advantages of using RS-based methodology, to construct the correlation, is the ability to determine which parameters have most significant effect on the response values. Based on this, factors corresponding these coefficients can be ranked from least to most effective parameters on the MMP value. But, actual values of utilized scaling groups (reduced temperatures, and acentric factors) can sometimes vary with order of magnitude. Consequently, a coefficient which has a large value and therefore shows great impact on the response surface can be less important than a smaller one but, more important coefficient for the same reason. Since upper and lower limits for all of 4 scaling values were known therefore, it was decided to normalize them. This converted all of the scaling groups into values which were changing from -1 to +1 and all of the

actual non-normalized parameters were changing linearly between these two scaled values. Following equation was employed to normalize the original scaling groups:

$$N = \frac{2\times(a - L_a)}{(H_a - L_a)} - 1 \tag{7.10}$$

where N is the final normalized value for each parameter, a is the actual scaling group value, L_a is the Minimum value for the parameter A, and H_a is the maximum value for the parameter A. Table 7.6 shows the actual range of variations for reduced temperatures and acentric factors along with their normalized values.

After performing normalization conversion, response equation for MMP was constructed based on the normalized values in a similar way as for the actual values. Since in the normalized equation, all of the independent variables have the same range of variations thus, the coefficients with higher values in the response MMP equation, have bigger impact on the MMP value. Table 7.7 shows the five most important variables on the MMP values. According to our statistical analysis, the order from most to least influential factors for MMP are reduced temperature for light pseudo-oil component, and second order of Acentric factor for light pseudo-oil component, also acentric factor for heavy pseudo-oil component, and finally reduced temperature for heavy pseudo-oil component. It is important to note that MMP value does not depend on the individual EOS parameters and it is rather combination of EOS parameters that affect the MMP value. This correlation mainly shows that properties for intermediate (C_2-C_6) hydrocarbon components which are imbedded inside light pseudo-oil component group have more impact on MMP value than properties of the heavier oil components.

7.5 VALIDATION OF THE CORRELATION

To test the performance of the new developed correlation, and in order to validate it, the predicted MMP values were compared against the MMP values determined from

slim tube simulations for several fluid models shown in Table 7.1. Therefore, slim tube simulations were performed using the EOS models for test fluids and also MMP was calculated from final MMP correlation. Results are presented in Figure 7.5. It is seen that results from the new RS-based MMP correlation was in a good agreement with tedious slim tube simulations. It should be noted that for any fluid sample at least 10 slim tube simulations should be performed in order to determine the MMP value for that fluid. But, in order to utilize our RS-based correlation, simple calculations which easily can be done in excel spreadsheet, are adequate to get the MMP value for any fluid. In addition, since there are some uncertainties in determining MMP values from ultimate recovery plots, such as different definition for determining MMP from plots, RS-based correlation can be applied to check the results from slim tube simulations.

Furthermore, the RS-based correlation was compared to previously published MMP correlations (Holm and Josendal, 1974; Cronquist, 1978; Dunyushkin and Namiot, 1978; Yellig and Metcalfe, 1980; Glaso, 1985; Yuan, et al. 2004). It was observed that our RS-based correlation presents much better predictions than other mentioned correlations. Appendix B illustrates details for these correlations. Some of the correlations are based on data for MMP which is read from standard plots. Figure 7.6 shows the comparison between these correlations and our new RS-based correlation. Also there are other sets of MMP correlations that have been presented by mathematical relations. A comparison between this set of correlations with new RS-based correlation is presented in Figure 7.7. New correlation has average error of 0.4 percent which compared to the average error from other correlations presented in Table 7.8 is much more accurate correlation developed so far. RS-based correlation takes into account the effect of important EOS properties for heavy- and light-oil components as well as the temperature effect which all gathered in the dimensionless form. In addition, performing multi-variate regression analysis allows us to utilize efficient statistical techniques to come up with more comprehensive MMP correlation.

7.6 SUMMARY AND CONCLUSIONS

According to an extensive literature survey, it is evident that the main factors affecting minimum miscibility pressure are the reservoir fluid composition, injection gas which is considered as CO_2 in our study, and reservoir temperature. In order to quantify the effect of all variables on MMP, numerous MMP correlations have been proposed to quickly assess the MMP values. These correlations are generally inexpensive, fast and easy to use. Developing comprehensive MMP correlation has still remained a big challenge for researches since long time ago. It is inevitable to admit that MMP is directly or indirectly linked with all of these factors. But on the other hand, developing a correlation that could gather all of these variables and link them individually to the MMP is almost impossible. Phase behavior-related dimensionless scaling groups could help to lump all of these parameters together in order to provide accurate and complete MMP correlation model.

The goal of this study was to use four phase behavior related dimensionless scaling groups (reduced temperature and acentric factors for light and heavy pseudo-hydrocarbon components) and then utilize multivariate regression analysis based on response surface methodology and propose an all-inclusive MMP correlation for broad range of reservoir fluids. Applying response surface method and multivariate regression analysis made it possible to quantify and rank the effect of each one of these dimensionless groups on the predicted MMP value.

A comprehensive fluid database covering wide range of reservoir fluids, mostly from published sources was constructed. Slim tube simulation input files were set up for each one of the fluids. Since reservoir temperature is one of the main parameters therefore, slim tube simulations were performed at 4 different reservoir temperatures (90, 150, 180, and 220 °F) on all of the fluid models. Based on the results from simulations, and by performing multi-variate regression analysis, MMP values were correlated by four EOS-related independent variables, using a response surface as linear, quadratic, and

third order equation. Multivariate regression analysis was performed to find coefficients which result in least error between calculated (using slim tube simulations) and estimated (from response surface equation) MMP values. In order to do so, sum of the squares of differences of corresponding values in two arrays as well as relative error percentages between them were minimized. Therefore, all coefficients were determined when this global minimum was reached.

To test the performance of new developed correlation, and in order to validate it, the predicted MMP values were compared against the MMP values determined from slim tube simulations for several other fluid models. Furthermore, the response surface-based correlation was compared to previously published MMP correlations. It was shown that the new correlation has lower average error compared to other previously published correlations. RS-based correlation takes into account the effect of important EOS properties for heavy- and light-oil components as well as temperature effect which were grouped in a dimensionless form. In addition, performing multi-variate regression analysis allows us to utilize efficient statistical techniques to come up with more comprehensive MMP correlation.

Table 7.1: List of reservoir fluid utilized for the development of MMP correlation.

Fluid name	Mw (gr/gr-mole)	Reference
APNDXD2-LK	31	Lake and Walsh (2003)
COATS85-TBL1	45	Coats (1985)
JCBY-TBL1	48	Jacoby and Berry (1957)
COATS86-OL2*	51	Coats and Smart (1986)
JRHFPOOLE	54	Lee et al. (1994)
Danesh-tbl2.1A*	79	Danesh (1998)
JRHFPOOLD	80	Lee et al. (1994)
COATS-OL6*	83	Coats and Smart (1986)
14923-SPE	86	Chaback and Williams (1988)
Tbl15.2-Pdsn*	86	Pedersen and Christensen (2007)
COATS86-OL7*	113	Coats and Smart (1986)
3483-B	114	Rathmell et al. (1971)
NWE	139	Khan et al.(1992)
RF7	149	Internal fluid
BSB5	153	Khan et al. (1992)
RF4	154	Interal fluid
JEMA	159	Khan et al. (1992)
RF6	161	Internal fluid
3.21-PDSN	181	Pedersen and Christensen (2007)
64730-SPE	251	Abdassah et al. (2000)
15.16-PDSN	421	Pedersen and Christensen (2007)

* Fluid samples used to validate the developed correlation.

Table 7.2: EOS parameters for fluid properties of COATS85-TBL1 oil sample.

	'CO2'	'C1'	'C2toNC4'	'IC5toC6'	'HYP01'	'HYP02'	'HYP03'
Specific Gravity	0.82	0.30	0.46	0.65	0.74	0.81	0.89
Boiling Point, °C	-109.21	-258.61	-8.97	111.69	259.49	552.71	920.44
Critical Pressure, atm	72.80	45.40	43.45	33.09	26.86	14.78	7.65
Critical Volume, m3/K-mole	0.09	0.10	0.19	0.32	0.46	0.92	1.78
Critical Temperature, °K	304.20	190.60	356.99	478.43	577.24	727.88	899.47
Acentric Factor	0.23	0.01	0.14	0.25	0.37	0.74	1.24
Molecular Weight, gr/gr-mole	44.01	16.04	41.19	76.54	113.66	222.02	452.50
Binary Interaction Coefficients:							
	0.06						
	0.06	0.00					
	0.06	0.00	0.00				
	0.11	0.00	0.00	0.00			
	0.11	0.00	0.00	0.00	0.00		
	0.11	0.00	0.00	0.00	0.00	0.00	
Volume shift Parameter	-0.09	-0.15	-0.08	-0.03	0.02	0.20	0.36
Mole Fraction of Components	0.04	0.61	0.16	0.04	0.08	0.06	0.01

Table 7.3: EOS parameters for fluid properties of 3483-B oil sample

	'CO2'	'C1'	'C2toNC4'	'IC5toC6'	'HYP01'	'HYP02'	'HYP03'
Specific Gravity	0.82	0.30	0.46	0.66	0.79	0.88	0.97
Boiling Point, °C	-109.21	-258.61	-9.37	127.93	295.21	662.20	1082.10
Critical Pressure, atm	72.80	45.40	43.51	32.86	28.44	14.23	7.18
Critical Volume, m3/K-mole	0.09	0.10	0.19	0.33	0.45	1.01	1.99
Critical Temperature, °K	304.20	190.60	357.96	489.84	607.62	795.43	992.16
Acentric Factor	0.23	0.01	0.14	0.26	0.39	0.84	1.35
Molecular Weight, gr/gr-mole	44.01	16.04	41.23	79.93	120.60	260.32	557.50
Binary Interaction Coefficients:							
	0.06						
	0.06	0.00					
	0.06	0.00	0.00				
	0.10	0.00	0.00	0.00			
	0.10	0.00	0.00	0.00	0.00		
	0.10	0.00	0.00	0.00	0.00	0.00	
Volume shift Parameter	-0.09	-0.15	-0.08	-0.02	0.06	0.14	0.06
Mole Fraction of Components	0.03	0.28	0.19	0.08	0.21	0.17	0.05

Table 7.4: Final determined MMP values for each fluid sample at different temperatures

Temperature (°F) / *Fluid sample*	**90**	**150**	**180**	**220**
NEW	1000	1850	2150	2700
JEMA	1100	1600	2000	2200
BSB5	1020	1700	2150	2500
3483-B	1050	1850	2400	3000
3.21-PDSN	1280	1980	2300	2800
15.16-PDSN	1750	3300	3950	4650
14923-SPE	1100	1750	2250	2750
64730-SPE	1350	2150	2550	3050
APNDXD2-LK	1250	2400	3050	3650
JCBY-TBL1	1150	2000	2500	3000
JRHFPOOLE	1150	1950	2350	2800
JRHFPOOLD	1050	2000	2450	2800
RF6	1550	2750	3600	4100
RF7	1950	3300	4250	4600
RF4	1700	2900	3950	4350
COATS85-TBL1	1050	1500	1900	2300

Table 7.5: Response surface coefficients and correlation coefficients for MMP

Parameter	Coefficient	Correlation Coefficient
A	27861.32	-0.16
B	-798.26	0.26
C	3056.25	-0.04
D	6990.16	0.14
AA	-25.73	0.43
AB	-1925.97	0.35
AC	-35.40	0.24
AD	-29489.29	-0.36
BB	318.34	-0.07
BC	2278.64	-0.16
BD	3045.12	-0.16
CC	2582.19	0.29
CD	1998.76	-0.33
DD	3322.46	0.23
A^2B	2049.89	0.15
A^2C	6574.60	-0.41
A^2D	1223.09	0.15
AB^2	83.29	0.13
AC^2	-32765.98	-0.22
AD^2	2322.60	-0.16
B^2C	-492.99	-0.04
B^2D	824.08	-0.09
BC^2	-48.54	0.08
BD^2	965.36	0.06
C^2D	-892.66	0.12
CD^2	5991.74	-0.13
ABC	-333.58	-0.36
ABD	1657.02	-0.13
ACD	-20174.90	0.33
BCD	1.78	0.39
A^3	-2.03	-0.13
B^3	767.35	0.27
C^3	487.49	-0.12
D^3	1422.53	0.13
Intercept	-3477.38	

Table 7.6: Actual and normalized range of variations for scaling group values

		Maximum	Median	Minimum
T_{r2}	Actual	6.55	0.79	-7.63
	Normalized	+1	0.19	-1
T_{r4}	Actual	0.30	0.17	0.05
	Normalized	+1	-0.07	-1
W_2	Actual	0.24	0.15	0.05
	Normalized	+1	0.02	-1
W_4	Actual	1.45	0.82	0.55
	Normalized	+1	-0.39	-1

Table 7.7: Ranked effect of phase behavior scaling groups on MMP

Rank	Terms in Equation	Actual Factors
1	AC^2	T_{r2}, W_2^2
2	AD	T_{r2}, W_4
3	A	T_{r2}
4	ACD	T_{r2}, W_2, W_4
5	D	W_4

Table 7.8: Average and standard deviation of error for various published MMP correlations

	RS-Based	Holm and Josendal	Yuan, et al.	Glaso	Yellig and Metcalfe	Cronquist	Dunyushkin and Namiot
Average percentage error	**0.4**	15.4	11.0	18.0	7.2	43.4	38.4
Standard deviation of error	**12.2**	28.8	41.0	20.4	21.1	31.3	53.3

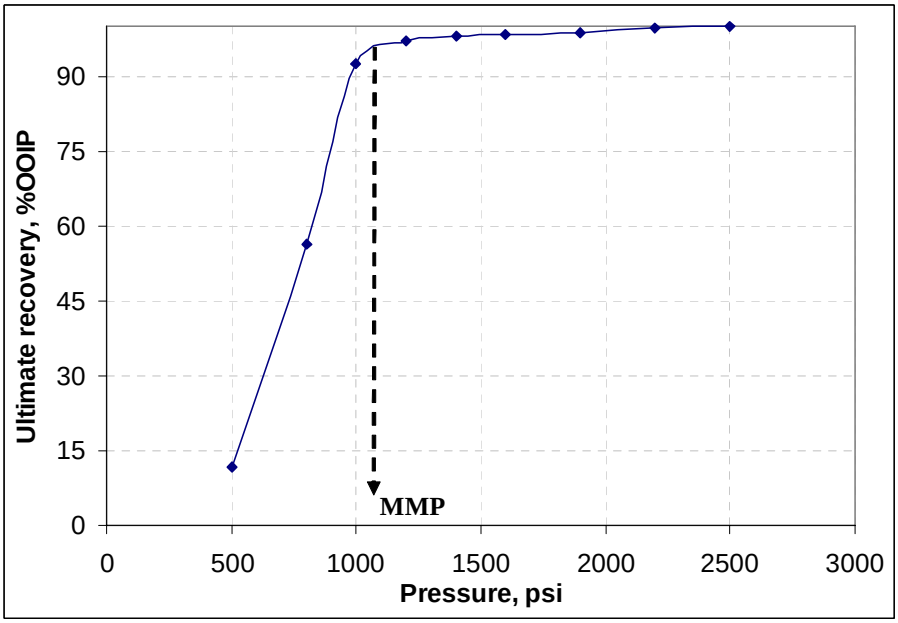

Figure 7.1: Schematic of slim tube recovery plot and its corresponding MMP value

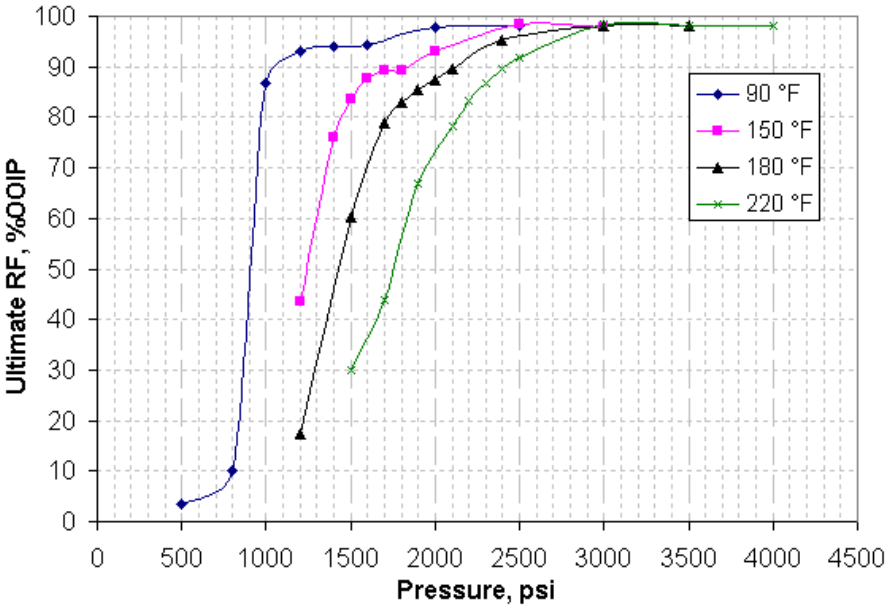

Figure 7.2: Ultimate oil recoveries for COATS85-TBL1 oil slim tube displacements

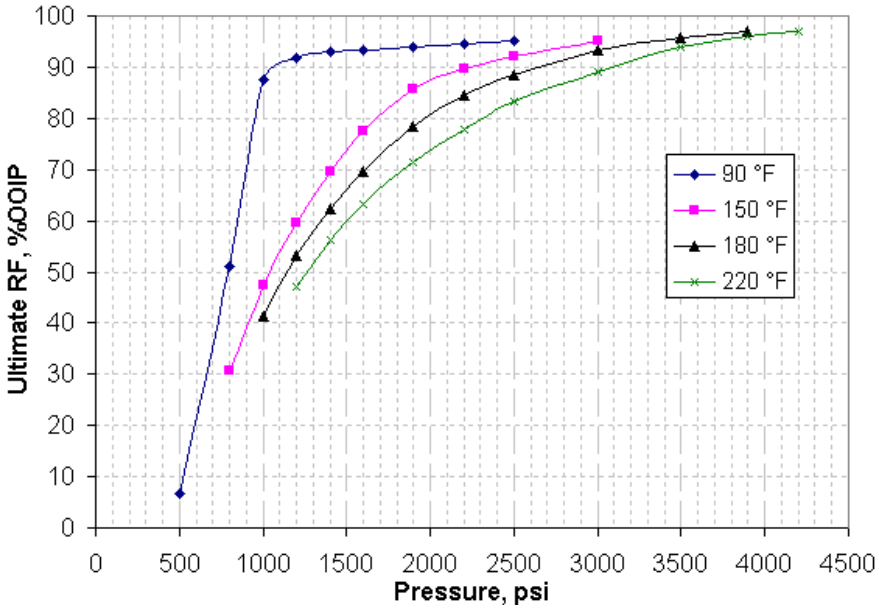

Figure 7.3: Ultimate oil recoveries for 3483-B oil slim tube displacements

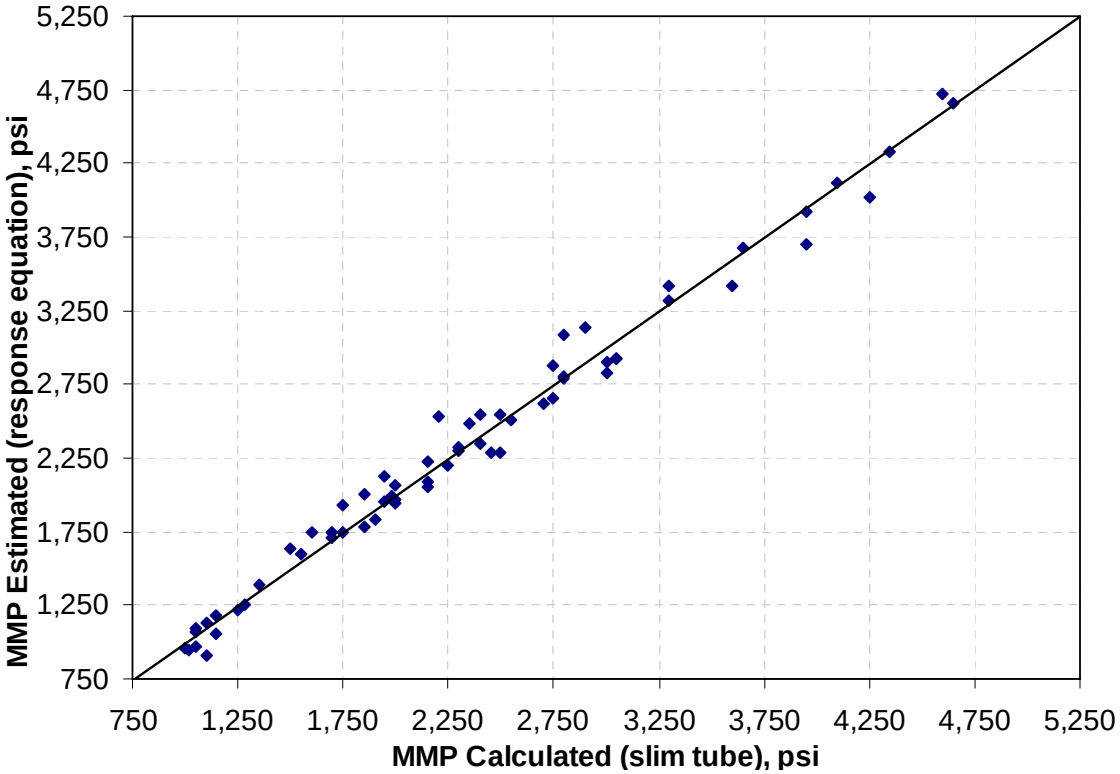

Figure 7.4: Comparison of calculated and also estimated MMP values from developed response surface equation

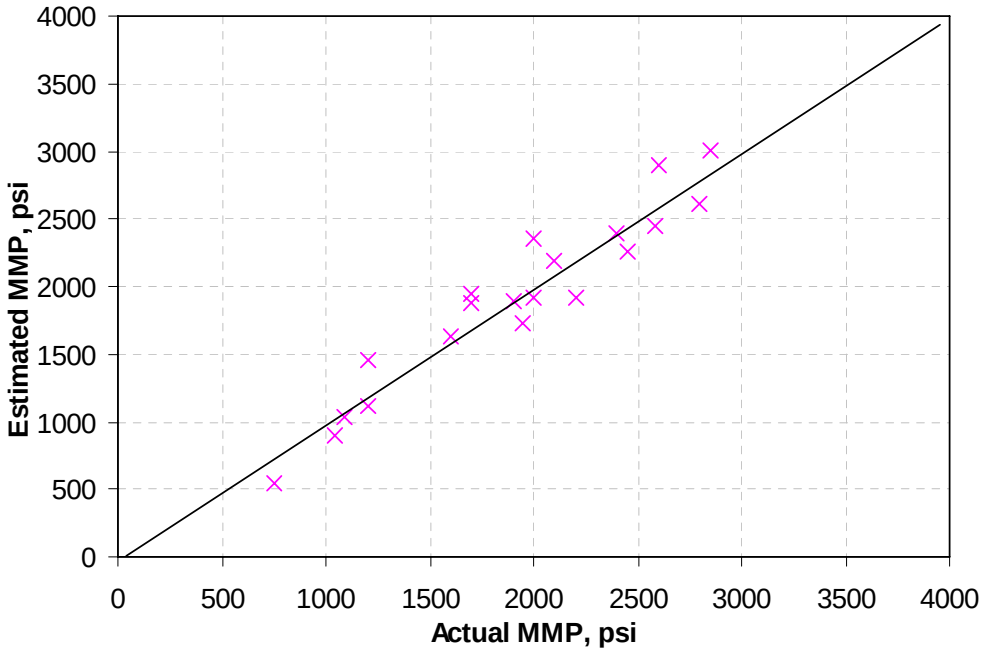

Figure 7.5: Results of RS-based MMP predictions to validate developed correlation

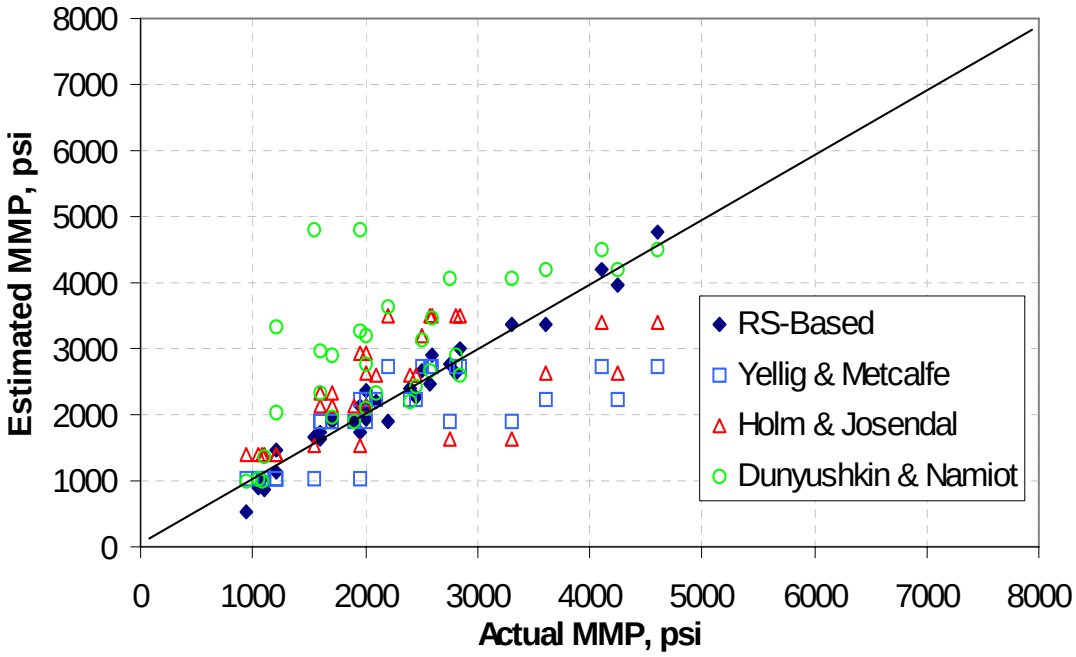

Figure 7.6: Comparison of MMP predictions between new RS-based MMP correlation and available correlations (read from plots) in literature

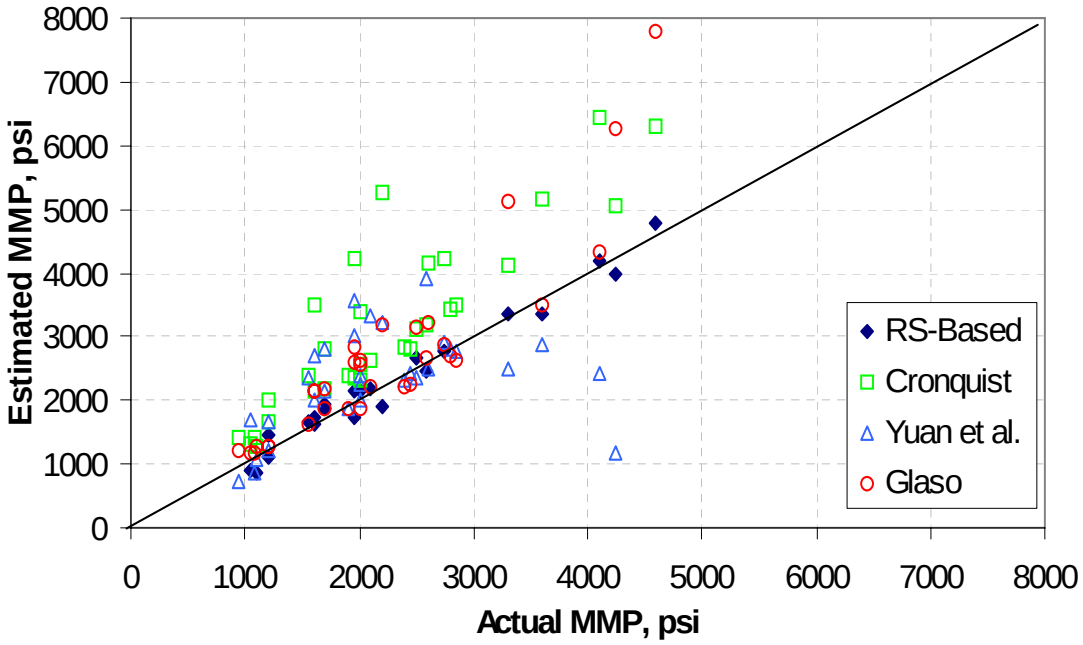

Figure 7.7- Comparison of MMP predictions between new RS-based MMP correlation and available correlations (mathematical models) in literature

Chapter 8: Investigation on Economic Incentives for CO_2 Sequestration

8.1 INTRODUCTION

CO_2 concentration in the atmosphere has drastically increased from 280 ppm during pre-industrial age to its current level of 380 ppm (Bryant, 1997). It is proven that, this is mainly due to the dramatic raise in the fossil fuel consumption. This has caused climate change concerns among environmentalists and it is gaining more publicity as international agencies and governmental sectors in different countries seriously considering CO_2 reduction policies implemented. It should be mentioned that there is no direct proven evident showing the relation between climate change and the CO_2 emissions. But, because of the greenhouse effect of CO_2, it is mainly suspected that a higher CO2 concentration in the atmosphere has caused these climate changes.

Geological CO_2 storage as the only effective option to mitigate atmospheric CO_2 emissions has been considered since 90's and has been implemented in large scale for the first time in Norway. Based on the data published by Moritis (2002) over 35 million tones of CO_2 have been injected into the oil reservoirs for the purpose of EOR, and currently few aquifer CO_2 storage projects are underway. Weyburn CO_2 sequestration and EOR project probably is the only on-going commercial coupled EOR and sequestration project which has shown great success in terms of both objectives of the project (Malik and Islam, 2000). Carbon Dioxide is transported from North Dakota coal-gasification plant through pipelines and is injected into the to Weyburn oil field.

One of the main aspects of all current EOR projects in the United States is using inexpensive CO_2 from natural resources. These sources have high CO_2 purity and there are no additional costs corresponding capture and compression of their stream. There are also limited amount of anthropogenic CO_2 available from fertilizer, petrochemical, and coal-gasification plants which are much more expansive than natural sources of CO_2. Due

to the recent high oil prices and assuming it will continue in similar fashion in the future, CO_2 flooding projects are expected to grow in the numbers and volume rapidly in the next decade. Therefore, there is going to be serious need for additional CO_2 sources. From another perspective, carbon emission regulations have already been set in place in some European countries as well as Japan under Kyoto protocol. If it gets fully implemented in the other industrialized countries such as United States, it can serve as double-purpose for both providing huge additional CO_2 sources for EOR processes and vast potential for geological storage of anthropogenic CO_2 emissions. Among all CO_2 emission sources, stationary sources such as power stations and petroleum industry facilities are main contributors.

There are two main issues regarding CO_2 emissions from stationary sources: Firstly, produced gas stream from these sources have some type of contaminations. These impurities are not proper components to be injected into the oil reservoirs because in most cases they are detrimental to the level of CO_2 miscibility with reservoir oil. This can impose significant capture and separation cost to the CO_2 price. Secondly, not in all of the cases, these CO_2 sources are in a reasonable distances from candidate mature oil reservoirs. Therefore, CO_2 should be transported by pipelines to the injection site and it should be re-compressed to maintain CO_2 pressure necessary for injection. It should be noted that, longer the distance between the sources and sinks and smaller the volume of CO_2 to be injected, the higher is the overall cost of transportation and compression. This adds large transportation and compression costs to the final deliverable price of CO_2. When sequestration is considered as the objective of process, additional monitoring expenditures should also be added to the total project costs.

These major cost-related problems should be overcome to stimulate the adoption of coupled CO_2 sequestration and EOR processes. The first and most important step is to reduce the very high cost of capture procedure. Research have been performed (Rochelle et al., 2005) and needed to be continued further to reduce the capture costs. In addition,

if the carbon credit regime is implemented and proper regulations are set in this regard, sequestration costs might get offset and these type of projects may become more attractive. These carbon credits can be defined in the form of tax regimes to present some type of incentives for performing efficient and large scale sequestration projects and thus reducing CO_2 emissions into atmosphere. Tax can potentially have a large effect on the economics. It should be noted that considering additional costs of capture, transportation, and monitoring, without any tax incentives, sequestration projects may not achieve enough attention and publicity from executive sectors of the industry.

As an example for the effect of carbon tax regulations on project economics, Sleipner project can be an outstanding example. In this project, rather than paying Norway's hefty carbon emissions tax of \$140/t CO_2 in 2000 (Bachu and Stewart, 2002), Statoil is compressing and injecting the emissions into an aquifer below the ocean floor. it approximately costs Statoil \$55/t CO_2 to store it in the aquifer. Considering \$80 million dollars of incremental investment cost, Statoil saves almost \$55 million dollars in annual carbon tax (McLean, 2004).

This study examines possibility of establishing direct sequestration tax incentives for coupled CO_2 sequestration and EOR projects considering uncertainties in the economic parameters of the projects such as, different capture and transportation costs, oil price, operational costs of the flood, drilling cost, and project discount rate. Previous studies which have been dealt with CO_2 tax incentives usually make superficial assumptions on the actual CO_2 flood performance in terms of oil recovery and amount of stored CO_2. Performing detailed simulation study of EOR and CO_2 sequestration is feasible and desired for different type of oil reservoirs such as carbonate and sandstone reservoirs using appropriate and detailed geological and reservoir engineering models, rather than superficial flood performance assumptions to do economic analysis. We have utilized detailed expletory compositional simulations using different oil reservoir types to examine flood performance effect on the economics of capture and storage. Considering

the foregoing discussion, and by applying method of response surfaces, various mathematical relationships between CO_2 credit incentives and projects' economic and flood characteristics have been constructed for different reservoir type and CO_2 injection schemes such as continuous and WAG injection o f CO_2.

8.2 ECONOMICS OF CO_2 SEQUESTRATION PROCESS

As mentioned before, among all anthropogenic CO_2 sources, stationary sources such as power stations and petroleum industry facilities are main contributors for CO_2 pollution. In the current study, our main assumption is that CO_2 source is considered as a nominal 500MWe Integrated Gasification Combined Cycle (IGCC) power plant, operating at 80 percent capacity factor. This type of power plants deliver over 7300 tones of CO_2 per day or 141 MMSCF/day and it corresponds to the annual total injection of 51.4 TSCF/yr (Heddle et al. 2003).

There are several components corresponding to the major costs of storing CO_2 which is produced from aforementioned power plant. These cost components can be categorized as capture, compression, transportation, and monitoring. Following are brief overview of each type of these costs. In general, costs of the CO_2 sequestration are in the range of $40 to $60 per ton of CO_2 stored (Davison et al., 2001) which depends on capture process applied, volume of CO_2, distance from source to sink and some other site-specific characteristics.

Capture and Compression: Major part of the total sequestration-associated costs is due to the capture and compression of CO_2 stream. There are different methods for capturing CO_2 from main power plant stream. In chemical adsorption/stripping, CO_2 reacts with some type of solvents to form a weak-bonded intermediate compound which then is broken utilizing heat, regenerating the original solvents for re-use and producing a CO_2 stream. Commonly used chemicals are alkanolamines such as monoethanolamine

(MEA) which can reduce the CO_2 concentration to as low as 100 ppm at low pressure (200 psi) (Nguyen, 2003). Jassim and Rochelle (2006) showed that in terms of energy costs, energy consumption of a simple MEA absorption and stripping process along with CO_2 compression at power plant may be about %38 of the total power plant energy requirement.

In order to transport the captured CO_2 through pipelines, it is necessary to compress it to pressures above 1200 psi to ensure a single-phase flow while keeping its density high. Similar to capture process, compression also requires consumption of energy by a power plant which itself again is a CO_2 emission source. Ennis-King and Paterson (2002) showed that the isothermal work required to compress the CO_2 at 35 °C from an initial pressure of 14.7 psi to 1750 psi requires 0.275 MJ. In other words, CO_2 production through compressor's power consumption is about 6 % of the CO_2 being compressed.

Considering all mentioned factors and assumptions for our study, Rochelle et al. (2005) have determined that total costs of capture and compression (to 2200 psi) is \$45/t CO_2 which is almost equivalent to \$2.6/MSCF.

Transporting CO_2: Transporting CO_2 through pipelines is possibly the best option and has been practiced almost in all existing EOR projects. Costs associated with pipeline transportation mainly depends on pipeline diameter, transportation distance, total volume of CO_2 to be transported through any pipeline, maximum and minimum operating pressures, and CO_2 flow rate. Heddle et al. (2003) have determined the total annual cost per tone of CO_2 by annualizing the construction cost using a capital charge rate of 15 percent per year and adding this to the annual operation and maintenance costs. Figure 8.1 shows the cost per tone of CO_2 per 100 km as a function of CO_2 mass flow rate. It is seen that above flow rates of 10 Mt (Megatons) CO_2 per year transport costs are less than \$1/t CO_2 per 100 km. According to our major initial assumption in which CO_2 source is considered as a nominal 500MWe (IGCC) power plant, its corresponding annual CO_2

flow rate is 2.16 Mt per year. Therefore, for this plant, the annual cost per tone of CO_2 per 100 km is in the order of $1.5 to $2. If it is assumed that CO_2 is going to be transported from sources at 200-400 miles far from reservoirs (e.g., from Houston vicinity to oil fields along gulf coast) total costs for CO_2 transportation in this pilot will vary from 0.5 to 1.2 $/MSCF of CO_2.

Considering all these cost, and the fact that capture and separation of CO_2 from power plant stream is a new scientific and research topic, there is a broad consensus in the literature that the cost of employing Carbon Capture and Storage (CCS) should decrease with time as more research studies are being performed. Due to the small scale deployment of current sequestration projects, it is not evident that how much cost reduction will occur by further research developments as well as performing large-scale capture and sequestration projects. In addition, there are large variability and uncertainty in all of the above-mentioned costs in terms of some site-specific characteristics of different projects as well as other economic parameters such as fuel prices, project discount rate, etc.

8.3 ECONOMICS ASSOCIATED WITH CO_2-ENHANCED OIL RECOVERY

Coupled CO_2 sequestration and EOR projects have the advantage of recovering oil which otherwise can not be recovered, as well as storing CO_2 in an economically attractive environment by offsetting the costs of sequestration. In the near future, this storage option is probably the most viable form of CO_2 sequestration among other options such as aquifer, coal seams, ocean storage and so on. Despite all these, there are several factors that can determine the practicality of these type of projects. Parameters such as oil price, operation costs, drilling costs for required new wells, final CO_2 price, and also flood performance.

One of the fundamental assumptions which has been made in our study is that the volume previously occupied by the produced oil and gas becomes available for storing CO_2. This assumption is generally valid for reservoirs that are not in contact with an aquifer or that are not flooded during secondary and tertiary oil recovery. Another important assumption for most of the screening studies is that CO_2 will be injected into the depleted oil and gas reservoirs until the reservoir pressure is brought back to the original reservoir pressure.

8.4 Economical Co-optimization of CO_2 sequestration and EOR

Based on all necessary high costs corresponding capture, and transportation for carbon capture and storage projects, it can be concluded that without regulatory incentives for CCS projects, their technical capabilities can be limited effectively. But, considering the fact that the oil industry has gained extensive technological improvements in the last few decades in utilizing CO_2 for enhanced oil recovery processes, it may help to alleviate some of the difficulties in terms of the economics and utilized techniques for the CCS projects. Using CO_2 for both EOR and storage purposes provides added value of oil production. On the other hand, due to the very high CO_2 prices, some sort of incentives in the form of accelerated depreciation or direct tax credits should be defined by regulatory sectors to support large scale CCS projects.

8.4.1 Reservoir Simulations

Flood performance of the coupled EOR and sequestration projects has great influence on the project economics and consequently on possible CO_2 incentives (are to be defined) for these type of projects. For instance, different reservoir types such as carbonate and sandstone reservoirs have different responses to CO_2 flooding depending on their major reservoir characteristics. In addition, well spacing is a key factor in

determining the economic viability of candidate reservoirs for CO_2 flooding projects. By choosing smaller well spacing, CO_2 starts to be produced early in the time of the project but sweep efficiency is much higher compared to large well spacing cases; this happens by jeopardizing the economics of the whole project as there is need for large number of wells to be drilled and utilized for flooding. Besides all of the above-mentioned technical issues which have big impact on the project economics, CO_2 injection scheme is another major factor in defining economic feasibility of coupled CO_2 sequestration and EOR projects. WAG injection of CO_2 can enhance and help in increasing sweep efficiency and consequently oil recovery compared to the continuous CO_2 injection but, jeopardizing the storage objective.

Previous studies which have investigated CO_2 tax incentives, usually make superficial assumptions on the actual CO_2 flood performance in terms of oil recovery and amount of stored CO_2. In this study we performed field-scale detailed compositional simulations utilizing CMG's GEM simulator. We considered simulating WAG and continuous CO_2 injection scenarios. Also by utilizing typical reservoir characteristics for carbonate and sandstone reservoirs it was strived to capture differences in economic performance of coupled CO_2 sequestration and EOR projects concerning differences in the reservoir rock types. Table 8.1 shows the summary of important reservoir characteristic and differences between carbonate and sandstone reservoirs which were implemented in our simulations.

In addition to the reservoir type and injection scheme (WAG or continuous CO_2), well spacing was considered as another parameter which affect economic performance of the CO_2 flooding projects. A preliminary study was performed to determine optimum well spacing in both carbonate and sandstone reservoirs for coupled CO_2 sequestration and EOR processes. Carbon dioxide injection scenarios with different well spacing such as 20, 40, 80, and 160 acres were simulated. According to the results obtained from these simulation cases, Discounted Cash Flow (DCF) analysis were performed for all

simulation cases. Figure 8.2 shows the profit of each project in $/bbl, defined as Net Present Value (NPV) of each simulation scenario divided by the total oil production. It shows that optimum well spacing is in the order of 40 acre for coupled CO_2 sequestration and EOR projects. Profit values for other well spacing scenarios such as 20 and 80 acres are almost equal. According to these observations, we decided to study 40 and 20 acre well spacing in more detail, during our investigation on the CO_2 tax incentives for coupled CO_2 sequestration and EOR projects.

8.4.2 Uncertainty Analysis

Considering the effect of reservoir rock type (carbonates or sandstones), Injection scheme (WAG or continuous CO_2 injection), and well spacing (20 acre and 40 acre) on flood performance, 8 different 3-D simulations were performed with combination of above-mentioned factors. These type of simulation studies are feasible and desired using appropriate and detailed geological and reservoir engineering data in order to make accurate predictions on the CO_2 flood performance as well as the amount of stored CO_2 which are crucial for detailed economic analysis.

Besides of technical factors, different economic parameters such as oil price, final deliverable CO_2 price, operational, drilling and recycling costs, project discount rate, and etc have great impact on the project economics as well as type of economic incentives which might be needed to encourage oil companies in the U.S. to store more of the CO_2 in the oil reservoirs. According to our analysis, it is seen that all of the mentioned cost categories have large uncertainty and variability. Experimental design and the method of response surfaces were utilized to perform this uncertainty analysis study in a systematic, efficient and accurate manner. Combination of reservoir parameters and economic factors were studied to achieve comprehensive understanding of the financial performance of the coupled CO_2 sequestration and EOR projects. Table 8.2

shows the six parameters which were considered in our study to quantify amount of CO_2 tax incentives and probability that these incentives might be needed. Three level of uncertainty were assumed for each one of them. Since all of these variables were numeric factors, fractional 3-level factorial design method was applied to perform a comprehensive sensitivity analysis. Therefore, 78 sensitivity scenarios were obtained with combination of all 6 parameters out of 6^3 (216) cases if conventional sensitivity analysis was supposed to be carried out. Table 8.3 shows all of the 78 economic sensitivity cases as well as settings for uncertain factors in each one them based on coded values shown in Table 8.2. Economic analysis, based upon the results of systematic compositional simulations of CO_2 EOR is performed to establish how much economic incentives are needed for coupled CO_2 sequestration and EOR projects. It should be noted that the economic analysis took into account factors such as detailed capture and transportation costs.

8.4.3 Discounted Cash Flow (DCF) Analysis

Since economic analysis was a major part of our study, a decent DCF analysis tool (in the Excel spreadsheet format) was developed in a way that could be utilized for coupled CO_2 sequestration and EOR projects. Other than uncertain economic factors which were mentioned before, data shown in Table 8.4 were considered as constant parameters in our economic analysis. By applying DCF method, it is possible to evaluate different projects by accounting the time value of the both income and expenses. Therefore, it actually gives less importance to the future income and expenses. After performing full DCF analysis for each sensitivity case, the amount of CO_2 credit was found as a value that makes NPV of project even or zero. Therefore positive CO_2 credit meant that CO_2 storage credit is not needed and project has positive net present value. In contrast, negative CO_2 credit meant that CO_2 storage credit is needed to change project's

NPV from a negative value to zero. Detailed equations and approach used in developing Excel-based economic spreadsheet are discussed in Appendix C. Previously-mentioned compositional simulation results were input to the final economic analysis spreadsheet.

All different reservoir simulation scenarios were performed considering the factors that affect flood performance. Therefore, 8 simulations with various well spacing (20 or 40 acres), at different reservoir rock types (sandstone or carbonates), and under WAG or continuous CO_2 injections were performed. Results from these simulations which had wide range of flood performances, were put in the DCF analysis spreadsheets. Using these spreadsheets all 78 economic sensitivity scenarios shown in Table 8.3 were studied. For all sensitivity scenarios, the amount of CO_2 credit was calculated and recorded. In addition, project profit as both $/bbl of oil produced without considering any CO_2 credit, and $/bbl of oil produced with considering $2.5/Mscf of stored CO_2 as credit, were calculated for each sensitivity scenario. These calculations were made for all of 8 simulation cases at different well spacing, reservoir rock type, and injection schemes. Tables 8.5 and 8.6 show the final results for 40 acre and 20 acre well spacing simulations.

In total, close to 624 economic DCF sensitivity analysis were performed and 1872 values for CO_2 credit and project profit with and without considering fixed CO_2 credit were determined for all sensitivity cases.

8.4.4 Construction of Response Surfaces for CO_2 Incentives

One of the final objectives of performing this study is to establish mathematical relationships for the CO_2 credit as a function of flood performance and uncertain economic parameters. Applying method of response surfaces allows us to achieve this goal in a comprehensive and efficient way. This method is based on performing multi-variate regression analysis between final CO_2 credit as dependent variable (or objective function) and other independent and uncertain economic variables mentioned in Table

8.2. In fact, response surface is a fitted equation between CO_2 credit values and uncertain flood and economic parameters. In our study, response equations were considered as linear, quadratic, and second order equation. Table 8.7 shows all of the mathematical relations (response equations) for CO_2 credit at different sensitivity scenarios.

Applying response surface methodology enables us to identify the high influential economic factors (first order effects) on the CO_2 credit objective function. Table 8.8 shows ranking of uncertain parameters based on their effect on the CO_2 storage credit. Based on the parameters and the reservoir conditions studied, the order from most to least influential factors on CO_2 credit are oil price, flood performance, and CO_2 price. This order was almost the same in all of the simulation scenarios such as at different reservoir rock types as well as different well spacing. After defining sensitive parameters and ranking them based on their importance on each objective function response surfaces are generated.

Figure 8.3 demonstrates the response surfaces for CO_2 credit objective function for WAG injection in carbonate reservoirs with 20 acre well spacing. It has been presented at different CO_2 prices and oil prices but other uncertain parameters corresponding to this response surface are kept constant as shown on the figure. It should be noted that vertical axis which shows CO_2 credit contains positive and negative values. Negative CO_2 credit means that CO_2 credit is needed as incentive to make the project NPV zero. In contrast positive CO_2 credit means that project has positive NPV without considering any CO_2 incentives and CO_2 credit is not necessary for the project. But, in this study we have considered adding these incentives to the project cash flow to be able to build comprehensive mathematical relationships between CO_2 credit and other uncertain variables. According to Figure 8.3, CO_2 credit response shows relatively linear behavior; it sharply increases with decrease in the oil price and increases with increase in the CO_2 price. It also is observed that CO_2 credit is more sensitive to the change in the oil price than to change in the CO_2 price.

Figure 8.4 also shows CO_2 credit response surface at different CO_2 and oil prices for WAG injection in carbonate reservoirs with 40 acre well spacing. This response surface is qualitatively very similar to the one presented at Figure 8.3 for 20 acre well spacing cases. Quantitatively it is seen from vertical axis that lower CO_2 credit is needed if 40 acre well spacing is utilized for CO_2 injection. This is aligned with the fact presented at Figure 8.2. It has already been shown that project profit is maximum in the well spacing around 40 acres and it decreases, as well spacing increases or decreases. Similarly, higher CO_2 incentives should be needed if well spacing decreases or increases from 40 acre.

Similar mathematical relations and response surfaces were obtained for projects' profit with and without accounting for constant CO_2 storage credit (assumed 2.5 $/Mscf).

8.5 QUANTIFYING UNCERTAINTIES FOR CO_2 CREDIT

After obtaining all mathematical relations (response surfaces equations) between CO_2 credit and input uncertain parameters shown in Table 8.2, a Monte Carlo-type risk analysis was also performed to assess the effect of Probability Distribution Functions (PDF) of uncertain input parameters on the CO_2 credit. Hence, a probability distribution function was also determined for CO_2 credit. PD functions for input parameters and their range of variations for the risk analysis are shown in Figure 8.5 through 8.10. It is seen that lognormal distributions are defined for operation cost, oil price, drilling cost, and flood performance. Also discount rate was modeled as a triangular PD function and CO_2 price was considered to have normal distribution function. For each response equation, more than 1000 Monte Carlo simulations were performed. Therefore, PDF of CO_2 credit for different simulation scenarios was defined. Figure 8.11 shows the PDF of CO_2 credit for CO_2 injection at sandstone reservoirs in 40 acre well spacing simulations. Figure 8.12 also shows the PDF of CO_2 credit for WAG injection at carbonate reservoirs in 40 acre

well spacing. The general conclusion is that usually in WAG injection there is greater need for CO_2 credit than for continuous CO_2 injection scenarios. This is probably due to lower amount of stored CO_2 in WAG injection compared to the continuous CO_2 injection. It is seen from Figure 8.12 that there is possibility of 83 % need for CO_2 credit for WAG injection in carbonate reservoirs and the mean of credit is equal to 7.1 $/Mscf of CO_2. Figures 8.13 and 8.14 also show the PDF for CO_2 credit for continuous CO_2 injection in carbonate reservoirs at 40 and 20 acre well spacing, respectively. The mean for CO_2 credit in 40 acre well spacing cases is 4.9 $/Mscf with 59 % probability and for 20 acre well spacing scenarios it is 10 $/Mscf of injected CO_2 with the probability of 68 %. Our study shows that in general, 40 acre well spacing CO_2 flood projects require lower CO_2 credit than 20 acre well spacing. This aligned with our conclusion presented in Figure 8.2 showing that 40 is optimum (or close to optimum) well spacing for coupled CO_2 sequestration and EOR projects.

Since response surface equations have been determined for project profit (as $/bbl) with and without considering constant 2.5 $/Mscf as CO_2 credit, Monte-Carlo simulations also were preformed employing these equations. Same PDF data (Figures 8.5 through 8.10) were assumed for input variables to determine PDF for project profits. Figures 8.15 and 8.16 show the results of Monte-Carlo simulations on Project profit without and with considering constant CO_2 credit in WAG injection scenarios for sandstone reservoirs, respectively. Figure 8.15 shows that without considering any CO_2 credit, WAG injection projects in sandstone reservoirs result in average loss of 0.51 $/bbl of oil with probability of 45 %. When constant CO_2 credit of 2.5 $/ Mscf is added to the project cash flow, Figure 8.16 displays that the same projects will gain 4.22 $/bbl of oil with probability of 71%. This clearly shows the importance of assigning reasonable CO_2 credit as incentive for oil companies to consider sequestering CO_2 at the same time as oil is produced from mature oil fields.

Table 8.9 summarizes the results for all uncertainty analyses that were performed in this study. It is seen that sandstone reservoirs have higher probability of need for CO_2 incentives. This is mostly due to the typical reservoir characteristics that were applied in our study for sandstone and carbonates. For sandstone reservoirs we considered typical properties of Gulf Coast sandstone reservoirs and for carbonates, typical reservoir properties of West Texas reservoirs were utilized. It is also seen from table that the mean for project profit is lower in the WAG injection processes compared to continuous CO_2 injection; therefore, higher CO_2 credit is needed for WAG injection scenarios than continuous CO_2 injection. This could be because of jeopardizing the amount of injected and stored CO_2 by injecting water for mobility control. Table 8.9 shows that without any CO_2 credit, almost all of the simulation scenarios will result in negative profit but, with considering constant CO_2 credit of 2.5 $/Mscf as CO_2 credit, the calculated profit is positive. Higher probability of increased CO_2 costs (capture and transportation) in sequestration projects is the main reason for negative profit of these processes; otherwise CO_2 flooding has been performed for years in different reservoirs throughout the world utilizing inexpensive natural CO_2 streams without considering any CO_2 credit.

8.6 SUMMARY AND CONCLUSIONS

It is evident that without regulatory incentives for CCS projects, their technical capabilities can be limited effectively. Using CO_2 for both EOR and storage purposes provides added value of oil production. In addition, due to the very high CO_2 prices, some sort of incentives in the form of accelerated depreciation or direct tax credits can be defined by regulatory sectors to support large scale CCS projects. Therefore, an exploratory economic analysis based upon systematic compositional simulations of CO_2 EOR was performed to establish how much and what type of economic incentives might be needed to promote storage of CO_2 in oil reservoirs. Previous studies which have been

dealt with CO_2 tax incentives usually make superficial assumptions on actual CO_2 flood performance in terms of oil recovery and amount of stored CO_2. Performing detailed simulation study of EOR and CO_2 sequestration is feasible and desired for different types of oil reservoirs such as carbonate and sandstone reservoirs using appropriate and detailed geological and reservoir engineering models, rather than superficial flood performance assumptions to do economic analysis. This economic analysis study took into account factors such as capture and transportation costs. Also, the combination of reservoir parameters and economic factors such as, flood performance, oil price, operational costs of the flood, drilling cost, and project discount rate were studied to achieve comprehensive understanding of the financial performance of coupled CO_2 sequestration and EOR projects.

Considering uncertainties in the economic parameters of the projects, experimental design and the method of response surfaces along with Monte Carlo-based simulations were utilized to perform this study in a systematic, efficient and accurate manner. Possible CO_2 credits were also quantified in a probability based distribution functions for various uncertain economic and geologic characteristics in different projects.

Based on the uncertainty analysis, it was shown that the oil price dominates the economics of CO_2 EOR and storage; but besides of that, flood performance, CO_2 cost, and operational costs are other important variables. Our results show that sandstone reservoirs have higher probability of need for CO_2 incentives. This is mostly due to the typical reservoir characteristics that were applied in our study for sandstone and carbonate reservoirs. In addition, the mean for project profit is lower in the WAG injection processes compared to continuous CO_2 injection; therefore, higher CO_2 credit is needed for WAG injection scenarios than continuous CO_2 injection. This could be because of jeopardizing the amount of injected and stored CO_2 by injecting water for mobility control. Considering high CO_2 cost in coupled sequestration and EOR projects,

almost all of the simulation scenarios resulted in negative profit but, with taking into account constant CO_2 credit profitability achieved for most of them.

Table 8.1: Important characteristic differences between carbonate and sandstone reservoirs

	Carbonates	**Sandstones**
Permeability Distribution	Layered	Stochastic
Vertical to horizontal Perm. Ratio	0.01	0.1
Average porosity, frac.	0.11	0.23
Reservoir temperature, °F	110	150
Remaining oil saturation before flood, frac.	0.58	0.33
Remaining oil saturation after flood, frac.	0.32	0.18

Table 8.2: Sensitivity parameters for economic incentives study with their range of uncertainty

Symbol	**Factor**		**Low (-1)**	**Median (0)**	**High (1)**
A	Oil price, $/bbl		15	35	55
B	CO_2 price, $/mscf		1	2.5	4
C	Flood performance, mscf/bbl		7	12	20
D	Drilling cost, $mm/well		0.75	0.9	1.05
E	Discount rate, %		0.1	0.15	0.2
F	Operational costs	Fixed op. costs, $mm/month	0.0192	0.024	0.029
		Recycle costs, $/mscf	0.56	0.7	0.84
		Lift costs, $/bbl	0.32	0.4	0.48

Table 8.3: Setting of uncertain factors in all of 78 economic analysis sensitivity cases

Case #	**Oil Price**	**CO_2 Price**	**Performance**	**Drilling Cost**	**Operating Cost**	**Discount Rate**
1	0	-1	1	1	0	1
2	1	0	0	-1	1	1
3	0	0	0	1	1	-1
4	1	1	-1	1	1	-1
5	1	1	0	0	1	1
6	1	-1	1	-1	1	1
7	0	1	1	0	1	-1
8	1	0	0	1	-1	0

Table 8.3 Continued

9	1	0	1	0	0	0
10	-1	0	0	-1	0	0
11	-1	1	-1	0	0	0
12	1	1	-1	-1	0	1
13	-1	0	-1	-1	1	-1
14	1	0	-1	1	0	0
15	0	1	-1	1	0	1
16	-1	1	-1	-1	-1	-1
17	0	0	1	1	-1	-1
18	-1	0	1	0	0	-1
19	-1	0	-1	0	1	0
20	0	1	-1	-1	1	1
21	0	-1	0	0	0	-1
22	0	-1	0	1	-1	1
23	-1	-1	0	1	-1	-1
24	0	-1	0	-1	0	1
25	-1	-1	0	-1	-1	1
26	0	0	-1	-1	-1	1
27	0	-1	-1	0	0	0
28	1	1	0	0	-1	0
29	-1	1	0	1	0	1
30	0	-1	-1	-1	1	0
31	0	-1	-1	0	1	-1
32	0	-1	1	-1	-1	-1
33	1	-1	1	0	-1	-1
34	-1	1	1	1	1	1
35	-1	0	0	0	-1	1
36	-1	1	1	1	-1	0
37	-1	1	-1	-1	1	0
38	-1	0	1	-1	0	1
39	1	1	-1	0	0	-1
40	-1	-1	-1	1	1	0
41	-1	-1	1	0	1	0
42	1	-1	0	0	0	1
43	-1	0	-1	-1	-1	0
44	-1	-1	-1	-1	0	-1
45	0	1	1	-1	0	0
46	1	0	-1	0	-1	1
47	0	-1	1	1	1	0
48	1	-1	-1	0	1	0
49	-1	1	1	-1	0	-1
50	0	-1	0	-1	-1	0
51	0	0	0	0	0	1
52	-1	-1	1	1	-1	1
53	1	1	1	1	-1	1

Table 8.3 Continued

54	0	0	1	0	1	1
55	1	-1	0	1	1	1
56	0	0	-1	-1	0	-1
57	1	0	-1	1	1	1
58	0	0	0	0	-1	-1
59	1	0	-1	-1	-1	-1
60	-1	-1	-1	0	1	1
61	-1	0	-1	1	0	-1
62	0	-1	0	1	0	0
63	1	1	1	-1	1	0
64	-1	-1	1	-1	1	-1
65	-1	0	1	1	0	0
66	0	1	1	0	-1	1
67	1	0	1	1	1	-1
68	0	1	-1	1	-1	0
69	1	-1	-1	1	-1	-1
70	1	0	0	1	0	-1
71	-1	1	0	0	1	-1
72	0	1	0	-1	-1	-1
73	0	1	0	0	1	0
74	-1	-1	-1	0	-1	0
75	1	-1	0	-1	1	-1
76	-1	1	-1	1	-1	1
77	1	-1	1	-1	0	0
78	0	0	1	-1	-1	0

Table 8.4: Constant economic parameters in DCF calculations

Inflation in prices	fraction/yr	0.1
Royalty	fraction	0.125
Fed tax rate	frac	0.32
EOR tax credit	frac	0.2

Table 8.5: Results for all economic sensitivity scenarios corresponding 40 acre well spacing simulations

	Sandstone- CO_2 Injection			Carbonates- CO_2 Injection			Sandstone-WAG Injection			Carbonates-WAG Injection		
Case#	$/bbl, with fixed credit	$/bbl, with no credit	CO_2 Credit	$/bbl, with fixed credit	$/bbl, with no credit	CO_2 Credit	$/bbl, with fixed credit	$/bbl, with no credit	CO_2 Credit	$/bbl, with fixed credit	$/bbl, with no credit	CO_2 Credit
1	10.96	6.30	3.40	3.64	1.98	3.00	4.87	3.03	4.00	-1.48	-2.51	-6.00
2	17.36	14.57	13.00	6.73	5.73	14.30	10.80	9.69	22.00	0.60	0.24	1.70
3	12.99	7.39	3.29	7.96	5.35	5.15	6.28	3.14	2.50	2.33	-0.16	-0.16
4	22.46	19.16	14.50	14.31	12.80	21.10	16.18	14.34	19.50	5.99	4.53	7.70
5	14.63	11.83	10.60	5.74	4.74	11.75	7.51	6.41	14.50	-0.39	-1.01	-4.00
6	18.54	13.87	7.45	6.90	5.24	7.90	11.26	9.42	12.80	0.63	-0.41	-0.98
7	5.27	-4.09	-1.09	4.18	-0.14	-0.08	-7.03	-12.27	-5.85	-2.50	-6.68	-4.00
8	20.84	16.91	10.75	9.96	8.36	13.10	13.56	11.72	15.90	2.32	1.09	2.20
9	17.60	11.04	4.20	8.47	5.82	5.50	7.93	4.86	3.96	0.45	-1.60	-1.97
10	2.51	-1.42	-0.90	1.23	-0.37	-0.58	-2.06	-3.91	-5.30	-1.27	-2.50	-5.10
11	2.41	0.09	0.10	1.35	0.42	1.10	-1.18	-2.26	-5.20	-1.04	-1.75	-6.10
12	18.17	16.53	25.10	7.16	6.58	28.40	12.29	11.64	45.00	1.50	1.14	7.80
13	4.86	1.56	1.20	3.04	1.52	2.50	1.24	-0.60	-0.80	0.70	-0.76	-1.30
14	21.92	19.61	21.20	10.59	9.66	25.90	16.24	15.17	35.10	3.54	2.82	9.80
15	9.88	8.23	12.51	3.83	3.25	14.00	5.45	4.80	18.60	-0.16	-0.52	-3.60
16	3.83	0.53	0.40	2.72	1.20	2.00	-0.55	-2.39	-3.30	-0.09	-1.55	-2.70
17	12.59	3.24	0.86	7.54	3.22	1.85	2.45	-2.80	-1.33	0.70	-3.47	-2.10
18	1.84	-7.51	-2.03	0.98	-3.34	-1.93	-7.33	-12.57	-6.00	-2.52	-6.69	-4.00
19	3.74	1.42	1.54	1.82	0.89	2.40	0.69	-0.39	-0.90	-0.37	-1.09	-3.80
20	9.62	7.97	12.10	3.84	3.26	14.00	5.29	4.65	18.00	0.09	-0.27	-1.80
21	16.86	11.26	5.02	9.81	7.20	6.90	11.51	8.37	6.67	4.56	2.07	2.00

Table 8.5 Continued

22	12.80	10.00	8.95	4.58	3.58	8.90	8.03	6.93	15.70	0.14	-0.48	-1.90
23	7.72	2.11	0.94	4.01	1.41	1.35	3.26	0.12	0.10	1.20	-1.29	-1.30
24	12.38	9.58	8.60	4.60	3.60	9.00	7.79	6.68	15.10	0.58	-0.04	-0.15
25	4.70	1.90	1.70	1.57	0.57	1.40	1.55	0.45	1.00	-0.68	-1.30	-5.30
26	11.87	10.23	15.52	4.59	4.00	17.10	7.76	7.11	27.50	0.78	0.42	2.88
27	14.74	12.42	13.40	6.94	6.01	16.20	10.88	9.80	22.70	2.43	1.72	6.00
28	17.50	13.57	8.67	8.76	7.16	11.10	9.57	7.73	10.50	1.29	0.06	0.13
29	-1.36	-4.15	-3.73	-0.61	-1.61	-4.00	-5.59	-6.69	-15.20	-3.28	-3.90	-16.00
30	14.40	12.09	13.10	6.84	5.91	15.90	10.60	9.52	22.10	2.51	1.79	6.30
31	16.44	13.14	9.95	9.87	8.35	13.76	12.64	10.80	14.70	4.91	3.45	5.84
32	18.06	8.71	2.33	10.13	5.81	3.38	10.31	5.06	2.40	4.54	0.36	0.22
33	27.72	18.37	4.90	16.06	11.73	6.80	18.96	13.71	6.54	7.42	3.25	2.00
34	-7.13	-11.79	-6.32	-2.84	-4.50	-6.80	-13.35	-15.20	-20.60	-6.28	-7.32	-17.50
35	1.94	-0.85	-0.75	0.57	-0.43	-1.10	-1.78	-2.89	-6.50	-1.94	-2.56	-10.50
36	-4.21	-10.76	-4.12	-1.74	-4.40	-4.10	-12.91	-15.98	-13.00	-5.88	-7.93	-9.80
37	2.07	-0.24	-0.26	1.24	0.31	0.85	-1.46	-2.54	-5.85	-0.96	-1.68	-5.80
38	-1.55	-6.22	-3.32	-0.72	-2.38	-3.60	-6.84	-8.68	-11.75	-3.60	-4.64	-11.30
39	22.89	19.59	14.82	14.60	13.08	21.60	16.62	14.78	20.10	6.25	4.79	8.20
40	5.41	3.09	3.35	2.39	1.46	3.90	2.83	1.75	4.05	0.21	-0.50	-1.75
41	3.60	-2.96	-1.12	1.18	-1.47	-1.40	-1.97	-5.04	-4.10	-1.63	-3.68	-4.50
42	20.54	17.75	15.86	7.71	6.71	16.80	14.38	13.27	30.00	1.67	1.05	4.22
43	4.51	2.20	2.37	2.20	1.27	3.40	1.44	0.36	0.82	-0.07	-0.79	-2.70
44	7.14	3.83	2.90	4.07	2.56	4.23	4.29	2.45	3.35	1.88	0.42	0.70
45	3.95	-2.61	-0.99	2.50	-0.15	-0.14	-5.82	-8.89	-7.20	-3.22	-5.27	-6.40
46	20.06	18.41	27.95	7.74	7.15	30.70	14.40	13.75	53.10	1.98	1.62	11.10
47	12.42	5.87	2.25	5.35	2.70	2.55	5.49	2.42	1.95	-0.07	-2.11	-2.60
48	23.29	20.98	22.66	11.12	10.19	27.40	18.17	17.10	39.60	4.35	3.63	12.65
49	-3.33	-12.68	-3.40	-1.12	-5.45	-3.15	-14.65	-19.89	-9.50	-5.08	-9.26	-5.60

Table 8.5 Continued

50	14.92	10.99	7.00	6.91	5.31	8.30	9.91	8.07	10.90	2.10	0.87	1.80
51	9.62	6.83	6.10	3.60	2.60	6.50	4.45	3.35	7.60	-0.67	-1.29	-5.20
52	3.62	-1.05	-0.56	0.72	-0.94	-1.40	-1.07	-2.91	-3.90	-2.69	-3.73	-9.00
53	11.06	6.40	3.45	4.17	2.51	3.80	1.58	-0.27	-0.34	-3.30	-4.33	-10.50
54	5.69	1.03	0.55	2.03	0.37	0.55	-1.08	-2.93	-3.95	-2.83	-3.87	-9.20
55	19.94	17.14	15.32	7.42	6.42	16.10	13.80	12.69	28.70	1.32	0.70	2.80
56	15.03	11.73	8.87	9.37	7.85	12.95	10.49	8.65	11.75	4.14	2.68	4.60
57	19.36	17.71	26.90	7.45	6.87	29.40	13.76	13.11	50.60	1.72	1.36	9.40
58	14.38	8.77	3.91	8.83	6.22	5.95	7.70	4.56	3.62	2.98	0.48	0.48
59	25.20	21.90	16.58	15.69	14.18	23.34	19.74	17.90	24.35	7.57	6.11	10.50
60	4.54	2.89	4.39	1.61	1.03	4.45	2.30	1.65	6.40	-0.25	-0.61	-4.20
61	5.21	1.90	1.45	3.16	1.65	2.70	1.53	-0.31	-0.42	0.54	-0.93	-1.60
62	14.20	10.28	6.53	6.45	4.85	7.60	9.13	7.29	9.90	1.46	0.24	0.49
63	11.90	5.34	2.05	6.41	3.76	3.56	0.91	-2.16	-1.80	-1.42	-3.47	4.25
64	6.12	-3.23	-0.86	2.78	-1.54	-0.90	-0.77	-6.01	-2.87	0.56	-3.61	-2.20
65	-0.35	-6.91	-2.64	-0.36	-3.02	-2.85	-7.53	-10.60	-8.60	-3.97	-6.02	-7.30
66	2.94	-1.72	-0.92	1.13	-0.53	-0.81	-4.94	-6.78	-9.20	-4.21	-5.25	-12.60
67	20.17	10.82	2.90	12.37	8.04	4.63	9.03	3.79	1.80	3.35	-0.82	-0.49
68	11.66	9.35	10.10	5.78	4.85	13.00	6.74	5.66	13.10	0.88	0.16	0.58
69	26.99	23.69	17.92	16.38	14.86	24.50	22.25	20.41	27.75	8.33	6.87	11.70
70	23.40	17.79	7.94	14.43	11.82	11.35	15.74	12.60	10.00	5.83	3.33	3.36
71	0.11	-5.49	-2.45	0.59	-2.02	-1.90	-7.00	-10.14	-8.10	-2.53	-5.02	-5.10
72	11.27	5.67	2.52	7.56	4.95	4.75	3.31	0.17	0.13	1.44	-1.05	-1.10
73	7.88	3.95	2.51	4.12	2.52	3.95	1.14	-0.71	-0.96	-0.92	-2.15	-4.40
74	6.18	3.87	4.18	2.77	1.84	4.95	3.58	2.50	5.80	0.52	-0.20	-0.70
75	26.01	20.40	9.09	15.60	12.99	12.50	19.76	16.62	13.20	7.92	5.42	5.40
76	1.99	0.35	0.54	0.74	0.15	0.66	-0.97	-1.61	-6.30	-1.46	-1.82	-12.60
77	22.52	15.97	6.10	10.44	7.78	7.30	14.41	11.34	9.20	2.99	0.94	1.20
78	9.74	3.19	1.30	4.72	2.07	1.98	1.39	-1.68	-1.38	-0.92	-2.96	-3.60

Table 8.6: Results for all economic sensitivity scenarios corresponding 20 acre well spacing simulations

	Sandstone- CO_2 Injection			Carbonates- CO_2 Injection			Sandstone-WAG Injection			Carbonates-WAG Injection		
Case#	$/bbl, with fixed credit	$/bbl, with no credit	CO_2 Credit	$/bbl, with fixed credit	$/bbl, with no credit	CO_2 Credit	$/bbl, with fixed credit	$/bbl, with no credit	CO_2 Credit	$/bbl, with fixed credit	$/bbl, with no credit	CO_2 Credit
1	13.27	7.33	3.10	5.39	3.48	4.70	5.16	3.79	6.90	1.79	1.11	4.10
2	21.74	18.21	12.90	15.24	14.09	30.70	14.87	14.05	42.70	8.39	7.99	49.50
3	14.52	7.42	2.60	9.56	6.58	5.50	6.49	4.16	4.45	4.70	3.08	4.70
4	25.05	20.91	12.60	20.92	19.17	27.40	19.06	17.70	32.40	13.62	12.66	33.20
5	17.34	13.80	9.70	12.73	11.58	25.30	10.97	10.14	30.90	6.37	5.97	37.00
6	23.78	17.84	7.50	14.02	12.11	15.80	14.04	12.67	23.10	7.62	6.95	25.80
7	4.61	-7.30	-1.53	1.89	-3.08	-1.53	-7.63	-11.52	-7.40	-4.20	-6.91	-6.40
8	24.64	19.67	9.88	18.44	16.61	22.70	17.43	16.06	29.30	10.79	9.99	31.40
9	20.24	11.89	3.56	13.54	10.50	8.61	9.95	7.67	8.40	6.62	5.29	9.95
10	2.27	-2.70	-1.36	0.01	-1.82	-2.50	-2.96	-4.33	-7.90	-1.45	-2.25	-7.10
11	2.13	-0.77	-0.67	1.36	0.28	0.65	-1.08	-1.88	-5.90	-0.29	-0.76	-4.10
12	22.70	20.64	25.05	17.27	16.60	61.70	17.53	17.05	88.80	9.76	9.52	100.00
13	5.55	1.41	0.85	3.22	1.46	2.09	1.11	-0.25	-0.47	1.04	0.09	0.23
14	26.45	23.55	20.31	20.53	19.46	45.31	20.85	20.05	62.66	12.87	12.40	66.28
15	12.00	9.94	12.05	9.04	8.36	31.10	8.22	7.74	40.29	4.71	4.48	47.27
16	3.69	-0.44	-0.27	2.61	0.86	1.23	-0.38	-1.75	-3.20	-0.08	-1.03	-2.71
17	13.83	1.91	0.40	8.07	3.11	1.56	2.48	-1.41	-0.91	1.97	-0.73	-0.68
18	1.76	-10.15	-2.13	-2.77	-7.74	-3.90	-9.31	-13.20	-8.48	-6.06	-8.77	-8.10
19	4.29	1.39	1.20	2.33	1.25	2.92	0.77	-0.03	-0.10	0.75	0.28	1.51
20	11.67	9.61	11.64	8.72	8.04	29.90	7.78	7.30	38.02	4.57	4.33	45.76
21	19.86	12.77	4.50	13.36	10.38	8.69	12.16	9.82	10.51	8.65	7.03	10.83
22	16.31	12.78	9.04	10.18	9.04	19.72	10.68	9.86	29.95	5.48	5.07	31.44

Table 8.6 Continued

23	9.29	2.19	0.77	4.26	1.27	1.07	2.66	0.32	0.34	1.78	0.16	0.24
24	15.78	12.25	8.66	9.66	8.52	18.58	9.96	9.14	27.77	5.25	4.85	30.03
25	5.62	2.08	1.47	1.95	0.80	1.76	1.37	0.55	1.66	0.43	0.03	0.17
26	14.78	12.72	15.42	10.61	9.94	36.96	10.80	10.32	53.76	5.84	5.60	59.17
27	18.05	15.15	13.06	12.94	11.87	27.62	13.38	12.58	39.31	8.14	7.67	40.99
28	20.35	15.38	7.74	16.18	14.35	19.60	13.44	12.07	22.00	8.69	7.89	24.74
29	-3.33	-6.86	-4.85	-2.85	-3.99	-8.71	-6.72	-7.54	-22.91	-3.15	-3.55	-22.00
30	17.70	14.81	12.77	12.58	11.51	26.79	12.90	12.10	37.82	7.95	7.48	39.97
31	19.25	15.11	9.13	14.40	12.65	18.06	14.03	12.67	23.23	10.03	9.07	23.80
32	21.20	9.28	1.95	12.10	7.13	3.59	9.75	5.86	3.77	6.71	4.01	3.70
33	32.34	20.42	4.29	21.87	16.90	8.50	20.13	16.24	10.43	14.03	11.32	10.46
34	-11.74	-17.68	-7.44	-9.57	-11.47	-15.04	-16.85	-18.22	-33.26	-8.06	-8.73	-32.46
35	1.41	-2.13	-1.50	-0.19	-1.33	-2.91	-2.32	-3.14	-9.54	-1.24	-1.65	-10.21
36	-7.90	-16.25	-4.87	-7.13	-10.18	-8.35	-15.02	-17.31	-18.96	-8.32	-9.65	-18.16
37	1.79	-1.11	-0.96	1.00	-0.08	-0.18	-1.56	-2.36	-7.38	-0.48	-0.95	-5.08
38	-3.82	-9.76	-4.11	-5.16	-7.07	-9.27	-9.55	-10.92	-19.93	-4.90	-5.57	-20.72
39	25.63	21.49	12.98	21.74	19.99	28.54	19.83	18.47	33.86	14.28	13.33	34.96
40	6.79	3.89	3.36	3.66	2.58	6.01	3.10	2.30	7.19	1.98	1.51	8.09
41	4.74	-3.61	-1.08	-1.48	-4.53	-3.71	-4.28	-6.57	-7.19	-2.31	-3.64	-6.84
42	26.48	22.94	16.22	17.89	16.75	36.55	19.27	18.45	56.06	10.30	9.89	61.29
43	4.97	2.07	1.79	3.05	1.97	4.59	1.72	0.92	2.89	1.13	0.66	3.54
44	8.46	4.32	2.61	5.04	3.29	4.70	4.19	2.82	5.18	2.98	2.03	5.33
45	2.12	-6.23	-1.86	0.85	-2.20	-1.80	-6.50	-8.78	-9.62	-2.85	-4.18	-7.86
46	25.48	23.42	28.39	18.85	18.17	67.57	20.11	19.63	102.27	10.89	10.65	112.43
47	15.65	7.30	2.19	7.45	4.40	3.61	5.52	3.23	3.54	3.66	2.33	4.38
48	28.62	25.72	22.18	21.50	20.43	47.56	22.70	21.90	68.46	13.91	13.45	71.84
49	-5.61	-17.52	-3.68	-6.80	-11.77	-5.92	-16.58	-20.47	-13.16	-10.80	-13.51	-12.48
50	18.02	13.05	6.56	11.78	9.95	13.60	11.63	10.26	18.70	6.92	6.12	19.20

Table 8.6 Continued

51	11.58	8.04	5.69	7.52	6.38	13.92	6.28	5.46	16.58	3.57	3.17	19.64
52	4.11	-1.83	-0.77	-0.76	-2.67	-3.50	-2.25	-3.62	-6.61	-1.74	-2.42	-8.98
53	11.38	5.44	2.29	8.59	6.68	8.76	4.11	2.74	5.01	2.76	2.09	7.77
54	6.02	0.08	0.03	2.23	0.32	0.42	-1.41	-2.77	-5.07	-0.22	-0.89	-3.32
55	25.95	22.41	15.85	17.37	16.23	35.41	18.56	17.73	53.88	10.07	9.66	59.88
56	17.04	12.91	7.80	13.39	11.64	16.62	12.01	10.65	19.52	8.63	7.68	20.14
57	24.82	22.76	27.58	18.20	17.53	65.18	19.24	18.76	97.71	10.60	10.36	109.41
58	16.04	8.95	3.15	11.61	8.62	7.23	8.66	6.32	6.76	6.25	4.63	7.13
59	28.54	24.40	14.74	23.57	21.82	31.15	22.91	21.55	39.51	16.22	15.27	40.06
60	5.88	3.81	4.62	2.99	2.32	8.62	2.76	2.28	11.90	1.49	1.26	13.26
61	5.90	1.76	1.07	3.62	1.87	2.67	1.64	0.27	0.50	1.31	0.36	0.95
62	17.47	12.50	6.29	11.20	9.37	12.80	10.84	9.47	17.27	6.61	5.82	18.24
63	12.14	3.80	1.14	8.83	5.78	4.74	2.02	-0.26	-0.29	2.63	1.30	2.44
64	8.22	-3.70	-0.78	0.17	-4.80	-2.41	-3.46	-7.35	-4.72	-2.04	-4.75	-4.38
65	-1.58	-9.93	-2.97	-4.30	-7.35	-6.03	-9.65	-11.94	-13.08	-5.31	-6.64	-12.50
66	0.68	-5.26	-2.21	0.36	-1.55	-2.03	-5.20	-6.57	-11.99	-2.28	-2.96	-10.99
67	23.13	11.21	2.35	15.69	10.72	5.39	10.02	6.13	3.94	7.85	5.15	4.76
68	13.38	10.48	9.04	10.64	9.57	22.27	9.19	8.39	26.24	5.86	5.40	28.84
69	31.10	26.96	16.29	24.99	23.24	33.18	25.46	24.10	44.18	17.89	16.94	44.44
70	26.61	19.52	6.88	20.71	17.73	14.85	18.16	15.83	16.93	13.13	11.50	17.71
71	-0.63	-7.72	-2.72	-1.91	-4.89	-4.10	-7.82	-10.16	-10.87	-4.79	-6.42	-9.88
72	11.65	4.56	1.61	9.19	6.21	5.20	4.29	1.95	2.09	3.41	1.79	2.75
73	8.34	3.37	1.70	6.08	4.25	5.81	2.06	0.69	1.26	2.11	1.31	4.11
74	7.47	4.58	3.95	4.37	3.30	7.68	4.05	3.25	10.17	2.36	1.90	10.13
75	30.43	23.34	8.23	22.46	19.48	16.32	21.66	19.33	20.67	15.53	13.90	21.41
76	1.63	-0.43	-0.52	1.13	0.45	1.69	-0.66	-1.14	-5.94	-0.19	-0.42	-4.48
77	27.45	19.10	5.72	17.31	14.27	11.71	16.60	14.32	15.68	10.12	8.79	16.54
78	10.22	1.87	0.56	5.56	2.52	2.07	1.43	-0.86	-0.94	1.14	-0.18	-0.35

Table 8.7: Response equations for CO_2 credit at different major sensitivity scenarios

Well Spacing	**Injection Scheme**	**Reservoir Rock Type**	**Response Equation for CO_2 Credit as \$/Mscf** (symbols shown in Table 8.2)
40 Acre Spacing	CO_2 Injection	Carbonates	7.64+0.64×A-0.095×B-2.05×C-2.55×D-0.08×E+38.96×F-0.0025×A×B-0.029×A×C-0.046×A×D+9.35e-5×A×E+1.22×A×F-0.0093×B×C-0.4516×B×D+0.0093×B×E-3.29×B×F+0.033×C×D-0.0002×C×E-2.89×C×F+0.09×D×E-34.14×D×F-0.289×E×F-0.0003×A^2-0.029×B^2+0.09×C^2+3.89×D^2-0.0001×E^2+48.16×F^2
		Sandstones	5.82+0.44×A+0.16×B-1.44×C-5.43×D-0.08×E+33.18×F-0.0027×A×B-0.024×A×C-0.047×A×D+9.24e-5×A×E+1.7×A×F-0.011×B×C-0.63×B×D+0.0084×B×E-3.004×B×F+0.073×C×D-0.0003×C×E-3.97×C×F+0.097×D×E-21.88×D×F-0.337×E×F-0.00023×A^2-0.0653×B^2+0.074×C^2+4.86×D^2-2.5e-5×E^2+79.99×F^2
	WAG Injection	Carbonates	1.08+0.36×A+1.33×B-1.11×C-15.09×D-0.04×E+151.59×F+0.01×A×B-0.02×A×C-0.13×A×D-0.001×A×E+1.08×A×F+0.02×B×C-1.83×B×D+0.02×B×E-12.66×B×F-0.18×C×D+0.001×C×E-2.95×C×F-0.02×D×E-41.58×D×F+0.0002×A^2-0.09×B^2+0.06× C^2+15.37× D^2-0.0003× E^2-427.62× F^2
		Sandstones	9.35+0.63×A+1.75×B-2.37×C-15.18×D-0.18×E+76.25×F-0.006×A×B-0.04×A×C-0.13×A×D+0.0001×A×E+4.67×A×F-0.033×B×C-2.007×B×D+0.018×B×E-14.73×B×F+0.2854×C×D-0.0009×C×E-10.92×C×F+0.24×D×E-58.29×D×F-0.812×E×F-0.0003×A^2-0.197×B^2+0.141×C^2+13.13×D^2+1.43e-5×E^2+233.84×F^2
20 Acre Spacing	CO_2 Injection	Carbonates	11.59+0.73×A+2.31×B-2.71×C-17.79×D-0.21×E+66.08×F-0.008×A×B-0.05×A×C-0.16×A×D+5.3e-5×A×E+5.58×A×F-0.032×B×C-2.38×B×D+0.019×B×E-5.31×B×F+0.329×C×D-0.0008×C×E-13.31×C×F+0.29×D×E-54.59×D×F-0.944×E×F-0.0002×A^2-0.24×B^2+0.165×C^2+14.98×D^2+6.9e-5×E^2+286.38× F^2
		Sandstones	5.08+0.38×A+0.57×B-1.33×C-6.17×D-0.082×E+36.12×F-0.003×A×B-0.0235×A×C-0.059×A×D+4.78e-5×A×E+2.08×A×F-0.013×B×C-0.86×B×D+0.008×B×E-4.93×B×F+0.11×C×D-0.0003×C×E-4.98×C×F+0.11×D×E-22.12×D×F-0.355×E×F-0.0002×A^2-0.084×B^2+0.073×C^2+5.49×D^2-1.2e-5× E^2+101.46× F^2
	WAG Injection	Carbonates	21.13+0.84×A+5.77×B-3.58×C-44.12×D-0.43×E+99.09×F-0.02×A×B-0.08×A×C-0.34×A×D-6.6e-5×A×E+11.4×A×F-0.07×B×C-5.18×B×D+0.03×B×E-14.9×B×F+0.73×C×D-0.002×C×E-27.3×C×F+0.57×D×E-107.4×D×F-1.58×E×F+6.78e-5×A^2-0.553×B^2+0.264×C^2+34.79×D^2+0.0005×E^2+647.06× F^2
		Sandstones	18.98+0.900×A+5.09×B-3.76×C-35.72×D-0.35×E+95.94×F-0.012×A×B-0.08×A×C-0.3×A×D+9.51e-5×A×E+9.89×A×F-0.065×B×C-4.53×B×D+0.031×B×E-21.74×B×F+0.65×C×D-0.0018×C×E-23.43×C×F+0.5×D×E-90.82×D×F-1.73×E×F-0.0003×A^2-0.44×B^2+0.25×C^2+28.46×D^2+0.00015×E^2+593.17× F^2

Table 8.8: Ranking the effect of uncertain parameters on CO_2 credit response.

Rank	Carbonates		Sandstones	
	WAG	**CO_2**	**WAG**	**CO_2**
1	A	A	A	A
2	C	C	C	C
3	F	C^2	C^2	C^2
4	B	AC	B	AC
5	C^2	B	AC	B
6	AC	AF	AF	AF
7	F^2	CF	CF	CF
8	CF	E	F	F
9	BF	F	BF	E
10	AF	EF	E	EF

Table 8.9: Summary of the final results for uncertainty analyses on CO_2 credit

	40 Acre Well Spacing				20 Acre Well Spacing			
	Carbonates		Sandstones		Carbonates		Sandstones	
	WAG	CO_2	WAG	CO_2	WAG	CO_2	WAG	CO_2
Probability of need for CO_2 credit,%	83.0	35.8	72.4	48.0	91.4	68.9	87.5	62.2
Profit, $/bbl	-2.0	0.9	-5.8	-0.5	-3.8	-2.1	-7.5	-2.4
Profit with 2.5 $/mscf as CO_2 credit, $/bbl	0.5	2.4	-1.5	4.2	0.1	1.3	-1.9	2.8

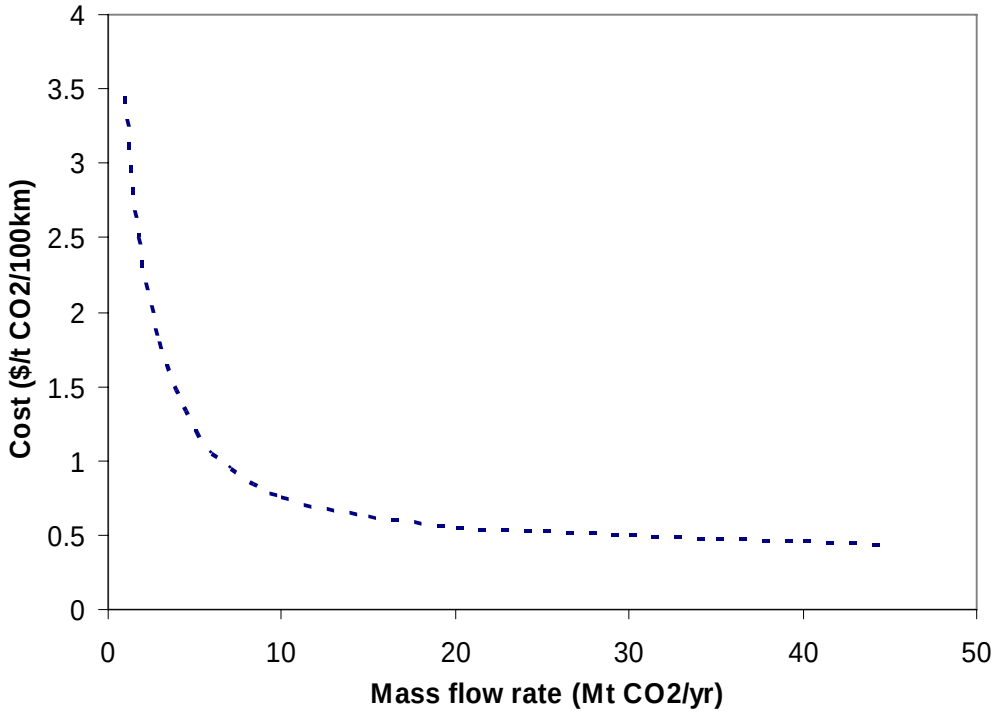

Figure 8.1- Cost associated with CO_2 transport through pipelines as a function of CO_2 mass flow rate (Heddle et al., 2003)

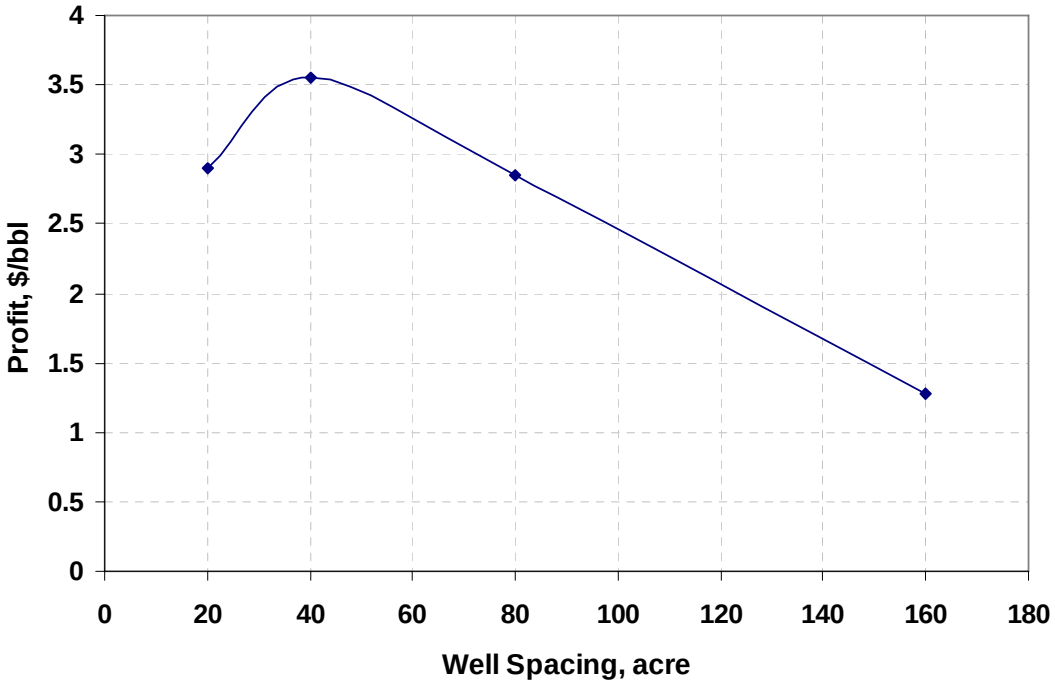

Figure 8.2- Profit, as NPV of each simulation scenario divided by total oil production, for CO_2 flooding simulations at different well spacing showing an optimum well spacing to obtain maximum profit

C: Performance =13
D: Drilling Costs =0.9 $mm/well
E: Operation Costs:
Fixed Op. Costs =0.03 $mm/mnth
Recycle Costs =0.8 $/Mscf
Lift Costs = 0.5 $/bbl
F: Discount Rate = 0.14

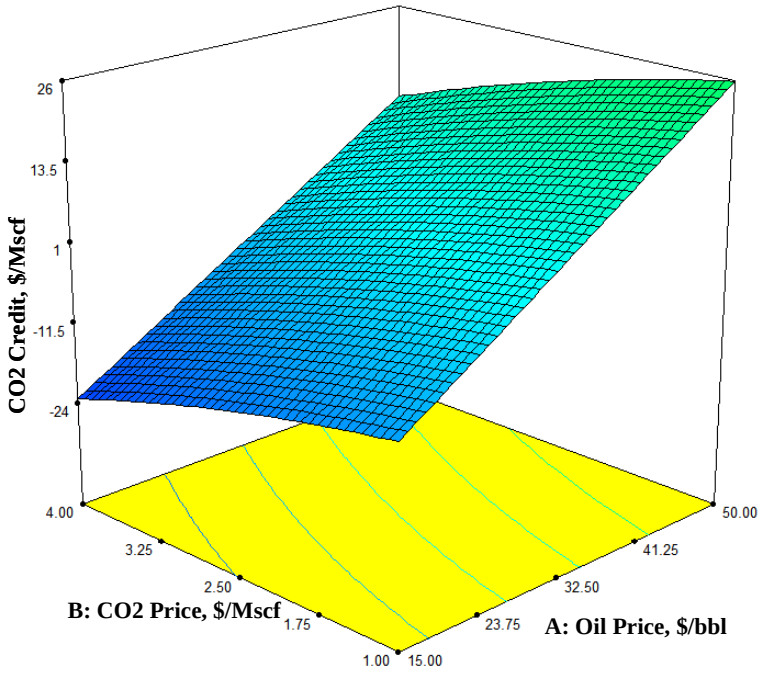

Figure 8.3- Response surface for CO_2 credit objective at different CO_2 prices, and oil prices and constant values for other factors (shown in the left) for WAG injection in carbonate reservoirs with 20 acre well spacing

C: Performance =13
D: Drilling Costs =0.9 $mm/well
E: Operation Costs:
Fixed Op. Costs =0.03 $mm/mnth
Recycle Costs =0.8 $/Mscf
Lift Costs = 0.5 $/bbl
F: Discount Rate = 0.14

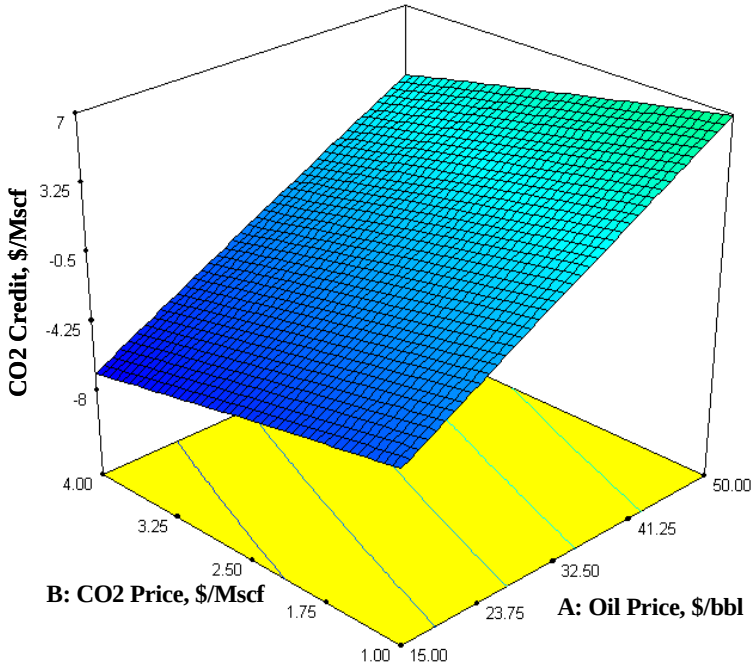

Figure 8.4- Response surface for CO_2 credit objective at different CO_2 prices, and oil prices and constant values for other factors(shown in the left) for WAG injection in carbonate reservoirs with 40 acre well spacing

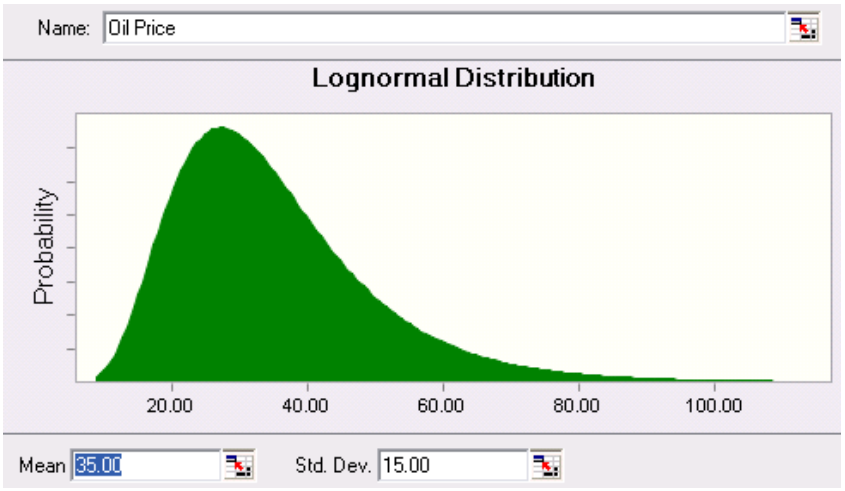

Figure 8.5- Assumed probability distribution function for oil price

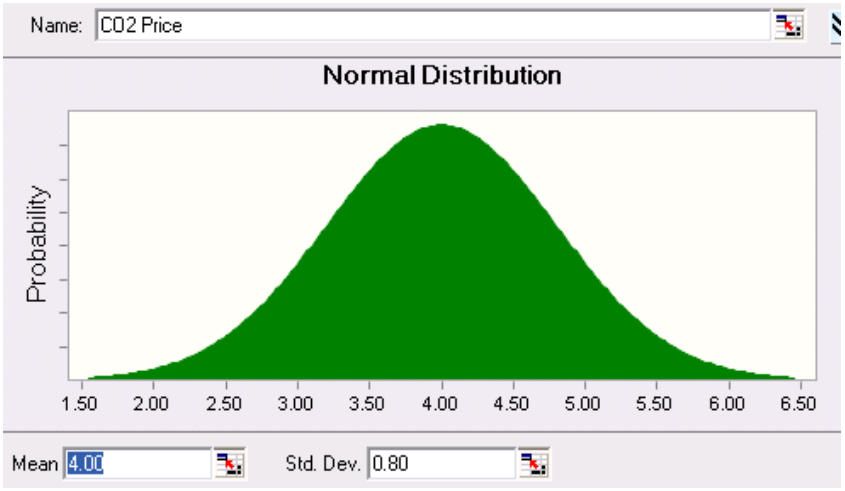

Figure 8.6- Assumed probability distribution function for CO_2 price

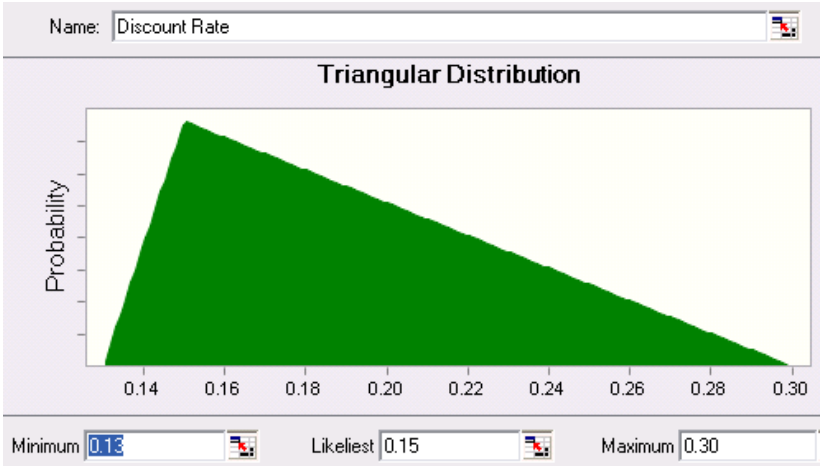

Figure 8.7- Assumed probability distribution function for discount rate

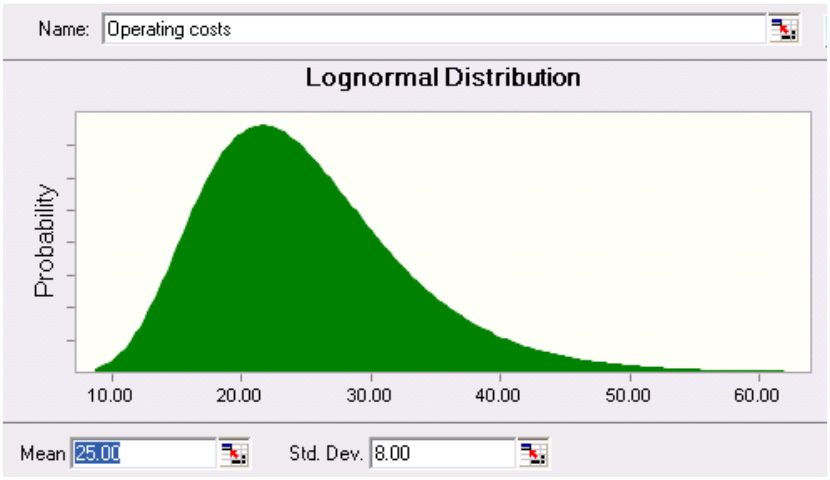

Figure 8.8- Assumed probability distribution function for operating costs

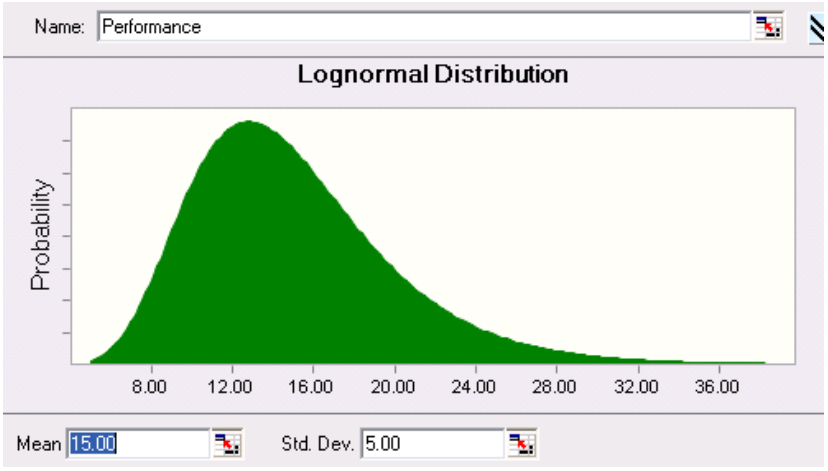

Figure 8.9- Assumed probability distribution function for flood performance

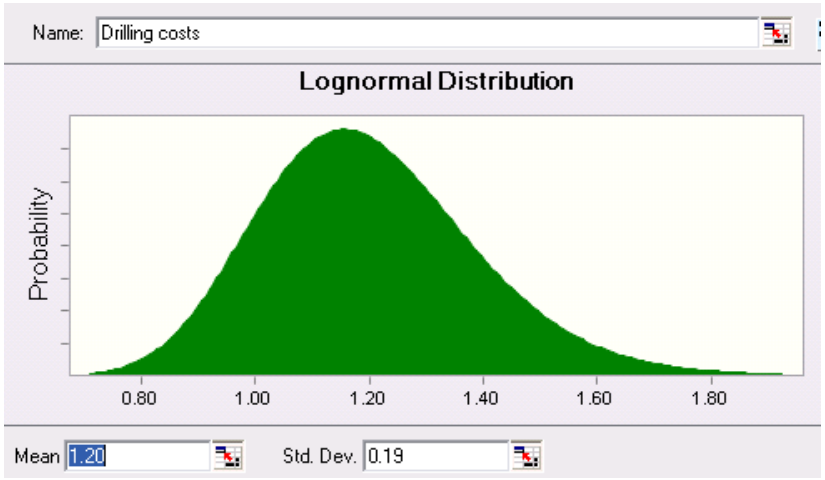

Figure 8.10- Assumed probability distribution function for drilling costs

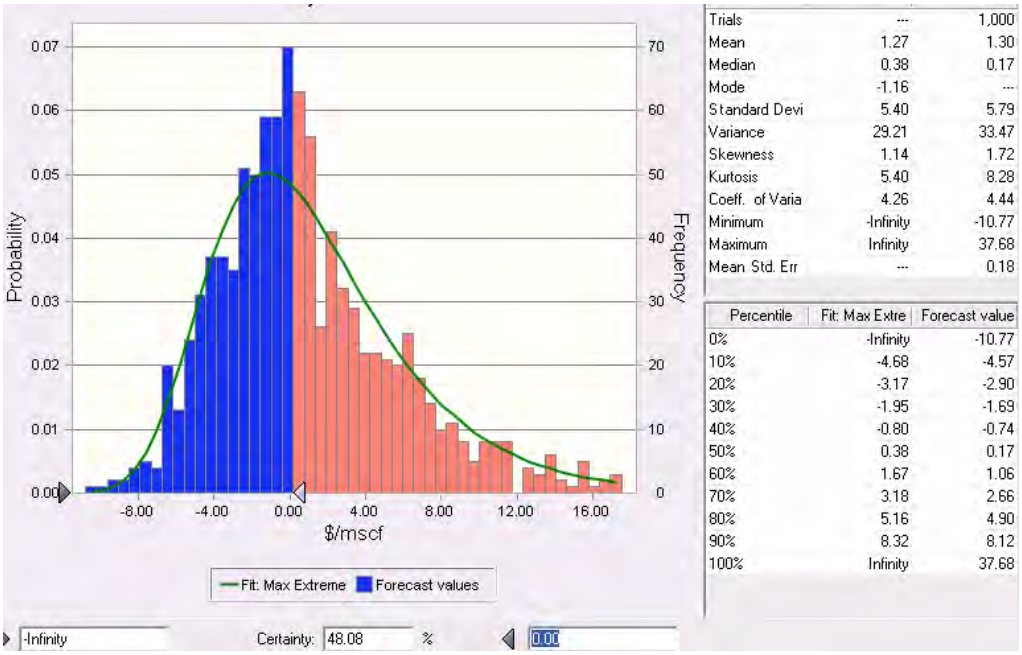

Trials	---	1,000
Mean	1.27	1.30
Median	0.38	0.17
Mode	-1.16	---
Standard Devi	5.40	5.79
Variance	29.21	33.47
Skewness	1.14	1.72
Kurtosis	5.40	8.28
Coeff. of Varia	4.26	4.44
Minimum	-Infinity	-10.77
Maximum	Infinity	37.68
Mean Std. Err	---	0.18

Percentile	Fit: Max Extre	Forecast value
0%	-Infinity	-10.77
10%	-4.68	-4.57
20%	-3.17	-2.90
30%	-1.95	-1.69
40%	-0.80	-0.74
50%	0.38	0.17
60%	1.67	1.06
70%	3.18	2.66
80%	5.16	4.90
90%	8.32	8.12
100%	Infinity	37.68

Figure 8.11- Probability Distribution function of CO_2 credit for continuous injection of CO_2 in sandstone reservoirs with 40 acre well spacing

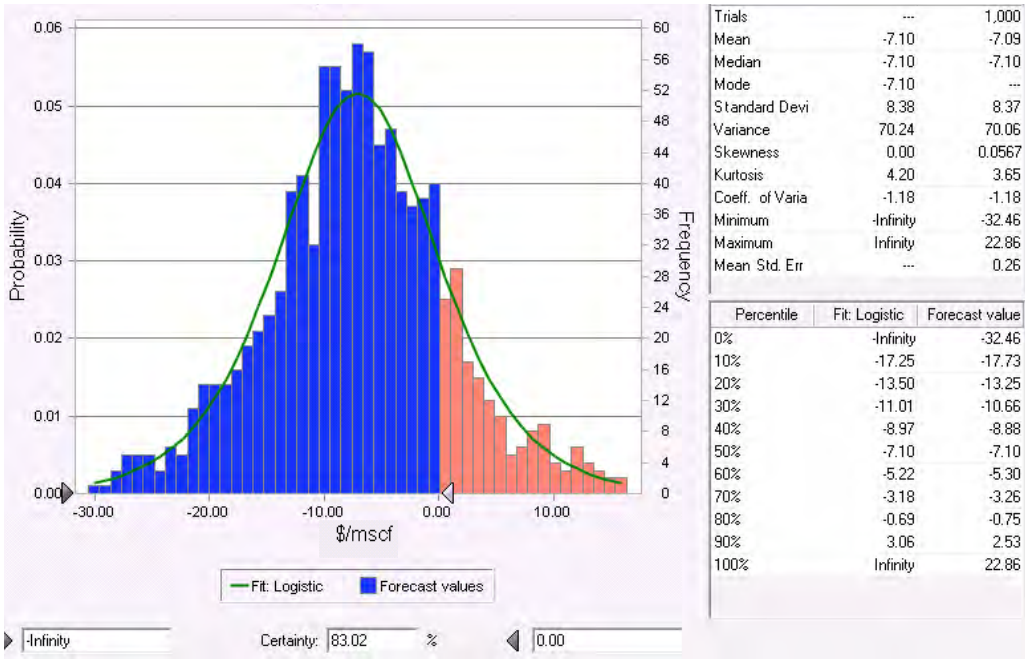

Trials	---	1,000
Mean	-7.10	-7.09
Median	-7.10	-7.10
Mode	-7.10	---
Standard Devi	8.38	8.37
Variance	70.24	70.06
Skewness	0.00	0.0567
Kurtosis	4.20	3.65
Coeff. of Varia	-1.18	-1.18
Minimum	-Infinity	-32.46
Maximum	Infinity	22.86
Mean Std. Err	---	0.26

Percentile	Fit: Logistic	Forecast value
0%	-Infinity	-32.46
10%	-17.25	-17.73
20%	-13.50	-13.25
30%	-11.01	-10.66
40%	-8.97	-8.88
50%	-7.10	-7.10
60%	-5.22	-5.30
70%	-3.18	-3.26
80%	-0.69	-0.75
90%	3.06	2.53
100%	Infinity	22.86

Figure 8.12- Probability distribution function of CO_2 credit for WAG injection of CO_2 in carbonate reservoirs with 40 acre well spacing

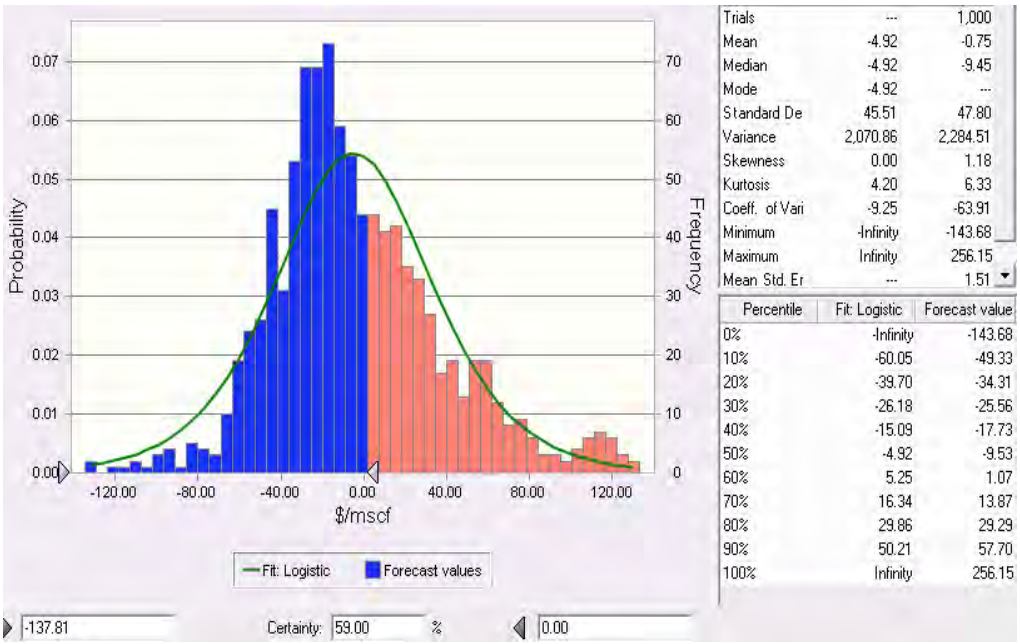

Figure 8.13- Probability distribution function for CO_2 credit for continuous injection of CO_2 in carbonate reservoirs with 40 acre well spacing

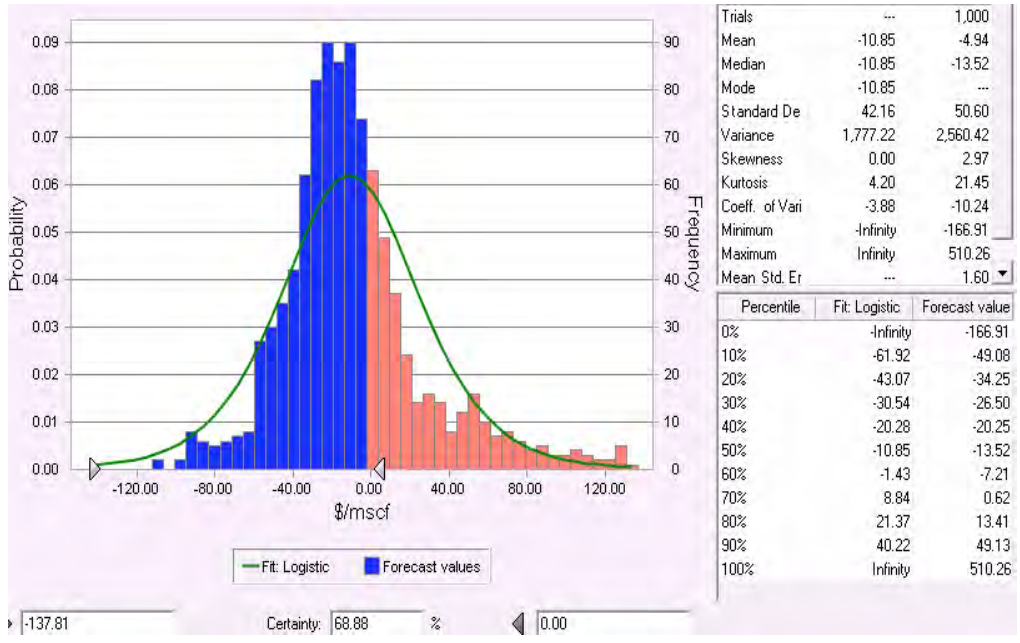

Figure 8.14- Probability distribution function of CO_2 credit for continuous injection of CO_2 in carbonate reservoirs with 20 acre well spacing

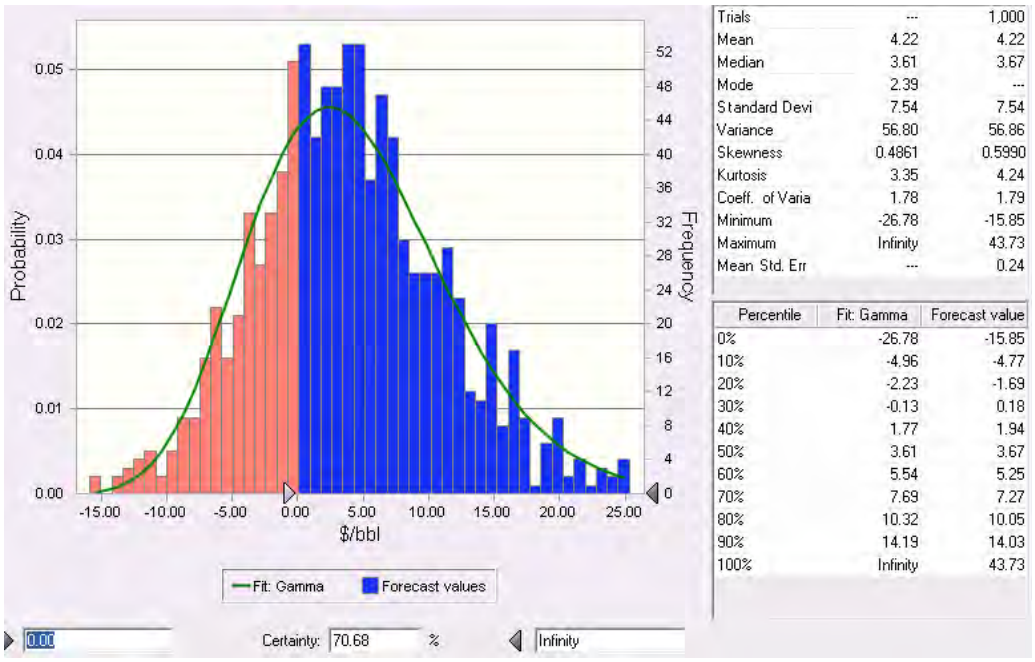

Trials	---	1,000
Mean	4.22	4.22
Median	3.61	3.67
Mode	2.39	---
Standard Devi	7.54	7.54
Variance	56.80	56.86
Skewness	0.4861	0.5990
Kurtosis	3.35	4.24
Coeff. of Varia	1.78	1.79
Minimum	-26.78	-15.85
Maximum	Infinity	43.73
Mean Std. Err	---	0.24

Percentile	Fit: Gamma	Forecast value
0%	-26.78	-15.85
10%	-4.96	-4.77
20%	-2.23	-1.69
30%	-0.13	0.18
40%	1.77	1.94
50%	3.61	3.67
60%	5.54	5.25
70%	7.69	7.27
80%	10.32	10.05
90%	14.19	14.03
100%	Infinity	43.73

Figure 8.15- Probability distribution function of project profit ($/bbl) for WAG injection of CO_2 in sandstone reservoirs considering 2.5 $/Mscf as constant CO_2 credit

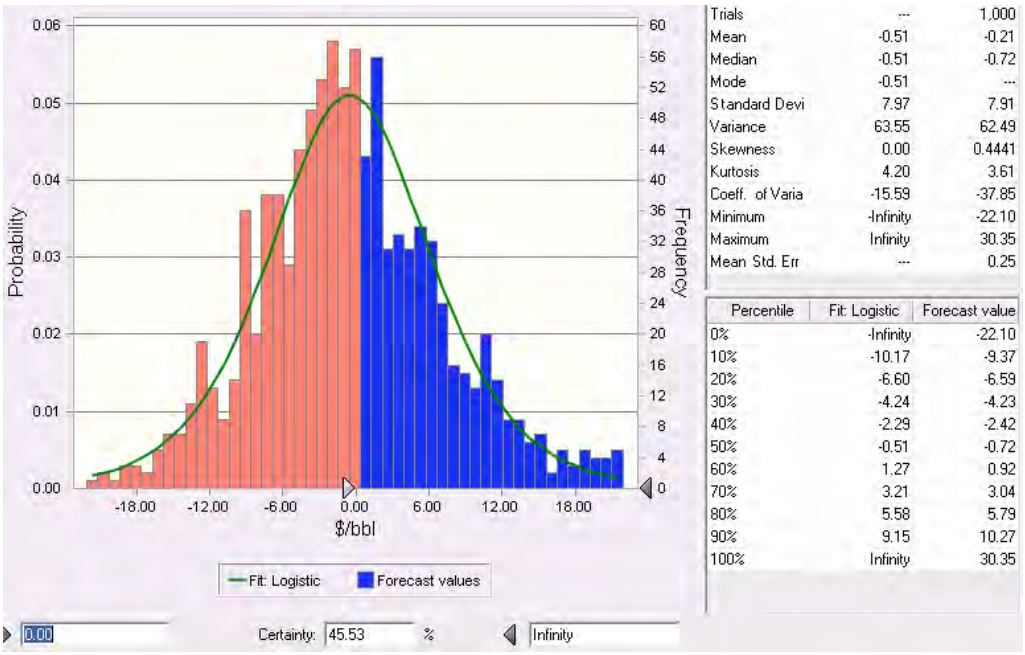

Trials	---	1,000
Mean	-0.51	-0.21
Median	-0.51	-0.72
Mode	-0.51	---
Standard Devi	7.97	7.91
Variance	63.55	62.49
Skewness	0.00	0.4441
Kurtosis	4.20	3.61
Coeff. of Varia	-15.59	-37.85
Minimum	-Infinity	-22.10
Maximum	Infinity	30.35
Mean Std. Err	---	0.25

Percentile	Fit: Logistic	Forecast value
0%	-Infinity	-22.10
10%	-10.17	-9.37
20%	-6.60	-6.59
30%	-4.24	-4.23
40%	-2.29	-2.42
50%	-0.51	-0.72
60%	1.27	0.92
70%	3.21	3.04
80%	5.58	5.79
90%	9.15	10.27
100%	Infinity	30.35

Figure 8.16- Probability distribution function of project profit ($/bbl) for WAG injection of CO_2 in sandstone reservoirs without considering any CO_2 credit

Chapter 9: Summary, Conclusions and Recommendations

9.1 Summary and Conclusions

Aquifer storage of CO_2 is one of the main options for reducing CO_2 level in atmosphere. As the first step in this research, a predictive and precise simulation model for the Frio brine pilot was built and accurately tuned to investigate different CO_2 injection scenarios before the actual field test starts. Then, a simulation model was validated by comparing the results with actual field data. This study showed that CO_2 breakthrough time was very close to the breakthrough time observed in the field test. In addition, the simulated gas saturation profiles taken at different times were in good agreement with the results inferred from the RST logs taken in the field.

As the second option for geological CO_2 storage, injecting CO_2 into mature oil reservoirs can increase the amount of oil produced, off setting some of the CO_2 storage expenses such as very high capture, transportation and compression costs. One of the goals of this research was to better understand the potential for both enhanced oil recovery and storage of CO_2 in mature oil reservoirs over a wide range of conditions. Compositional reservoir simulator was the main tool used to investigate this combined process. This study focused on assessing uncertainties in coupled CO_2 sequestration and EOR processes in generic 3-D reservoir models representing typical sandstone and carbonate reservoirs. Due to the vast amount of uncertainties in the reservoir parameters and different flooding designs and schemes, a large number of simulations were needed. To increase the efficiency of the study and save time and computational expenses, design of experiment and method of response surfaces were employed.

Based on the type and level of uncertainty of different parameters affecting the coupled CO_2 sequestration and EOR processes, the study was classified into different sections for which their corresponding conclusions are presented as follows:

Hysteresis and WAG Optimization Study:

Several uncertain parameters such as WAG ratio, CO_2 slug size, hysteresis, Dykstra-Parsons coefficient, and correlation lengths were studied to assess their effect on the amount of stored CO_2 and profit gained from the project in coupled CO_2 sequestration and EOR projects. The Effect of hysteresis on the amount of stored CO_2 and oil recovery is significant. Trapping of CO_2 in the reservoir as residual gas increases when hysteresis is accounted for in the simulation model.

Following the statistical analysis of the simulation results, it was concluded that the most to less influential factors for optimizing profit are the Dykstra-Parsons coefficient and combinations of WAG ratio and slug size; however, for optimizing CO_2 storage by far the most influential factor is the WAG ratio, followed by combinations of WAG ratio and hysteresis, and lastly hysteresis. In all cases, no significant reduction of profit occurred when the storage of CO_2 was maximized.

Flood Design Optimization:

Different flood design parameters such as the produced gas-oil ratio constraint, well spacing, production and injection well types, operational constraints for production and injection wells, injection scheme (WAG or continuous CO_2 injection), shut/open strategy, recycling, along with some important reservoir characteristics such as Kv/Kh and average reservoir permeability were studied to determine effective flood design strategies for coupled CO_2 EOR and sequestration.

This study showed that carbonate reservoirs, typical of the Permian Basin, are preferable to sandstone reservoirs, typical of the U.S. Gulf Coast, for combined CO_2 EOR and sequestration projects. According to the statistical analysis, the most sensitive design parameters are the GOR constraint on the production wells, well spacing, injection scheme (WAG or continuous CO_2 injection) and combinations of them. Optimal well types in sandstone reservoirs are vertical producers and horizontal injectors and in carbonate reservoirs, are combination of both vertical producers and injectors. It was

concluded that well spacing is more important when optimizing both profit and storage objective functions with equal weighting whereas, it is less important when maximizing only the storage objective. Based on our results the optimum well spacing is smaller for carbonate reservoirs than for sandstone reservoirs.

Derivation of Dimensionless Scaling Groups for CO_2 Flooding:

Scaling groups are useful for reducing the number of variables that need to be considered and in generalizing results. Inspectional analysis was employed to derive dimensionless scaling groups for CO_2 flooding in three-dimensional oil reservoirs. Special emphasis was given to the phase behavior equations, which are used as auxiliary equations in any compositional simulation.

The governing equations for CO_2 flooding include 41 parameters and 27 dependent variables.Inspectional analysis showed that 17 dimensionless groups are needed to scale the governing equations for CO_2 flooding. Fourteen of the 17 scaling groups are related to the flow equations and the other three groups are related to the equation-of-state equation used for the phase behavior calculations.

Development of Response Surface-Based Correlation for MMP:

Multivariate regression analysis based on the response surface method was used along with four dimensionless scaling groups (reduced temperature and acentric factor for the light pseudo component and for the heavy pseudo component) to develop a comprehensive MMP correlation between CO_2 and broad range of reservoir crude oils. The new MMP correlation was compared with the predictions from six published correlations. The average error for the new correlation was less than any of the published correlations.

Investigation of Economic Incentives for Coupled CO_2 Sequestration and EOR:

The main economic concern in coupled CO_2 sequestration and EOR projects is the very high CO_2 prices typical of CO_2 capture from power plants. In this part of the

study, economic incentives were investigated to determine how much incentive would be needed to make such projects profitable. Economic calculations based upon results from compositional simulations were performed to quantify the need for CO_2 credits. Different simulation scenarios were performed to account for uncertainties in flood performance. In addition, various economic parameters with their range of uncertainties were studied by employing experimental design and Monte-Carlo-based simulations to perform this study in efficient manner.

This study showed that as expected, the oil price dominates the economics of CO_2 EOR and storage, but flood performance, CO_2 cost, and operational costs are also significant variables. Almost all of the calculations showed that the projects would be unprofitable when using costs typical of current CO_2 capture from power plants unless there is some form of credit for storage.

Considering all of the foregoing conclusions and despite the differences in the assumptions between CO_2 EOR and CO_2 storage in oil reservoirs, no significant differences in terms of flood design and favorable reservoir characteristics were observed between these two objectives. In other words, reservoirs that are good candidates for CO_2-EOR projects are good candidates for coupled sequestration and EOR as well. Similar flood designs can be applied for coupled CO_2 sequestration and EOR projects compared to EOR projects.

CO_2 EOR is profitable in the Permian Basin because there is an abundant supply of inexpensive CO_2 from naturally occurring sources, the existing infrastructure, and the favorable reservoir conditions. When the CO_2 must be captured and transported long distances and new infrastructure installed, then both EOR and coupled EOR and sequestration become much more expensive.

9.2 RECOMMENDATIONS AND FUTURE WORK

Even though comprehensive uncertainty analysis was performed on different parameters and factors affecting coupled CO_2 sequestration and EOR processes, there still remain some other reservoir parameters and design variables to be considered for further studies. It is almost impossible to account for all of the variables at the same time and all together. Therefore, derived scaling group variables along with the results from flood design optimization study can be utilized to achieve more comprehensive results. Experimental design and the response surface method can help to obtain efficient methodology and more accurate results.

More emphasis on the phase behavior related factors such as the effect of impurities at the CO_2 stream on the flood performance and amount of stored CO_2 is another concern that was not given enough attention in our study. Since most of the produced CO_2 stream by power plants and other emission sources are contaminated with some other gases such as N_2, H_2S, and etc, it is important to perform this type of study. It was shown that the cost to separate CO_2 from these gases is dominating the project economics; therefore an optimization study can be performed to see what level and what type of impurities should be allowed in injectant stream for coupled CO_2 sequestration and EOR projects to still achieve relatively high profit as well as high amount of stored CO_2. In other words, how much capture costs can be reduced without jeopardizing the coupled CO_2 sequestration and EOR flood performance.

Since most of the coupled CO_2 sequestration and EOR projects will be performed in mature oil fields, it is necessary to account for modifications on well configuration in the target reservoirs. Therefore, it is imperative to examine the effect of additional injectors and producers to be drilled during life of the project. This will give a dynamic nature to the problem compared to what was performed in our study. Addition of time as another uncertain variable could affect the outcome results significantly. Questions such as "what type of wells to be added?" and "what time they should be added?" will change

the economic pattern of the process. Therefore, it is recommended to perform detailed studies considering dynamic factors for coupled CO_2 sequestration and EOR projects in addition to static uncertain variables which were mostly investigated in this study.

Appendix A: Derivations of Scaling Groups for Miscible CO_2 Flooding

In this appendix, miscible displacement of residual oil phase (subscript 2) by gas phase (subscript 3) which is considered as pure CO_2, following by water flooding is non-dimensionalized. Governing equations for this process are conservation equations, Darcy's equations, capillary pressure equations, phase equilibrium equations and two auxiliary equations as:

$$\frac{\partial}{\partial t}\phi\sum_{j=1}^{n_p} x_{ij}\rho_j S_j + \nabla\bullet\sum_{j=1}^{n_p} x_{ij}\rho_j \vec{u}_j - \nabla\bullet\phi\sum_{j=1}^{n_p}\overrightarrow{\overrightarrow{K}}_{ij}\cdot\nabla\rho_j x_{ij} = 0 \qquad i=1,...,n_c \qquad j=1,...,n_p \quad \text{(A.1)}$$

$$\vec{u}_j = -\frac{kk_{rj}}{\mu_j}(\nabla P_j + \rho_j \overrightarrow{g}) \qquad j=1,...,n_p \quad \text{(A.2)}$$

$$P_j - P_k = P_{ckj} = j(S)\sigma_{kj}\sqrt{\frac{\phi}{k}} \qquad j=1,...,n_p, \qquad k=1,...,n_p, \qquad k\neq j \quad \text{(A.3)}$$

$$K_i^{j,k} = \frac{C_{ij}}{C_{ik}} \qquad i=1,...,n_c, \qquad j=1,...,n_p, \qquad k=1,n_p, \qquad k\neq j \quad \text{(A.4)}$$

$$\sum_{i=1}^{n_c} x_{ij} = 1 \qquad i=1,...,n_c \qquad j=1,...,n_p \quad \text{(A.5)}$$

$$\sum_{j=1}^{n_p} S_j = 1 \qquad j=1,...,n_p \quad \text{(A.6)}$$

It should be noted that conservation equations are slightly modified in order to reduce the number of variables that have to be dealt with. In order to do this, $\rho_j x_{ij}$ (product of phase density and component mole fraction) was assumed to be C_{ij} which is the phase concentration of component

Introducing arbitrary scaling factors:

Two arbitrary scaling factors are introduced for each variable. In total, 56 scaling factors are introduced (corresponding to 28 original variables) in which 28 of them are additive and the rest are multiplicative scaling factors. Following linear transformations

convert all of the original variables into dimensionless format. In all of these equations, scaling parameters with "*" sign as superscript, are considered as arbitrary scaling factors. In addition, variables with subscript "D" are final dimensionless variables that are going to replace dimensional variables.

$$C_{21} \equiv C^*_{212} C_{21D} + C^*_{211} \qquad S_1 \equiv S^*_{12} S_{1D} + S^*_{11} \qquad P_1 \equiv P^*_{12} P_{1D} + P^*_{11} \qquad u_{x1} \equiv u^*_{x12} u_{x1D} + u^*_{x11}$$
$$C_{22} \equiv C^*_{222} C_{22D} + C^*_{221} \qquad S_2 \equiv S^*_{22} S_{2D} + S^*_{21} \qquad P_2 \equiv P^*_{22} P_{2D} + P^*_{21} \qquad u_{x2} \equiv u^*_{x22} u_{x2D} + u^*_{x21}$$
$$C_{23} \equiv C^*_{232} C_{23D} + C^*_{231} \qquad S_3 \equiv S^*_{32} S_{3D} + S^*_{31} \qquad P_3 \equiv P^*_{32} P_{3D} + P^*_{31} \qquad u_{x3} \equiv u^*_{x32} u_{x3D} + u^*_{x31}$$
$$C_{31} \equiv C^*_{312} C_{31D} + C^*_{311} \qquad u_{z1} \equiv u^*_{z12} u_{z1D} + u^*_{z11}$$
$$C_{32} \equiv C^*_{322} C_{32D} + C^*_{321} \qquad u_{z2} \equiv u^*_{z22} u_{z2D} + u^*_{z21}$$
$$C_{33} \equiv C^*_{332} C_{33D} + C^*_{331} \qquad x \equiv x^*_2 x_D + x^*_1 \qquad u_{z3} \equiv u^*_{z32} u_{z3D} + u^*_{z31}$$
$$C_{41} \equiv C^*_{412} C_{41D} + C^*_{411} \qquad y \equiv y^*_2 y_D + y^*_1 \qquad u_{y1} \equiv u^*_{z12} u_{z1D} + u^*_{z11}$$
$$C_{42} \equiv C^*_{422} C_{42D} + C^*_{421} \qquad z \equiv z^*_2 z_D + z^*_1 \qquad u_{y1} \equiv u^*_{z12} u_{z1D} + u^*_{z11}$$
$$C_{43} \equiv C^*_{432} C_{43D} + C^*_{431} \qquad t \equiv t^*_2 t_D + t^*_1 \qquad u_{y1} \equiv u^*_{z12} u_{z1D} + u^*_{z11}$$

Replacing Dimensional Variables with Scaling Factors in Conservation Equations:

By expanding the derivatives in each conservation equation, and then by introducing scaling factors, their size will grow rapidly and it will be going to hard to handle all of the terms at the same time. Therefore, it was decided to split the terms in each conservation equations and continue with each term separately and then lump the final results back into the original equation. Following is the general form for conservation equation considering all of the assumptions that were made at the beginning of our derivation.

Conservation Equation for Light Oil Component:

Arbitrary scaling factors are introduced into the conservation equation for light oil component. Expanding this equation will give:

$$\frac{\partial}{\partial t}(\phi C_{21} S_1) + \frac{\partial}{\partial t}(\phi C_{22} S_2) + \frac{\partial}{\partial t}(\phi C_{23} S_3) + \frac{\partial}{\partial x}(u_{1x} C_{21}) + \frac{\partial}{\partial x}(u_{2x} C_{22}) + \frac{\partial}{\partial x}(u_{3x} C_{23}) + \frac{\partial}{\partial x}(u_{1y} C_{21}) + \frac{\partial}{\partial x}(u_{2y} C_{22}) + \frac{\partial}{\partial x}(u_{3y} C_{23}) + \frac{\partial}{\partial z}(u_{1z} C_{21}) + \frac{\partial}{\partial z}(u_{2z} C_{22}) + \frac{\partial}{\partial z}(u_{3z} C_{23}) = 0 \qquad \text{(A.7)}$$

and using product rules in derivatives we have:

$$\begin{aligned}
&\left(\phi S_1 \frac{\partial C_{21}}{\partial t} + \phi C_{21} \frac{\partial S_1}{\partial t}\right) + \left(\phi S_2 \frac{\partial C_{22}}{\partial t} + \phi C_{22} \frac{\partial S_2}{\partial t}\right) + \left(\phi S_3 \frac{\partial C_{23}}{\partial t} + \phi C_{23} \frac{\partial S_3}{\partial t}\right) + \\
&+ \left(C_{21} \frac{\partial u_{1x}}{\partial x} + u_{1x} \frac{\partial C_{21}}{\partial x}\right) + \left(C_{22} \frac{\partial u_{2x}}{\partial x} + u_{2x} \frac{\partial C_{22}}{\partial x}\right) + \left(C_{23} \frac{\partial u_{3x}}{\partial x} + u_{3x} \frac{\partial C_{23}}{\partial x}\right) + \\
&+ \left(C_{21} \frac{\partial u_{1y}}{\partial y} + u_{1y} \frac{\partial C_{21}}{\partial y}\right) + \left(C_{22} \frac{\partial u_{2y}}{\partial y} + u_{2y} \frac{\partial C_{22}}{\partial y}\right) + \left(C_{23} \frac{\partial u_{3y}}{\partial y} + u_{3y} \frac{\partial C_{23}}{\partial y}\right) + \\
&+ \left(C_{21} \frac{\partial u_{1z}}{\partial z} + u_{1z} \frac{\partial C_{21}}{\partial z}\right) + \left(C_{22} \frac{\partial u_{2z}}{\partial z} + u_{2z} \frac{\partial C_{22}}{\partial z}\right) + \left(C_{23} \frac{\partial u_{3z}}{\partial z} + u_{3z} \frac{\partial C_{23}}{\partial z}\right) = 0
\end{aligned} \tag{A.8}$$

Accumulation terms:

Substituting the arbitrary scale factors for the first accumulation term, $\left(\phi S_1 \frac{\partial C_{21}}{\partial t} + \phi C_{21} \frac{\partial S_1}{\partial t}\right)$, gives:

$$\begin{aligned}
&\left(\phi\left(S_{12}^* S_{1D} + S_{11}^*\right) \frac{\partial\left(C_{212}^* C_{21D} + C_{211}^*\right)}{\partial(t_2^* t_D + t_1^*)} + \phi\left(C_{212}^* C_{21D} + C_{211}^*\right) \frac{\partial\left(S_{12}^* S_{1D} + S_{11}^*\right)}{\partial(t_2^* t_D + t_1^*)}\right) = \\
&= \left(\frac{\phi}{t_2^*}\left(S_{12}^* S_{1D} + S_{11}^*\right) \frac{\partial\left(C_{212}^* C_{21D}\right)}{\partial t_D} + \frac{\phi}{t_2^*}\left(C_{212}^* C_{21D} + C_{211}^*\right) \frac{\partial\left(S_{12}^* S_{1D}\right)}{\partial t_D}\right) =
\end{aligned} \tag{A.9}$$

and then expanding:

$$\begin{aligned}
&= \left(\begin{array}{l}
\frac{\phi(S_{12}^* C_{212}^*)}{t_2^*} S_{1D} \frac{\partial\left(C_{21D}\right)}{\partial t_D} + \frac{\phi(S_{11}^* C_{212}^*)}{t_2^*} \frac{\partial\left(C_{21D}\right)}{\partial t_D} + \frac{\phi(C_{212}^* S_{12}^*)}{t_2^*} C_{21D} \frac{\partial\left(S_{1D}\right)}{\partial t_D} + \\
+ \frac{\phi(C_{211}^* S_{12}^*)}{t_2^*} \frac{\partial\left(S_{1D}\right)}{\partial t_D}
\end{array}\right) = \\
&= \left(\frac{\phi(S_{12}^* C_{212}^*)}{t_2^*} \frac{\partial\left(S_{1D} C_{21D}\right)}{\partial t_D} + \frac{\phi(S_{11}^* C_{212}^*)}{t_2^*} \frac{\partial\left(C_{21D}\right)}{\partial t_D} + \frac{\phi(C_{211}^* S_{12}^*)}{t_2^*} \frac{\partial\left(S_{1D}\right)}{\partial t_D}\right)
\end{aligned} \tag{A.10}$$

Since we do not want the original form of the equation to be changed and also C_{211}^* and S_{11}^* are arbitrary scale-factors we can set them equal to zero; hence equation (A.10) is turned into a much simpler form of:

$$\phi \frac{\partial (C_{21} S_1)}{\partial t} \equiv \left[\frac{\phi (S_{12}^* C_{212}^*)}{t_2^*} \right] \frac{\partial (S_{1D} C_{21D})}{\partial t_D} \tag{A.11}$$

therefore, the first part of the accumulation term is transformed to a dimensionless form of equation (A.11).

Similarly, we can have the same type of derivations for other two parts of accumulation term in the conservation equation; and hence:

$$\begin{aligned} \phi \frac{\partial (C_{22} S_2)}{\partial t} &\equiv \left[\frac{\phi (C_{222}^* S_{22}^*)}{t_2^*} \right] \frac{\partial (C_{22D} S_{2D})}{\partial t_D} \\ \phi \frac{\partial (C_{23} S_3)}{\partial t} &\equiv \left[\frac{\phi (C_{232}^* S_{32}^*)}{t_2^*} \right] \frac{\partial (C_{23D} S_{3D})}{\partial t_D} \end{aligned} \tag{A.12}$$

In obtaining above two equations, C_{221}^*, C_{231}^* and S_{21}^*, S_{31}^* are set to zero since they are arbitrary scale-factors. In summary, for non-dimensionalizing accumulation terms in one of the conservation equations (light oil component equation) these assumptions have been made for arbitrary scaling factors.

$$\begin{aligned} C_{211}^* = C_{221}^* = C_{231}^* = 0 \\ S_{21}^* = S_{31}^* = S_{41}^* = 0 \end{aligned} \tag{A.13}$$

<u>*Convection Term in x direction:*</u>

Substituting the arbitrary scale factors for the x direction convection term in the light oil component conservation equation, $\left(C_{21} \frac{\partial u_{1x}}{\partial x} + u_{1x} \frac{\partial C_{21}}{\partial x} \right)$, gives:

$$\begin{aligned} &\left(\left(C_{212}^* C_{21D} + C_{211}^* \right) \frac{\partial \left(u_{1x2}^* u_{1xD} + u_{1x1}^* \right)}{\partial (x_2^* x_D + x_1^*)} + \left(u_{1x2}^* u_{1xD} + u_{1x1}^* \right) \frac{\partial \left(C_{212}^* C_{21D} + C_{211}^* \right)}{\partial (x_2^* x_D + x_1^*)} \right) = \\ &= \left(\frac{\left(C_{212}^* C_{21D} + C_{211}^* \right)}{x_2^*} \frac{\partial \left(u_{1x2}^* u_{1xD} \right)}{\partial x_D} + \frac{\left(u_{1x2}^* u_{1xD} + u_{1x1}^* \right)}{x_2^*} \frac{\partial \left(C_{212}^* C_{21D} \right)}{\partial x_D} \right) = \end{aligned} \tag{A.14}$$

and then expanding:

$$
\begin{aligned}
&= \left(\begin{array}{l} \dfrac{(C^*_{212}u^*_{1x2})}{x^*_2} C_{21D} \dfrac{\partial(u_{1xD})}{\partial x_D} + \dfrac{(C^*_{211}u^*_{1x2})}{x^*_2} \dfrac{\partial(u_{1xD})}{\partial x_D} + \dfrac{(C^*_{212}u^*_{1x2})}{x^*_2} u_{1xD} \dfrac{\partial(C_{21D})}{\partial x_D} + \\ + \dfrac{(C^*_{212}u^*_{1x1})}{x^*_2} \dfrac{\partial(C_{21D})}{\partial x_D} \end{array} \right) = \\
&= \left(\frac{(C^*_{212}u^*_{1x2})}{x^*_2} \frac{\partial(C_{21D}u_{1xD})}{\partial x_D} + \frac{(C^*_{211}u^*_{1x2})}{x^*_2} \frac{\partial(u_{1xD})}{\partial x_D} + \frac{(C^*_{212}u^*_{1x1})}{x^*_2} \frac{\partial(C_{21D})}{\partial x_D} \right)
\end{aligned}
\tag{A.15}
$$

From equation (A.13) we have $C^*_{211} = C^*_{221} = C^*_{231} = 0$ and Since we do not want the original form of equation also to be changed and u^*_{1x1} is an arbitrary scale-factor, we can set it equal to zero; hence above equation is reduced to:

$$
\frac{\partial(C_{21}u_{1x})}{\partial x} \equiv \left[\frac{(C^*_{212}u^*_{1x2})}{x^*_2} \right] \frac{\partial(C_{21D}u_{1xD})}{\partial x_D} \tag{A.16}
$$

Therefore, the first part of the convection term in X direction is transformed to a dimensionless form of equation (A.16). Similarly, we can have the same type of derivations for other two parts of convection term in the conservation equation; and hence,

$$
\begin{aligned}
\frac{\partial(C_{22}u_{2x})}{\partial x} &\equiv \left[\frac{(C^*_{222}u^*_{2x2})}{x^*_2} \right] \frac{\partial(C_{22D}u_{2xD})}{\partial x_D} \\
\frac{\partial(C_{23}u_{3x})}{\partial x} &\equiv \left[\frac{(C^*_{232}u^*_{3x2})}{x^*_2} \right] \frac{\partial(C_{23D}u_{3xD})}{\partial x_D}
\end{aligned}
\tag{A.17}
$$

In obtaining above two equations, u^*_{2x1}, u^*_{3x1} are set to zero since they are arbitrary scale-factors. In summary, for non-dimensionalizing convection terms in x direction for conservation equation of light oil component, these assumptions have been made for arbitrary scaling factors.

$$u^*_{1x1} = u^*_{2x1} = u^*_{3x1} = 0 \tag{A.18}$$

Convection Term in y direction:

Substituting the arbitrary scale factors for the y direction convection term in the light oil component conservation equation, $\left(C_{21} \frac{\partial u_{1y}}{\partial y} + u_{1y} \frac{\partial C_{21}}{\partial y} \right)$, gives:

$$\left(\left(C^*_{212} C_{21D} + C^*_{211} \right) \frac{\partial \left(u^*_{1y2} u_{1yD} + u^*_{1y1} \right)}{\partial (y^*_2 y_D + y^*_1)} + \left(u^*_{1y2} u_{1yD} + u^*_{1y1} \right) \frac{\partial \left(C^*_{212} C_{21D} + C^*_{211} \right)}{\partial (y^*_2 y_D + y^*_1)} \right) =$$

$$= \left(\frac{\left(C^*_{212} C_{21D} + C^*_{211} \right)}{y^*_2} \frac{\partial \left(u^*_{1y2} u_{1xD} \right)}{\partial y_D} + \frac{\left(u^*_{1y2} u_{1yD} + u^*_{1y1} \right)}{y^*_2} \frac{\partial \left(C^*_{212} C_{21D} \right)}{\partial y_D} \right) = \tag{A.19}$$

and then expanding it:

$$= \left(\begin{array}{l} \frac{(C^*_{212} u^*_{1y2})}{y^*_2} C_{21D} \frac{\partial \left(u_{1yD} \right)}{\partial y_D} + \frac{(C^*_{211} u^*_{1y2})}{y^*_2} \frac{\partial \left(u_{1yD} \right)}{\partial y_D} + \frac{(C^*_{212} u^*_{1y2})}{y^*_2} u_{1yD} \frac{\partial \left(C_{21D} \right)}{\partial y_D} + \\ + \frac{(C^*_{212} u^*_{1y1})}{y^*_2} \frac{\partial \left(C_{21D} \right)}{\partial y_D} \end{array} \right) = \tag{A.20}$$

$$= \left(\frac{(C^*_{212} u^*_{1y2})}{y^*_2} \frac{\partial \left(C_{21D} u_{1yD} \right)}{\partial y_D} + \frac{(C^*_{211} u^*_{1y2})}{y^*_2} \frac{\partial \left(u_{1yD} \right)}{\partial y_D} + \frac{(C^*_{212} u^*_{1y1})}{y^*_2} \frac{\partial \left(C_{21D} \right)}{\partial y_D} \right)$$

From equation (A.14) we have $C^*_{211} = C^*_{221} = C^*_{231} = 0$ and Since we do not want the original form of equation also to be changed and u^*_{1y1} is an arbitrary scale-factor, we can set it equal to zero; hence above equation is reduced to

$$\frac{\partial \left(C_{21} u_{1y} \right)}{\partial y} \equiv \left[\frac{(C^*_{212} u^*_{1y2})}{y^*_2} \right] \frac{\partial \left(C_{21D} u_{1yD} \right)}{\partial y_D} \tag{A.21}$$

hence, the first part of the convection term in y direction is transformed to the dimensionless form shown by equation (A.21). Similarly, we can have the same type of

derivations for other two parts of convection term in the conservation equation; and hence,

$$\frac{\partial\left(C_{22}u_{2y}\right)}{\partial y} \equiv \left[\frac{(C^*_{222}u^*_{2y2})}{y^*_2}\right]\frac{\partial\left(C_{22D}u_{2yD}\right)}{\partial y_D}$$
$$\frac{\partial\left(C_{23}u_{3y}\right)}{\partial y} \equiv \left[\frac{(C^*_{232}u^*_{3y2})}{y^*_2}\right]\frac{\partial\left(C_{23D}u_{3yD}\right)}{\partial y_D} \qquad \text{(A.22)}$$

In obtaining above two equations, u^*_{2y1}, u^*_{3y1} are set to zero since they are arbitrary scale-factors. In summary, for non-dimensionalizing convection terms in y direction for conservation equation of light oil component, these assumptions have been made for arbitrary scaling factors.

$$u^*_{1y1} = u^*_{2y1} = u^*_{3y1} = 0 \qquad \text{(A.23)}$$

Convection Term in Z direction:

Substituting the arbitrary scale factors for the Z direction convection term in the light oil component conservation equation, $\left(C_{21}\frac{\partial u_{1z}}{\partial z} + u_{1z}\frac{\partial C_{21}}{\partial z}\right)$, gives:

$$\left(\left(C^*_{212}C_{21D} + C^*_{211}\right)\frac{\partial\left(u^*_{1z2}u_{1zD} + u^*_{1z1}\right)}{\partial(z^*_2 z_D + z^*_1)} + \left(u^*_{1z2}u_{1zD} + u^*_{1z1}\right)\frac{\partial\left(C^*_{212}C_{21D} + C^*_{211}\right)}{\partial(z^*_2 z_D + z^*_1)}\right) =$$
$$= \left(\frac{\left(C^*_{212}C_{21D} + C^*_{211}\right)}{z^*_2}\frac{\partial\left(u^*_{1z2}u_{1zD}\right)}{\partial z_D} + \frac{\left(u^*_{1z2}u_{1zD} + u^*_{1z1}\right)}{z^*_2}\frac{\partial\left(C^*_{212}C_{21D}\right)}{\partial z_D}\right) = \qquad \text{(A.24)}$$

and then expanding:

$$= \left(\begin{array}{l} \dfrac{(C^*_{212}u^*_{1z2})}{z^*_2} C_{21D} \dfrac{\partial(u_{1zD})}{\partial z_D} + \dfrac{(C^*_{211}u^*_{1z2})}{z^*_2} \dfrac{\partial(u_{1zD})}{\partial z_D} + \dfrac{(C^*_{212}u^*_{1z2})}{z^*_2} u_{1zD} \dfrac{\partial(C_{21D})}{\partial z_D} + \\ + \dfrac{(C^*_{212}u^*_{1z1})}{z^*_2} \dfrac{\partial(C_{21D})}{\partial z_D} \end{array} \right) =$$

$$= \left(\frac{(C^*_{212}u^*_{1z2})}{z^*_2} \frac{\partial(C_{21D}u_{1zD})}{\partial z_D} + \frac{(C^*_{211}u^*_{1z2})}{z^*_2} \frac{\partial(u_{1zD})}{\partial z_D} + \frac{(C^*_{212}u^*_{1z1})}{z^*_2} \frac{\partial(C_{21D})}{\partial z_D} \right) \tag{A.25}$$

From equation (A.13) we have $C^*_{211} = C^*_{221} = C^*_{231} = 0$ and Since we don't want the original form of equation also to be changed and u^*_{1z1} is an arbitrary scale-factor, we can set it equal to zero; hence above equation is reduced to

$$\frac{\partial(C_{21}u_{1z})}{\partial z} \equiv \left[\frac{(C^*_{212}u^*_{1z2})}{z^*_2} \right] \frac{\partial(C_{21D}u_{1zD})}{\partial z_D} \tag{A.26}$$

so the first part of the convection term in z direction is transformed to a dimensionless form of equation (A.26). Similarly, we can have the same type of derivations for other two parts of convection term in the conservation equation; and hence:

$$\begin{aligned} \frac{\partial(C_{22}u_{2z})}{\partial z} &\equiv \left[\frac{(C^*_{222}u^*_{2z2})}{z^*_2} \right] \frac{\partial(C_{22D}u_{2zD})}{\partial z_D} \\ \frac{\partial(C_{23}u_{3z})}{\partial z} &\equiv \left[\frac{(C^*_{232}u^*_{3z2})}{z^*_2} \right] \frac{\partial(C_{23D}u_{3zD})}{\partial z_D} \end{aligned} \tag{A.27}$$

In obtaining above two equations, u^*_{2z1}, u^*_{3z1} are set to zero since they are arbitrary scale-factors. In summary, for non-dimensionalizing convection terms in z direction for conservation equation of light oil component, these assumptions have been made for arbitrary scaling factors.

$$u^*_{1z1} = u^*_{2z1} = u^*_{3z1} = 0 \tag{A.28}$$

In summary, following assumptions have been made on arbitrary scaling factors which are inferred from equations A.13, A.18, A.23, and A.28.

$$
\begin{aligned}
&u^*_{1x1} = u^*_{2x1} = u^*_{3x1} = 0 \\
&u^*_{1y1} = u^*_{2y1} = u^*_{3y1} = 0 \\
&u^*_{1z1} = u^*_{2z1} = u^*_{3z1} = 0 \\
&C^*_{211} = C^*_{221} = C^*_{231} = 0 \\
&S^*_{21} = S^*_{31} = S^*_{41} = 0
\end{aligned}
\tag{A.29}
$$

According to the above derivations, the conservation equation for component 2 is converted to the following dimensionless form.

$$
\begin{aligned}
\equiv &\left(\left[\frac{\phi(S^*_{12}C^*_{212})}{t^*_2} \right] \frac{\partial\left(S_{1D}C_{21D}\right)}{\partial t_D} + \left[\frac{\phi(C^*_{222}S^*_{22})}{t^*_2} \right] \frac{\partial\left(C_{22D}S_{2D}\right)}{\partial t_D} + \right. \\
&\left. + \left[\frac{\phi(C^*_{232}S^*_{32})}{t^*_2} \right] \frac{\partial\left(C_{23D}S_{3D}\right)}{\partial t_D} \right) + \\
+ &\left(\left[\frac{(C^*_{212}u^*_{1x2})}{x^*_2} \right] \frac{\partial\left(C_{21D}u_{1xD}\right)}{\partial x_D} + \left[\frac{(C^*_{222}u^*_{2x2})}{x^*_2} \right] \frac{\partial\left(C_{22D}u_{2xD}\right)}{\partial x_D} + \right. \\
&\left. + \left[\frac{(C^*_{232}u^*_{3x2})}{x^*_2} \right] \frac{\partial\left(C_{23D}u_{3xD}\right)}{\partial x_D} \right) + \\
+ &\left(\left[\frac{(C^*_{212}u^*_{1y2})}{y^*_2} \right] \frac{\partial\left(C_{21D}u_{1yD}\right)}{\partial y_D} + \left[\frac{(C^*_{222}u^*_{2y2})}{y^*_2} \right] \frac{\partial\left(C_{22D}u_{2yD}\right)}{\partial y_D} + \right. \\
&\left. + \left[\frac{(C^*_{232}u^*_{3y2})}{y^*_2} \right] \frac{\partial\left(C_{23D}u_{3yD}\right)}{\partial y_D} \right) + \\
+ &\left(\left[\frac{(C^*_{212}u^*_{1z2})}{z^*_2} \right] \frac{\partial\left(C_{21D}u_{1zD}\right)}{\partial z_D} + \left[\frac{(C^*_{222}u^*_{2z2})}{z^*_2} \right] \frac{\partial\left(C_{22D}u_{2zD}\right)}{\partial z_D} + \right. \\
&\left. + \left[\frac{(C^*_{232}u^*_{3z2})}{z^*_2} \right] \frac{\partial\left(C_{23D}u_{3zD}\right)}{\partial z_D} \right) = 0
\end{aligned}
\tag{A.30}
$$

Since the scale-parameters are arbitrary, we can assume following equalities:

$$
\begin{aligned}
&C^*_{212} = C^*_{222} = C^*_{232} = C^*_{22} \\
&S^*_{12} = S^*_{22} = S^*_{32} = S^*_2 \\
&u^*_{1x2} = u^*_{2x2} = u^*_{3x2} = u^*_{x2} \\
&u^*_{1y2} = u^*_{2y2} = u^*_{3y2} = u^*_{y2} \\
&u^*_{1z2} = u^*_{2z2} = u^*_{3z2} = u^*_{z2}
\end{aligned}
\tag{A.31}
$$

Therefore, equation (A.31) can be converted into the following dimensionless form:

$$
\begin{aligned}
&\left[\frac{\phi(S^*_2 C^*_{22})}{t^*_2}\right]\frac{\partial}{\partial t_D}\left(C_{21D}S_{1D} + C_{22D}S_{2D} + C_{23D}S_{3D}\right) + \\
&+\left[\frac{(C^*_{22}u^*_{x2})}{x^*_2}\right]\frac{\partial}{\partial x_D}\left(u_{1xD}C_{21D} + u_{2xD}C_{22D} + u_{3xD}C_{23D}\right) + \\
&+\left[\frac{(C^*_{22}u^*_{y2})}{y^*_2}\right]\frac{\partial}{\partial y_D}\left(u_{1yD}C_{21D} + u_{2yD}C_{22D} + u_{3yD}C_{23D}\right) + \\
&+\left[\frac{(C^*_{22}u^*_{z2})}{z^*_2}\right]\frac{\partial}{\partial z_D}\left(u_{1zD}C_{21D} + u_{2zD}C_{22D} + u_{3zD}C_{23D}\right) = 0
\end{aligned}
\tag{A.32}
$$

Rearranging the equation (A.32) gives:

$$
\begin{aligned}
&\frac{\partial}{\partial t_D}\left(C_{21D}S_{1D} + C_{22D}S_{2D} + C_{23D}S_{3D}\right) + \\
&+\left[\frac{u^*_{x2}t^*_2}{\phi S^*_2 x^*_2}\right]\frac{\partial}{\partial x_D}\left(u_{1xD}C_{21D} + u_{2xD}C_{22D} + u_{3xD}C_{23D}\right) + \\
&+\left[\frac{u^*_{y2}t^*_2}{\phi S^*_2 y^*_2}\right]\frac{\partial}{\partial y_D}\left(u_{1yD}C_{21D} + u_{2yD}C_{22D} + u_{3yD}C_{23D}\right) + \\
&+\left[\frac{u^*_{z2}t^*_2}{\phi S^*_2 z^*_2}\right]\frac{\partial}{\partial z_D}\left(u_{1zD}C_{21D} + u_{2zD}C_{22D} + u_{3zD}C_{23D}\right) = 0
\end{aligned}
\tag{A.33}
$$

In a very same way, conservation equations for other two components, CO_2, (subscript 3) and heavy oil component (subscript 4), can be written as following:

$$
\begin{aligned}
&\frac{\partial}{\partial t_D}\left(C_{31D}S_{1D}+C_{32D}S_{2D}+C_{33D}S_{3D}\right)+\\
&+\left[\frac{u_{x2}^{*}t_2^{*}}{\phi S_2^{*}x_2^{*}}\right]\frac{\partial}{\partial x_D}\left(u_{1xD}C_{31D}+u_{2xD}C_{32D}+u_{3xD}C_{33D}\right)+\\
&+\left[\frac{u_{y2}^{*}t_2^{*}}{\phi S_2^{*}y_2^{*}}\right]\frac{\partial}{\partial y_D}\left(u_{1yD}C_{31D}+u_{2yD}C_{32D}+u_{3yD}C_{33D}\right)+\\
&+\left[\frac{u_{z2}^{*}t_2^{*}}{\phi S_2^{*}z_2^{*}}\right]\frac{\partial}{\partial z_D}\left(u_{1zD}C_{31D}+u_{2zD}C_{32D}+u_{3zD}C_{33D}\right)=0
\end{aligned}
\qquad \text{(A.34)}
$$

and for heavy oil component:

$$
\begin{aligned}
&\frac{\partial}{\partial t_D}\left(C_{41D}S_{1D}+C_{42D}S_{2D}+C_{43D}S_{3D}\right)+\\
&+\left[\frac{u_{x2}^{*}t_2^{*}}{\phi S_2^{*}x_2^{*}}\right]\frac{\partial}{\partial x_D}\left(u_{1xD}C_{41D}+u_{2xD}C_{42D}+u_{3xD}C_{43D}\right)+\\
&+\left[\frac{u_{y2}^{*}t_2^{*}}{\phi S_2^{*}y_2^{*}}\right]\frac{\partial}{\partial y_D}\left(u_{1yD}C_{41D}+u_{2yD}C_{42D}+u_{3yD}C_{43D}\right)+\\
&+\left[\frac{u_{z2}^{*}t_2^{*}}{\phi S_2^{*}z_2^{*}}\right]\frac{\partial}{\partial z_D}\left(u_{1zD}C_{41D}+u_{2zD}C_{42D}+u_{3zD}C_{43D}\right)=0
\end{aligned}
\qquad \text{(A.35)}
$$

It should be noted that in order to obtain final form of equations (A.34) and (A.35), it was necessary to make following assumptions on arbitrary scaling factors.

$$
\begin{aligned}
&C_{311}^{*}=C_{321}^{*}=C_{331}^{*}=0\\
&C_{411}^{*}=C_{421}^{*}=C_{431}^{*}=0\\
&C_{312}^{*}=C_{322}^{*}=C_{332}^{*}=C_{32}^{*}\\
&C_{412}^{*}=C_{422}^{*}=C_{432}^{*}=C_{42}^{*}
\end{aligned}
\qquad \text{(A.36)}
$$

Replacing Dimensional Variables with Scaling Factors in Darcy's Equations

After substituting arbitrary scaling factors in the original Darcy equations, we have

$$
u_{1x2}^{*}u_{1xD}+u_{1x1}^{*}=-\frac{k_x k_{r1}}{\mu_1}\left(\frac{P_{12}^{*}}{x_2^{*}}\frac{\partial P_{1D}}{\partial x_D}+\rho_1 g\sin\alpha\right) \qquad \text{(A.37)}
$$

$$u^*_{1y2}u_{1zD}+u^*_{1y1}=-\frac{k_yk_{r1}}{\mu_1}\left(\frac{P^*_{12}}{y^*_2}\frac{\partial P_{1D}}{\partial y_D}+\rho_1 g\right) \tag{A.38}$$

$$u^*_{1z2}u_{1zD}+u^*_{1z1}=-\frac{k_zk_{r1}}{\mu_1}\left(\frac{P^*_{12}}{z^*_2}\frac{\partial P_{1D}}{\partial z_D}+\rho_1 g\cos\alpha\right) \tag{A.39}$$

$$u^*_{2x2}u_{2xD}+u^*_{2x1}=-\frac{k_xk_{r2}}{\mu_2}\left(\frac{P^*_{22}}{x^*_2}\frac{\partial P_{2D}}{\partial x_D}+\rho_2 g\sin\alpha\right) \tag{A.40}$$

$$u^*_{2y2}u_{2yD}+u^*_{2y1}=-\frac{k_yk_{r2}}{\mu_2}\left(\frac{P^*_{22}}{y^*_2}\frac{\partial P_{2D}}{\partial y_D}+\rho_2 g\right) \tag{A.41}$$

$$u^*_{2z2}u_{2zD}+u^*_{2z1}=-\frac{k_zk_{r2}}{\mu_2}\left(\frac{P^*_{22}}{z^*_2}\frac{\partial P_{2D}}{\partial z_D}+\rho_2 g\cos\alpha\right) \tag{A.42}$$

$$u^*_{3x2}u_{1xD}+u^*_{3x1}=-\frac{k_xk_{r3}}{\mu_3}\left(\frac{P^*_{32}}{x^*_2}\frac{\partial P_{3D}}{\partial x_D}+\rho_3 g\sin\alpha\right) \tag{A.43}$$

$$u^*_{3y2}u_{1yD}+u^*_{3y1}=-\frac{k_yk_{r3}}{\mu_3}\left(\frac{P^*_{32}}{y^*_2}\frac{\partial P_{3D}}{\partial y_D}+\rho_3 g\right) \tag{A.44}$$

$$u^*_{3z2}u_{1zD}+u^*_{3z1}=-\frac{k_zk_{r3}}{\mu_3}\left(\frac{P^*_{32}}{z^*_2}\frac{\partial P_{3D}}{\partial z_D}+\rho_3 g\cos\alpha\right) \tag{A.45}$$

After simplifying these equations we have

$$u_{1xD}=-\left[\frac{k_xk_{r1}P^*_{12}}{u^*_{1x2}\mu_1x^*_2}\right]\left(\frac{\partial P_{1D}}{\partial x_D}+\left[\frac{x^*_2\rho_1 g\sin\alpha}{P^*_{12}}\right]\right)-\left[\frac{u^*_{1x1}}{u^*_{1x2}}\right] \tag{A.46}$$

$$u_{1yD}=-\left[\frac{k_yk_{r1}P^*_{12}}{u^*_{1y2}\mu_1y^*_2}\right]\left(\frac{\partial P_{1D}}{\partial y_D}+\left[\frac{y^*_2\rho_1 g}{P^*_{12}}\right]\right)-\left[\frac{u^*_{1y1}}{u^*_{1y2}}\right] \tag{A.47}$$

$$u_{1zD}=-\left[\frac{k_zk_{r1}P^*_{12}}{u^*_{1z2}\mu_1z^*_2}\right]\left(\frac{\partial P_{1D}}{\partial z_D}+\left[\frac{z^*_2\rho_1 g\cos\alpha}{P^*_{12}}\right]\right)-\left[\frac{u^*_{1z1}}{u^*_{1z2}}\right] \tag{A.48}$$

$$u_{2xD}=-\left[\frac{k_xk_{r2}P^*_{22}}{u^*_{2x2}\mu_2x^*_2}\right]\left(\frac{\partial P_{2D}}{\partial x_D}+\left[\frac{x^*_2\rho_2 g\sin\alpha}{P^*_{22}}\right]\right)-\left[\frac{u^*_{2x1}}{u^*_{2x2}}\right] \tag{A.49}$$

$$u_{2yD}=-\left[\frac{k_yk_{r2}P^*_{22}}{u^*_{2y2}\mu_2y^*_2}\right]\left(\frac{\partial P_{2D}}{\partial y_D}+\left[\frac{y^*_2\rho_2 g}{P^*_{22}}\right]\right)-\left[\frac{u^*_{2y1}}{u^*_{2y2}}\right] \tag{A.50}$$

$$u_{2zD}=-\left[\frac{k_zk_{r2}P^*_{22}}{u^*_{2z2}\mu_2z^*_2}\right]\left(\frac{\partial P_{2D}}{\partial z_D}+\left[\frac{z^*_2\rho_2 g\cos\alpha}{P^*_{22}}\right]\right)-\left[\frac{u^*_{2z1}}{u^*_{2z2}}\right] \tag{A.51}$$

$$u_{3xD} = -\left[\frac{k_x k_{r3} P_{32}^*}{u_{3x2}^* \mu_3 x_2^*}\right]\left(\frac{\partial P_{3D}}{\partial x_D} + \left[\frac{x_2^* \rho_3 g \sin\alpha}{P_{32}^*}\right]\right) - \left[\frac{u_{3x1}^*}{u_{3x2}^*}\right] \tag{A.52}$$

$$u_{3yD} = -\left[\frac{k_y k_{r3} P_{32}^*}{u_{3y2}^* \mu_3 y_2^*}\right]\left(\frac{\partial P_{3D}}{\partial y_D} + \left[\frac{y_2^* \rho_3 g}{P_{32}^*}\right]\right) - \left[\frac{u_{3y1}^*}{u_{3y2}^*}\right] \tag{A.53}$$

$$u_{3xD} = -\left[\frac{k_z k_{r3} P_{32}^*}{u_{3z2}^* \mu_3 z_2^*}\right]\left(\frac{\partial P_{3D}}{\partial z_D} + \left[\frac{z_2^* \rho_3 g \cos\alpha}{P_{32}^*}\right]\right) - \left[\frac{u_{3z1}^*}{u_{3z2}^*}\right] \tag{A.54}$$

Replacing Dimensional Variables with Scaling Factors in Capillary Pressure Equations

After substituting arbitrary scaling factors in the original capillary pressure equations, we have

$$P_{2D} - \left[\frac{P_{12}^*}{P_{22}^*}\right] P_{1D} + \left[\frac{P_{21}^* - P_{11}^*}{P_{22}^*}\right] = j(S)\left[\frac{\sigma_{21}\sqrt{\frac{\phi}{k}}}{P_{22}^*}\right] \tag{A.55}$$

$$P_{3D} - \left[\frac{P_{22}^*}{P_{32}^*}\right] P_{2D} + \left[\frac{P_{31}^* - P_{21}^*}{P_{32}^*}\right] = j(S)\left[\frac{\sigma_{32}\sqrt{\frac{\phi}{k}}}{P_{32}^*}\right] \tag{A.56}$$

Replacing Dimensional Variables with Scaling Factors in Initial and Boundary Conditions

Entering arbitrary scaling factors into equations original initial and boundary condition equations and then rearranging them will give

$$S_{2D} = \left[\frac{S_{2r} - S_{21}^*}{S_{22}^*}\right] \qquad at \qquad t_D = -\left[\frac{t_1^*}{t_2^*}\right] \quad \forall \quad x_D, y_D, z_D \tag{A.57}$$

$$S_{3D} = -\left[\frac{S_{31}^*}{S_{32}^*}\right] \qquad at \qquad t_D = -\left[\frac{t_1^*}{t_2^*}\right] \quad \forall \quad x_D, y_D, z_D \tag{A.58}$$

$$C_{21D} = -\left[\frac{C^*_{211}}{C^*_{212}}\right] \qquad at \qquad t_D = -\left[\frac{t^*_1}{t^*_2}\right] \quad \forall \quad x_D, y_D, z_D \tag{A.59}$$

$$C_{22D} = \left[\frac{C^I_2 + C^*_{221}}{C^*_{222}}\right] \qquad at \qquad t_D = -\left[\frac{t^*_1}{t^*_2}\right] \quad \forall \quad x_D, y_D, z_D \tag{A.60}$$

$$C_{23D} = -\left[\frac{C^*_{231}}{C^*_{232}}\right] \qquad at \qquad t_D = -\left[\frac{t^*_1}{t^*_2}\right] \quad \forall \quad x_D, y_D, z_D \tag{A.61}$$

$$C_{31D} = -\left[\frac{C^*_{311}}{C^*_{312}}\right] \qquad at \qquad t_D = -\left[\frac{t^*_1}{t^*_2}\right] \quad \forall \quad x_D, y_D, z_D \tag{A.62}$$

$$C_{32D} = \left[\frac{C^I_3 - C^*_{321}}{C^*_{322}}\right] \qquad at \qquad t_D = -\left[\frac{t^*_1}{t^*_2}\right] \quad \forall \quad x_D, y_D, z_D \tag{A.63}$$

$$C_{33D} = -\left[\frac{C^*_{331}}{C^*_{332}}\right] \qquad at \qquad t_D = -\left[\frac{t^*_1}{t^*_2}\right] \quad \forall \quad x_D, y_D, z_D \tag{A.64}$$

$$C_{41D} = -\left[\frac{C^*_{411}}{C^*_{412}}\right] \qquad at \qquad t_D = -\left[\frac{t^*_1}{t^*_2}\right] \quad \forall \quad x_D, y_D, z_D \tag{A.65}$$

$$C_{42D} = \left[\frac{C^I_4 - C^*_{421}}{C^*_{422}}\right] \qquad at \qquad t_D = -\left[\frac{t^*_1}{t^*_2}\right] \quad \forall \quad x_D, y_D, z_D \tag{A.66}$$

$$C_{43D} = -\left[\frac{C^*_{431}}{C^*_{432}}\right] \qquad at \qquad t_D = -\left[\frac{t^*_1}{t^*_2}\right] \quad \forall \quad x_D, y_D, z_D \tag{A.67}$$

$$C_{33D} = \left[\frac{C^J_3 - C^*_{331}}{C^*_{332}}\right] \qquad at \qquad x_D = -\left[\frac{x^*_1}{x^*_2}\right] \quad \forall \quad y_D, z_D, t_D \tag{A.68}$$

$$P_{1D} = \left[\frac{P_{wf} - P^*_{11}}{P^*_{12}}\right] + \left[\frac{z^*_2 \rho_1 g \cos\alpha}{P^*_{12}}\right]\left(\left[\frac{H - z^*_1}{z^*_2}\right] - z_D\right) \tag{A.69}$$

$$at \qquad x_D = \left[\frac{L - x^*_1}{x^*_2}\right], \quad \forall \quad y_D, z_D, t_D$$

$$P_{2D} = \left[\frac{P_{wf} - P_{21}^*}{P_{22}^*}\right] + \left[\frac{z_2^* \rho_2 g \cos\alpha}{P_{22}^*}\right]\left(\left[\frac{H - z_1^*}{z_2^*}\right] - z_D\right) \qquad \text{(A.70)}$$

$$at \qquad x_D = \left[\frac{L - x_1^*}{x_2^*}\right], \quad \forall \quad y_D, z_D, t_D$$

$$P_{3D} = \left[\frac{P_{wf} - P_{31}^*}{P_{32}^*}\right] + \left[\frac{z_2^* \rho_3 g \cos\alpha}{P_{32}^*}\right]\left(\left[\frac{H - z_1^*}{z_2^*}\right] - z_D\right) \qquad \text{(A.71)}$$

$$at \qquad x_D = \left[\frac{L - x_1^*}{x_2^*}\right], \quad \forall \quad y_D, z_D, t_D$$

$$u_{1zD} = -\left[\frac{u_{1z1}^*}{u_{1z2}^*}\right] \qquad at \qquad z_D = -\left[\frac{z_1^*}{z_2^*}\right] \quad \forall \quad x_D, y_D, t_D \qquad \text{(A.72)}$$

$$u_{1zD} = -\left[\frac{u_{1z1}^*}{u_{1z2}^*}\right] \qquad at \qquad z_D = \left[\frac{H - z_1^*}{z_2^*}\right] \quad \forall \quad x_D, y_D, t_D \qquad \text{(A.73)}$$

$$u_{2zD} = -\left[\frac{u_{2z1}^*}{u_{2z2}^*}\right] \qquad at \qquad z_D = -\left[\frac{z_1^*}{z_2^*}\right] \quad \forall \quad x_D, y_D, t_D \qquad \text{(A.74)}$$

$$u_{2zD} = -\left[\frac{u_{2z1}^*}{u_{2z2}^*}\right] \qquad at \qquad z_D = \left[\frac{H - z_1^*}{z_2^*}\right] \quad \forall \quad x_D, y_D, t_D \qquad \text{(A.75)}$$

$$u_{3zD} = -\left[\frac{u_{3z1}^*}{u_{3z2}^*}\right] \qquad at \qquad z_D = -\left[\frac{z_1^*}{z_2^*}\right] \quad \forall \quad x_D, y_D, t_D \qquad \text{(A.76)}$$

$$u_{3zD} = -\left[\frac{u_{3z1}^*}{u_{3z2}^*}\right] \qquad at \qquad z_D = \left[\frac{H - z_1^*}{z_2^*}\right] \quad \forall \quad x_D, y_D, t_D \qquad \text{(A.77)}$$

$$u_{1yD} = -\left[\frac{u_{1y1}^*}{u_{1y2}^*}\right] \qquad at \qquad y_D = -\left[\frac{y_1^*}{y_2^*}\right] \quad \forall \quad x_D, z_D, t_D \qquad \text{(A.78)}$$

$$u_{1yD} = -\left[\frac{u_{1y1}^*}{u_{1y2}^*}\right] \qquad at \qquad y_D = \left[\frac{W - y_1^*}{y_2^*}\right] \quad \forall \quad x_D, z_D, t_D \qquad \text{(A.79)}$$

$$u_{2yD} = -\left[\frac{u_{2y1}^*}{u_{2y2}^*}\right] \qquad at \qquad y_D = -\left[\frac{y_1^*}{y_2^*}\right] \quad \forall \quad x_D, z_D, t_D \qquad \text{(A.80)}$$

$$u_{2yD} = -\left[\frac{u_{2y1}^*}{u_{2y2}^*}\right] \qquad at \qquad y_D = \left[\frac{W - y_1^*}{y_2^*}\right] \quad \forall \quad x_D, z_D, t_D \qquad \text{(A.81)}$$

$$u_{3yD} = -\left[\frac{u^*_{3y1}}{u^*_{3y2}}\right] \qquad at \qquad y_D = -\left[\frac{y^*_1}{y^*_2}\right] \quad \forall \quad x_D, z_D, t_D \tag{A.82}$$

$$u_{3yD} = -\left[\frac{u^*_{3y1}}{u^*_{3y2}}\right] \qquad at \qquad y_D = \left[\frac{W - y^*_1}{y^*_2}\right] \quad \forall \quad x_D, z_D, t_D \tag{A.83}$$

$$u_{1xD} = -\left[\frac{u^*_{1x1}}{u^*_{1x2}}\right] \qquad at \qquad x_D = -\left[\frac{x^*_1}{x^*_2}\right] \quad \forall \quad y_D, z_D, t_D \tag{A.84}$$

$$u_{1xD} = -\left[\frac{u^*_{1x1}}{u^*_{1x2}}\right] \qquad at \qquad x_D = \left[\frac{L - x^*_1}{x^*_2}\right] \quad \forall \quad y_D, z_D, t_D \tag{A.85}$$

$$u_{2xD} = -\left[\frac{u^*_{2x1}}{u^*_{2x2}}\right] \qquad at \qquad x_D = -\left[\frac{x^*_1}{x^*_2}\right] \quad \forall \quad y_D, z_D, t_D \tag{A.86}$$

$$u_{2xD} = -\left[\frac{u^*_{2x1}}{u^*_{2x2}}\right] \qquad at \qquad x_D = \left[\frac{L - x^*_1}{x^*_2}\right] \quad \forall \quad y_D, z_D, t_D \tag{A.87}$$

$$u_{3xD} = -\left[\frac{u^*_{3x1}}{u^*_{3x2}}\right] \qquad at \qquad x_D = -\left[\frac{x^*_1}{x^*_2}\right] \quad \forall \quad y_D, z_D, t_D \tag{A.88}$$

$$u_{3xD} = -\left[\frac{u^*_{3x1}}{u^*_{3x2}}\right] \qquad at \qquad x_D = \left[\frac{L - x^*_1}{x^*_2}\right] \quad \forall \quad y_D, z_D, t_D \tag{A.89}$$

$$\int_0^{\left[(W-y^*_1)/y^*_2\right]} \left(\int_0^{\left[(H-z^*_1)/z^*_2\right]} (u_{3xD} + \left[\frac{u^*_{3x1}}{u^*_{3x2}}\right]) dz_D \right) dy_D = \left[\frac{HWu_{inj}}{y^*_2 z^*_2 u^*_{3x2}}\right] \qquad at \qquad x_D = -\left[\frac{x^*_1}{x^*_2}\right] \quad \forall \quad y_D, z_D, t_D \tag{A.90}$$

Saturation and Concentrations Sum to One

Arbitrary scaling factors have been introduced in the original equations; then we have

$$S_{1D} + \left[\frac{S^*_{22}}{S^*_{12}}\right] S_{2D} + \left[\frac{S^*_{32}}{S^*_{12}}\right] S_{3D} + \left[\frac{S^*_{31} + S^*_{21} + S^*_{11}}{S^*_{12}}\right] = 1 \tag{A.91}$$

$$C_{21D}+\left[\frac{C^*_{312}}{C^*_{212}}\right]C_{31D}+\left[\frac{C^*_{412}}{C^*_{212}}\right]C_{41D}=1 \tag{A.92}$$

$$C_{22D}+\left[\frac{C^*_{322}}{C^*_{222}}\right]C_{32D}+\left[\frac{C^*_{422}}{C^*_{222}}\right]C_{42D}=1 \tag{A.93}$$

$$C_{23D}+\left[\frac{C^*_{332}}{C^*_{232}}\right]C_{33D}+\left[\frac{C^*_{432}}{C^*_{232}}\right]C_{43D}=1 \tag{A.94}$$

Non-Dimensionalizing Phase Equilibrium Equations:

After substituting equations 6.55 and 6.56 in the equation 6.54, following equation is resulted.

$$\left[P+\Omega_a\frac{R^2T_c^2}{P_c}\times\frac{\alpha(T)}{\left[\begin{array}{l}\left(V+\zeta_c\frac{RT_c}{P_c}Z'_{RA}\right)\left(V+2\zeta_c\frac{RT_c}{P_c}Z'_{RA}+\Omega_b\frac{RT_c}{P_c}\right)+\\+\left(\Omega_b\frac{RT_c}{P_c}+\zeta_c\frac{RT_c}{P_c}Z'_{RA}\right)\left(V-\Omega_b\frac{RT_c}{P_c}\right)\end{array}\right]}\right](V-\Omega_b\frac{RT_c}{P_c})=RT \tag{A.95}$$

Considering the more general form of equation of state, $P_cV_c=Z_cRT_c\Rightarrow\frac{V_c}{Z_c}=\frac{RT_c}{P_c}$, and entering it into equation (A.95):

$$\left[P+\Omega_a\frac{V_c^2P_c}{Z_c^2}\times\frac{\alpha(T)}{\left[\begin{array}{l}\left(V+\zeta_c\frac{V_c}{Z_c}Z'_{RA}\right)\left(V+2\zeta_c\frac{V_c}{Z_c}Z'_{RA}+\Omega_b\frac{V_c}{Z_c}\right)+\\+\left(\Omega_b\frac{V_c}{Z_c}+\zeta_c\frac{V_c}{Z_c}Z'_{RA}\right)\left(V-\Omega_b\frac{V_c}{Z_c}\right)\end{array}\right]}\right](V-\Omega_b\frac{V_c}{Z_c})=\frac{V_cP_cT}{Z_cT_c} \tag{A.96}$$

after simplifying:

$$\left[\frac{P}{P_c}+\frac{\Omega_a}{Z_c^2}\times\frac{\alpha(T)}{\frac{V^2}{V_c^2}\left\{\begin{array}{l}\left(1+\zeta_c\frac{V_c}{V}\frac{Z'_{RA}}{Z_c}\right)\left(1+2\zeta_c\frac{V_c}{V}\frac{Z'_{RA}}{Z_c}+\frac{\Omega_b}{Z_c}\frac{V_c}{V}\right)+\\ +\left(\frac{\Omega_b}{Z_c}\frac{V_c}{V}+\zeta_c\frac{V_c}{V}\frac{Z'_{RA}}{Z_c}\right)\left(1-\frac{\Omega_b}{Z_c}\frac{V_c}{V}\right)\end{array}\right\}}\right](\frac{V}{V_c}-\frac{\Omega_b}{Z_c})=\frac{1}{Z_c}\frac{T}{T_c} \tag{A.97}$$

By introducing reduced form of temperature, pressure, and volume as

$$T_r=\frac{T}{T_c},\quad P_r=\frac{P}{P_c},\quad and\quad V_r=\frac{V}{V_c} \tag{A.98}$$

And also note that $k=0.37464+1.54226\omega-0.26992\omega^2$. Introducing reduced form of temperature, pressure, and molar volume to Equation (A.97) gives:

$$\left[P_r+\frac{\Omega_a}{Z_c^2}\times\frac{\sqrt{1+k\left(1-\sqrt{T_r}\right)}}{V_r^2\left\{\begin{array}{l}\left(1+\zeta_c V_r\frac{Z'_{RA}}{Z_c}\right)\left(1+2\zeta_c V_r\frac{Z'_{RA}}{Z_c}+\frac{\Omega_b}{Z_c}V_r\right)+\\ +\left(\frac{\Omega_b}{Z_c}V_r+\zeta_c V_r\frac{Z'_{RA}}{Z_c}\right)\left(1-\frac{\Omega_b}{Z_c}V_r\right)\end{array}\right\}}\right](V_r-\frac{\Omega_b}{Z_c})=\frac{1}{Z_c}T_r \tag{A.99}$$

In addition, we have $P_rV_r=\frac{Z}{Z_c}T_r$; therefore, $V_r=\frac{Z}{Z_c}\frac{T_r}{P_r}$. Substituting these into the Equation (A.99) results:

$$\left[P_r+\frac{\Omega_a}{Z_c^2}\times\frac{\sqrt{1+k\left(1-\sqrt{T_r}\right)}}{\left(Z\frac{T_r}{P_r}\right)^2\left\{\begin{array}{l}\left(1+\zeta_c\frac{Z}{Z_c}\frac{T_r}{P_r}\frac{Z'_{RA}}{Z_c}\right)\left(1+2\zeta_c\frac{Z}{Z_c}\frac{T_r}{P_r}\frac{Z'_{RA}}{Z_c}+\frac{\Omega_b}{Z_c}\frac{Z}{Z_c}\frac{T_r}{P_r}\right)+\\ +\left(\frac{\Omega_b}{Z_c}\frac{Z}{Z_c}\frac{T_r}{P_r}+\zeta_c\frac{Z}{Z_c}\frac{T_r}{P_r}\frac{Z'_{RA}}{Z_c}\right)\left(1-\frac{\Omega_b}{Z_c}\frac{Z}{Z_c}\frac{T_r}{P_r}\right)\end{array}\right\}}\right](\frac{Z}{Z_c}\frac{T_r}{P_r}-\frac{\Omega_b}{Z_c})=\frac{1}{Z_c}T_r \tag{A.100}$$

By simplifying we obtain:

$$\left[P_r + \frac{\Omega_a \sqrt{1 + k\left(1 - \sqrt{T_r}\right)}}{\left(Z \frac{T_r}{P_r}\right)^2 \left(1 + \frac{\Omega_b}{Z} \frac{P_r}{T_r}\right) + \Omega_b \frac{Z T_r}{P_r} \left(1 - \frac{\Omega_b}{Z} \frac{P_r}{T_r}\right)} \right] (Z \frac{T_r}{P_r} - \Omega_b) = T_r \quad \text{(A.101)}$$

Equation (A.101) is dimensionless form of the PR-EOS and can be used along with other dimensionless equations to scale the CO_2 flooding displacement process. Three Reduced temperature (T_r), reduced pressure (P_r), along with acentric factor, which is embedded in the definition of "k" in Equation 6.55, are three main scaling parameters that were derived from EOS as an auxiliary equations for CO_2 flooding displacement process. Since there are 3 components present in our assumed system, and three scaling groups are introduced from all derivations of the phase behavior part, 9 scaling groups should be considered for phase behavior section of equations.

Phase behavior equations constitute of 12 parameters $(R, a, b, c, c', c'', \alpha, \omega, T_c, P_c, V_c, \ Z_c)$ and 3 independent variables (T, P, V) and are being utilized to supplement flow equations in order to model the CO_2 flooding process.

Final Simplification of Derived Scaling Groups:

Considering the assumptions that we have made so far on arbitrary scaling factors, following simplifications have already been performed on these equations.

$$S_{21}^* = S_{31}^* = S_{41}^* = 0$$
$$S_{12}^* = S_{22}^* = S_{32}^* = S_2^*$$
$$u_{1x1}^* = u_{2x1}^* = u_{3x1}^* = 0$$
$$u_{1y1}^* = u_{2y1}^* = u_{3y1}^* = 0$$
$$u_{1z1}^* = u_{2z1}^* = u_{3z1}^* = 0$$

$$u^*_{1x2} = u^*_{2x2} = u^*_{3x2} = u^*_{x2}$$
$$u^*_{1y2} = u^*_{2y2} = u^*_{3y2} = u^*_{y2}$$
$$u^*_{1z2} = u^*_{2z2} = u^*_{3z2} = u^*_{z2}$$
$$C^*_{211} = C^*_{221} = C^*_{231} = 0$$
$$C^*_{311} = C^*_{321} = C^*_{331} = 0$$
$$C^*_{411} = C^*_{421} = C^*_{431} = 0$$
$$C^*_{212} = C^*_{222} = C^*_{232} = C^*_{22}$$
$$C^*_{312} = C^*_{322} = C^*_{332} = C^*_{32}$$
$$C^*_{412} = C^*_{422} = C^*_{432} = C^*_{42}$$

In addition, following equations are dimensionless form of governing relations for CO_2 flooding displacement process. Comparing these dimensionless equations to their corresponding dimensional form shows that dimensionless equations are very similar to the general form of dimensional equations. In addition, they still constitute of dimensionless parameters as well as some arbitrary scaling factors in the form of coefficients or additions. Defining these additive and multiplicative arbitrary scale factors is not a robust approach; they have to be assigned in a way that final dimensionless form of the equations not to be different than that of initial governing equations. Also they have to be defined in a way that the number of final scaling groups is minimized.

Conservation Equations:

$$\frac{\partial}{\partial t_D}\left(C_{21D}S_{1D} + C_{22D}S_{2D} + C_{23D}S_{3D}\right) + \left[\frac{u^*_{x2}t^*_2}{\phi S^*_2 x^*_2}\right]\frac{\partial}{\partial x_D}\left(u_{1xD}C_{21D} + u_{2xD}C_{22D} + u_{3xD}C_{23D}\right) + \boxed{1} \tag{A.102}$$

$$+\left[\frac{u^*_{y2}t^*_2}{\phi S^*_2 y^*_2}\right]\frac{\partial}{\partial y_D}\left(u_{1yD}C_{21D} + u_{2yD}C_{22D} + u_{3yD}C_{23D}\right) + \boxed{2} \tag{A.103}$$

$$+\left[\frac{u^*_{z2}t^*_2}{\phi S^*_2 z^*_2}\right]\frac{\partial}{\partial z_D}\left(u_{1zD}C_{21D} + u_{2zD}C_{22D} + u_{3zD}C_{23D}\right) = 0 \tag{A.103-a}$$

3

$$\frac{\partial}{\partial t_D}\left(C_{31D}S_{1D}+C_{32D}S_{2D}+C_{33D}S_{3D}\right)+$$
$$+\left[\frac{u_{x2}^{*}t_{2}^{*}}{\phi S_{2}^{*}x_{2}^{*}}\right]\frac{\partial}{\partial x_D}\left(u_{1xD}C_{31D}+u_{2xD}C_{32D}+u_{3xD}C_{33D}\right)+ \quad \text{(A.104)}$$

4

$$+\left[\frac{u_{y2}^{*}t_{2}^{*}}{\phi S_{2}^{*}y_{2}^{*}}\right]\frac{\partial}{\partial y_D}\left(u_{1yD}C_{31D}+u_{2yD}C_{32D}+u_{3yD}C_{33D}\right)+ \quad \text{(A.105)}$$

5

$$+\left[\frac{u_{z2}^{*}t_{2}^{*}}{\phi S_{2}^{*}z_{2}^{*}}\right]\frac{\partial}{\partial z_D}\left(u_{1zD}C_{31D}+u_{2zD}C_{32D}+u_{3zD}C_{33D}\right)=0 \quad \text{(A.106)}$$

6

$$\frac{\partial}{\partial t_D}\left(C_{41D}S_{1D}+C_{42D}S_{2D}+C_{43D}S_{3D}\right)+$$
$$+\left[\frac{u_{x2}^{*}t_{2}^{*}}{\phi S_{2}^{*}x_{2}^{*}}\right]\frac{\partial}{\partial x_D}\left(u_{1xD}C_{41D}+u_{2xD}C_{42D}+u_{3xD}C_{43D}\right)+ \quad \text{(A.107)}$$

7

$$+\left[\frac{u_{y2}^{*}t_{2}^{*}}{\phi S_{2}^{*}y_{2}^{*}}\right]\frac{\partial}{\partial y_D}\left(u_{1yD}C_{41D}+u_{2yD}C_{42D}+u_{3yD}C_{43D}\right)+ \quad \text{(A.108)}$$

8

$$+\left[\frac{u_{z2}^{*}t_{2}^{*}}{\phi S_{2}^{*}z_{2}^{*}}\right]\frac{\partial}{\partial z_D}\left(u_{1zD}C_{41D}+u_{2zD}C_{42D}+u_{3zD}C_{43D}\right)=0 \quad \text{(A.109)}$$

9

Darcy's Equations:

$$u_{1xD}=-\left[\frac{k_x k_{r1}P_{12}^{*}}{u_{x2}^{*}\mu_1 x_2^{*}}\right]\left(\frac{\partial P_{1D}}{\partial x_D}+\left[\frac{x_2^{*}\rho_1 g\sin\alpha}{P_{12}^{*}}\right]\right) \quad \text{(A.110)}$$

10 11

$$u_{1yD} = -\left[\frac{k_y k_{r1} P_{12}^*}{u_{y2}^* \mu_1 y_2^*}\right]\left(\frac{\partial P_{1D}}{\partial y_D} + \left[\frac{y_2^* \rho_1 g}{P_{12}^*}\right]\right) \quad \text{(A.111)}$$

12 13

$$u_{1zD} = -\left[\frac{k_z k_{r1} P_{12}^*}{u_{z2}^* \mu_1 z_2^*}\right]\left(\frac{\partial P_{1D}}{\partial z_D} + \left[\frac{z_2^* \rho_1 g \cos\alpha}{P_{12}^*}\right]\right) \quad \text{(A.112)}$$

14 15

$$u_{2xD} = -\left[\frac{k_x k_{r2} P_{22}^*}{u_{x2}^* \mu_2 x_2^*}\right]\left(\frac{\partial P_{2D}}{\partial x_D} + \left[\frac{x_2^* \rho_2 g \sin\alpha}{P_{22}^*}\right]\right) \quad \text{(A.113)}$$

16 17

$$u_{2yD} = -\left[\frac{k_y k_{r2} P_{22}^*}{u_{y2}^* \mu_2 y_2^*}\right]\left(\frac{\partial P_{2D}}{\partial y_D} + \left[\frac{y_2^* \rho_2 g}{P_{22}^*}\right]\right) \quad \text{(A.114)}$$

18 19

$$u_{2zD} = -\left[\frac{k_z k_{r2} P_{22}^*}{u_{z2}^* \mu_2 z_2^*}\right]\left(\frac{\partial P_{2D}}{\partial z_D} + \left[\frac{z_2^* \rho_2 g \cos\alpha}{P_{22}^*}\right]\right) \quad \text{(A.115)}$$

20 21

$$u_{3xD} = -\left[\frac{k_x k_{r3} P_{32}^*}{u_{x2}^* \mu_3 x_2^*}\right]\left(\frac{\partial P_{3D}}{\partial x_D} + \left[\frac{x_2^* \rho_3 g \sin\alpha}{P_{32}^*}\right]\right) \quad \text{(A.116)}$$

22 23

$$u_{3yD} = -\left[\frac{k_y k_{r3} P_{32}^*}{u_{y2}^* \mu_3 y_2^*}\right]\left(\frac{\partial P_{3D}}{\partial y_D} + \left[\frac{y_2^* \rho_3 g}{P_{32}^*}\right]\right) \quad \text{(A.117)}$$

24 25

$$u_{3xD} = -\left[\frac{k_z k_{r3} P_{32}^*}{u_{z2}^* \mu_3 z_2^*}\right]\left(\frac{\partial P_{3D}}{\partial z_D} + \left[\frac{z_2^* \rho_3 g \cos\alpha}{P_{32}^*}\right]\right) \quad \text{(A.118)}$$

26 27

Capillary Pressure Equations:

$$P_{2D} - \left[\frac{P_{12}^*}{P_{22}^*}\right] P_{1D} + \left[\frac{P_{21}^* - P_{11}^*}{P_{22}^*}\right] = j(S)\left[\frac{\sigma_{21}\sqrt{\frac{\phi}{k}}}{P_{22}^*}\right] \qquad \text{(A.119)}$$

28 29 30

$$P_{3D} - \left[\frac{P_{22}^*}{P_{32}^*}\right] P_{2D} + \left[\frac{P_{31}^* - P_{21}^*}{P_{32}^*}\right] = j(S)\left[\frac{\sigma_{32}\sqrt{\frac{\phi}{k}}}{P_{32}^*}\right] \qquad \text{(A.120)}$$

31 32 33

Initial and Boundary Conditions:

$$S_{2D} = \left[\frac{S_{2r}}{S_2^*}\right] \quad at \quad t_D = -\left[\frac{t_1^*}{t_2^*}\right] \quad \forall \quad x_D, y_D, z_D \qquad \text{(A.121)}$$

34 35

$$C_{21D} = C_{23D} = 0 \quad at \quad t_D = -\left[\frac{t_1^*}{t_2^*}\right] \quad \forall \quad x_D, y_D, z_D \qquad \text{(A.122)}$$

36

$$C_{22D} = \left[\frac{C_2^I}{C_{22}^*}\right] \quad at \quad t_D = -\left[\frac{t_1^*}{t_2^*}\right] \quad \forall \quad x_D, y_D, z_D \qquad \text{(A.123)}$$

37 38

$$C_{31D} = C_{33D} = 0 \quad at \quad t_D = -\left[\frac{t_1^*}{t_2^*}\right] \quad \forall \quad x_D, y_D, z_D \qquad \text{(A.124)}$$

39

$$C_{32D} = \left[\frac{C_3^I}{C_{32}^*}\right] \quad at \quad t_D = -\left[\frac{t_1^*}{t_2^*}\right] \quad \forall \quad x_D, y_D, z_D \qquad \text{(A.125)}$$

40 41

$$C_{41D} = C_{43D} = 0 \quad at \quad t_D = -\left[\frac{t_1^*}{t_2^*}\right] \quad \forall \quad x_D, y_D, z_D \qquad \text{(A.126)}$$

42

$$C_{42D} = \left[\frac{C_4^I}{C_{42}^*}\right] \qquad at \qquad t_D = -\left[\frac{t_1^*}{t_2^*}\right] \quad \forall \quad x_D, y_D, z_D \tag{A.127}$$

43 44

$$C_{33D} = \left[\frac{C_3^J}{C_{32}^*}\right] \qquad at \qquad x_D = -\left[\frac{x_1^*}{x_2^*}\right] \quad \forall \quad y_D, z_D, t_D \tag{A.128}$$

45 46

$$P_{1D} = \left[\frac{P_{wf} - P_{11}^*}{P_{12}^*}\right] + \left[\frac{z_2^* \rho_1 g \cos\alpha}{P_{12}^*}\right]\left(\left[\frac{H - z_1^*}{z_2^*}\right] - z_D\right) \tag{A.129}$$

47 48 49

$$at \qquad x_D = \left[\frac{L - x_1^*}{x_2^*}\right], \quad \forall \quad z_D, t_D$$

50

$$P_{2D} = \left[\frac{P_{wf} - P_{21}^*}{P_{22}^*}\right] + \left[\frac{z_2^* \rho_2 g \cos\alpha}{P_{22}^*}\right]\left(\left[\frac{H - z_1^*}{z_2^*}\right] - z_D\right) \tag{A.130}$$

51 52 53

$$at \qquad x_D = \left[\frac{L - x_1^*}{x_2^*}\right], \quad \forall \quad z_D, t_D$$

54

$$P_{3D} = \left[\frac{P_{wf} - P_{31}^*}{P_{32}^*}\right] + \left[\frac{z_2^* \rho_3 g \cos\alpha}{P_{32}^*}\right]\left(\left[\frac{H - z_1^*}{z_2^*}\right] - z_D\right) \tag{A.131}$$

55 56 57

$$at \qquad x_D = \left[\frac{L - x_1^*}{x_2^*}\right], \quad \forall \quad z_D, t_D$$

58

$$u_{1zD} = u_{2zD} = u_{3zD} = 0 \qquad at \qquad z_D = -\left[\frac{z_1^*}{z_2^*}\right] \quad \forall \quad x_D, y_D, t_D \tag{A.132}$$

59

$$u_{1zD} = u_{2zD} = u_{3zD} = 0 \qquad at \qquad z_D = \left[\frac{H - z_1^*}{z_2^*}\right] \quad \forall \quad x_D, y_D, t_D \tag{A.133}$$

60

$$u_{1yD} = u_{2yD} = u_{3yD} = 0 \qquad at \qquad y_D = -\left[\frac{y_1^*}{y_2^*}\right] \quad \forall \quad x_D, z_D, t_D \tag{A.134}$$

61

$$u_{1yD} = u_{2yD} = u_{3yD} = 0 \qquad at \qquad y_D = \left[\frac{W - y_1^*}{y_2^*}\right] \quad \forall \quad x_D, z_D, t_D \tag{A.135}$$

62

$$u_{1xD} = u_{2xD} = u_{3xD} = 0 \qquad at \qquad x_D = -\left[\frac{x_1^*}{x_2^*}\right] \quad \forall \quad y_D, z_D, t_D \tag{A.136}$$

63

$$u_{1xD} = u_{2xD} = u_{3xD} = 0 \qquad at \qquad x_D = \left[\frac{L - x_1^*}{x_2^*}\right] \quad \forall \quad y_D, z_D, t_D \tag{A.137}$$

64

$$\int_0^{\left[(W - y_1^*)/y_2^*\right]} \left(\int_0^{\left[(H - z_1^*)/z_2^*\right]} u_{3xD} dz_D \right) dy_D = \left[\frac{HWu_{inj}}{y_2^* z_2^* u_{x2}^*}\right] \tag{A.138}$$

65 66 67

$$at \qquad x_D = -\left[\frac{x_1^*}{x_2^*}\right] \quad \forall \quad y_D, z_D, t_D$$

68

Saturation and concentrations constraints:

$$S_{1D} + S_{2D} + S_{3D} = 1 \tag{A.139}$$

$$C_{21D} + \left[\frac{C_{32}^*}{C_{22}^*}\right] C_{31D} + \left[\frac{C_{42}^*}{C_{22}^*}\right] C_{41D} = 1 \qquad \text{(A.140)}$$

69 70

$$C_{22D} + \left[\frac{C_{32}^*}{C_{22}^*}\right] C_{32D} + \left[\frac{C_{42}^*}{C_{22}^*}\right] C_{42D} = 1 \qquad \text{(A.141)}$$

71 72

$$C_{23D} + \left[\frac{C_{32}^*}{C_{22}^*}\right] C_{33D} + \left[\frac{C_{42}^*}{C_{22}^*}\right] C_{43D} = 1 \qquad \text{(A.142)}$$

73 74

Phase Behavior Equation:

$$\left[P_r + \frac{\Omega_a \sqrt{1 + k\left(1 - \sqrt{T_r}\right)}}{\left(Z \frac{T_r}{P_r}\right)^2 \left(1 + \frac{\Omega_b}{Z} \frac{P_r}{T_r}\right) + \Omega_b \frac{Z T_r}{P_r} \left(1 - \frac{\Omega_b}{Z} \frac{P_r}{T_r}\right)} \right] \left(Z \frac{T_r}{P_r} - \Omega_b\right) = T_r \qquad \text{(A.143)}$$

It should be noted that the quantities inside brackets are dimensionless, because all of the equations are in dimensionless form. Overall, 79 dimensionless groups have been derived so far from flow equations in addition to 9 more groups which are resulted from phase behavior equations. But the scale factors are arbitrary therefore above dimensionless equations can be simplified to obtain reasonable number of dimensionless groups.

Following are more simplifications which can be made on the dimensionless equations.

1-Since non-dimensionalizing should not change the form of equations; groups 29, 32 are set to zero and equations 69, 70, 71, 72, 73, and 74 are set to 1. Therefore, it is concluded that:

$$P_{31}^{*} = P_{21}^{*} = P_{11}^{*} \tag{A.144}$$

$$C_{22}^{*} = C_{32}^{*} = C_{42}^{*} \tag{A.145}$$

2-a-Furthermore, variables that have known limits such as distance can be put between two known limits of 0 and 1; therefore groups 46, 59, 61, 63, and 68 can be set to zero, and groups 49, 50, 53, 54, 57, 58, 60, 62, 64, 65, and 66 can be set equal to 1. Hence:

$$x_1^{*} = y_1^{*} = z_1^{*} = 0$$

and

$$x_2^{*} = L \tag{A.146}$$

$$y_2^{*} = W$$

$$z_2^{*} = H$$

2-b-Also we can choose the dimensionless time to begin with zero which results in group numbers 35, 36, 38, 39, 41, 42, 44, 46, and 51 to be equal to zero then;

$$t_1^{*} = 0 \tag{A.147}$$

3- Dimensionless saturations, concentrations, pressures, and fluxes can also be set to vary between 0 and 1; therefore, equations 34, 45, and 67 are set to 1. Hence

$$S_{22}^{*} = S_2^{*} = S_{2r} \tag{A.148}$$

$$C_{332}^{*} = C_{32}^{*} = C_3^{J} \tag{A.149}$$

$$u_{3x2}^{*} = u_{x2}^{*} = u_{inj} \tag{A.150}$$

4- Among remaining dimensionless groups we set groups 1, 2, 3, 4, 5, 6, 7, 8, 9, 10, 16, and 22 to 1 and groups 47, 51, and 55 to 0. Hence

$$t_2^{*} = \frac{\phi S_{2r} L}{u_{inj}} \tag{A.151}$$

$$u_{y2}^{*} = \frac{u_{inj} W}{L} \tag{A.152}$$

$$u_{z2}^{*} = \frac{u_{inj} H}{L} \tag{A.153}$$

$$P_{12}^{*} = -\frac{u_{inj} L}{k_x \lambda_{r1}} \tag{A.154}$$

$$P_{22}^{*} = -\frac{u_{inj} L}{k_x \lambda_{r2}} \tag{A.155}$$

$$P_{32}^{*} = -\frac{u_{inj} L}{k_x \lambda_{r3}} \tag{A.156}$$

$$P_{11}^{*} = P_{21}^{*} = P_{31}^{*} = P_{wf} \tag{A.157}$$

If defined scale factors are put into 25 undefined remaining dimensionless groups, following scaling groups will be introduced.

$$G_1 = \frac{k_z}{k_x} \frac{L^2}{H^2}$$

$$G_2 = \frac{k_y}{k_x} \frac{L^2}{W^2}$$

$$G_3 = \frac{\lambda_{r2}}{\lambda_{r1}}$$

$$G_4 = \frac{\lambda_{r3}}{\lambda_{r2}}$$

$$G_5 = \frac{\sigma_{21} k_x \lambda_{r2} \sqrt{\frac{\phi}{k_x}}}{u_{inj}.L}$$

$$G_6 = \frac{\sigma_{32} k_x \lambda_{r3} \sqrt{\frac{\phi}{k_x}}}{u_{inj}.L}$$

$$G_7 = \frac{k_x \lambda_{r1} \rho_1 g \sin\alpha}{u_{inj}}$$

$$G_8 = \frac{k_x \lambda_{r2} \rho_2 g \sin\alpha}{u_{inj}}$$

$$G_9 = \frac{k_x \lambda_{r3} \rho_3 g \sin\alpha}{u_{inj}}$$

$$G_{10} = \frac{k_x \lambda_{r1} \rho_1 g}{u_{inj}} \frac{W}{L}$$

$$G_{11} = \frac{k_x \lambda_{r2} \rho_2 g}{u_{inj}} \frac{W}{L}$$

$$G_{12} = \frac{k_x \lambda_{r3} \rho_3 g}{u_{inj}} \frac{W}{L}$$

$$G_{13} = \frac{k_x \lambda_{r1} \rho_1 g \cos\alpha}{u_{inj}} \frac{H}{L}$$

$$G_{14} = \frac{k_x \lambda_{r2} \rho_2 g \cos\alpha}{u_{inj}} \frac{H}{L}$$

$$G_{15} = \frac{k_x \lambda_{r3} \rho_3 g \cos\alpha}{u_{inj}} \frac{H}{L}$$

$$G_{16} = \frac{P}{P_{ci}}$$

$$G_{17} = \frac{T}{T_{ci}}$$

$$G_{18} = \alpha(T) \quad or \quad k \quad or \quad \omega$$

$$G_{19} = \frac{C_2^I}{C_3^J}$$

$$G_{20} = \frac{C_3^I}{C_3^J}$$

$$G_{21} = \frac{C_4^I}{C_3^J}$$

5- In addition to the scaling groups that have been developed for CO_2 flooding process, if injection and production wells were set to constant bottom hole pressure constraint, following two new boundary conditions should be introduced to the system of equations that were being dealt with.

$$P_3 = P_{T_j} = P_{inj} \qquad at \qquad x = 0 \quad \forall \quad y, z, t \tag{A.158}$$

$$P_{T_p} = P_p \qquad at \qquad x = L \quad \forall \quad y, z, t \tag{A.159}$$

in which P_{T_j} and P_{Tp} are total injection and production pressures, respectively. After introducing arbitrary scaling factors and rearranging these equations we have

$$P_{T_jD} = \left[\frac{P_{inj} - P^*_{T_j1}}{P^*_{T_j2}} \right] \qquad at \qquad x_D = -\left[\frac{x^*_1}{x^*_2} \right] \quad \forall \quad y_D, z_D, t_D \tag{A.160}$$

$$P_{T_pD} = \left[\frac{P_P - P^*_{T_p1}}{P^*_{T_p2}} \right] \qquad at \qquad x_D = \left[\frac{L - x^*_1}{x^*_2} \right] \quad \forall \quad y_D, z_D, t_D \tag{A.161}$$

Since scaling factors are arbitrary, we can set $P^*_{T_p1}$ and $P^*_{T_j1}$ equal to zero and put $P^*_{T_p2} = P^*_{T_j2}$ and make assume minimum miscibility pressure as reference for non-dimensionalizing of these scaling factors; therefore $P^*_{T_p2} = P^*_{T_j2} = P_{MMP}$; hence

$$G_{22} = \frac{P_{inj}}{P_{MMP}}$$
$$and \tag{A.162}$$
$$G_{23} = \frac{P_P}{P_{MMP}}$$

Dimensionless Scaling Groups

Since relative permeability in above dimensionless groups is indeed dimensionless function of saturation not dimensionless number we can replace it with end point relative permeability for each phase which is independent of saturation and is a dimensionless number. Hence

$$G_3 = \frac{\lambda^\circ_{r2}}{\lambda^\circ_{r1}} \tag{A.163}$$

$$G_4 = \frac{\lambda^\circ_{r3}}{\lambda^\circ_{r2}} \tag{A.164}$$

$$G_5 = \frac{\sigma_{21} k_x \lambda^\circ_{r2} \sqrt{\frac{\phi}{k_x}}}{u_{inj}.L} \tag{A.165}$$

$$G_6 = \frac{\sigma_{32} k_x \lambda^\circ_{r3} \sqrt{\frac{\phi}{k_x}}}{u_{inj}.L} \tag{A.166}$$

$$G_7 = \frac{k_x \lambda_{r1}^{\circ} \rho_1 g \sin\alpha}{u_{inj}} \tag{A.167}$$

$$G_8 = \frac{k_x \lambda_{r2}^{\circ} \rho_2 g \sin\alpha}{u_{inj}} \tag{A.168}$$

$$G_9 = \frac{k_x \lambda_{r3}^{\circ} \rho_3 g \sin\alpha}{u_{inj}} \tag{A.169}$$

$$G_{10} = \frac{k_x \lambda_{r1}^{\circ} \rho_1 g}{u_{inj}} \frac{W}{L} \tag{A.170}$$

$$G_{11} = \frac{k_x \lambda_{r2}^{\circ} \rho_2 g}{u_{inj}} \frac{W}{L} \tag{A.171}$$

$$G_{12} = \frac{k_x \lambda_{r3}^{\circ} \rho_3 g}{u_{inj}} \frac{W}{L} \tag{A.172}$$

$$G_{13} = \frac{k_x \lambda_{r1}^{\circ} \rho_1 g \cos\alpha}{u_{inj}} \frac{H}{L} \tag{A.173}$$

$$G_{14} = \frac{k_x \lambda_{r2}^{\circ} \rho_2 g \cos\alpha}{u_{inj}} \frac{H}{L} \tag{A.174}$$

$$G_{15} = \frac{k_x \lambda_{r3}^{\circ} \rho_3 g \cos\alpha}{u_{inj}} \frac{H}{L} \tag{A.175}$$

$$G_1 = \frac{k_z}{k_x} \frac{L^2}{H^2} \tag{A.176}$$

$$G_2 = \frac{k_y}{k_x} \frac{L^2}{W^2} \tag{A.177}$$

Also the third scaling group (G_3) is the inverse of the mobility ratio for water-oil two-phase flow, therefore this group is inverted to $\frac{\lambda_{r1}^{\circ}}{\lambda_{r2}^{\circ}}$ which is more popular scaling group for mobility ratio. In addition, all gravity related scaling groups have the absolute value of fluid density in each phase. It is widely known that the fluid density differences are responsible for gravity driving mechanism. Therefore the existing gravity related dimensionless groups can be manipulated to obtain the buoyancy effects groups as follow:

$$G_7 = \frac{k_x \lambda_{r2}^{\circ} \rho_1 g \sin\alpha}{u_{inj}} \frac{\lambda_{r1}^{\circ}}{\lambda_{r2}^{\circ}} = G_7^* M^{\circ} \quad \text{(A.178)}$$

$$G_9 = \frac{k_x \lambda_{r2}^{\circ} \rho_3 g \sin\alpha}{u_{inj}} \frac{\lambda_{r3}^{\circ}}{\lambda_{r2}^{\circ}} = G_9^* M^{\circ} \quad \text{(A.179)}$$

$$G_{10} = \frac{k_x \lambda_{r2}^{\circ} \rho_1 g}{u_{inj}} \frac{W}{L} \frac{\lambda_{r1}^{\circ}}{\lambda_{r2}^{\circ}} = G_{10}^* M^{\circ} \quad \text{(A.180)}$$

$$G_{12} = \frac{k_x \lambda_{r2}^{\circ} \rho_1 g}{u_{inj}} \frac{W}{L} \frac{\lambda_{r3}^{\circ}}{\lambda_{r2}^{\circ}} = G_{12}^* M^{\circ} \quad \text{(A.181)}$$

$$G_{13} = \frac{k_x \lambda_{r2}^{\circ} \rho_1 g \cos\alpha}{u_{inj}} \frac{H}{L} \frac{\lambda_{r1}^{\circ}}{\lambda_{r2}^{\circ}} = G_{13}^* M^{\circ} \quad \text{(A.182)}$$

$$G_{15} = \frac{k_x \lambda_{r2}^{\circ} \rho_3 g \cos\alpha}{u_{inj}} \frac{H}{L} \frac{\lambda_{r3}^{\circ}}{\lambda_{r2}^{\circ}} = G_{15}^* M^{\circ} \quad \text{(A.183)}$$

Then the density differences between G_7^* and G_8, G_9^* and G_8, and also G_{10}^* and G_{11}, G_{12}^* and D_{11}, as well as G_{13}^* and G_{14}, G_{15}^* and G_{14} are new scaling parameters:

$$G_7^* - G_9 = \frac{k_x \lambda_{r2}^{\circ} \Delta\rho g \sin\alpha}{u_{inj}} = G_{24} \qquad \textit{where} \qquad \Delta\rho_{12} = \rho_1 - \rho_3 \quad \text{A.184)}$$

$$G_9^* - G_8 = \frac{k_x \lambda_{r2}^{\circ} \Delta\rho g \sin\alpha}{u_{inj}} = G_{25} \qquad \textit{where} \qquad \Delta\rho_{32} = \rho_3 - \rho_2 \quad \text{(A.185)}$$

$$G_{10}^* - G_{12} = \frac{k_x \lambda_{r2}^{\circ} \Delta\rho g}{u_{inj}} \frac{W}{L} = G_{26} \qquad \textit{where} \qquad \Delta\rho_{12} = \rho_1 - \rho_3 \quad \text{(A.186)}$$

$$G_{12}^* - G_{11} = \frac{k_x \lambda_{r2}^{\circ} \Delta\rho g}{u_{inj}} \frac{W}{L} = G_{27} \qquad \textit{where} \qquad \Delta\rho_{32} = \rho_3 - \rho_2 \quad \text{(A.187)}$$

$$G_{13}^* - G_{15} = \frac{k_x \lambda_{r2}^{\circ} \Delta\rho g \cos\alpha}{u_{inj}} \frac{H}{L} = G_{28} \quad \textit{where} \quad \Delta\rho_{12} = \rho_1 - \rho_3 \quad \text{(A.188)}$$

$$G_{15}^* - G_{14} = \frac{k_x \lambda_{r2}^{\circ} \Delta\rho g \cos\alpha}{u_{inj}} \frac{H}{L} = G_{29} \quad \textit{where} \quad \Delta\rho_{32} = \rho_3 - \rho_2 \quad \text{(A.189)}$$

Usually scaling groups that contain density differences rather than absolute density values are more widely used groups. It should be noted that, groups with density differences can be replaced with one of the gravity related groups to keep the groups independent of each other. Therefore following are final configuration of dimensionless scaling groups:

$$G_1 = \frac{k_z}{k_x}\frac{L^2}{H^2} \tag{A.190}$$

$$G_2 = \frac{k_y}{k_x}\frac{L^2}{W^2} \tag{A.191}$$

$$G_3 = \frac{1}{G_3} = \frac{\lambda^\circ_{r1}}{\lambda^\circ_{r2}} \tag{A.192}$$

$$G_4 = \frac{1}{G_4} = \frac{\lambda^\circ_{r2}}{\lambda^\circ_{r3}} \tag{A.193}$$

$$G_5 = \frac{\sigma_{21} k_x \lambda^\circ_{r2} \sqrt{\frac{\phi}{k_x}}}{u_{inj}.L} \tag{A.194}$$

$$G_6 = \frac{\sigma_{32} k_x \lambda^\circ_{r3} \sqrt{\frac{\phi}{k_x}}}{u_{inj}.L} \tag{A.195}$$

$$G_7 = \frac{k_x \lambda^\circ_{r1} \rho_1 g \sin\alpha}{u_{inj}} \tag{A.196}$$

$$G_8 = \frac{k_x \lambda^\circ_{r2} \Delta\rho_{32} g \sin\alpha}{u_{inj}} \qquad \textit{where} \qquad \Delta\rho_{32} = \rho_3 - \rho_2 \tag{A.197}$$

$$G_9 = \frac{k_x \lambda^\circ_{r3} \rho_3 g \sin\alpha}{u_{inj}} \tag{A.198}$$

$$G_{10} = \frac{k_x \lambda^\circ_{r1} \rho_1 g \cos\alpha}{u_{inj}}\frac{H}{L} \tag{A.199}$$

$$G_{11} = \frac{k_x \lambda^\circ_{r2} \Delta\rho_{32} g \cos\alpha}{u_{inj}}\frac{H}{L} \qquad \textit{where} \qquad \Delta\rho_{32} = \rho_3 - \rho_2 \tag{A.200}$$

$$G_{12} = \frac{k_x \lambda^\circ_{r3} \rho_3 g \cos\alpha}{u_{inj}}\frac{H}{L} \tag{A.201}$$

$$G_{13} = \frac{k_x \lambda^\circ_{r2} \Delta\rho_{13} g \sin\alpha}{u_{inj}} \qquad \textit{where} \qquad \Delta\rho_{12} = \rho_1 - \rho_3 \tag{A.202}$$

$$G_{14} = \frac{k_x \lambda^\circ_{r2} \Delta\rho_{13} g \cos\alpha}{u_{inj}}\frac{H}{L} \qquad \textit{where} \qquad \Delta\rho_{13} = \rho_1 - \rho_3 \tag{A.203}$$

$$G_{15} = \frac{C_2^I}{C_3^J} \tag{A.204}$$

$$G_{16} = \frac{C_3^I}{C_3^J} \tag{A.205}$$

$$G_{17} = \frac{C_4^I}{C_3^J} \tag{A.206}$$

$$G_{18} = \frac{P}{P_{ci}} \tag{A.207}$$

$$G_{19} = \frac{T}{T_{ci}} \tag{A.208}$$

$$G_{20} = \omega_i \tag{A.209}$$

$$G_{21} = \frac{P_{inj}}{P_{MMP}} \tag{A.210}$$

$$G_{22} = \frac{P_P}{P_{MMP}} \tag{A.211}$$

Minimizing the Number of Scaling Groups

Final step in deriving scaling groups is to determine whether they are independent. In order to this, logarithm of both sides of Equations A.190 through A.206 is taken. The rank of coefficient matrix will denote the number of independent scaling groups. It should be noted that since Equations A.207 through A.209 are phase behavior-related dimensionless groups, and have been derived from auxiliary equations, they are completely independent of scaling groups derived from flow equations. Equations A. 210 and A.211 is also valid only in the scenarios that both injection and production wells are operated under BHP constraint, and is not part of major scaling groups.

After taking the logarithm a linear system of equations with 17 equations and 24 unknowns, which is shown as Equation A.212, is obtained. The arrays in the coefficient matrix are the exponents of different variables in the dimensionless scaling groups presented in Equations A.190 through A.206. Applying linear algebraic methods and simple row operations indicates that the rank of the coefficient matrix is 13. According to

these principles, modified form of coefficient matrix was found and it is shown as Equation A.213.

Fourteen scaling groups are resulted from matrix operations which should also be added to the three EOS-related scaling groups. The total number of scaling groups were determined as 17 groups. Following equations show the final dimensionless independent scaling groups for any CO_2 injection process.

$$G_1^f = \frac{k_z}{k_x}\frac{L^2}{H^2}$$

$$G_2^f = \frac{k_y}{k_x}\frac{L^2}{W^2}$$

$$G_3^f = \frac{1}{G_3} = \frac{\lambda_{r1}^{\circ}}{\lambda_{r2}^{\circ}}$$

$$G_4^f = \frac{1}{G_4} = \frac{\lambda_{r2}^{\circ}}{\lambda_{r3}^{\circ}}$$

$$G_5^f = \frac{\sigma_{21} k_x \lambda_{r2}^{\circ} \sqrt{\frac{\phi}{k_x}}}{u_{inj}.L}$$

$$G_6^f = \frac{\sigma_{32} k_x \lambda_{r3}^{\circ} \sqrt{\frac{\phi}{k_x}}}{u_{inj}.L}$$

$$G_7^f = \frac{H}{L}\tan\alpha$$

$$G_8^f = \frac{\Delta\rho_{32}}{\Delta\rho_{13}}$$

$$G_9^f = \frac{k_x \lambda_{r2}^{\circ} \Delta\rho_{32} g\cos\alpha}{u_{inj}}\frac{H}{L}$$

$$G_{10}^f = \frac{k_x \lambda_{r2}^{\circ} \Delta\rho g\cos\alpha}{u_{inj}}\frac{H}{L}$$

$$G_{11}^f = \frac{C_2^I}{C_3^J}$$

$$G_{12}^f = \frac{C_3^I}{C_3^J}$$

$$G_{13}^{f} = \frac{C_4^I}{C_3^J}$$

EOS-related scaling groups:

$$G_{14}^{f} = \frac{P}{P_{ci}}$$

$$G_{15}^{f} = \frac{T}{T_{ci}}$$

$$G_{16}^{f} = \omega_i$$

Alternate scaling groups when CO_2 flooding is performed under bottom hole pressure constraint:

$$\overline{G_{17}^{f}} = \frac{P_{inj}}{P_{MMP}}$$

$$\overline{G_{18}^{f}} = \frac{P_P}{P_{MMP}}$$

Therefore the final number of dimensionless scaling groups is 16, besides of two alternate scaling groups.

$$
\begin{bmatrix}
-1 & 0 & 1 & 2 & -2 & 0 & 0 & 0 & 0 & 0 & 0 & 0 & 0 & 0 & 0 & 0 & 0 & 0 & 0 & 0 & 0 & 0 & 0 & 0 \\
-1 & 1 & 0 & 2 & 0 & -2 & 0 & 0 & 0 & 0 & 0 & 0 & 0 & 0 & 0 & 0 & 0 & 0 & 0 & 0 & 0 & 0 & 0 & 0 \\
0 & 0 & 0 & 0 & 0 & 0 & 1 & -1 & 0 & 0 & 0 & 0 & 0 & 0 & 0 & 0 & 0 & 0 & 0 & 0 & 0 & 0 & 0 & 0 \\
0 & 0 & 0 & 0 & 0 & 0 & 0 & 1 & -1 & 0 & 0 & 0 & 0 & 0 & 0 & 0 & 0 & 0 & 0 & 0 & 0 & 0 & 0 & 0 \\
1/2 & 0 & 0 & -1 & 0 & 0 & 0 & 1 & 0 & 1 & 0 & 1/2 & -1 & 0 & 0 & 0 & 0 & 0 & 0 & 0 & 0 & 0 & 0 & 0 \\
1/2 & 0 & 0 & -1 & 0 & 0 & 0 & 0 & 1 & 0 & 1 & 1/2 & -1 & 0 & 0 & 0 & 0 & 0 & 0 & 0 & 0 & 0 & 0 & 0 \\
1 & 0 & 0 & 0 & 0 & 0 & 1 & 0 & 0 & 0 & 0 & 0 & -1 & 1 & 0 & 0 & 1 & 1 & 0 & 0 & 0 & 0 & 0 & 0 \\
1 & 0 & 0 & 0 & 0 & 0 & 0 & 1 & 0 & 0 & 0 & 0 & -1 & 0 & 0 & 1 & 1 & 1 & 0 & 0 & 0 & 0 & 0 & 0 \\
1 & 0 & 0 & 0 & 0 & 0 & 0 & 0 & 1 & 0 & 0 & 0 & -1 & 0 & 1 & 0 & 1 & 1 & 0 & 0 & 0 & 0 & 0 & 0 \\
1 & 0 & 0 & -1 & 1 & 0 & 1 & 0 & 0 & 0 & 0 & 0 & -1 & 1 & 0 & 0 & 1 & 0 & 1 & 0 & 0 & 0 & 0 & 0 \\
1 & 0 & 0 & -1 & 1 & 0 & 0 & 1 & 0 & 0 & 0 & 0 & -1 & 0 & 0 & 1 & 1 & 0 & 1 & 0 & 0 & 0 & 0 & 0 \\
1 & 0 & 0 & -1 & 1 & 0 & 0 & 0 & 1 & 0 & 0 & 0 & -1 & 0 & 1 & 0 & 1 & 0 & 1 & 0 & 0 & 0 & 0 & 0 \\
1 & 0 & 0 & 0 & 0 & 0 & 0 & 1 & 0 & 0 & 0 & 0 & -1 & 0 & 0 & 0 & 1 & 1 & 0 & 0 & 0 & 0 & 0 & 1 \\
1 & 0 & 0 & -1 & 1 & 0 & 0 & 1 & 0 & 0 & 0 & 0 & -1 & 0 & 0 & 0 & 1 & 0 & 1 & 0 & 0 & 0 & 0 & 1 \\
0 & 0 & 0 & 0 & 0 & 0 & 0 & 0 & 0 & 0 & 0 & 0 & 0 & 0 & 0 & 0 & 0 & 0 & 0 & 0 & 1 & 0 & 0 & -1 & 0 \\
0 & 0 & 0 & 0 & 0 & 0 & 0 & 0 & 0 & 0 & 0 & 0 & 0 & 0 & 0 & 0 & 0 & 0 & 0 & 0 & 0 & 1 & 0 & -1 & 0 \\
0 & 0 & 0 & 0 & 0 & 0 & 0 & 0 & 0 & 0 & 0 & 0 & 0 & 0 & 0 & 0 & 0 & 0 & 0 & 0 & 0 & 0 & 1 & -1 & 0
\end{bmatrix}
\begin{bmatrix}
\ln k_x \\ \ln k_y \\ \ln k_z \\ \ln L \\ \ln H \\ \ln W \\ \ln \lambda_{r1}^{\circ} \\ \ln \lambda_{r2}^{\circ} \\ \ln \lambda_{r3}^{\circ} \\ \ln \sigma_{21} \\ \ln \sigma_{32} \\ \ln \phi \\ \ln u_{inj} \\ \ln \rho_1 \\ \ln \rho_3 \\ \ln \Delta\rho_{32} \\ \ln g \\ \ln \sin \alpha \\ \ln \cos \alpha \\ \ln C_2^I \\ \ln C_3^I \\ \ln C_4^I \\ \ln C_3^J \\ \ln \Delta\rho_{13}
\end{bmatrix}
=
\begin{bmatrix}
\ln G_1 \\ \ln G_2 \\ \ln G_3 \\ \ln G_4 \\ \ln G_5 \\ \ln G_6 \\ \ln G_7 \\ \ln G_8 \\ \ln G_9 \\ \ln G_{10} \\ \ln G_{11} \\ \ln G_{12} \\ \ln G_{13} \\ \ln G_{14} \\ \ln G_{15} \\ \ln G_{16} \\ \ln G_{17}
\end{bmatrix}
\tag{A.212}
$$

$$\begin{bmatrix}
-1 & 0 & 1 & 2 & -2 & 0 & 0 & 0 & 0 & 0 & 0 & 0 & 0 & 0 & 0 & 0 & 0 & 0 & 0 & 0 & 0 & 0 & 0 \\
-1 & 1 & 0 & 2 & 0 & -2 & 0 & 0 & 0 & 0 & 0 & 0 & 0 & 0 & 0 & 0 & 0 & 0 & 0 & 0 & 0 & 0 & 0 \\
0 & 0 & 0 & 0 & 0 & 0 & 1 & -1 & 0 & 0 & 0 & 0 & 0 & 0 & 0 & 0 & 0 & 0 & 0 & 0 & 0 & 0 & 0 \\
0 & 0 & 0 & 0 & 0 & 0 & 0 & 1 & -1 & 0 & 0 & 0 & 0 & 0 & 0 & 0 & 0 & 0 & 0 & 0 & 0 & 0 & 0 \\
1/2 & 0 & 0 & -1 & 0 & 0 & 0 & 1 & 0 & 1 & 0 & 1/2 & -1 & 0 & 0 & 0 & 0 & 0 & 0 & 0 & 0 & 0 & 0 & 0 \\
1/2 & 0 & 0 & -1 & 0 & 0 & 0 & 0 & 1 & 0 & 1 & 1/2 & -1 & 0 & 0 & 0 & 0 & 0 & 0 & 0 & 0 & 0 & 0 & 0 \\
0 & 0 & 0 & -1 & 1 & 0 & 0 & 0 & 0 & 0 & 0 & 0 & 0 & 0 & 0 & 0 & 0 & 1 & -1 & 0 & 0 & 0 & 0 & 0 \\
0 & 0 & 0 & 0 & 0 & 0 & 0 & 0 & 0 & 0 & 0 & 0 & 0 & 0 & 0 & 1 & 0 & 0 & 0 & 0 & 0 & 0 & 0 & -1 \\
0 & 0 & 0 & 0 & 0 & 0 & 0 & 0 & 0 & 0 & 0 & 0 & 0 & 0 & 0 & 0 & 0 & 0 & 0 & 0 & 0 & 0 & 0 & 0 \\
0 & 0 & 0 & 0 & 0 & 0 & 0 & 0 & 0 & 0 & 0 & 0 & 0 & 0 & 0 & 0 & 0 & 0 & 0 & 0 & 0 & 0 & 0 & 0 \\
1 & 0 & 0 & -1 & 1 & 0 & 0 & 1 & 0 & 0 & 0 & 0 & -1 & 0 & 0 & 1 & 1 & 0 & 1 & 0 & 0 & 0 & 0 & 0 \\
0 & 0 & 0 & 0 & 0 & 0 & 0 & 0 & 0 & 0 & 0 & 0 & 0 & 0 & 0 & 0 & 0 & 0 & 0 & 0 & 0 & 0 & 0 & 0 \\
0 & 0 & 0 & 0 & 0 & 0 & 0 & 0 & 0 & 0 & 0 & 0 & 0 & 0 & 0 & 0 & 0 & 0 & 0 & 0 & 0 & 0 & 0 & 0 \\
1 & 0 & 0 & -1 & 1 & 0 & 0 & 1 & 0 & 0 & 0 & 0 & -1 & 0 & 0 & 0 & 1 & 0 & 1 & 0 & 0 & 0 & 0 & 1 \\
0 & 0 & 0 & 0 & 0 & 0 & 0 & 0 & 0 & 0 & 0 & 0 & 0 & 0 & 0 & 0 & 0 & 0 & 0 & 1 & 0 & 0 & -1 & 0 \\
0 & 0 & 0 & 0 & 0 & 0 & 0 & 0 & 0 & 0 & 0 & 0 & 0 & 0 & 0 & 0 & 0 & 0 & 0 & 0 & 1 & 0 & -1 & 0 \\
0 & 0 & 0 & 0 & 0 & 0 & 0 & 0 & 0 & 0 & 0 & 0 & 0 & 0 & 0 & 0 & 0 & 0 & 0 & 0 & 0 & 1 & -1 & 0
\end{bmatrix} \tag{A.213}$$

Appendix B: Data Corresponding to the Development of MMP Correlation

APPENDIX B-1: PREVIOUSLY PUBLISHED MMP CORRELATIONS

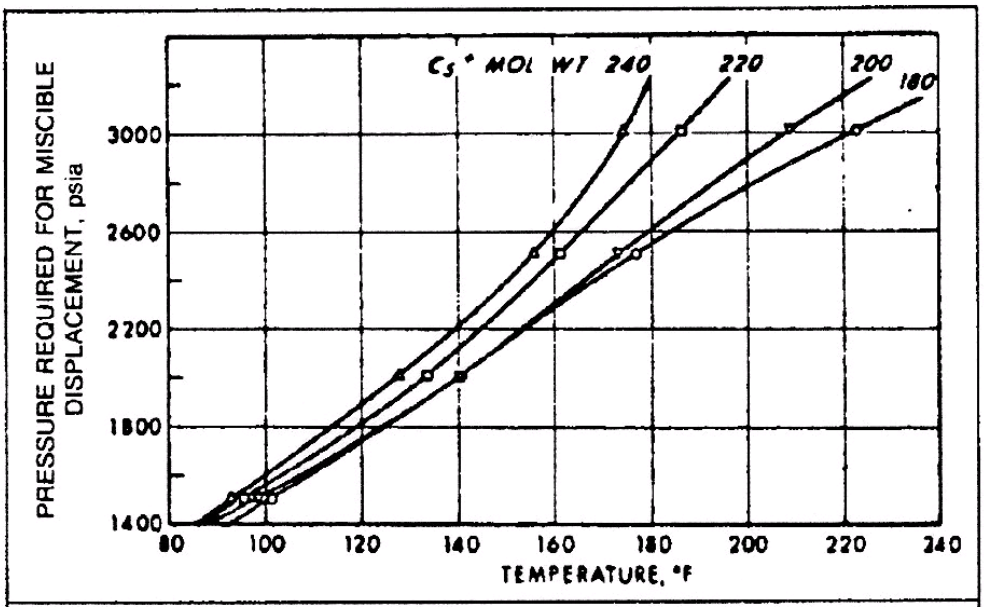

(a)

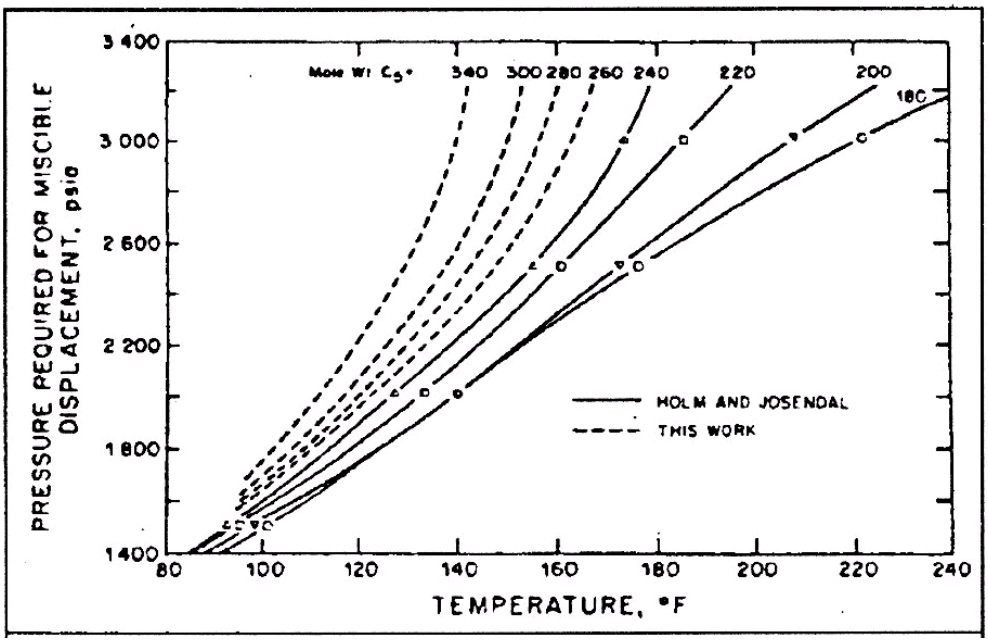

(b)

Figure B.1 -MMP correlation (a) in CO2 flooding from Holm and Josendal (1974) and its extended version by Mungan (b) (1981).

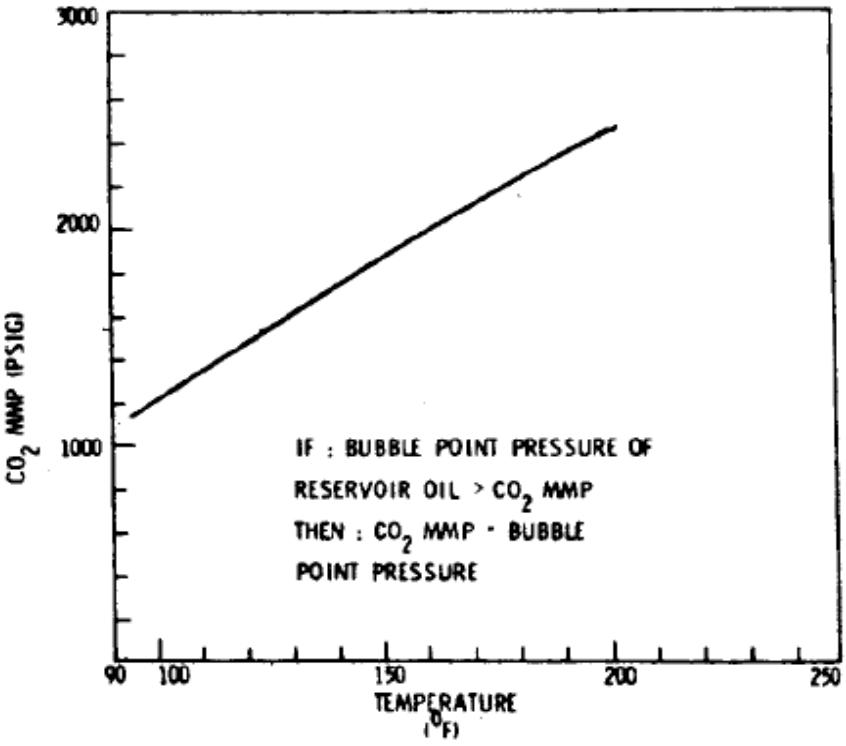

Figure B.2 -MMP Correlation by Yellig and Metcalfe (1980)

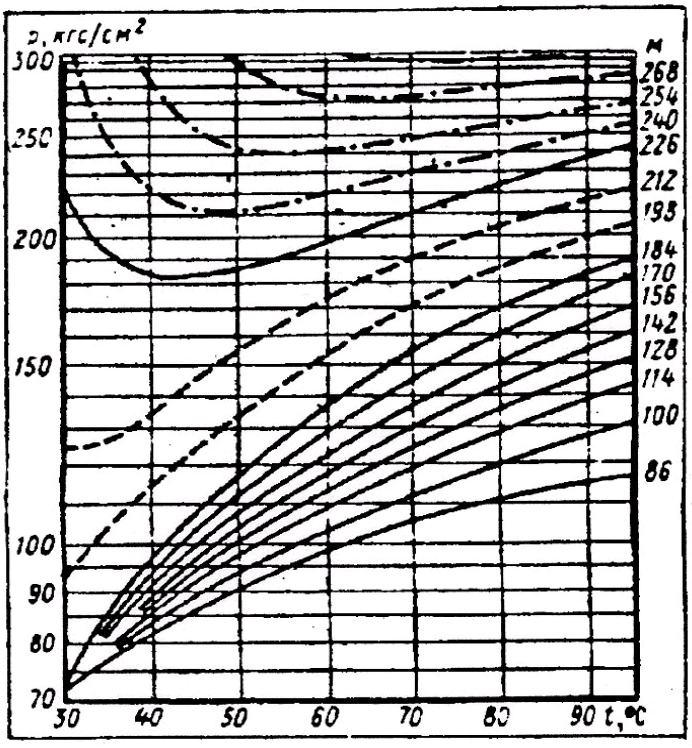

Figure B.3 -MMP Correlation by Dunyushkin and Namiot (1978)

Glaso (1985) Correlation for CO_2 MMP:

for C_{2-6}> 18%:

$$MMP = 810 - 3.404 M_{C_{7+}} + 1.7E-9 M_{C_{7+}}^{3.730} e^{786.8 M_{C_{7+}}^{-1.058}} T$$

and for for C_{2-6}< 18%:

$$MMP = 2947.9 - 3.404 M_{C_{7+}} + 1.7E-9 M_{C_{7+}}^{3.730} e^{786.8 M_{C_{7+}}^{-1.058}} T - 121.2 f_{RF}$$

where M_{C7+} is molecular weight of C_{7+} , T is reservoir temperature, and f_{RF} is mole percent of C_{2-4} in reservoir fluid.

Cronquist (1978) Correlation for CO_2 MMP:

$$MMP = 15.988 T^{0.744206 + 0.0011038 M_{C5+} + 0.0015279 y_{c1}}$$

where yc1 is mole percent of Methane and Nitrogen in the reservoir fluid.

Yuan et al. (2004) Correlation for CO_2 MMP:

$$MMP = a_1 + a_2 M_{C_{7+}} + a_3 P_{C_{2-6}} + \left(a_4 + a_5 M_{C_{7+}} + a_6 \frac{P_{C_{2-6}}}{M_{C_{7+}}} \right) T + \left(a_7 + a_8 M_{C_{7+}} + a_9 M_{C_{7+}}^2 + a_{10} P_{C_{2-6}} \right) T^2$$

APPENDIX B-2: EOS PARAMETERS FOR THE FLUID DATABASE UTILIZED IN DEVELOPING MMP CORRELATION

Table B.1: EOS parameters for fluid properties of APNDXD2-LK oil sample.

	'CO2'	'C1'	'C2toNC4'	'IC5toC6'	'HYP01'	'HYP02'	'HYP03'
Specific Gravity	0.82	0.30	0.43	0.66	0.75	0.81	0.89
Boiling Point, °C	-109.21	-258.61	-39.87	119.04	244.73	491.82	829.71
Critical Pressure, atm	72.80	45.40	44.91	32.99	29.35	17.79	9.66
Critical Volume, m3/K-mole	0.09	0.10	0.18	0.32	0.42	0.77	1.45
Critical Temperature, °K	304.20	190.60	341.11	483.40	573.12	703.96	864.98
Acentric Factor	0.23	0.01	0.12	0.25	0.35	0.64	1.10
Molecular Weight, gr/gr-mole	44.01	16.04	37.57	78.01	108.21	191.93	370.00
Binary Interaction Coefficients:							
	0.08						
	0.08	0.00					
	0.09	0.00	0.00				
	0.11	0.00	0.00	0.00			
	0.11	0.00	0.00	0.00	0.00		
	0.11	0.00	0.00	0.00	0.00	0.00	
Volume shift Parameter	-0.09	-0.15	-0.09	-0.02	0.04	0.13	0.09
Mole Fraction of Components	0.03	0.68	0.20	0.03	0.04	0.02	0.00

Table B.2: EOS parameters for fluid properties of COATS85-TBL1 oil sample

	'CO2'	'C1'	'C2toNC4'	'IC5toC6'	'HYP01'	'HYP02'	'HYP03'
Specific Gravity	0.82	0.30	0.46	0.65	0.74	0.81	0.89
Boiling Point, °C	-109.21	-258.61	-8.97	111.69	259.49	552.71	920.44
Critical Pressure, atm	72.80	45.40	43.45	33.09	26.86	14.78	7.65
Critical Volume, m3/K-mole	0.09	0.10	0.19	0.32	0.46	0.92	1.78
Critical Temperature, °K	304.20	190.60	356.99	478.43	577.24	727.88	899.47
Acentric Factor	0.23	0.01	0.14	0.25	0.37	0.74	1.24
Molecular Weight, gr/gr-mole	44.01	16.04	41.19	76.54	113.66	222.02	452.50
Binary Interaction Coefficients:							
	0.06						
	0.06	0.00					
	0.06	0.00	0.00				
	0.11	0.00	0.00	0.00			
	0.11	0.00	0.00	0.00	0.00		
	0.11	0.00	0.00	0.00	0.00	0.00	
Volume shift Parameter	-0.09	-0.15	-0.08	-0.03	0.02	0.20	0.36
Mole Fraction of Components	0.04	0.61	0.16	0.04	0.08	0.06	0.01

Table B.3: EOS parameters for fluid properties of JCBY-TBL1 oil sample

	'CO2'	'C1'	'C2toNC4'	'IC5toC6'	'HYP01'	'HYP02'	'HYP03'
Specific Gravity	0.82	0.30	0.46	0.65	0.74	0.81	0.89
Boiling Point, °C	-109.21	-258.61	-8.97	111.69	259.49	552.71	920.44
Critical Pressure, atm	72.80	45.40	43.45	33.09	26.86	14.78	7.65
Critical Volume, m3/K-mole	0.09	0.10	0.19	0.32	0.46	0.92	1.78
Critical Temperature, °K	304.20	190.60	356.99	478.43	577.24	727.88	899.47
Acentric Factor	0.23	0.01	0.14	0.25	0.37	0.74	1.24
Molecular Weight, gr/gr-mole	44.01	16.04	41.19	76.54	113.66	222.02	452.50
Binary Interaction Coefficients:							
	0.06						
	0.06	0.00					
	0.06	0.00	0.00				
	0.10	0.00	0.00	0.00			
	0.10	0.00	0.00	0.00	0.00		
	0.10	0.00	0.00	0.00	0.00	0.00	
Volume shift Parameter	-0.09	-0.15	-0.08	-0.03	0.02	0.20	0.36
Mole Fraction of Components	0.04	0.61	0.16	0.04	0.08	0.06	0.01

Table B.4: EOS parameters for fluid properties of COATS86-OL2 oil sample

	'CO2'	'C1'	'C2toNC4'	'IC5toC6'	'HYP01'	'HYP02'	'HYP03'
Specific Gravity	0.82	0.30	0.46	0.66	0.78	0.85	0.94
Boiling Point, °C	-109.21	-258.61	-20.62	119.21	265.21	559.39	937.16
Critical Pressure, atm	72.80	45.40	43.79	32.99	29.92	16.89	8.84
Critical Volume, m3/K-mole	0.09	0.10	0.19	0.32	0.42	0.83	1.62
Critical Temperature, °K	304.20	190.60	352.69	483.48	589.72	744.23	923.19
Acentric Factor	0.23	0.01	0.13	0.25	0.36	0.70	1.20
Molecular Weight, gr/gr-mole	44.01	16.04	40.20	77.96	112.34	214.72	432.50
Binary Interaction Coefficients:							
	0.05						
	0.05	0.00					
	0.05	0.00	0.00				
	0.1	0.00	0.00	0.00			
	0.1	0.00	0.00	0.00	0.00		
	0.1	0.00	0.00	0.00	0.00	0.00	
Volume shift Parameter	-0.09	-0.15	-0.08	-0.02	-0.01	0.17	0.34
Mole Fraction of Components	0.01	0.53	0.25	0.04	0.09	0.06	0.01

Table B.5: EOS parameters for fluid properties of JRHFPOOLE oil sample

	'CO2'	'C1'	'C2toNC4'	'IC5toC6'	'HYP01'	'HYP02'	'HYP03'
Specific Gravity	0.82	0.30	0.46	0.67	0.76	0.83	0.92
Boiling Point, °C	-109.21	-258.61	-15.69	129.99	268.17	579.97	963.72
Critical Pressure, atm	72.80	45.40	43.73	32.82	27.53	14.80	7.58
Critical Volume, m3/K-mole	0.09	0.10	0.19	0.33	0.45	0.93	1.83
Critical Temperature, °K	304.20	190.60	353.42	491.61	585.33	745.65	924.91
Acentric Factor	0.23	0.01	0.13	0.26	0.38	0.76	1.27
Molecular Weight, gr/gr-mole	44.01	16.04	40.40	80.69	115.31	231.14	477.50
Binary Interaction Coefficients:							
	0.06						
	0.06	0.00					
	0.06	0.00	0.00				
	0.11	0.00	0.00	0.00			
	0.11	0.00	0.00	0.00	0.00		
	0.11	0.00	0.00	0.00	0.00	0.00	
Volume shift Parameter	-0.09	-0.15	-0.08	-0.02	0.01	0.20	0.36
Mole Fraction of Components	0.01	0.59	0.17	0.05	0.09	0.07	0.01

Table B.6: EOS parameters for fluid properties of Danesh-tbl2.1A oil sample

	'CO2'	'C1'	'C2toNC4'	'IC5toC6'	'HYP01'	'HYP02'	'HYP03'
Specific Gravity	0.82	0.30	0.46	0.67	0.77	0.86	0.95
Boiling Point, °C	-109.21	-258.61	-9.62	129.19	286.48	639.08	1048.81
Critical Pressure, atm	72.80	45.40	43.35	32.83	27.45	13.87	6.97
Critical Volume, m3/K-mole	0.09	0.10	0.19	0.33	0.46	1.01	2.01
Critical Temperature, °K	304.20	190.60	357.64	490.99	598.32	778.03	968.95
Acentric Factor	0.23	0.01	0.14	0.26	0.39	0.83	1.35
Molecular Weight, gr/gr-mole	44.01	16.04	41.35	80.50	119.78	255.76	545.00
Binary Interaction Coefficients:							
	0.05						
	0.05	0.00					
	0.05	0.00	0.00				
	0.01	0.00	0.00	0.00			
	0.01	0.00	0.00	0.00	0.00		
	0.01	0.00	0.00	0.00	0.00	0.00	
Volume shift Parameter	-0.09	-0.15	-0.08	-0.02	0.01	0.22	0.38
Mole Fraction of Components	0.01	0.36	0.22	0.07	0.17	0.13	0.00

Table B.7: EOS parameters for fluid properties of JRHFPOOLD oil sample

	'CO2'	'C1'	'C2toNC4'	'IC5toC6'	'HYP01'	'HYP02'	'HYP03'
Specific Gravity	0.82	0.30	0.47	0.67	0.77	0.84	0.93
Boiling Point, °C	-109.21	-258.61	-8.75	129.40	277.46	609.91	1007.84
Critical Pressure, atm	72.80	45.40	43.20	32.83	27.62	14.40	7.30
Critical Volume, m3/K-mole	0.09	0.10	0.19	0.33	0.45	0.97	1.91
Critical Temperature, °K	304.20	190.60	358.98	491.08	592.30	762.62	948.31
Acentric Factor	0.23	0.01	0.14	0.26	0.38	0.79	1.31
Molecular Weight, gr/gr-mole	44.01	16.04	41.68	80.44	117.46	242.99	510.00
Binary Interaction Coefficients:							
	0.06						
	0.06	0.00					
	0.06	0.00	0.00				
	0.10	0.00	0.00	0.00			
	0.10	0.00	0.00	0.00	0.01		
	0.10	0.00	0.00	0.00	0.03	0.01	
Volume shift Parameter	-0.09	-0.15	-0.08	-0.02	0.01	0.21	0.37
Mole Fraction of Components	0.01	0.42	0.21	0.07	0.15	0.11	0.03

Table B.8: EOS parameters for fluid properties of COATS-OL6 oil sample

	'CO2'	'C1'	'C2toNC4'	'IC5toC6'	'HYP01'	'HYP02'	'HYP03'
Specific Gravity	0.82	0.30	0.47	0.66	0.77	0.84	0.93
Boiling Point, °C	-109.21	-258.61	-8.10	122.79	275.53	602.95	998.23
Critical Pressure, atm	72.80	45.40	42.96	32.94	27.83	14.65	7.45
Critical Volume, m3/K-mole	0.09	0.10	0.19	0.32	0.45	0.95	1.88
Critical Temperature, °K	304.20	190.60	360.81	486.09	591.48	759.65	944.34
Acentric Factor	0.23	0.01	0.14	0.26	0.38	0.78	1.30
Molecular Weight, gr/gr-mole	44.01	16.04	42.17	78.87	116.80	239.34	500.00
Binary Interaction Coefficients:							
	0.055						
	0.055	0.00					
	0.055	0.00	0.00				
	0.10	0.00	0.00	0.00			
	0.10	0.00	0.00	0.00	0.00		
	0.10	0.00	0.00	0.00	0.00	0.00	
Volume shift Parameter	-0.09	-0.15	-0.08	-0.02	0.00	0.20	0.37
Mole Fraction of Components	0.02	0.36	0.24	0.07	0.16	0.12	0.03

Table B.9: EOS parameters for fluid properties of 14923-SPE oil sample

	'CO2'	'C1'	'C2toNC4'	'IC5toC6'	'HYP01'	'HYP02'	'HYP03'
Specific Gravity	0.82	0.30	0.47	0.66	0.77	0.84	0.93
Boiling Point, °C	-109.21	-258.61	-8.93	121.26	270.10	583.82	971.03
Critical Pressure, atm	72.80	45.40	43.02	32.97	28.22	15.22	7.80
Critical Volume, m3/K-mole	0.09	0.10	0.19	0.32	0.44	0.92	1.79
Critical Temperature, °K	304.20	190.60	362.35	484.84	588.63	750.68	932.13
Acentric Factor	0.23	0.01	0.14	0.26	0.37	0.76	1.26
Molecular Weight, gr/gr-mole	44.01	16.04	42.28	78.21	115.15	230.23	475.00
Binary Interaction Coefficients:							
	0.06						
	0.07	0.00					
	0.07	0.00	0.00				
	0.095	0.00	0.00	0.00			
	0.095	0.00	0.00	0.00	0.00		
	0.095	0.00	0.00	0.00	0.00	0.00	
Volume shift Parameter	-0.09	-0.15	-0.08	-0.02	0.05	0.16	0.07
Mole Fraction of Components	0.00	0.30	0.29	0.08	0.17	0.13	0.03

Table B.10: EOS parameters for fluid properties of Tbl15.2-Pdsn oil sample

	'CO2'	'C1'	'C2toNC4'	'IC5toC6'	'HYP01'	'HYP02'	'HYP03'
Specific Gravity	0.82	0.30	0.47	0.66	0.77	0.84	0.93
Boiling Point, °C	-109.21	-258.61	-8.93	121.26	270.10	583.82	971.03
Critical Pressure, atm	72.80	45.40	43.02	32.97	28.22	15.22	7.80
Critical Volume, m3/K-mole	0.09	0.10	0.19	0.32	0.44	0.92	1.79
Critical Temperature, °K	304.20	190.60	362.35	484.84	588.63	750.68	932.13
Acentric Factor	0.23	0.01	0.14	0.26	0.37	0.76	1.26
Molecular Weight, gr/gr-mole	44.01	16.04	42.28	78.21	115.15	230.23	475.00
Binary Interaction Coefficients:							
	0.07						
	0.08	0.00					
	0.09	0.00	0.00				
	0.11	0.00	0.00	0.00			
	0.15	0.00	0.00	0.00	0.00		
	0.15	0.00	0.00	0.00	0.00	0.00	
Volume shift Parameter	-0.09	-0.15	-0.08	-0.02	0.05	0.16	0.07
Mole Fraction of Components	0.00	0.30	0.29	0.08	0.17	0.13	0.03

Table B.11: EOS parameters for fluid properties of COATS86-OL7 oil sample

	'CO2'	'C1'	'C2toNC4'	'IC5toC6'	'HYP01'	'HYP02'	'HYP03'
Specific Gravity	0.82	0.30	0.47	0.66	0.77	0.84	0.93
Boiling Point, °C	-109.21	-258.61	-8.93	121.26	270.10	583.82	971.03
Critical Pressure, atm	72.80	45.40	43.02	32.97	28.22	15.22	7.80
Critical Volume, m3/K-mole	0.09	0.10	0.19	0.32	0.44	0.92	1.79
Critical Temperature, °K	304.20	190.60	362.35	484.84	588.63	750.68	932.13
Acentric Factor	0.23	0.01	0.14	0.26	0.37	0.76	1.26
Molecular Weight, gr/gr-mole	44.01	16.04	42.28	78.21	115.15	230.23	475.00
Binary Interaction Coefficients:							
	0.05						
	0.05	0.00					
	0.05	0.00	0.00				
	0.09	0.00	0.00	0.00			
	0.09	0.00	0.00	0.00	0.00		
	0.09	0.00	0.00	0.00	0.00	0.00	
Volume shift Parameter	-0.09	-0.15	-0.08	-0.02	0.05	0.16	0.07
Mole Fraction of Components	0.00	0.30	0.29	0.08	0.17	0.13	0.03

Table B.12: EOS parameters for fluid properties of 3483-B oil sample

	'CO2'	'C1'	'C2toNC4'	'IC5toC6'	'HYP01'	'HYP02'	'HYP03'
Specific Gravity	0.82	0.30	0.46	0.66	0.79	0.88	0.97
Boiling Point, °C	-109.21	-258.61	-9.37	127.93	295.21	662.20	1082.10
Critical Pressure, atm	72.80	45.40	43.51	32.86	28.44	14.23	7.18
Critical Volume, m3/K-mole	0.09	0.10	0.19	0.33	0.45	1.01	1.99
Critical Temperature, °K	304.20	190.60	357.96	489.84	607.62	795.43	992.16
Acentric Factor	0.23	0.01	0.14	0.26	0.39	0.84	1.35
Molecular Weight, gr/gr-mole	44.01	16.04	41.23	79.93	120.60	260.32	557.50
Binary Interaction Coefficients:							
	0.06						
	0.06	0.00					
	0.06	0.00	0.00				
	0.10	0.00	0.00	0.00			
	0.10	0.00	0.00	0.00	0.00		
	0.10	0.00	0.00	0.00	0.00	0.00	
Volume shift Parameter	-0.09	-0.15	-0.08	-0.02	0.06	0.14	0.06
Mole Fraction of Components	0.03	0.28	0.19	0.08	0.21	0.17	0.05

Table B.13: EOS parameters for fluid properties of NWE oil sample

	'CO2'	'C1'	'C2toNC4'	'IC5toC6'	'HYP01'	'HYP02'	'HYP03'
Critical Pressure, atm	72.80	45.40	44.46	33.07	23.92	17.79	17.03
Critical Volume, m3/K-mole	0.09	0.10	0.18	0.31	0.55	1.00	1.24
Critical Temperature, °K	304.20	190.60	343.64	466.41	603.08	733.79	923.21
Acentric Factor	0.23	0.01	0.13	0.24	0.60	0.90	1.23
Molecular Weight, gr/gr-mole	44.01	16.04	38.40	72.82	135.82	257.75	479.95
Binary Interaction Coefficients:							
	0.055	0.00					
	0.055	0.00	0.00				
	0.055	0.00	0.00	0.00			
	0.105	0.00	0.00	0.00	0.00		
	0.105	0.00	0.00	0.00	0.00	0.00	
	0.105	-0.15	-0.09	-0.04	0.06	0.18	0.30
Volume shift Parameter	0.14	-0.15	-0.09	-0.04	0.06	0.18	0.30
Mole Fraction of Components	0.01	0.20	0.12	0.15	0.29	0.15	0.09
Parachor	92.65	39.90	102.10	205.40	416.30	762.40	1109.60

Table B.14: EOS parameters for fluid properties of RF7 oil sample

	'CO2'	'C1'	'C2toNC4'	'IC5toC6'	'HYP01'	'HYP02'	'HYP03'
Critical Pressure, atm	72.80	45.40	41.26	29.84	17.11	11.42	10.61
Critical Volume, m3/K-mole	0.94	0.99	2.14	3.89	10.45	30.57	45.11
Critical Temperature, °K	304.20	190.60	375.50	526.15	889.52	1353.33	1628.12
Acentric Factor	0.23	0.01	0.15	0.31	0.78	1.06	0.39
Molecular Weight, gr/gr-mole	44.01	16.04	43.75	90.33	216.54	674.44	996.77
Binary Interaction Coefficients:							
	0.04						
	0.04	0.00					
	0.07	0.00	0.00				
	0.07	0.00	0.00	0.00			
	0.07	0.00	0.00	0.00	0.00		
	0.07	0.00	0.00	0.00	0.00	0.00	
Volume shift Parameter	-0.06	-0.04	-0.02	0.01	0.03	0.03	0.06
Mole Fraction of Components	0.45	35.55	15.51	20.32	18.45	5.96	3.78
Parachor	78.00	77.30	157.10	285.00	655.90	1681.90	2404.10

Table B.15: EOS parameters for fluid properties of BSB5 oil sample

	'CO2'	'C1'	'C2toNC4'	'IC5toC6'	'HYP01'	'HYP02'	'HYP03'
Critical Pressure, atm	72.80	45.40	44.40	33.55	21.46	16.32	16.20
Critical Volume, m3/K-mole	0.09	0.10	0.18	0.30	0.56	1.06	2.02
Critical Temperature, °K	304.20	160.00	344.21	463.23	605.76	751.02	942.49
Acentric Factor	0.23	0.01	0.13	0.24	0.62	0.96	1.27
Molecular Weight, gr/gr-mole	44.01	16.04	37.20	69.50	140.96	280.99	519.62
Binary Interaction Coefficients:							
	0.055						
	0.055	0.00					
	0.055	0.00	0.00				
	0.105	0.00	0.00	0.00			
	0.105	0.00	0.00	0.00	0.00		
	0.105	0.00	0.00	0.00	0.00	0.00	
Volume shift Parameter	0.14	-0.15	-0.09	-0.04	0.06	0.18	0.30
Parachor	49.00	71.00	135.00	231.62	439.15	788.22	1112.46
Mole Fraction of Components	0.03	0.09	0.15	0.17	0.33	0.16	0.07

Table B.16: EOS parameters for fluid properties of RF6 oil sample

	'CO2'	'C1'	'C2toNC4'	'IC5toC6'	'HYP01'	'HYP02'	'HYP03'
Specific Gravity	0.49	0.27	0.53	0.64	0.81	0.98	1.25
Boiling Point, °C	-109.30	-258.79	-38.47	125.18	472.01	818.23	1115.36
Critical Pressure, atm	73.76	46.00	42.23	28.04	17.78	12.19	10.61
Critical Volume, m3/K-mole	0.09	0.10	0.21	0.35	0.81	1.83	3.67
Critical Temperature, °K	304.20	190.60	372.84	500.24	699.93	921.83	1204.94
Acentric Factor	0.23	0.01	0.15	0.32	0.76	1.27	1.11
Molecular Weight, gr/gr-mole	44.01	16.04	42.96	77.94	176.43	396.50	719.15
Binary Interaction Coefficients:							
	0.02						
	0.02	0.00					
	0.04	0.00	0.00				
	0.04	0.00	0.00	0.00			
	0.04	0.00	0.00	0.00	0.00		
	0.04	0.00	0.00	0.00	0.00	0.00	
Volume shift Parameter	-0.07	-0.21	-0.12	-0.02	0.14	-0.01	-0.18
Mole Fraction of Components	0.00	0.35	0.12	0.06	0.28	0.12	0.07

Table B.17: EOS parameters for fluid properties of JEMA oil sample

	'CO2'	'C1'	'C2toNC4'	'IC5toC6'	'HYP01'	'HYP02'	'HYP03'
Critical Pressure, atm	72.80	45.40	44.93	33.24	20.68	15.68	15.64
Critical Volume, m3/K-mole	0.09	0.10	0.18	0.31	0.59	1.12	2.17
Critical Temperature, °K	303.89	166.67	338.34	466.11	611.12	777.78	972.23
Acentric Factor	0.23	0.01	0.13	0.24	0.64	1.00	1.28
Molecular Weight, gr/gr-mole	44.01	16.04	36.01	70.52	147.18	301.48	562.81
Binary Interaction Coefficients:							
	0.05						
	0.05	0.00					
	0.05	0.00	0.00				
	0.09	0.00	0.00	0.00			
	0.09	0.00	0.00	0.00	0.00		
	0.09	0.00	0.00	0.00	0.00	0.00	
Volume shift Parameter	0.14	-0.15	-0.01	-0.04	0.06	0.18	0.30
Mole Fraction of Components	0.02	0.07	0.17	0.19	0.31	0.15	0.07
Parachor	49.00	71.00	135.00	231.62	439.15	788.22	1112.46

Table B.18: EOS parameters for fluid properties of RF4 oil sample

	'CO2'	'C1'	'C2toNC4'	'IC5toC6'	'HYP01'	'HYP02'	'HYP03'
Critical Pressure, atm	72.80	45.40	41.07	30.56	16.46	11.40	10.70
Critical Volume, m3/K-mole	0.09	0.10	0.22	0.38	1.29	3.35	4.76
Critical Temperature, °K	304.20	190.60	379.12	585.40	864.43	1275.25	1507.89
Acentric Factor	0.23	0.01	0.16	0.24	0.66	0.81	0.29
Molecular Weight, gr/gr-mole	44.01	16.04	38.96	85.41	238.10	709.56	1003.80
Binary Interaction Coefficients:							
	0.04						
	0.04	0.00					
	0.08	0.00	0.00				
	0.10	0.00	0.00	0.00			
	0.10	0.00	0.00	0.00	0.00		
	0.10	0.00	0.00	0.00	0.00	0.00	
Volume shift Parameter	-0.04	-0.12	-0.07	0.00	0.06	0.14	0.22
Mole Fraction of Components	0.00	0.44	0.07	0.21	0.18	0.06	0.04
Parachor	78.00	77.30	159.40	282.10	752.80	1753.30	2419.10

Table B.19: EOS parameters for fluid properties of 3.21-PDSN oil sample

	'CO2'	'C1'	'C2toNC4'	'IC5toC6'	'HYP01'	'HYP02'	'HYP03'
Specific Gravity	0.82	0.30	0.46	0.64	0.75	0.83	0.93
Boiling Point, °C	-109.21	-258.61	-15.86	98.01	298.21	679.96	1095.93
Critical Pressure, atm	72.80	45.40	43.37	33.25	24.26	11.38	5.61
Critical Volume, m3/K-mole	0.09	0.10	0.19	0.31	0.51	1.20	2.39
Critical Temperature, °K	304.20	190.60	356.34	469.86	597.15	786.41	977.43
Acentric Factor	0.23	0.01	0.14	0.24	0.42	0.93	1.45
Molecular Weight, gr/gr-mole	44.01	16.04	41.11	73.96	125.73	288.59	635.00
Binary Interaction Coefficients:							
	0.05						
	0.05	0.00					
	0.05	0.00	0.00				
	0.09	0.00	0.00	0.00			
	0.09	0.00	0.00	0.00	0.01		
	0.09	0.00	0.00	0.00	0.04	0.01	
Volume shift Parameter	-0.09	-0.15	-0.08	-0.03	0.05	0.27	0.41
Mole Fraction of Components	0.01	0.17	0.13	0.01	0.32	0.27	0.08

Table B.20: EOS parameters for fluid properties of 64730-SPE oil sample

	'CO2'	'C1'	'C2toNC4'	'IC5toC6'	'HYP01'	'HYP02'	'HYP03'
Specific Gravity	0.82	0.30	0.54	0.67	0.71	0.80	0.89
Boiling Point, °C	-109.21	-258.61	20.14	129.56	307.60	697.42	1101.66
Critical Pressure, atm	72.80	45.40	39.17	32.82	20.76	9.30	4.59
Critical Volume, m3/K-mole	0.09	0.10	0.23	0.33	0.59	1.41	2.77
Critical Temperature, °K	304.20	190.60	395.81	491.33	592.59	780.75	964.08
Acentric Factor	0.23	0.01	0.17	0.26	0.45	1.01	1.52
Molecular Weight, gr/gr-mole	44.01	16.04	51.58	80.67	129.66	310.31	694.55
Binary Interaction Coefficients:							
	0.04						
	0.04	0.00					
	0.04	0.00	0.00				
	0.08	0.00	0.00	0.00			
	0.08	0.00	0.00	0.00	0.00		
	0.08	0.00	0.00	0.00	0.00	0.00	
Volume shift Parameter	-0.09	-0.15	-0.06	-0.02	0.12	0.32	0.44
Mole Fraction of Components	0.00	0.00	0.03	0.09	0.40	0.35	0.12

Table B.21: EOS parameters for fluid properties of 15.16-PDSN oil sample

	'CO2'	'C1'	'C2toNC4'	'IC5toC6'	'HYP01'	'HYP02'	'HYP03'
Specific Gravity	0.82	0.30	0.41	0.67	0.78	0.91	1.03
Boiling Point, °C	-109.21	-258.61	-61.04	131.58	430.69	1013.84	1512.32
Critical Pressure, atm	72.80	45.40	45.90	32.81	18.77	6.56	3.07
Critical Volume, m3/K-mole	0.09	0.10	0.17	0.33	0.70	2.07	4.23
Critical Temperature, °K	304.20	190.60	330.10	492.37	667.66	942.16	1170.90
Acentric Factor	0.23	0.01	0.12	0.26	0.58	1.35	1.82
Molecular Weight, gr/gr-mole	44.01	16.04	35.24	80.38	171.04	538.61	1320.46
Binary Interaction Coefficients:							
	0.04						
	0.04	0.00					
	0.04	0.00	0.00				
	0.06	0.00	0.00	0.00			
	0.06	0.00	0.00	0.00	0.02		
	0.06	0.00	0.00	0.00	0.05	0.01	
Volume shift Parameter	-0.09	-0.15	-0.09	-0.02	0.12	0.39	0.49
Mole Fraction of Components	0.01	0.19	0.00	0.01	0.29	0.37	0.13

APPENDIX B-3: ULTIMATE RECOVERY PLOTS FOR ALL SLIM TUBE SIMULATIONS

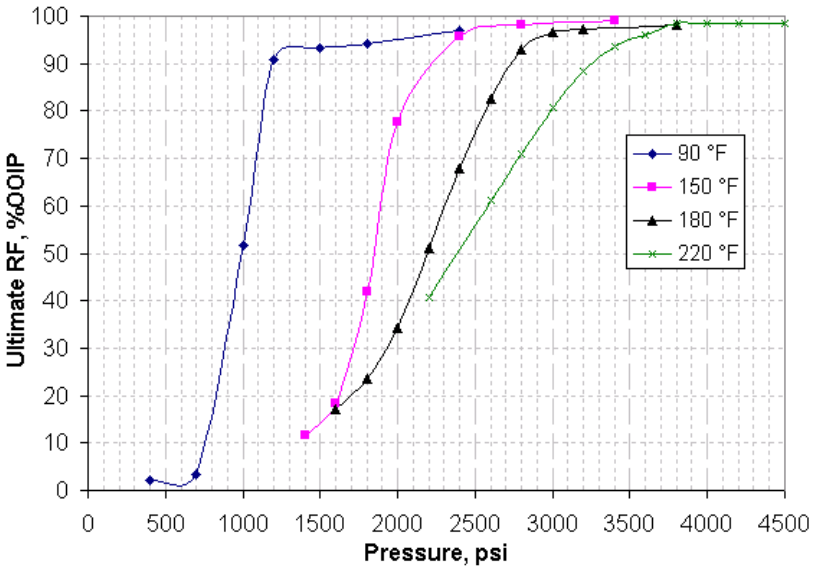

Figure B.4- Ultimate oil recoveries for APNDXD2-LK oil slim tube displacements

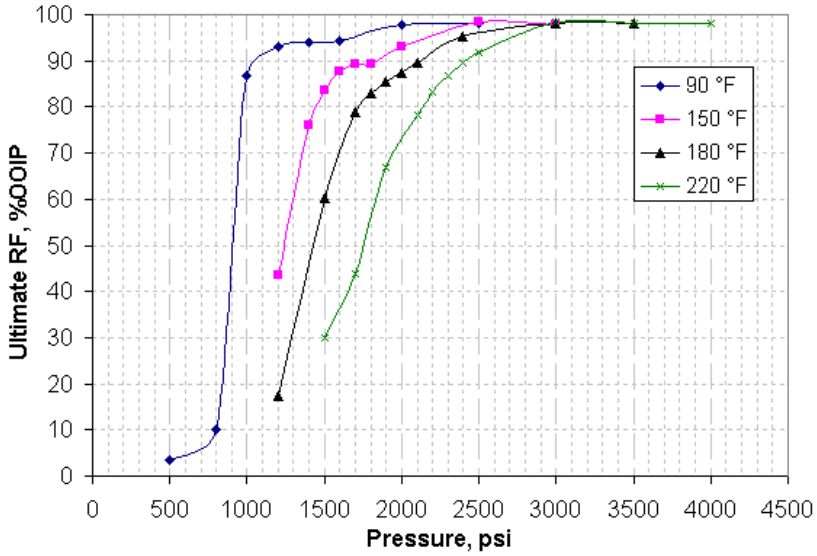

Figure B.5-Ultimate oil recoveries for COATS85-TBL1 oil slim tube displacements

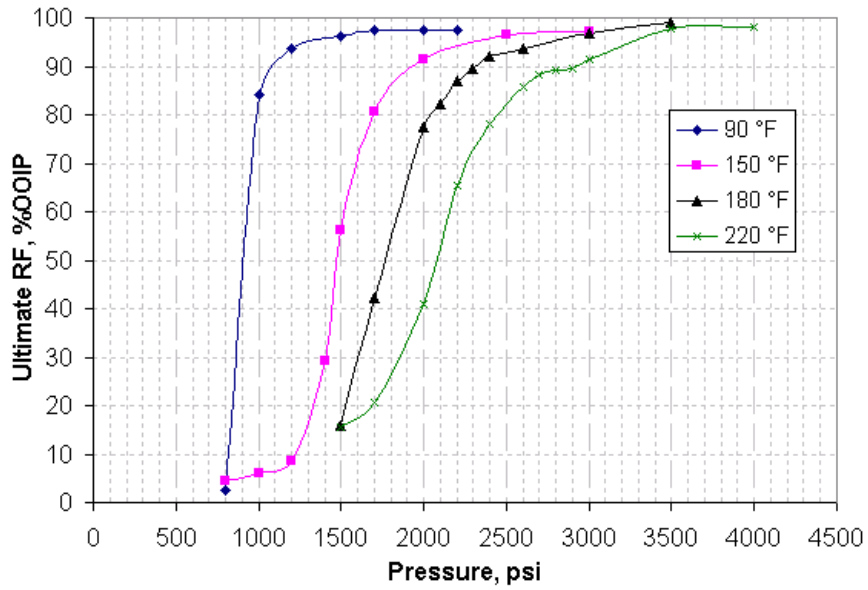

Figure B.6 -Ultimate oil recoveries for JCBY-TBL1 oil slim tube displacements

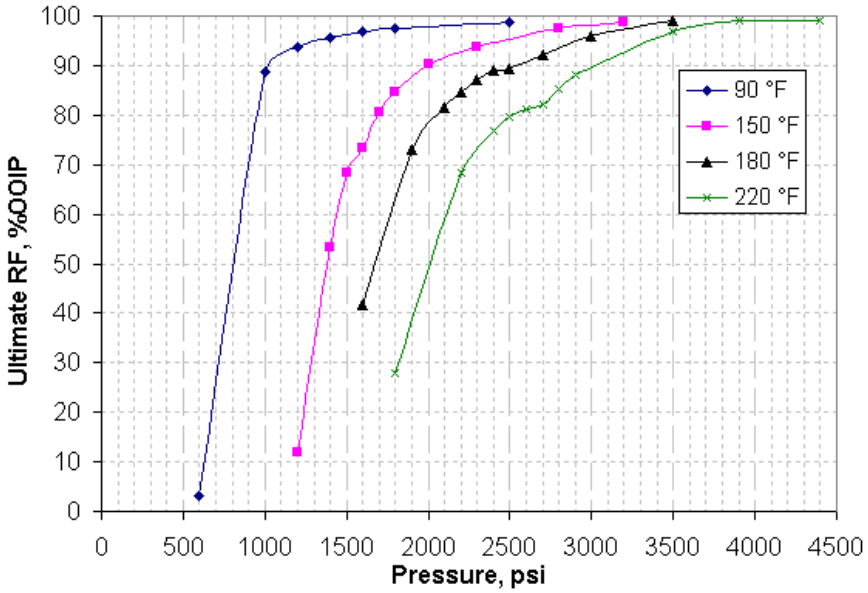

Figure B.7 -Ultimate oil recoveries for COATS86-OL2 oil slim tube displacements

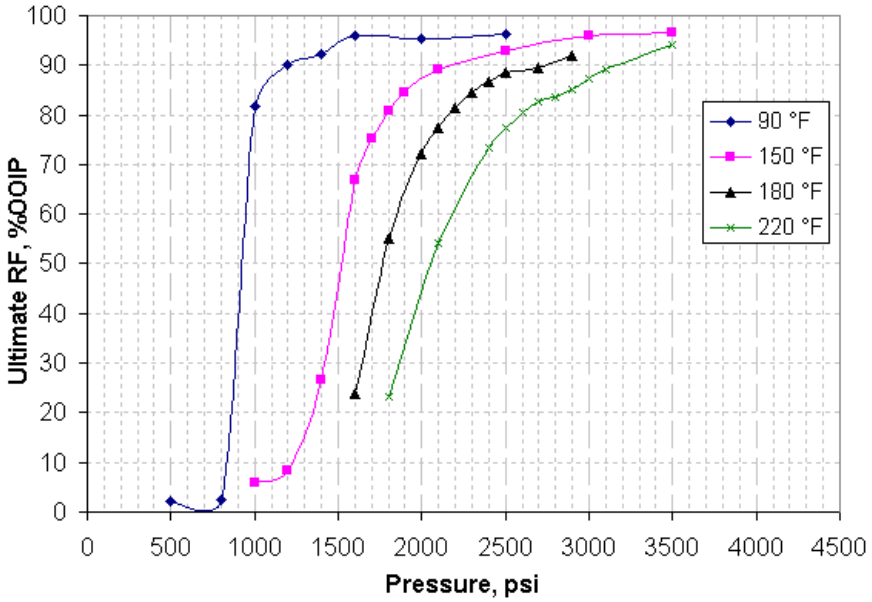

Figure B.8 -Ultimate oil recoveries for JRHFPOOLE oil slim tube displacements

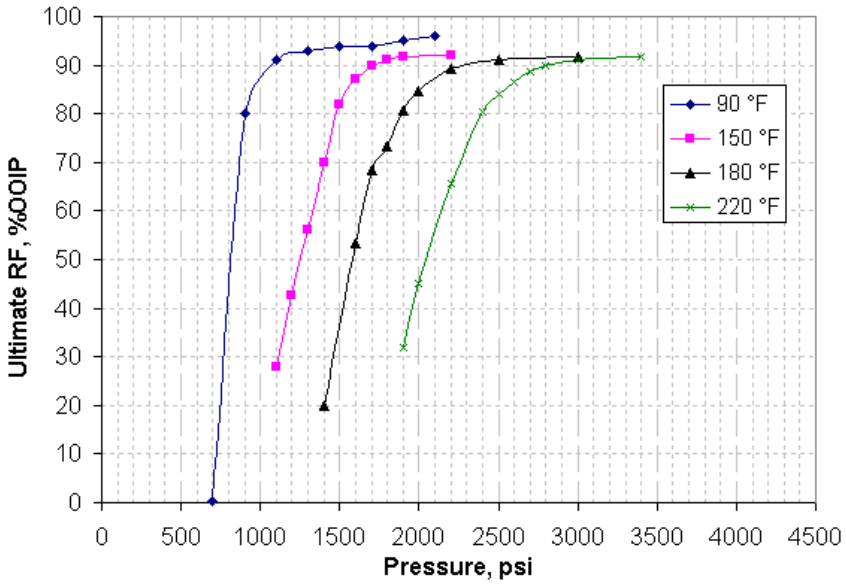

Figure B.9 -Ultimate oil recoveries for Danesh-tbl2.1A oil slim tube displacements

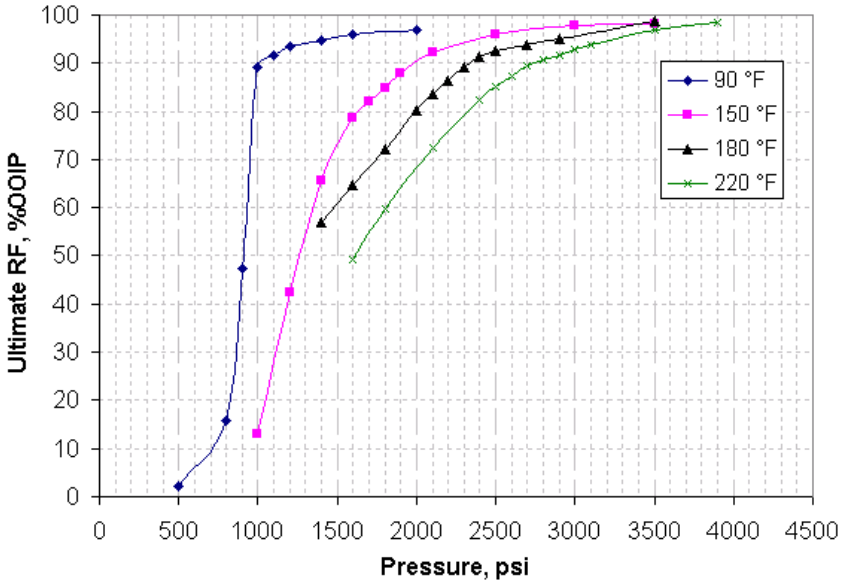

Figure B.10 -Ultimate oil recoveries for JRHFPOOLD oil slim tube displacements

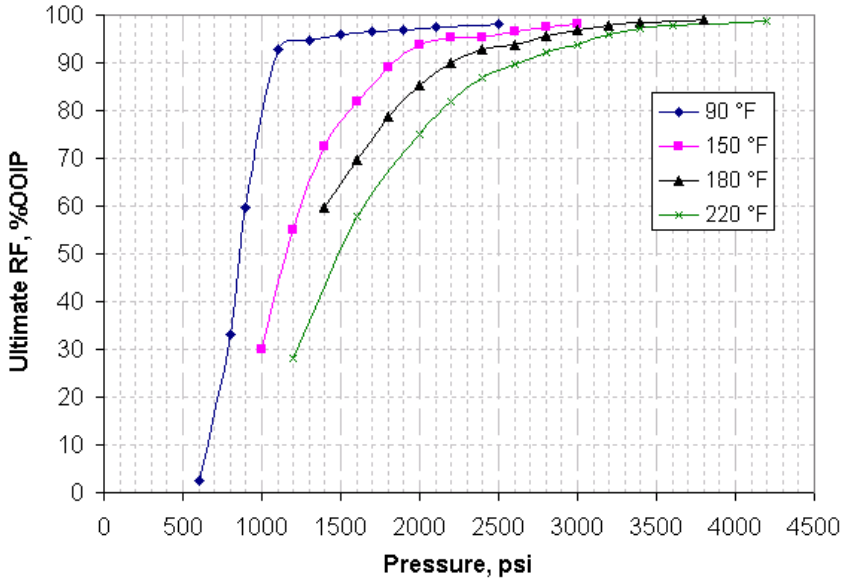

Figure B.11 -Ultimate oil recoveries for COATS-OL6 oil slim tube displacements

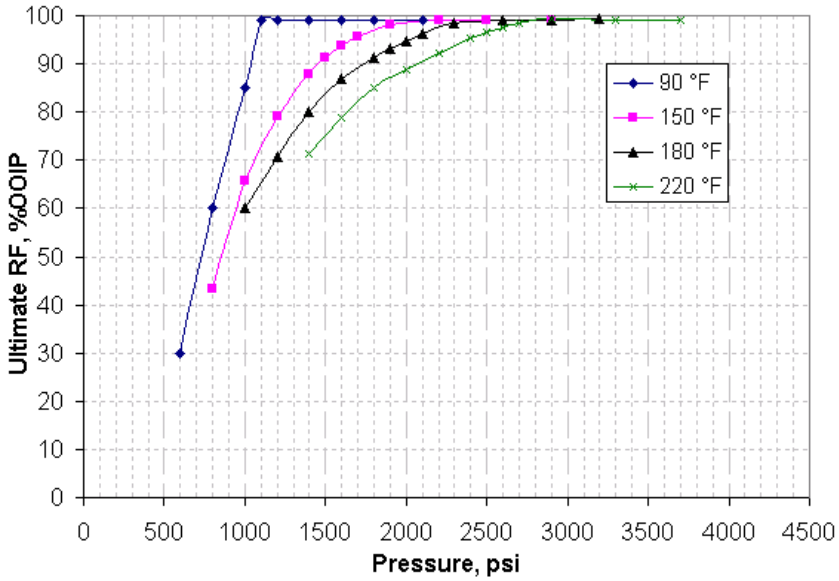

Figure B.12 -Ultimate oil recoveries for 14923-SPE oil slim tube displacements

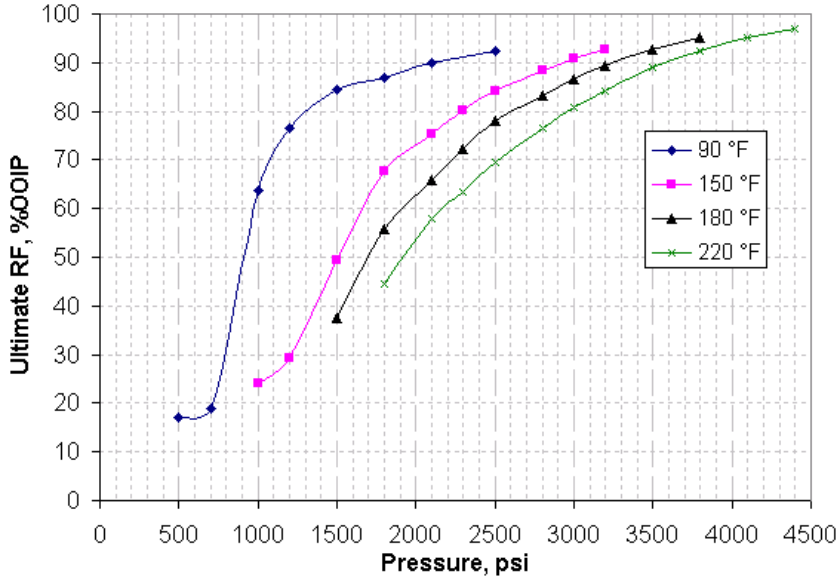

Figure B.13 -Ultimate oil recoveries for Tbl15.2-Pdsn oil slim tube displacements

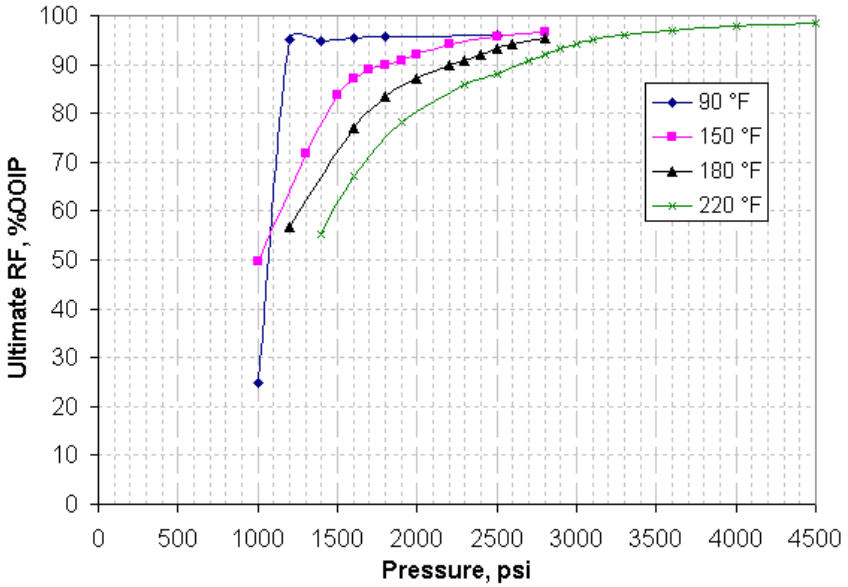

Figure B.14 -Ultimate oil recoveries for COATS86-OL7 oil slim tube displacements

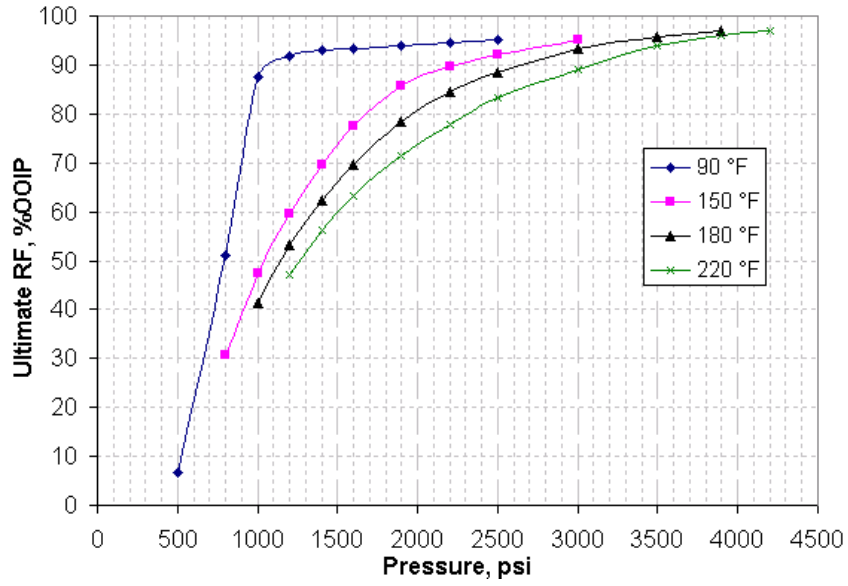

Figure B.15 -Ultimate oil recoveries for 3483-B oil slim tube displacements

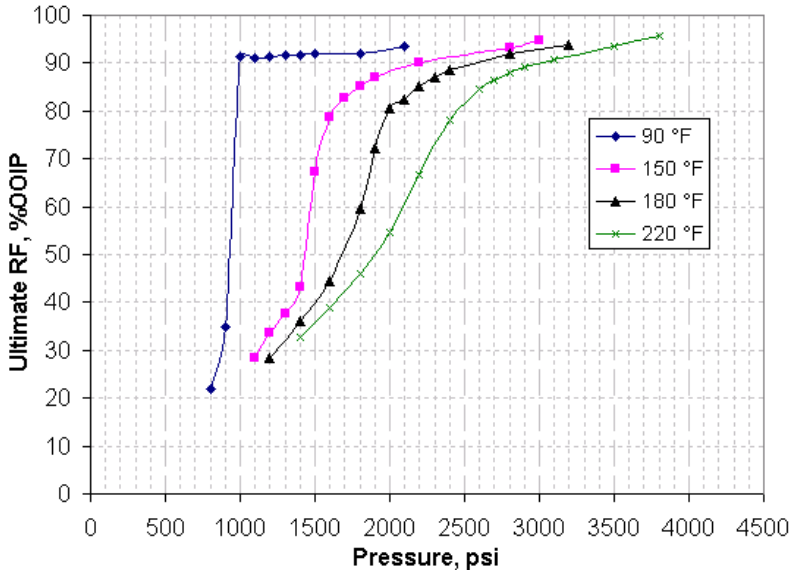

Figure B.16 -Ultimate oil recoveries for NWE oil slim tube displacements

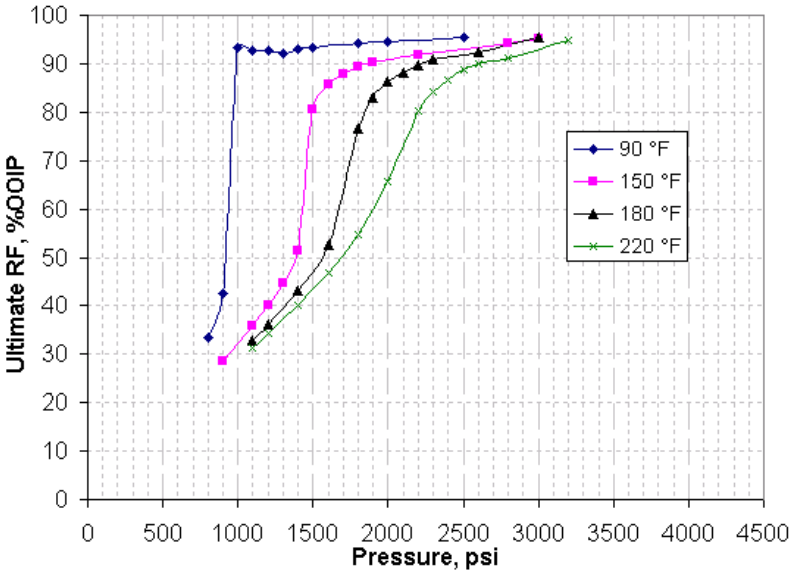

Figure B.17 -Ultimate oil recoveries for BSB5 oil slim tube displacements

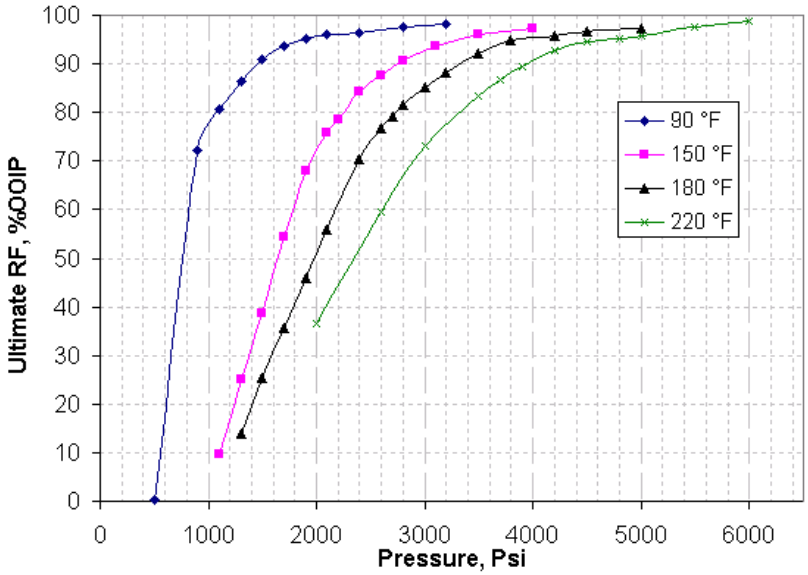

Figure B.18 -Ultimate oil recoveries for RF6 oil slim tube displacements

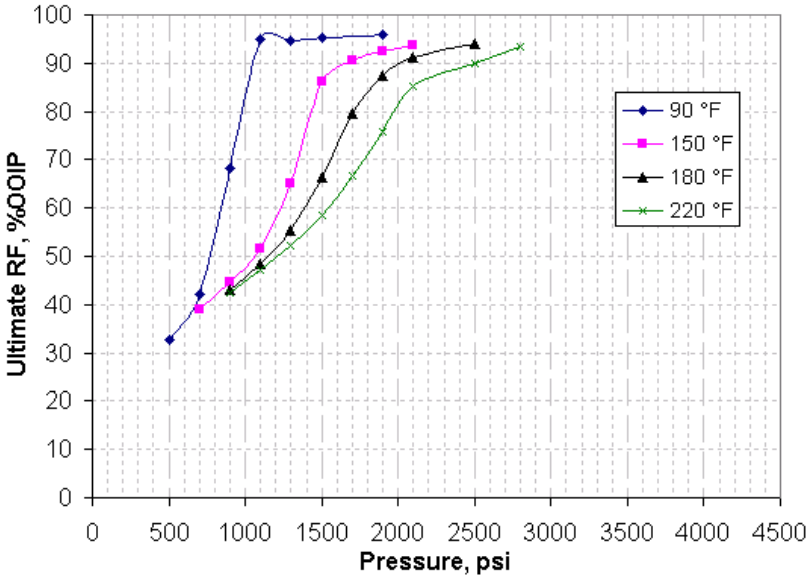

Figure B.19 -Ultimate oil recoveries for JEMA oil slim tube displacements

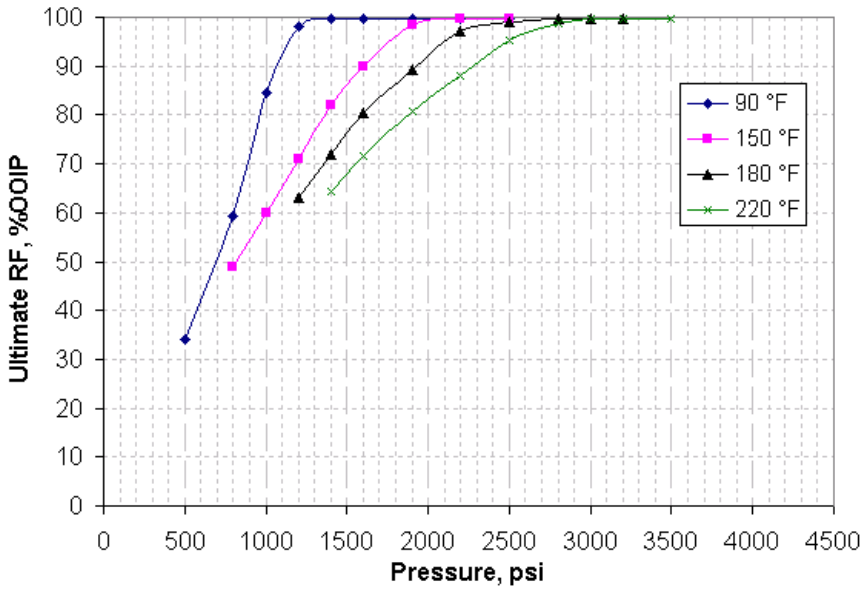

Figure B.20 -Ultimate oil recoveries for 3.21-PDSN oil slim tube displacements

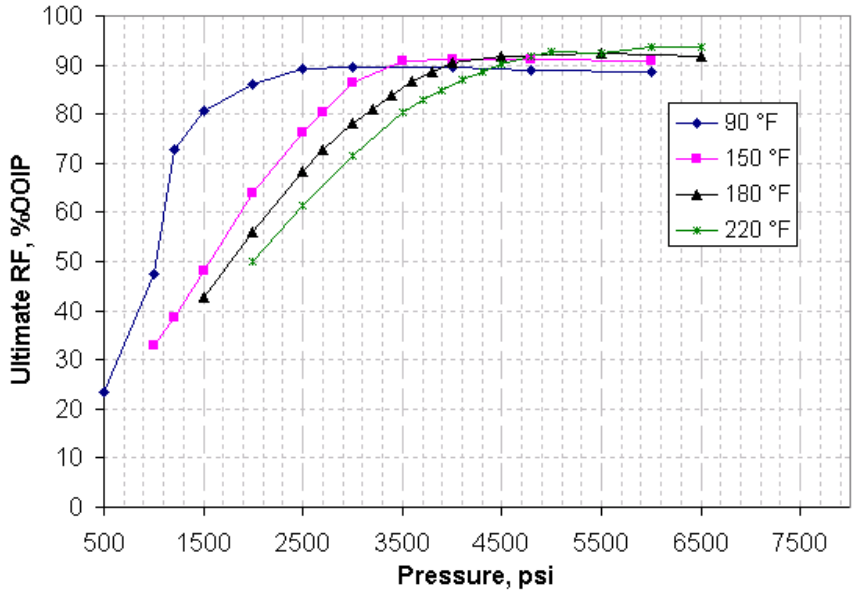

Figure B.21 -Ultimate oil recoveries for 15.16-PDSN oil slim tube displacements

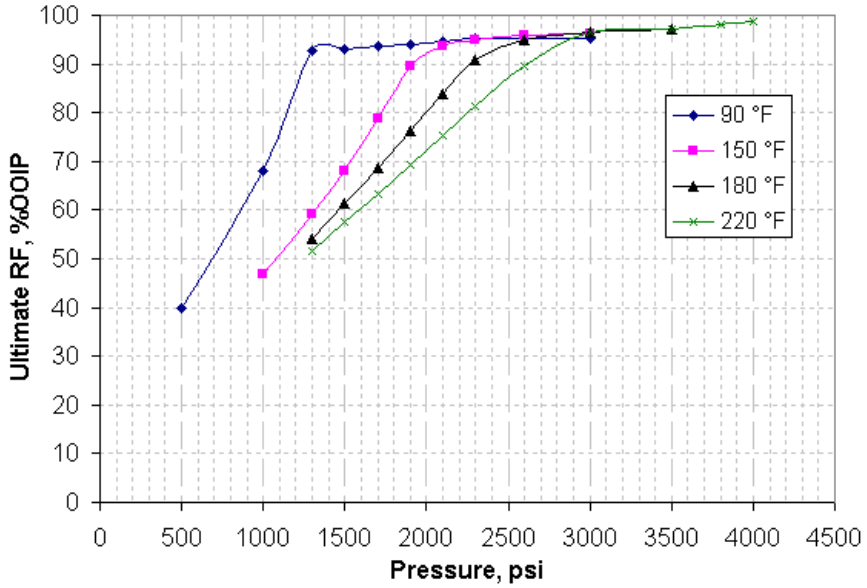

Figure B.22 -Ultimate oil recoveries for 64730-SPE oil slim tube displacements

Appendix C: Details for developed DCF spreadsheet for coupled CO2 sequestration and EOR

Since CO_2 injection mostly occurs in the mature oil fields, it was assumed that there is no additional drilling cost for the project. Therefore, initial investment for CO_2 injection project will include well reworks, surface facility, recycle system, trunk line, and some other minor expenses. In addition, below table show the variables that are changing in time and are obtained mainly from simulation results. These parameters are input in the ***columns A to E*** in the spreadsheet:

Time	Oil Produced at SC.	Water Produced at SC.	CO_2 Produced at SC.	CO_2 Injected at SC.
Yrs.	(bbl/day)	(bbl/day)	(ft3/day)	(ft3/day)

Corresponding equations for other columns are as follow:

Column F to I: Water, oil, and gas production as well as CO_2 injection data were divided into 1000, because all of the coming calculations were in terms of MMscf/day or MSTB/day units.

Column K (Oil Revenue) [mm$/yr]: Below equation was used:

$$\frac{\text{Oil Production[mstb/d]}\times 365.25\times\text{Oil price[\$]}}{1000}\times\left((1+\text{Oil price inflation})^{\text{t[yr]}}\right)\times(1\text{-Royalty})$$

Column L (*CO_2 *Purchase Price) [mm$/yr]: Below equation was applied:

$$\frac{\text{MAX}\left((\text{CO2 Injected[MMscf/d]-CO2 Produced[MMscf/d]}),0\right)\times 365.25}{1000}\times\text{CO2 Price[\$/mcf]}$$

Column M (Gas Recycling and Operation Costs) [mm$/yr]: Below equation was applied:

$$\frac{(\text{CO2 Prod.[MMscf/d]}+\text{HC gas Prod.[MMscf/d]})\times 365.25\times \text{Recycle Cost[\$/mcf]}}{1000}\times\left((1+\text{Oper. cost inflat.})^{\text{t[yr]}}\right)$$

Column N (Lift Costs) [mm$/yr]: Below equation was applied:

$$\frac{(\text{Oil Prod.[Mstb/d]}+\text{Water Prod.[Mstb/d]})\times \text{Lift Cost[\$/bbl]}\times 365.25}{1000}\times\left((1+\text{Oper. cost inflat.})^{\text{t[yr]}}\right)$$

Column O (Fixed Dl & F) [mm$/yr]: This column was assumed zero in all of the calculations.

Column P (OC income before TAX-OCIBT) [mm$/yr]: Below equation was applied:

OCIBT=Oil Revenue- CO_2 Purchase Price-Gas Recycling and Operation Costs-Lift Costs

Column Q (Cumulative NCF before TAX-NCFBT) [mm$]: Below equation was applied:

First Cell: $(\text{-Total Investment[mm\$]}+\text{OCIBT}\times\text{t[yr]})$

Other Cells: (Q= Column Q_{prev}+(Column P×(Column A-Column A_{prev})))

Column R (Depreciation) [mm$/yr]: Below equation was applied:

$$\text{Total Investment[mm\$]}\times(1-\text{EOR Tax Credit Rate[frac.]})\times\text{MAX}\left((0.2857-(\text{t[yr]}-0.5)\times 0.0476),0\right)$$

Column S (Federal Income Tax-FIT) [mm$/yr]: Below equation was applied:

$$\text{S}=\left\{\text{OCIBT-Depreciation}+(\text{Gas Purchase + Gas Operating})\times\text{EOR Tax Credit Rate}\right\}\times\text{Fed. Tax Rate}$$

Column T (EOR Tax credit) [mm$/yr]: Below equation was applied:

First Cell:

$$T = (\text{Gas Purchase} + \text{Gas Operating}) \times \text{EOR Tax Credit Rate} + \text{EOR Tax Credit Rate} \times \text{Total Investment}$$

Other Cells: $T = (\text{Gas Purchase} + \text{Gas Operating}) \times \text{EOR Tax Credit Rate}$

Column U (Sev. Tax Relief) [mm$/yr]: This item was assumed zero in all of our calculations.

Column V (OC income after TAX-OCIAT) [mm$/yr]: Below equation was applied:

OCIAT= OCIBT - FIT + EOR Tax Credit + Sev. Tax Credit

Column W (Cumulative NCF after TAX-NCFAT) [mm$]: Below equation was applied:

First Cell: $\left(\text{-Total Investment[mm\$]} + \text{OCIAT} \times \text{t[yr]}\right)$

Other Cells: $(W = \text{Column } W_{prev.} + (\text{Column V} \times (\text{Column A} - \text{Column } A_{prev.})))$

Column X (Discounted Net Cash Flow After Tax-DCNCFAT) [mm$]: Below equation was applied:

First Cell: $X = \left(\frac{\text{Cum. NCFAT}}{(1 + \text{Discounte Rate})^{t=0}} \right)$

Other Cells: $X = \frac{\left(\text{Column X} - \text{Column } X_{prev.}\right)}{(1+\text{Discounte Rate})^{t_{prev.}}} + X_{prev.}$

Appendix D: Introduction to Experimental Design and Response Surface Methodology

This Appendix provides some general information regarding Experimental Design and Method of Response Surfaces. Most of the information in this Appendix are referenced to Montgomery (2001) and Croarkin and Tobias (2006).

Introduction

Design of Experiments (DOE) is a method to select simulations to maximize the information gained from each simulation and to evaluate statistically the significance of the different uncertain variables, defined as factors. An experimental design study is used to generate response surfaces that identify the various factors that cause changes in the responses and also predicting these variations in a simple mathematical form. The purpose of Response Surface Methodology (RSM) (Myers and Montgomery, 1995) is to approximate a process over a region of interest called the operating region. The components of the operating region include objectives, requirements, state parameters (with or without uncertainty), decision variables, and constraints. An objective is the statement of the goal, and requirements can be imposed on it too. State parameters are those that can not be controlled and most of the times have uncertainties associated with them. They can be discrete or continuous. Discrete parameters are also referred to as "scenarios". Decision variables are those that are controllable and are usually choices available to the decision maker. Constraints are boundary conditions, which restrict values available for the decision variables.

Engineers define objectives of the process called responses as the output and settings for the state parameters and decision variables as input. Employing RSM provides tools for (1) identifying the variables that influence the responses (screening) and (2) building regression models relating the responses to the strategic variables

(modeling). The final models are used to make predictions of the process over the domain.

In order to compute the regression model, the process has to be sampled over the operating region through experimentation. Design of Experiment is the use of statistical methods to determine the number and the conditions of the experiments in order to get the most information at the lowest experimental cost. A commercial package, Design-Expert from Stat-Ease, Inc. (2005) is used for performing experimental design analysis in this research. Figure 1 shows the design configuration for five different methods of experimental design with three factors. It includes the one-factor-at-a-time (OFAT) design, two-level full-factorial design, three-level full-factorial design, Box-Behnken design, and Central Composite design.

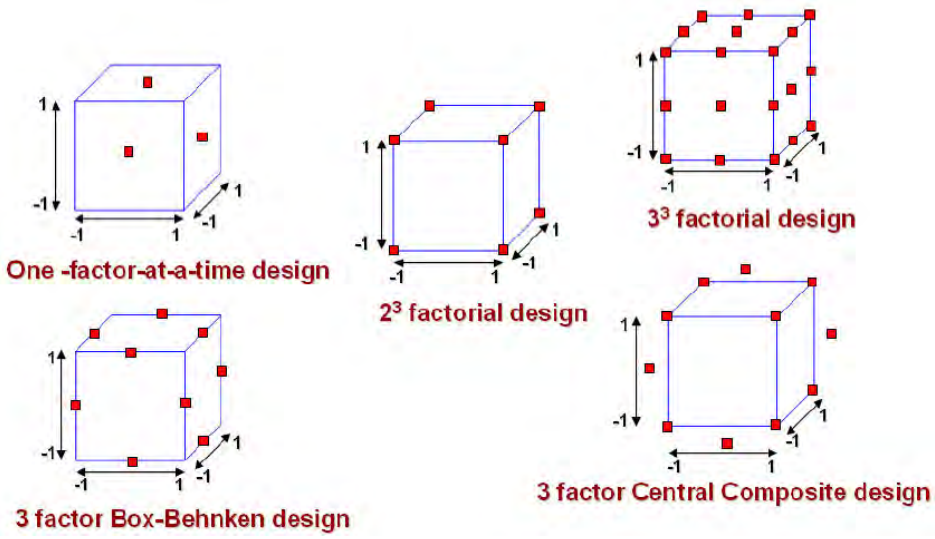

Figure D.1- Five Different Types of Experimental Design for Three Factors

Basic Statistics for DOE

Mean and variance of the Sample

The effective statistic for measuring the distribution of the results from DOE is the mean, which most people refer to as the “average”. The formula for the mean of a response (*Y*) is shown below:

$$\overline{X} = \frac{\sum_{i=1}^{n} X_i}{n} \tag{D.1}$$

where *n* is the sample size and *i* is the individual response. The mean, or *X*-bar, is calculated by adding up the data and dividing by the number of "observations".

Means do not tell the whole story. Besides knowing the central point of a data set, we would like to describe the data’s spread, or how far from the center the data tend to range. In probability theory and statistics, the variance of a random variable (or somewhat more precisely, of a probability distribution) is a measure of its statistical dispersion, indicating how its possible values are spread around the expected value. Where the expected value shows the location of the distribution, the variance indicates the scale of the values. A more understandable measure is the square root of the variance, called the standard deviation (*S*). As its name implies it gives a standard form to the mean, which is an indication of the possible deviations from the mean.

$$S^2 = \frac{\sum_{i=1}^{n} (X_i - \overline{X})^2}{n-1} \tag{D.2}$$

z-score

The z score reveals how many units of the standard deviation a case is above or below the mean. The z score allows us to compare the results of different normal distributions, something done frequently in research.

$$z_i = \frac{X_i - \overline{X}}{S} \tag{D.3}$$

For nearly normally distributed data set, approximately 68% of the data is within one standard deviation of the mean and 95% of the data is within two standard deviations of the mean.

t-statistic

In probability and statistics, the *t*-distribution or Student's *t*-distribution is a probability distribution that arises in the problem of estimating the mean of a normally distributed population when the sample size is small. It is the basis of the popular Student's *t*-tests for the statistical significance of the difference between two sample means, and for confidence intervals for the difference between two population means. The Student's *t*-distribution is a special case of the generalized hyperbolic distribution. Equation D.4 shows the general formula to calculate t value for each sample size.

$$t = \frac{\overline{X} - \mu}{S / \sqrt{n}} \tag{D.4}$$

where μ is the average for all of the data population, *X-bar* is the mean for the sample, *n* is the sample size, and *S* is the standard deviation of sample.

Student's distribution arises when (as in nearly all practical statistical work) the population standard deviation is unknown and has to be estimated from the data. Textbook problems treating the standard deviation, as if it were known, are of two kinds: (1) those in which the sample size is so large that one may treat a data-based estimate of the variance as if it were certain and (2) those that illustrate mathematical reasoning, in which the problem of estimating the standard deviation is temporarily ignored because that is not the point that is then explained.

What is Experimental Design?

In an experiment, we deliberately change one or more process variables (or factors) in order to observe the effect the changes have on one or more response variables. The (statistical) design of experiments (*DOE*) is an efficient procedure for planning experiments so that the data obtained can be analyzed to yield valid and objective conclusions.

DOE begins with determining the objectives of an experiment and selecting the process factors for the study. An *Experimental Design* is the laying out of a detailed experimental plan in advance of doing the experiment. Well chosen experimental designs maximize the amount of "information" that can be obtained for a given amount of experimental effort.

This process starts with several discrete or continuous input factors that can be controlled and one or more measured output responses. The output responses are usually assumed continuous. Experimental data are used to derive an empirical (approximation) model linking the outputs and inputs. These empirical models generally contain first and second-order terms.

Often the experiment has to account for a number of uncontrolled factors that may be discrete, such as different machines or operators, and/or continuous such as ambient temperature or humidity. The most common empirical models fit to the experimental data take either a *linear* form or *quadratic* form. A linear model with two factors, X_1 and X_2, can be written as

$$Y = \beta_0 + \beta_1 X_1 + \beta_2 X_2 + \beta_1 \beta_2 X_1 X_2 + \exp erimental \quad error \tag{D.5}$$

Here, Y is the response for given levels of the main effects X_1 and X_2 and the X_1X_2 term is included to account for a possible interaction effect between X_1 and X_2. The constant β_0 is the response of Y when both main effects are 0. For a more complicated

example, a linear model with three factors X_1, X_2, X_3 and one response, Y, would look like (if all possible terms were included in the model)

$$Y = \beta_0 + \beta_1 X_1 + \beta_2 X_2 + \beta_3 X_3 + \beta_{12} X_1 X_2 + \\ + \beta_{13} X_1 X_3 + \beta_{23} X_2 X_3 + \beta_{123} X_1 X_2 X_3 + \exp erimental \quad error \tag{D.6}$$

The three terms with single X's are the *main effects* terms. There are $k(k\text{-}1)/2$ = 3*2/2 = 3 *two-way* interaction terms and 1 *three-way* interaction term (which can be omitted, for simplicity or it really has negligible effect on the response). When the experimental data are analyzed, all the unknown β parameters are estimated and the coefficients of the X terms are tested to see which coefficients will give response values close to the actual experiments that have been performed. A second-order (quadratic) model (typically used in *response surface* DOE's with suspected curvature) does not include the three-way interaction term but adds three more terms to the linear model as shown below:

$$\beta_{11} X_1^2 + \beta_{22} X_2^2 + \beta_{33} X_3^2 \tag{D.7}$$

Clearly, a full model could include many cross-product (or interaction) terms involving squared X's. However, in some cases these terms are not needed and most DOE software defaults to leaving them out of the model.

Steps for Performing an Experimental Design Process

Obtaining good results from a DOE involves these seven steps:

-Set objectives

The objectives for an experiment are best determined by a team discussion. All of the objectives should be written down, even the "unspoken" ones. The group should discuss which objectives are the key ones, and which ones are "nice but not really

necessary". Prioritization of the objectives helps you decide which direction to go with regard to the selection of the factors, responses and the particular design. Sometimes prioritization will force you to start over from scratch when you realize that the experiment you decided to run does not meet one or more critical objectives.

-Select process variables

Process variables include both *inputs* and *outputs* - i.e., *factors* and *responses*. The selection of these variables is best done as a team effort. We have to choose the range of the settings for input factors, and it is wise to give this some thought beforehand rather than just try extreme values. In some cases, extreme values will give runs that are not feasible; in other cases, extreme ranges might move one out of a smooth area of the response surface into some jagged region, or close to an asymptote.

-Select an experimental design and make simulations based on design

The choice of an experimental design depends on the objectives of the experiment and the number of factors to be investigated. Types of designs are listed here according to the experimental objective they meet.

-Comparative objective

-Screening objective

-Response Surface (method) objective

-Optimizing responses when factors are proportions of a mixture objective

-Optimal fitting of a regression model objective

-Analyze and interpret the results

Assuming you have a starting model that you want to fit to your experimental data and the experiment was designed correctly for your objective, most DOE software packages will analyze your DOE data. Steps for analyzing the date are:

-DOE analysis steps

-Plotting DOE data

-Modeling DOE data

-Testing and revising DOE models

-Interpreting DOE results

-Confirming DOE results

-Use/present the results (may lead to further runs or DOE's).

Experimental Design Methods

The choice of an experimental design depends on the objectives of the experiment and the number of factors to be investigated. Below are some brief descriptions of some of important and more popular DOE methods.

Full factorial Design

A common experimental design is one with all input factors set at two levels each. These levels are called 'high' and 'low' or '+1' and '-1', respectively. A design with all possible high/low combinations of all the input factors is called a full factorial design in two levels. As the number of factors increases, a full factorial design requires a large number of runs and is not very efficient. Therefore, Fractional Factorial Design or Plackett-Burman designs are used as other possible alternate methods.

Two-Level Factorial Design

Considering the two-level full factorial design for three factors, there will be the 2^3 experiments to be run. This implies eight runs (not counting replications or center point runs). Graphically, we can represent the 2^3 design by the cube shown in Figure D.1. The arrows show the direction of increase of the factors. The numbers 1 through 8 at the

corners of the design box, reference the standard order of the runs. In tabular form, this design (also showing eight observations y_j j = 1,...,8) is given by:

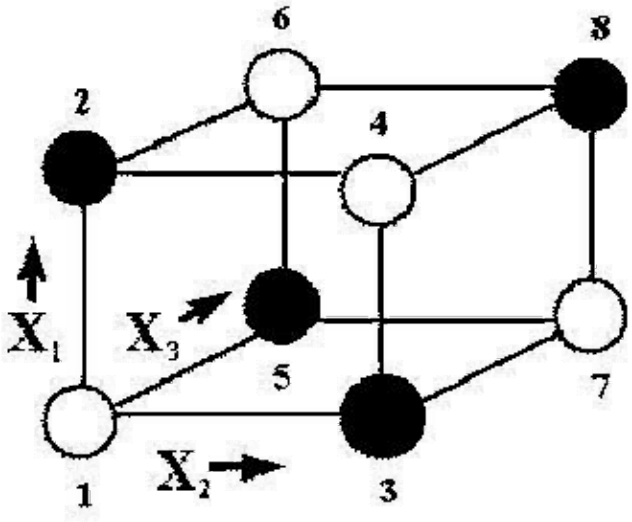

Figure D.1- A two-level full factorial design for three variables, X1, X2, and X3

Table D.1: Design settings for full two-level factorial design with three factors

Run#	X1	X2	X3	Yi
1	-1	-1	-1	y_1
2	+1	-1	-1	y_2
3	-1	+1	-1	y_3
4	+1	+1	-1	y_4
5	-1	-1	+1	y_5
6	+1	-1	+1	y_6
7	-1	+1	+1	y_7
8	+1	+1	+1	y_8

The right-most column of the table lists y_1 through y_8 to indicate the responses measured for the experimental runs when listed in standard order. For example, y_1 is the

response (i.e., output) observed when the three factors were all run at their "low" setting. The numbers entered in the Yi column will be used to illustrate calculations of effects.

Three-Level Factorial Design

The three-level design is written as a 3^k factorial design. It means that *k* factors are considered, each at 3 levels. These are (usually) referred to as low, intermediate and high levels. These levels are numerically expressed as 0, 1, and 2. One could have considered the digits -1, 0, and +1, but this may be confusing with respect to the 2-level designs since 0 is reserved for center points. Therefore, we will use the 0, 1, 2 scheme. The reason that the three-level designs were proposed is to model possible curvature in the response function and to handle the case of nominal factors at 3 levels. A third level for a continuous factor facilitates investigation of a quadratic relationship between the response and each of the factors.

Unfortunately, the three-level design is prohibitive in terms of the number of runs, and thus in terms of cost and effort. For example a two-level design with center points is much less expensive while it still is a very good (and simple) way to establish the presence or absence of curvature.

Fractional Factorial Design

Even if the number of factors, *k*, in a design is small, the 2^k or even 3^k runs specified for a full factorial can quickly become very large. For example, 2^6 (64) runs is for a two-level, full factorial design with six factors. To do this design we need to add a good number of center point runs and we can thus quickly run up a very large resource requirement for runs with only a modest number of factors.

The solution to this problem is to use only a fraction of the runs specified by the full factorial design. Which runs to make and which to leave out is the subject of interest here. In general, we pick a fraction such as half, quarter, or etc. of the runs called for by

the full factorial. Various strategies that ensure an appropriate choice of runs can be utilized. The following sections will show how to choose an appropriate fraction of a full factorial design to suit the purpose at hand. Properly chosen fractional factorial designs for 2-level experiments have the desirable properties of being both “balanced” and “orthogonal”. Following is a discussion describing one of the simple fractional factorial designs, half-fraction design and issues related to this type of design.

Identifying Main Effects and Interactions

Before going further in this illustration, let us begin the analysis by investigating the main effects of three factors (X1, X2, and X3) on a response (Y). By averaging the highs and the lows, determine the difference or contrast: this is the effect of a factor. Mathematically, the calculation of an effect is expressed as follows:

$$Effect = \frac{\sum Y^{+}}{n^{+}} - \frac{\sum Y^{-}}{n^{-}} \tag{D.8}$$

where the *n*’s refer to the number of data points you have collected at each level. TheY’s refer to the associated responses.

The half normal probability curve is used to identify the sensitivities of the factors along with their interactions. If the estimates of the effects plotted on normal probability paper, the effects that are negligible are normally distributed and will tend to fall along a straight line, whereas significant effects will have non-zero means and will not lie along the straight line. Half normal probability plot is used to take the absolute value of the effect.

The full-factorial design allows estimates of all the main effects (ME), the two-factor interactions and the three-factor interaction. A rule of thumb, called "sparsity of effects", says that in most systems, only 20% of the main effects and two-factor interactions (2FIs) will be significant. The other ME and 2FIs, as well as any three factor

interactions (3FI) or greater will be used as an estimate of error for Analysis Of Variance (ANOVA).

Fortunately, when factorials are restricted to two levels, the procedure becomes relatively simple. To do the ANOVA, we must compute the sums of squares (SS), which are related to the effects as follows:

$$SS = \frac{N}{4} effect^2 \tag{D.9}$$

where N is number of runs.

From the sensitivity analysis, let us assume that three effects (X2, X3, and X2X3) are most likely significant in a statistical sense. All the other effects (A, AB, AC, and ABC) fall in line, which represents the normal scatter. Therefore:

$$\begin{aligned} SS_{Model} &= SS_{X2} + SS_{X3} + SS_{X2X3} \\ SS_{residual} &= SS_{X1} + SS_{X1X2} + SS_{X1X3} + SS_{X1X2X3} \end{aligned} \tag{D.10}$$

Therefore, for our example, from the entries in the table we are able to compute all 'effects' such as main effects, first-order 'interaction' effects, etc. For example, to compute the main effect estimate 'C_1' of factor X_1, we compute the average response at all runs with X_1 at the 'high' setting, namely (1/4)(y_2 + y_4 + y_6 + y_8), minus the average response of all runs with X_1 set at `low,' namely (1/4)(y_1 + y_3 + y_5 + y_7).

Suppose, however, that we only have enough resources to do four runs. Is it still possible to estimate the main effect for X_1? Or any other main effect? The answer is yes, and there are even different choices of the four runs that will accomplish this. For example, suppose we select only the four light (un-shaded) corners of the design cube.

Using these four runs (1, 4, 6 and 7), we can still compute C_1 as follows:

C_1 = (1/2) (y_4 + y_6) - (1/2) (y_1 + y_7) (D.11)

Similarly, we would compute c_2, the effect due to X_2, as

$$C_2 = (1/2)\,(y_4 + y_7) - (1/2)\,(y_1 + y_6) \quad \text{(D.11)}$$

Finally, the computation of c_3 for the effect due to X_3 would be

$$C_3 = (1/2)\,(y_6 + y_7) - (1/2)\,(y_1 + y_4) \quad \text{(D.12)}$$

We could also have used the four dark (shaded) corners of the design cube for our runs and obtained similar, but slightly different, estimates for the main effects. In either case, we would have used half the number of runs that the full factorial requires.

Constructing the 2^{3-1} half-fraction design

First note that, mathematically, $2^{3-1} = 2^2$. This gives us the first step, which is to start with a regular 2^2 full factorial design. That is, we start with the following design setting shown in Table D.2.

Table D.2: Settings for simple 2-level, 2-factorial design

	***X*1**	***X*2**
1	-1	-1
2	+1	-1
3	-1	+1
4	+1	+1

This design has four runs, the right number for a half-fraction of a 2^3, but there is no column for factor *X*3. We need to add a third column to take care of this, and we do it by adding the *X*1**X*2 interaction column. This column is, as you will recall from full factorial designs, constructed by multiplying the row entry for *X*1 with that of *X*2 to obtain the row entry for *X*1**X*2. Table D.3 shows the settings for this new design.

Table D.3: Settings for 2-level, 2-factorial design with interaction term

	***X*1**	***X*2**	***X*1*X2**
1	-1	-1	+1
2	+1	-1	-1
3	-1	+1	-1
4	+1	+1	+1

We may now substitute X3 in place of X1*X2 in this table. Note that the rows of Table D.3 give the dark-shaded corners of the design in Figure D.1. If we had set X3 = -X1*X2 as the rule for generating the third column of our 2^{3-1} design, we would have obtained a new design shown in Table D.4.

Table D.4: Alternate settings for 2-level, 2-factorial design with interaction term

	***X*1**	***X*2**	***X*1*X2**
1	-1	-1	-1
2	+1	-1	+1
3	-1	+1	+1
4	+1	+1	-1

This design gives the light-shaded corners of the box of Figure D.1. Both 2^{3-1} designs that we have generated are equally good, and both save half the number of runs over the original 2^3 full factorial design. If C_1, C_2, and C_3 are our estimates of the main effects for the factors $X1$, $X2$, $X3$ (i.e., the difference in the response due to going from "low" to "high" for an effect), then the precision of the estimates C_1, C_2, and C_3 are not quite as good as for the full 8-run factorial because we only have four observations to construct the averages instead of eight; this is one price we have to pay for using fewer runs.

Confounding (Aliasing)

One price we pay for using the design table of column X1*X2 to obtain the column X3 in the Table D.3 is, clearly, our inability to obtain an estimate of the interaction effect for X1*X2 (i.e., C_{12}) that is separate from an estimate of the main effect for X3. In other words, we have “confounded” the main effect estimate for factor X3 (i.e., C_3) with the estimate of the interaction effect for X1 and X2 (i.e., with C_{12}). The whole issue of confounding is fundamental to the construction of fractional factorial designs, and it ahs been discussed below in more detail. In using the 2^{3-1} design, we also assume that C_{12} is small compared to C_3; this is called a 'sparsity of effects' assumption. Our computation of C_3 is in fact a computation of $C_3 + C_{12}$. If the desired effects are only confounded with non-significant interactions, then we are OK.

A Notation and Method for Generating Confounding or Aliasing

A short way of writing 'X3 = X1*X2' (understanding that we are talking about multiplying columns of the design table together) is: '3 = 12' (similarly 3 = -12 refers to X3 = -X1*X2). Note that '12' refers to column multiplication of the kind we are using to construct the fractional design and any column multiplied by itself gives the identity column of all 1's.

Next we multiply both sides of 3=12 by 3 and obtain 33=123, or I=123 since 33=I (or a column of all 1's). Playing around with this algebra, we see that 2I=2123, or 2=2123, or 2=1223, or 2=13 (since 2I=2, 22=I, and 1I3=13). Similarly 1=23.

I=123 is called a design generator or a generating relation for this 2^{3-1}design (the dark-shaded corners of Figure 3.4). Since there is only one design generator for this design, it is also the defining relation for the design. Equally, I=-123 is the design generator (and defining relation) for the light-shaded corners of Figure 3.4. We call I=123 the defining relation for the 2^{3-1} design because with it we can generate (by "multiplication") the complete confounding pattern for the design. That is, given I=123,

we can generate the set of {1=23, 2=13, 3=12, I=123}, which is the complete set of aliases, as they are called, for this 2^{3-1} fractional factorial design. With I=123, we can easily generate all the columns of the half-fraction design 2^{3-1}.

It also should be noted that we can replace any design generator by its negative counterpart and have an equivalent, but different fractional design. The fraction generated by positive design generators is sometimes called the principal fraction.

The confounding pattern described by 1=23, 2=13, and 3=12 tells us that all the main effects of the 2^{3-1} design are confounded with two-factor interactions. That is the price we pay for using this fractional design. Other fractional designs have different confounding patterns; for example, in the typical quarter-fraction of a 2^6 design, i.e., in a 2^{6-2} design, main effects are confounded with three-factor interactions (e.g., 5=123) and so on. In the case of 5=123, we can also readily see that 15=23 (etc.), which alerts us to the fact that certain two-factor interactions of a 2^{6-2} are confounded with other two-factor interactions.

A convenient summary diagram of the discussion so far about the 2^{3-1} design is as shown in Figure D.2:

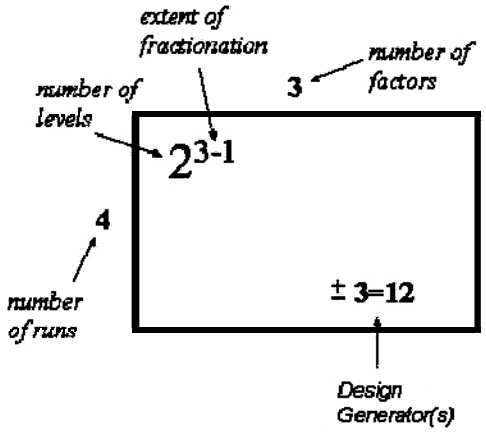

Figure D.2- Essential Elements of a 23-1 Design

The next section will add one more item to the above box, and then we will be able to select the right two-level fractional factorial design for a wide range of experimental tasks.

Fractional factorial design specifications and design resolution

We considered the 2^{3-1} design in the previous section and saw that its generator written in "I = ... " form is {I = +123}. Next we look at a one-eighth fraction of a 2^8 design, namely the 2^{8-3} fractional factorial design. Using a diagram similar to Figure D.2, we have the following:

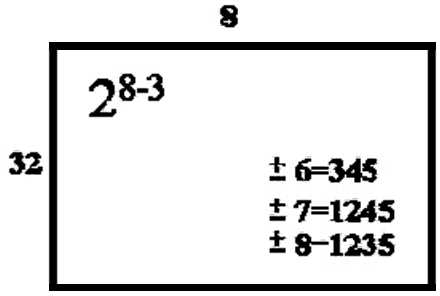

Figure D.3- Essential Elements of a 2^{3-1} Design

Figure D.3 shows us that a 2^{8-3} design has 32 runs, not including center point runs, and eight factors. There are three generators since this is a $1/8=2^{-3}$ fraction (in general, a 2^{k-p} fractional factorial needs *p* generators which define the settings for *p* additional factor columns to be added to the 2^{k-p} full factorial design columns.

In order to construct the design, we perform the following steps:

-Write down a full factorial design in standard order for *k-p* factors (8-3=5 factors for the example above). In the specification above we start with a 2^5 full factorial design. Such a design has $2^5=32$ rows.

-Add a sixth column to the design table for factor 6, using 6=345 (or 6=-345) to manufacture it (i.e., create the new column by multiplying the indicated old columns together).

-Do likewise for factor 7 and for factor 8, using the appropriate design generators.

-The resultant design matrix gives the 32 trial runs for an 8-factor fractional factorial design. (When actually running the experiment, we would of course randomize the run order.

We note further that the design generators, written in 'I = ...' form, for the principal 2^{8-3} fractional factorial design are: { I = + 3456; I = + 12457; I = +12358 }.

These design generators result from multiplying the "6 = 345" generator by "6" to obtain "I = 3456" and so on for the other two generators.

The total collection of design generators for a factorial design, including all new generators that can be formed as products of these generators, is called a defining relation. There are seven "words", or strings of numbers, in the defining relation for the 2^{8-3} design, starting with the original three generators and adding all the new "words" that can be formed by multiplying together any two or three of these original three words. These seven turn out to be I = 3456 = 12457 = 12358 = 12367 = 12468 = 3478 = 5678. In general, there will be $(2^p - 1)$ words in the defining relation for a 2^{k-p} fractional factorial.

The length of the shortest word in the defining relation is called the resolution of the design. Resolution describes the degree to which estimated main effects are aliased (or confounded) with estimated 2-level interactions, 3-level interactions, etc.

The length of the shortest word in the defining relation for the 2^{8-3} design is four. This is written in Roman numeral script, and subscripted as 2^{8-3}_{IV}. Note that the 2^{3-1} design has only one word, "I = 123" (or "I = -123"), in its defining relation since there is only one design generator, and so this fractional factorial design has resolution three; that is, we may write 2^{3-1}_{III}. Now Figure D.3 may be completed as shown in Figure D.4.

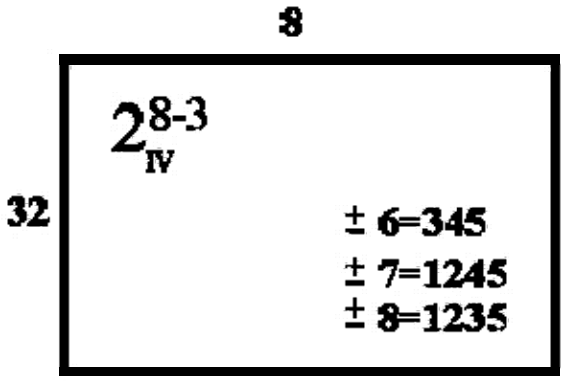

Figure D.4- Essential Elements of a 2^{3-1} Design

The design resolution tells us how badly the design is confounded. Previously, in the 2^{3-1} design, we saw that the main effects were confounded with two-factor interactions. However, main effects were not confounded with other main effects. So, at worst, we have 3=12, or 2=13, etc., but we do not have 1=2, etc. In fact, a resolution II design would be pretty useless for any purpose whatsoever!

Similarly, in a resolution IV design, main effects are confounded with at worst three-factor interactions. We can see, in Figure D.4, that 6=345. We also see that 36=45, 34=56, etc. (i.e., some two-factor interactions are confounded with certain other two-factor interactions) etc.; but we never see anything like 2=13, or 5=34, (i.e., main effects confounded with two-factor interactions).

The complete confounding pattern, for confounding of up to two-factor interactions, arising from the design given in Figure D.4 is

34 = 56 = 78

35 = 46

36 = 45

37 = 48

38 = 47

57 = 68

58 = 67

All of these relations can be easily verified by multiplying the indicated two-factor interactions by the generators. For example, to verify that 38= 47, multiply both sides of 8=1235 by 3 to get 38=125. Then, multiply 7=1245 by 4 to get 47=125. From that it follows that 38=47.

For this 2^{8-3}_{IV} fractional factorial design, 15 two-factor interactions are aliased (confounded) in pairs or in a group of three. The remaining 28 - 15 = 13 two-factor interactions are only aliased with higher-order interactions (which are generally assumed to be negligible). This is verified by noting that factors "1" and "2" never appear in a length-4 word in the defining relation. So, all 13 interactions involving "1" and "2" are clear of aliasing with any other two factor interaction. If one or two factors are suspected of possibly having significant first-order interactions, they can be assigned d in such a way as to avoid having them aliased.

A resolution IV design is "better" than a resolution III design because we have less-severe confounding pattern in the 'IV' than in the 'III' situation; higher-order interactions are less likely to be significant than low-order interactions. A higher-resolution design for the same number of factors will, however, require more runs and so it is worse than a lower order design in that sense.

Similarly, with a resolution V design, main effects would be confounded with four-factor (and possibly higher-order) interactions and two-factor interactions would be confounded with certain three-factor interactions. To obtain a resolution V design for 8 factors requires more runs than the 2^{8-3} design. One option, if estimating all main effects and two-factor interactions is a requirement, is a 2^{8-2}_{V} design..

There are other 2^{8-3}_{IV} fractional designs that can be derived starting with different choices of design generators for the "6", "7" and "8" factor columns. However, they are either equivalent (in terms of the number of words of length of length of four) to the fraction with generators 6 = 345, 7 = 1245, 8 = 1235 (obtained by re-labeling the factors), or they are inferior to the fraction given because their defining relation contains more

words of length four (and therefore more confounded two-factor interactions). For example, the 2_{IV}^{8-3} design with generators 6 = 12345, 7 = 135, and 8 = 245 has five length-four words in the defining relation (the defining relation is I = 123456 = 1357 = 2458 = 2467 = 1368 = 123478 = 5678). As a result, this design would confound more two factor-interactions (23 out of 28 possible two-factor interactions are confounded, leaving only "12", "14", "23", "27" and "34" as estimable two-factor interactions).

As an example of an equivalent "best" 2_{IV}^{8-3} fractional factorial design, obtained by "re-labeling", consider the design specified in Figure D.5. This design is equivalent to the design specified in Figure D.4 after re-labeling the factors as follows: 1 becomes 5, 2 becomes 8, 3 becomes 1, 4 becomes 2, 5 becomes 3, 6 remains 6, 7 becomes 4 and 8 becomes 7.

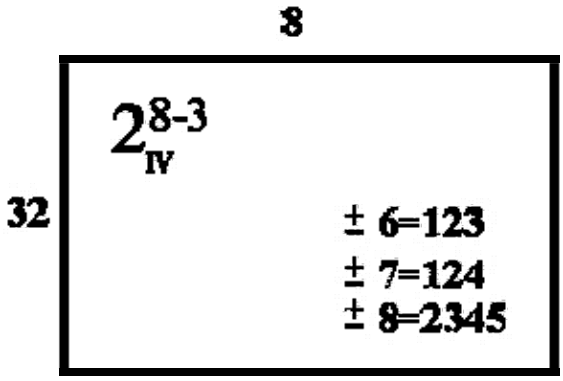

Figure D.5- Essential Elements of a 2^{3-1} Design

Design Resolution Summary

The meaning of the most prevalent resolution levels is as follows:

Resolution III Designs

Main effects are confounded (aliased) with two-factor interactions.

Resolution IV Designs

No main effects are aliased with two-factor interactions, but two-factor interactions are aliased with each other.

Resolution V Designs

No main effect or two-factor interaction is aliased with any other main effect or two-factor interaction, but two-factor interactions are aliased with three-factor interactions.

Table D.5 summarizes a collection of useful fractional factorial designs that, for a given k (from 3 to 7) and p, maximize the possible resolution and minimize the number of short words in the defining relation (which minimizes two-factor aliasing). The term for this is "minimum aberration".

Table D.5: Summary of Useful Fractional Factorial Designs

Number of Factors, k	Design Specification	Number of Runs N
3	2_{III}^{3-1}	4
4	2_{IV}^{4-1}	8
5	2_{V}^{5-1}	16
5	2_{III}^{5-2}	8
6	2_{VI}^{6-1}	32
6	2_{IV}^{6-2}	16
6	2_{III}^{6-3}	8
7	2_{VII}^{7-1}	64
7	2_{IV}^{7-2}	32
7	2_{IV}^{7-3}	16
7	2_{III}^{7-4}	8

D-Optimal Designs

D-optimal designs are one form of design provided by a computer algorithm. These types of computer-aided designs are particularly useful when classical designs do not apply. Unlike standard classical designs such as factorials and fractional factorials, D-optimal design matrices are usually not orthogonal and effect estimates are correlated.

These types of designs are always an option regardless of the type of model the experimenter wishes to fit (for example, first order, first order plus some interactions, full quadratic, cubic, etc.) or the objective specified for the experiment (for example,

screening, response surface, etc.). D-optimal designs are straight optimizations based on a chosen optimality criterion and the model that will be fit. The optimality criterion used in generating D-optimal designs is one of maximizing |X'X|, the determinant of the information matrix X'X.

This optimality criterion results in minimizing the generalized variance of the parameter estimates for a pre-specified model. As a result, the 'optimality' of a given D-optimal design is model dependent. That is, the experimenter must specify a model for the design before a computer can generate the specific treatment combinations. Given the total number of treatment runs for an experiment and a specified model, the computer algorithm chooses the optimal set of design runs from a *candidate set* of possible design treatment runs. This candidate set of treatment runs usually consists of all possible combinations of various factor levels that one wishes to use in the experiment.

In other words, the candidate set is a collection of treatment combinations from which the D-optimal algorithm chooses the treatment combinations to include in the design. The computer algorithm generally uses a stepping and exchanging process to select the set of treatment runs. The reasons for using D-optimal designs instead of standard classical designs generally fall into two categories:

1-standard factorial or fractional factorial designs require too many runs for the amount of resources or time allowed for the experiment

2-the design space is constrained (the process space contains factor settings that are not feasible or are impossible to run).

References

Abdassah, D., Siregar, S., and Kristanto, D. , "The Potential of Carbon Dioxide Gas Injection Application in Improving Oil Recovery," paper SPE 64730 presented at International Oil and Gas Conference and Exhibition in Beijing, China, 7-10 November 2000.

Alston, R. B., Kokolis, G. P., and James, C. F., " CO_2 Minimum Miscibility Pressure: A Correlation for Impure CO_2 Streams and Live Oil Systems," SPE Journal, p. 268-274, April, 1985.

Bachu, S., Gunter, W.D., and Perkins, E.H., "Aquifer Disposal of CO_2: Hydrodynamic and Mineral Trapping," Energy Conversion Management, Vol. 35, No. 4, p. 269-279, 1994.

Bachu, S., "Sequestration of CO_2 in Geological Media: Criteria and Approach for Site Selection in Response to Climate Change," Energy Conversion Management, No.41, p. 953-970, 2000.

Bachu, S., and Stewart, S., "Geological Sequestration of Anthropogenic Carbon Dioxide in the Western Canada Sedimentary Basin: Solubility Analysis," Journal of Canadian Petroleum Technology, Vol. 41, No. 2, p. 32-40, 2002.

Bachu, S., Shaw, J. C., and Pearson, R. M., "Estimation of Oil Recovery and CO_2 Storage Capacity in CO_2 EOR Incorporating the Effect of Underlying Aquifers," paper SPE 89340, presented at the SPE/DOE Fourteenth Symposium on Improved Oil recovery held in Tulsa, Oklahoma, 17-21 April, 2004.

Baker, L. E., “Three-Phase Relative Permeability Correlations,” paper SPE 17369, presented at SPE/DOE Enhanced Oil Recovery Symposium, Tulsa, Oklahoma, 17-20 April, 1988.

Bank, G. C., Riestenberg, D., Koperna,, G. J., "CO_2-Enhanced Oil Recovery Potential of the Appalachian Basin," paper SPE 111282 presented at the Eastern Regional Meeting in Lexington, Kentucky, 17-19 October 2007.

Benson, S. M., "Monitoring Carbon Dioxide sequestration in Deep Geological Formations for Inventory Verification and Carbon Credits," paper SPE 102833 presented at the SPE Annual Technical Conference and Exhibition held in San Antonio, TX, November 2006.

Baklid, A., Korbol, R., and Owren, G., "Sleipner Vest CO_2 Disposal, CO_2 Injection into a Shallow Underground Aquifer," paper SPE 36600 presented at SPE Annual Technical Conference and Exhibition, Denver, Colorado, 6-9 October, 1996.

Bank, G. C., Riestenberg, D., and Koperna, G. J., "CO_2-Enhanced Oil Recovery Potential of the Appalachian Basin," paper SPE 111282 presented at the SPE Eastern Regional Meeting in Lexington, Kentucky, 17-19 October, 2007.

Bradshaw, J., Allinson G., Bradshaw B. E., Nguyen V., Rigg A. J., Spencer L., and Wilson P.," Australia’s CO_2 geological storage potential and matching of emission sources to potential sinks," Energy, No. 29, p. 1621-1632, March 2004.

Bryant, E.: *Climate Process and Change*, Cambridge University Press, Cambridge, UK, p. 209, 1997.

Chaback, J. J., and Williams, M. L., "Phase Equilibria in the SACROC Oil/CO_2 System," SPE Reservoir Engineering, Vol. 3, No. 1, p.103-111, February 1988.

Chadwick R. A., Zweigel P., Gregersen U., Kirby G. A., Holloway S., and Johannessen, P. N., "Geological Reservoir Characterization of a CO_2 Storage Site: The Utsira Sand, Sleipner, Northern North Sea," Energy, Vol. 29, p. 1371–1381, 2004.

Christensen, J. R., Larsen, M., and Nicolaisen, H., "Compositional Simulation of Water-Alternating-Gas Processes," paper SPE 62999 presented at SPE Annual Technical Conference and Exhibition, Dallas, Texas, 1-4 October, 2000.

Christensen, J. R., Stenby, E. H., and Skauge, A., "Review of WAG Field Experience," SPE Reservoir Evaluation & Engineering, Vol. 4, No. 2, p. 97-106, April 2001.

Coats, K. H., "Simulation of Gas Condensate Reservoir Performance," Journal of Petroleum Technology, p.1870-1886, October 1985.

Coats, K. H., and Smart, G. T., "Application of a Regression-Based EOS PVT Program to Laboratory Data," Soc. Pet. Eng. Reservoir Engineering, p. 277-290, May 1986.

Corey, A. T., "The Interrelation Between Gas and Oil relative Permeabilities," Producers Monthly, p.38-41, November 1954.

Croarkin C., and Tobias, P., *NIST/SEMATECH e-Handbook of Statistical Methods*, http://www.itl.nist.gov/div898/handbook/, 2006.

Cronquist, C., "Contracts and Grants for Cooperative Research on Enhanced Oil and Gas Recovery and Improved Drilling Methods," U.S. DOE Progress Review No. 12, BERC, Bartlesville, p. 21-24, December 1977.

Cronquist, C., "Carbon Dioxide Dynamic Miscibility with Light Reservoir Oils," paper presented at the U.S. DOE Annual Symposium, Tulsa, August 28-30, 1978.

Danesh, A., *PVT and Phase Behavior of Petroleum Reservoir Fluids*, Elsevier Science, B. V., Amsterdam, 1998.

Davison, J. E., Freund, P. and Smith, A.: *Putting Carbon Back in the Ground*, IEA Greenhouse Gas R&D Program, Cheltenham, U.K., ISBN1 89837328, 2001.

Design-Expert ®, Version 6.0.11, Stat-Ease, Inc., 2005.

Delshad, M., and Pope, G. A., "Comparison of the three-Phase oil relative Permeability Models," Transport in Porous Media, Vol. 4, p. 59-83, 1989.

Doughty, C., Pruess, K., and Benson, S., "Flow Modeling for the Frio Brine Pilot," Fourth Annual Conference on Carbon Capture & Sequestration, Alexandria, VA, 2-5 May, 2005.

Dria, D.E., Pope, G.A., and Sepehrnoori, K., "Three-Phase Gas/Oil/Brine Relative Permeabilities Measured Under CO_2 Flooding Conditions," SPE Reservoir Engineering, Vol. 8, No. 2, p. 143, May 1993.

Dunyushkin, I. I. and Namiot, A. Y., "Mixing Conditions of Oil with Carbon Dioxide," Neft. Khozyaistov, p. 59-61, March 1978.

Edwards, K. A., Anderson, B., and Reavie, B., "Horizontal Injectors Rejuvenate Mature Miscible Flood-South swan Hills Field," paper SPE 77302 presented at the SPE Permian Basin Oil and Gas Recovery Conference, Midland, Texas, 15-16 May, 2002.

Elsayed, S. A., Baker, R., Churcher, P. L., and Edmunds, A. S., "A Multidisciplinary reservoir Characterization and simulator Study of the Weyburn Unit, Saskatchewan, Canada," paper SPE 25852 presented at the SPE Rocky Mountain Regional/ Low permeability Reservoirs Symposium, Denver, Colorado, April 12-14, 1993.

Emberley, S., Hutcheon, I., Shevalier, M., Durocher, K., Gunter, W.D., and Perkins, E. H., "Geochemical Monitoring of Fluid-Rock interaction and CO_2 Storage at the Weyburn CO_2-Injection Enhanced Oil Recovery Site," Proceeding 6th Greenhouse Gas Technologies Conference, Kyoto, Japan, 1-4 October, 2002.

Ennis-King, J., Paterson, L., "Engineering Aspects of Geological Sequestration of Carbon Dioxide," paper SPE 77809 presented at the SPE Asia Pacific Oil and Gas Conference and Exhibition held in Melbourne, Australia, 8-10 October, 2002.

Freifeld, B. M., Trautz R.C., Kharaka Y.K., Phelps T.J., Myer L.R., Hovorka S.D., and Collins, D.J., "The U-tube: A Novel System for Acquiring Borehole Fluid Samples from a Deep Geologic CO_2 Sequestration Experiment," Journal of Geophysical Research-Solid Earth, Vol. 10, B10203, 2005.

GEM, Advanced Compositional Reservoir Simulator, Computer Modeling Group Ltd., 2004.

Garcia, J. E., "Density of Aqueous Solutions of CO_2," Lawrence Berkeley National Laboratory, report LBNL-49023, 9 pages, October 2001.

Ghomian, Y., Pope, G. A., and Sepehrnoori, K., " Field-scale Optimization of WAG Injection for Coupled CO_2-EOR and Sequestration," paper SPE 110639, will be presented at the 2008 SPE Improved Oil Recovery Symposium held in Tulsa, Oklahoma, USA, April 2008.

Ghomian, Y., Sepehrnoori, K., and Pope, G. A., "Reservoir Simulation of CO_2 Sequestration Pilot in Frio Brine, Formation, USA Gulf Coast," In press for publication in Energy Journal, Elsevier publications, 2008.

Ghomian, Y., Sepehrnoori, K., and Pope, G. A., "Optimization of Geological storage of CO_2 and Enhanced Oil Recovery," paper presented at SIAM conference on Mathematical & Computational Issues in the Geosciences, Santa Fe, NM, 19-22 March 2007.

Ghomian, Y., Pope, G. A., and Sepehrnoori, K., "Economical Co-optimization of CO_2 Sequestration and Enhanced Oil Recovery," Sixth Annual Conference on Carbon Capture & Sequestration Proceeding, Pittsburgh, PA, May 7-10, 2007

Glaso, G., "Generalized Minimum Miscibility Pressure Correlation," SPE Journal, Vol. 26, No. 6, p. 927-934, December 1985.

Guler, B., Wang, P., Delshad M., Pope, G. A., and Sepehrnoori, K., "Three- and Four-Phase Flow Compositional Simulations of CO_2/NGL EOR," paper SPE 71485 presented at the SPE Annual Technical Conference and Exhibition, New Orleans, Louisiana, 30 September-3 October, 2001.

Gunter, W. D., Wiwchar, B., and Perkins, E. H., "Aquifer Disposal of CO_2 Rich Greenhouses Gases: Extension of the Time Scale of Experiment for CO_2 - Sequestering Reactions by Geochemical Modeling," Mineralogy and Petrology, Vol. 59, p.121-140, 1997.

Gupta, N., Sass, B., Sminchak, J., Naymik, T., and Bergman, P., "Hydrodynamics of CO_2 Disposal in a Deep Saline Formation in the Midwestern United States," Proceedings of the 4th International Conference on Greenhouse Gas Control Technologies, Edited by Riemer, P., Eliasson, B., and Wokaun, A., Elsevier Science Ltd: p. 157–162, Amsterdam, 1999.

Heddle, G., Herzog, H., and Klett, M., "The Economics of CO_2 Storage," Report No. MIT LFEE 2003-003, Laboratory for Energy and the Environment, Massachusetts Institute of Technology, 2003.

Hendriks, C.A., and Block, K., "Underground Storage of Carbon Dioxide," Energy Conversion Management, Vol. 34, p. 949–957, 1993.

Herzog, H., Eliasson, B., and Karstad, O., "Capturing Greenhouse Gases," Scientific American, p.72–79, 2000.

Herzog, H., "What Future for Carbon Capture and Sequestration?," Environmental Science and Technology, Vol. 37, p. 148-153, 2001.

Hill, W. J., and Tinney, T. J., "CO_2 Operation plan, South Welch, Dawson County, Texas," paper SPE 27676 presented at the SPE Permian Basin Oil and Gas Recovery Conference, Midland, Texas, March 16-18, 1994.

Holm, L. W., and Josendal, V. A., "Mechanism of Oil Displacement by Carbon Dioxide," Journal of Petroleum Technology, p.1427-1436, December 1974.

Holm, L. W., and Josendal, V. A., "Effect of Oil Composition on Miscible Type Displacement by Carbon Dioxide," SPE Journal , p. 87-98, Febraury 1982.

Holtz, M.H., "Residual Gas Saturation to Aquifer Influx: A Calculation Method for 3-D Computer Reservoir Model Construction," paper SPE 75502 presented at SPE Gas Technology Symposium, Calgary, Alberta, Canada, May 2002.

Hovorka, S.D., Romero, M.L., Warne, A.G, Ambrose, W.A., Tremblay, T.A., Trevin˜o, R.H., and Sasson, D., "Sequestration of Greenhouse Gases in Brine Formations," The University of Texas at Austin, Bureau of Economic Geology, hypertext publication at: http://www.beg.utexas.edu/environqlty/co2seq/dispslsaln, 2000

Hovorka, S. D., Benson, S. M., Doughty, C., Freifeld, B. M., Sakurai, S., Daley, T. M., Kharaka, Y. K., Holtz, M. H., Trautz, R. C., Seay Nance, H., Myer, L. R., and

Knauss, K. G., "Measuring Permanence of CO_2 Storage in Saline Formations: the Frio Experiment," Environmental Geosciences, Vol. 13, No. 2, pp. 105-121, 2006.

Jacoby, R. H., and Berry Jr., V. J., "A Method for Predicting Depletion Performance of a Reservori Producing Volatile Crude Oil," Trans. AIME, Vol. 210, p. 27-33, 1957.

Jarrell, P. M., Fox, C.E., Stein, M. H., and Webb, S. L.: *Practical Aspects of CO_2 Flooding*, SPE Monograph Series, 2002.

Jassim, M. S., Rochelle, G. T., "Innovative Absorber/Stripper Configuration for CO_2 Capture by Aqueous Monoethanolamine," Ind. Eng. Chem.Res., Vol. 45, p. 2465-2472, 2006.

Jaubert, J.N., Avaullee, L., and Pierre, C. "Is It Still Necessary to Measure the Minimum Miscibility Pressure?," Industrial Engineering Chemistry Research, Vol. 41 , p. 303-310, 2002.

Jerauld, G. R., "General Three-Phase Relative Permeability Model for Purhoe Bay," paper SPE 39627, presented at 7th ADIPEC, Abu Dhabi, UAE, 13-16 October 1996.

Jerauld, G. R., and Rathmell, J.J., "Wettability and Relative Permeability of Prudhoe Bay: A Case Study in Mixed-Wet Reservoirs," SPE Reservoir Engineering, February 1997.

Jessen, K., Kovscek, A. R., and Orr, F. M., "Increasing CO_2 Storage in Oil recovery," Energy Conversion Management, No.46, p. 293–311, 2005.

Jessen, K., Wang, Y., Ermakov, P., Zhu, J., and Orr, F. M. Jr., "Fast Approximate Solutions for 1-D Multicomponent Gas Injection Problems," SPE Journal, Vol. 6, No. 4, p. 442-451, 2001.

Johns, R. T., and Orr, F. M. Jr., "Miscible Gas Displacements of Multi-component Oils," SPE Journal, Vol. 39, March 1996,

Johnson J. P. and Pollin J. S., "Measurement and Correlation of CO_2 Miscibility Pressures," paper SPE 9790 presented at the SPE/DOE Enhanced Oil Recovery Symposium, Tulsa, April 5-8, 1981.

Johnston, J. R., "Weeks Island Gravity Stable CO_2 Pilot," paper SPE/DOE 17351, presented at the SPE/DOE Symposium on Enhanced Oil Recovery, Tulsa, Oklahoma, April 17-20, 1988.

Khan, S. A., "An Expert System to Aid in Compositional Simulation of Miscible Gas Flooding, "Ph.D. dissertation, The University of Texas at Austin, 1992.

Kim, J. S., Dong, Y., and Rossen, W. R., "Steady-State Flow Behavior of CO_2," paper SPE/DOE 89351, presented at the Symposium on Improved Oil Recovery, Tulsa, Oklahoma, 17-21 April 2004.

Kleinstelber, S. W., "The Wertz Tensleep CO_2 Flood: Design and Initial Performance," JPT, Vol. 44, p. 630, May 1990.

Knox, P. R., Paine, J. G., and Hovorka, S. D., "Optimal Geological Environment for CO_2 Disposal in Brine Formations (Saline Aquifers) in the US-Pilot Experiment in the

Frio Formation, Houston Area," Bureau of Economic Geology, Report DOE/EA-000, April 2003.

Kovscek, A. R., "Screening Criteria for CO_2 Storage in Oil Reservoirs," Petroleum Science and Technology, Vol. 20, No. 7, p. 841-866, 2002.

Kovscek, A. R., and Cakici, M., D., "Geologic Storage of CO_2 and Enhanced Oil Recovery. II. Co-optimization of Storage and Recovery," Energy Conversion Management, Vol. 46, Issues 11-12, p. 1941-1956, 2005.

Knox, Paul R., Paine, Jeffery G., and Hovorka, S. D., "Optimal Geological Environment for CO_2 Disposal in Brine Formations (Saline Aquifers) in the US-Pilot Experiment in the Frio Formation, Houston Area," Bureau of Economic Geology, Report DOE/EA-000, p. 35, April 2003.

Kumar, A., Ozah, R., Noh, M., Pope, G. A., Bryant, S. L., Sepehrnoori, K., and Lake, L. W., "Reservoir Simulation of CO_2 Storage in Deep Saline Aquifers," paper SPE 89343 presented at the SPE/DOE Symposium on Improved Oil Recovery, Tulsa, 17-21 April, 2004.

Kumar, A., "A Simulation Study of Carbon Dioxide Sequestration in Deep Saline Aquifers," M.Sc. Thesis, University of Texas at Austin, p.192, 2004.

Lake, L. W., and Walsh, M.: *A Generalized Approach To Primary Hydrocarbon Recovery Of Petroleum Exploration & Production*, Elsevier Science B. V., Amsterdam, 2003.

Lake, L. W.: *Enhanced Oil Recovery*, Prentice Hall Englewood Cliffs, NJ, 1989.

Land. C. S., "Comparison of Calculated and Experimental Imbibition Relative Permeability," paper SPE 3360 presented at the Rocky Mountain Regional Meeting, Billings, Montana, June 2-4, 1971.

Law, D.H-S., and Bachu, S., "Hydro Geological and Numerical Analysis of CO_2 Disposal in Deep Aquifers in the Alberta Sedimentary Basin," Energy Conversion Management, Vol. 37, p. 1167–1174, 1996.

Lee, J. I., Astete, E. L., and Jerhoff, T. F., "Performance Review of Brazeau River Nisku dry-Gas Miscible Flood Projects," Soc. Pet. Eng. Reservoir Engineering, p. 29-34, February 1994.

Leonard, J. "EOR Set to Make Significant Contribution," Oil & Gas Journal, Vol. 82., p. 83, April 2, 1984.

Lim, M. T., Khan, S. A., Sepehrnoori, K., and Pope, G. A., "Simulation of Carbon Dioxide Flooding Using Horizontal Wells," paper SPE 24929 presented at the SPE Annual Technical Conference and Exhibition, Washington D.C., October 4-7, 1992.

Lim, M. T., Pope, G. A., and Sepehrnoori, K., "Mechanistic Study of Carbon Dioxide Flooding Using Horizontal Wells," paper SPE/DOE 27807 presented at the SPE/DOE Ninth Symposium on Improved Oil Recovery, Tulsa, Oklahoma, April 17-20, 1994.

Lucia F. J., and Fogg G. E., "Geological/Stochastic Mapping of Heterogeneity in a Carbonate Reservoir," Journal of Petroleum Technology, Vol. 42, No.10, p. 1298, October 1990.

Malik, Q. M., and Islam, M. R., "CO_2 Injection in the Weyburn Field of Canada: Optimization of Enhanced Oil Recovery and Greenhouse Gas Storage With Horizontal Wells," paper SPE 59327 presented at the SPE/DOE eighth Symposium on Improved Oil Recovery, Tulsa, Oklahoma, April 3-5, 2000.

McLean, B., "Initial Thoughts on Safe and Effective Deployment of Geologic Sequestration," Proceeding of third Annual Conference on Carbon Capture and Sequestration, DOE/NETL, Alexandria, VA, 2004.

Montgomery, D. C.: *Design and Analysis of Experiments*, 5th Edition, John Wiley & Sons, New York, 2001.

Moritis, G. "EOR Increases 24% Worldwide; Claims 10% of U.S. Production," Oil & Gas Journal. Vol. 90, issue16, p. 51, April 20, 1992.

Moritis, G. "EOR Dips in U.S. But Remains a Significant Factor," Oil & Gas Journal, Vol. 92, No. 39, p. 51, September 26, 1994.

Moritis, G., "More CO_2 Floods Start up in West Texas," Oil & Gas Journal, Vol. 94, No. 34, p. 87, August 19, 1996.

Moritis, G., "EOR Oil Production Up Slightly," Oil & Gas Journal, Vol. 96, No. 16, p. 49, April 20, 1998.

Moritis, G., "EOR Weathers Low Oil Prices.(Statistical Data Included)," Oil & Gas Journal, Vol. 98, No. 12, p. 39, March 20, 2000.

Moritis, G., "California Steam EOR Produces Less; Other EOR Continues," Oil & Gas Journal, Vol. 100, No. 15, p. 43, April 15, 2002.

Moritis, G., "EOR Continues to Unlock Oil Resources," Oil & Gas Journal, Vol. 102, No. 14, p. 45, April 12, 2004.

Moritis, G., "EOR Awaits New CO_2 Sources," Oil & Gas Journal, Vol. 105, No. 2, p. 15, January 8, 2007.

Murray, M. D., Frailey, S. M., and Lawal, A. S., "New Approach to CO_2 Flood: Soak Alternating Gas," paper SPE 70023 presented at the SPE Permian Basin Oil ad Gas Recovery Conference, Midland, Texas, May 15-16, 2001.

National Petroleum Council (NPC): "Enhanced Oil Recovery-An Analysis of the Potential for Enhanced Oil recovery from Known Fields in the United States-1976-2000," Washington, DC, December 1976.

Ngheim, L., Sammon, P., Grabenstetter, J., and Ohkuma, H., "Modeling CO_2 Storage in Aquifers with a Fully-Coupled Geochemical EOS Compositional Simulator," paper SPE 89474 presented at the SPE/DOE Fourteenth Symposium on Improved Oil Recovery, Tulsa, Oklahoma, April 17-21, 2004.

Nguyen, D. N., "Carbon Dioxide Geological Sequestration: Technical and Economic Reviews," paper SPE 81199 presented at the SPE/EPA/DOE Exploration and

Production Environmental Conference held in San Antonio, Texas, 10-12 March, 2003.

Nute, A. J., "Design and Evaluation of a Gravity-Stable, Miscible CO_2-Solvent Flood, Bay St. Elaine Filed," paper SPE 11506 presented at the SPE Middle East Oil Technical Conference, Manama, Bahrain, March 14-17, 1983.

Orr, F. M., and Jensen, C. M., "Interpretation of Pressure-Composition Phase Diagrams for CO_2/Crude Oil Systems," SPE Journal, p. 485-497, October 1984.

Ozah, R., Lakshminarasimhan S., Pope, G. A., Sepehrnoori, K., and Bryant, S. L., "Numerical Simulation of the Storage of Pure CO_2 and CO_2-H_2S Gas Mixtures in Deep Saline Aquifers," paper SPE 97255 presented at SPE Annual Technical Conference and Exhibition, Dallas, TX, 9-12 October 2005.

Paul, G.W., Lake, L.W., and Gould, T.L., "A Simplified Predictive Model for CO_2 Miscible Flooding," paper SPE 13238, presented at SPE Annual Technical Conference and Exhibition, Houston, Texas, 16-19 September 1984.

Pariani, G. J., "An Approach to Optimize Economics in a West Texas CO_2 Flood," JPT, Vol. 46, p. 984, September 1992.

Perry, G. A., "Weeks Island "S" Sand Reservoir B Gravity Stable Miscible CO_2 Displacement, Iberia Parish, Louisiana," paper SPE/DOE 10695 presented at the SPE/DOE Third Joint Symposium on Enhanced Oil Recovery, Tulsa, Oklahoma, April 4-7, 1982.

Pedersen, K. S., Fredenslund, A., Christensen, P.L., and Thomassen, P., "Viscosity of Crude Oils," Chemical Engineering Science Vol. 36, No. 6, 1984.

Pedersen, K. S., Thomassen, P., and Fredenslund, Aa., "Thermodynamics of Petroleum Mixtures Containing Heavy Hydrocarbons. Phase Behavior Calculations by Use of the SRK Equation of State," Ind. Eng. Chem., Process Des. Dev., Vol. 23, p.163-170, 1988.

Pedersen, K. S., and Christensen, P. L.: *Phase Behavior of Petroleum Reservoir Fluids*, CRC Press, Taylor & Francis Group, Florida, 2007.

Potter, G. F., "The Effects Of CO_2 Flooding on Wettability of West Texas Dolomitic Formations," paper SPE 16716 presented at the Annual Technical Conference and Exhibition, Dallas, Texas, 27-30 September 1987.

Prieditis, J., and Paulett, G. S., "CO_2 Foam Mobility Tests at Reservoir Conditions in San Andres Cores," paper SPE/DOE 24178 presented at the SPE/DOE Eighth Symposium on Enhanced Oil Recovery, Tulsa, Oklahoma, April 22-24, 1992.

"PVTSim 14 Method Documentation," Calsep, 2004.

Rathmell, J.J., Stalkup, F.I., and Hassinger, R.C., "A Laboratory Investigation of Miscible Displacement by Carbon Dioxide," paper SPE 3483 presented at Fall Meeting of the Society of Petroleum Engineers of AIME, New Orleans, Louisiana, 3-6 October, 1971.

Ravagnani, G., "Technical-Economic Modeling of CO_2 Sequestration Considering Injection in Mature Oil Fields," paper SPE 113414 presented at the Annual Technical Conference and Exhibition in Anaheim, California, 11-14 November, 2007.

Reichle, D., Houghton, J., and Benson, S., "Working Paper on Carbon Sequestration Science and Technology," Office of Science, Office of Fossil Energy, U.S. Department of Energy, http://www.doe.gov//, 1999.

Robinson, D. B., and Peng, D.-Y., "The Characterization of Heptanes and Heavier Fractions," GPA Research Report 28, Tulsa, 1978.

Rochelle, G., Jassim M., Beitler, C., Rueter, C., and Searcy, K., "Integrating MEA Regeneration with CO_2 Compression and Peaking to Reduce CO_2 Capture Costs," U.S. Department of Energy Report No. DE-FG02-04ER84111, June 2005.

Roper Jr., M. K., Pope, G. A., and Sepehrnoori, K., "Analysis of Tertiary Injectivity of Carbon Dioxide," paper SPE 23974 presented at the Permian Basin Oil and Gas Recovery Conference, Midland, Texas, 18-20 March, 1992.

Rossen, W. R., Zeilinger, S. C., Shi, J. X., and Lim, M. T., "Simplified Mechanistic Simulation of Foam Processes in Porous Media," SPE Journal Vol. 4, No.3, 1999.

Sakurai, S., Ramakrishnan T.S., Austin, B., Nadja, M., and Hovorka S.D., "Monitoring Saturation Changes of CO_2 Sequestration: Petrophysical Support of the Frio Brine Pilot Experiment," 46th Annual Logging Symposium Society of Petrophysicists and Well Log Engineers, New Orleans, Louisiana, 2005.

Scharlin, P., "Carbon Dioxide in Water and Aqueous Electrolyte Solutions," Vol. 62 of Solubility Data Series. Oxford University Press, International Union of Pure and Applied Chemistry, Oxford, UK, 1996.

Scharf, C., and Clemens, T., "CO_2-Sequestration Potential in Austrian Oil and Gas Fields," paper SPE 100176 presented at the Europec/EAGE Annual Conference and Exhibition in Vienna, Austria, 12-15 June, 2006.

Schechter, D. S., Putra, E., Baker, R. O., Knight, W. H., Mc Donald, W. P., Leonardo, P., and Rounding, C., "CO_2 Pilot Design and Water Injection Performance in the Naturally Fractured Spraberry Trend Area, West Texas," paper SPE 71605 presented at the SPE Annual Technical Conference and Exhibition, New Orleans, Louisiana, September 30-October 3, 2001.

Schneider, F.N., "Relative Permeability Studies of Gas-Water Flow Following Solvent Injection in Carbonate Rocks," SPE Journal, Vol. 16, No. 1, p. 23, February, 1976.

Sebastian, H. M., Wenger, R. S., and Renner, T. A., "Correlation for Minimum Miscibility Pressures for Impure CO_2 Streams," paper SPE/DOE 12648 presented at the SPE/DOE 4th Symposium on EOR, Tulsa, OK, April 15-18, 1984.

Shook, M., Li, D., Lake, L. W., "Scaling Immiscible Flow Through Permeable Media by Inspectional Analysis," Is Situ, Vol. 16, No. 4, p. 311-349, 1992.

Spiteri, E. J., and Juanes, R., "Impact of Relative Permeability hysteresis on the Numerical Simulation of WAG injection," paper SPE 89921 presented at SPE Annual Technical Conference and Exhibition, Houston, Texas, 26-29 September 2004.

Spiteri, E. J., Juanes, R., Blunt, M. J., and Orr, F. M., "Relative Permeability hysteresis: Trapping Models and Application to Geological CO_2 Sequestration," paper SPE 96448 presented at SPE Annual Technical Conference and Exhibition, Dallas, Texas, 9-12 October 2005.

Stalkup, F. I.: *Miscible Flooding Fundamentals*, Society of Petroleum Engineers Monograph Series, 1983.

Stalkup, F. I., "Effect of Gas Enrichement and Numerical Dispersion on Enriched Gas Drive Predictions," SPE Reservoir Engineering Vol. 5, No. 4, p. 647-655, 1990.

Stosur, G. J., Singer, M.I., Luhning, R. W., and Yurko, W.J., "Enhanced Oil Recovery in North America: Status, and Prospects," Energy Resources, Vol. 12, 429-437, 1990.

Taber, J., and Orr, M. F. Jr., "Contracts for EOR and Improved Drilling Technology," U.S. DOE Progress Review No. 37, BERC, Bartlesville, December 1983.

Taber, J.J., Martin, F.D., and Seright, R.S., "EOR Screening Criteria Revisited- Part 1: Introduction to Screening Criteria and Enhanced Recovery Field Projects," SPE Res. Eng., p. 189-198, August 1997.

Vikas, B., "Simulation of CO_2 Sequestration," M.Sc. Thesis, University of Texas at Austin, 2002.

Wang, Y., and Orr, F. M. Jr., "Calculation of Minimum Miscibility Pressure," paper SPE 39683 presented at the SPE/DOE Improved Oil Recovery Symposium, Tulsa, OK, 19-22 April, 1998.

Wang, G. C., "A Laboratory Study of CO_2 Foam Properties and Displacement Mechanism," paper SPE/DOE 12645 presented at the SPE/DOE Forth Symposium on Enhanced Oil Recovery, Tulsa, Oklahoma, April 15-18, 1984.

White, C.D., B.J. Willis, K. Narayanan, and S.P. Dutton, "Identifying and Estimating Significant Geologic Parameters with Experimental Design," SPE Journal, p.311-324, September 2001.

Yamasaki, A., "An Overview of CO_2 Mitigation Options for Global Warming-Emphasizing CO_2 Sequestration Options," Journal of Chemical Engineering of Japan, Vol. 36, No. 4, p. 361-375, April 2003.

Yang D., Tontiwachwuthikul P., and Gu, Y., "Interfacial Tensions of the Crude Oil + Reservoir Brine + CO_2 Systems at Pressures up to 31MPa and Temperatures of 27 °C and 58 °C," Journal of Chemical Engineering Data, No. 50, p. 1242-1249, 2005.

Yellig, W.F., and Metcalfe, R.S., "Determination and Prediction of CO_2 Minimum Miscibility Pressures," Journal of Petroleum Technology, Vol. 32, No. 1, p.160-168,, January 1980.

Yuan, H., Johns, R. T., Egwuenu, A. M., Dindoruk, B., "Improved MMP Correlations for CO_2 Floods Using Analytical Gas Flooding Theory," paper SPE/DOE 89359 presented at the Fourteenth Symposium on Improved Oil Recovery held in Tulsa, Oklahoma, April 17-21, 2004.

Zhang, P.Y., Huang, S., Sayegh, S., and Zhou, X. L., "Effect of Impurities on Gas-Injection Processes," paper SPE/DOE 89477, presented at the SPE/DOE Fourteenth Symposium on Improved Oil Recovery, Tulsa, Oklahoma, April 17-24, 2004.

Zaytsev, I.D., and Aseyev, G.G.: *Properties of Aqueous Solutions of Electrolytes*, CRC Press, Boca Raton, FL, p. 1729, 1992.